Spectroscopy of Prototypical Thin Film Mott Materials

Dissertation zur Erlangung des
naturwissenschaftlichen Doktorgrades
der Julius-Maximilians-Universität Würzburg

vorgelegt von
Philipp Scheiderer
aus Hardheim

Würzburg 2019

Eingereicht am: 31.01.2019
bei der Fakultät für Physik und Astronomie

1. Gutachter: Prof. Dr. Ralph Claessen
2. Gutachter: Prof. Dr. Friedrich Reinert
3. Gutachter: Prof. Dr. Hiroshi Kumigashira
der Dissertation

Vorsitzender Prof. Dr. Karl Brunner

1. Prüfer: Prof. Dr. Ralph Claessen
2. Prüfer: Prof. Dr. Matthias Bode
3. Prüfer: Prof. Dr. Hiroshi Kumigashira
4. Prüfer: Prof. Dr. Giorgio Sangiovanni
im Promotionskolloquium

Tag des Promotionskolloquiums: 26.07.2019

Doktorurkunde ausgehändigt am:................................

Abstract

The rich phase diagram of transition metal oxides essentially roots in the many body physics arising from strong Coulomb interactions within the underlying electron system. Understanding such electronic correlation effects remains challenging for modern solid state physics, therefore experimental data is required for further progress in the field. For this reason, spectroscopic investigations of prototypical correlated materials are the scope of this thesis. The experimental methods focus on photoelectron spectroscopy, and the test materials are the correlated metal $SrVO_3$ and the Mott insulator $LaTiO_3$, both of which are fabricated as high quality thin films.

In $SrVO_3$ thin films, a reduction of the film thickness induces a dimensional crossover from the metallic into the Mott insulating phase. In this thesis, an extrinsic chemical contribution from a surface over-oxidation is revealed that emerges additionally to the intrinsic change of the effective bandwidth usually identified to drive the transition. The two contributions are successfully disentangled by applying a capping layer that prevents the oxidation, allowing for a clean view on the dimensional crossover in fully stoichiometric samples. Indeed, these stoichiometric layers exhibit a higher critical thickness for the onset of the metallic phase than the bare and therefore over-oxidized thin films.

For $LaTiO_3$ thin films, the tendency to over-oxidize is even stronger. An uncontrolled oxygen diffusion from the substrate into the film is found to corrupt the electronic properties of $LaTiO_3$ layers grown on $SrTiO_3$. The Mott insulating phase is only detected in stoichiometric films fabricated on more suitable $DyScO_3$ substrates. In turn, it is demonstrated that a *controlled* incorporation of excess oxygen ions by increasing the oxygen growth pressure is an effective way of p doping the material which is used to drive the band filling induced Mott transition.

Gaining control of the oxygen stoichiometry in both materials allows for a systematic investigation of correlation effects in general and of the Mott transition in particular. The investigations are realized by various photoelectron spectroscopy techniques that provide a deep insight into the electronic structure. Resonant photoemission not only gives access to the titanium and vanadium related partial density of states of the valence band features, but also shows how the corresponding signal is enhanced by tuning the photon energy to the L absorption threshold. The enhanced intensity turns out to be very helpful for probing the Fermi surface topology and band dispersions by means of angular-resolved photoemission. The resulting momentum resolved electronic structure verifies central points of the theoretical description of the Mott transition, viz. the renormalization of the band width and a constant Luttinger volume in a correlated metal as the Mott phase is approached.

Zusammenfassung

Das reichhaltige Phasendiagramm von Übergansmetalloxiden ist im Wesentlichen auf Aspekte der Vielteilchenphysik zurückzuführen, welche durch starke Coulomb Wechselwirkungen im zugrundeliegenden Elektronensystem auftreten. Die Beschreibung solcher Korrelationseffekte stellt immernoch eine Herausforderung für die moderne Festkörperphysik dar, wobei für weitere Fortschritte experimentelle Daten nötig sind. Aus diesem Grund beschäftigt sich diese Arbeit mit spektroskopischen Untersuchungen an prototypischen korrelierten Materialien. Die experimentellen Methoden fokussieren sich dabei auf die Photoelektronenspektroskopie. Diese wird auf das korrelierte Metall $SrVO_3$ und dem Mott Isolator $LaTiO_3$ angewandt, welche beide als dünne Filme in hoher Qualität hergestellt werden.

Eine Verkleinerung der Schichtdicke kann in $SrVO_3$-Dünnfilmen einen dimensionsgetriebenen Übergang von der metallischen in die Mott-isolierende Phase induzieren. In dieser Arbeit konnte der extrinsische Beitrag einer Oberflächenoxidation identifiziert werden, der zusätzlich zu den intrinsischen Veränderungen der effektiven Bandbreite, die für gewöhnlich als Grund für den Phasenübergang angeführt werden, auftritt. Durch das Aufbringen einer Deckschicht wird die Oxidation verhindert. So kann der dimensionsinduzierte Übergang ohne extrinsische Einflüsse in stöchiometrischen Proben untersucht werden, die tatsächlich eine höhere kritische Schichtdicke für das Einsetzen des metallischen Verhaltens aufweisen als die freiliegenden und damit überoxidierten Dünnfilme.

Bei $LaTiO_3$-Dünnfilmen ist die Tendenz zur Überoxidation noch stärker. Eine unkontrollierte Diffusion von Sauerstoff aus dem Substrat in den Film verfälscht die elektronischen Eigenschaften von $LaTiO_3$-Schichten, die auf $SrTiO_3$ gewachsen werden. Die Mott-isolierende Phase kann nur in stöchiometrischen Filmen stabilisiert werden, die auf geeigneteren $DyScO_3$ Substraten hergestellt werden. Dahingegen kann eine *kontrollierte* p-Dotierung durch eine Erhöhung des Sauerstoffdrucks während des Wachstumsprozesses angewendet werden um den bandfüllungsinduzierten Mott-Übergang zu treiben.

Die Kontrolle der Sauerstoffstöchiometrie in beiden Materialien erlaubt eine systematische Untersuchung von Korrelationseffekten im Allgemeinen und des Mott-Übergangs im Speziellen. Dies wird durch die Anwendung diverser spezialisierter Techniken der Photoelektronenspektroskopie realisiert, welche weitreichende Einblicke in die elektronische Struktur gewähren. Resonante Photoelektronenspektroskopie macht nicht nur die partielle Zustandsdichte mit Titan- und Vanadium-Charakter im Valenzband zugänglich, sondern zeigt auch, wie stark die zugehörigen Signale an der L-Absorptionskante verstärkt werden. Diese Intensitätsverstärkung erweist sich zudem als hilfreich bei der Untersuchung der Fermiflächentopologie und Banddispersion mittels winkelaufgelöster Photoemission. Die daraus gewonnenen Erkenntnisse zur impulsaufgelösten, elektronischen Struktur bestätigen zentrale Punkte der theoretischen Beschreibung des Mott-Übergangs, nämlich eine Renormierung der Bandbreite und ein konstantes Luttingervolumen in einem korrelierten Metall, welches sich der Mott-Phase annähert.

Contents

1 Introduction

The achievements of solid state physics research throughout the last century set the basis for technological developments that became indispensable for today's daily life. One impressive example for the relevance of fundamental research is band theory that has been established almost 100 years ago and is still very successfully used to describe the behavior of electrons in modern semiconductor materials—the class of materials on which the transistors for our computers and smartphones are built. However, nature provides us with even more exciting materials that go beyond semiconductor physics. For instance transition metal oxides (TMOs) brought forward a plethora of phenomena such as high temperature superconductivity in cuprates, the colossal magnetoresistance in manganites, or the Mott transition in various $3d$ oxide compounds. One of the key features inducing the exciting physics in these materials is the short-range Coulomb interaction between valence electrons that is not considered in conventional band theory.

Let us briefly elaborate on these so called correlation effects. The terminology arises from the fact that materials with a sizable coupling between the electrons cannot be described by a mere sum over independent electrons, but cooperative phenomena—or in other words *correlations*—are at play. Catching these effects in a theoretical approach in principle requires a full many-body treatment of the system taking into account all microscopic degrees of freedom of the 10^{23} electrons per cubic centimeter in a solid. The dimension of the Hilbert spaces involved in a quantum mechanical description of this problem would be unrealistically large exceeding any available computation power. It is therefore clear that one cannot rely on an exact numerical solution to fully understand the physics of correlated electron systems. However, the energetics provided by the Mott-Hubbard model Hamiltonian can provide some vital insights. For instance the Mott metal-to-insulator transition can be understood by considering the balance between short range Coulomb interactions of the conduction electrons and the hybridization of their wave functions, where the first favors localization and the latter delocalization. This simple reasoning allows to explain some material trends, such as the Mott insulating behavior of several TMOs with $3d$ valence electrons. In such cases, the balance is often tipped toward an insulating solution, since $3d$ orbitals exhibit a rather strong spatial confinement.

To gain a deeper understanding of correlated electron systems, however, experimental investigations are indispensable. Spectroscopic methods are perfectly suited for this task since they can provide a direct access to a material's electronic properties—including correlation effects. For this reason photoelectron spectroscopy in various spectral ranges and modes, i.e. angle-resolved, also under resonant conditions, etc., is employed throughout this thesis. The materials of interest here are the prototypical correlated electron

compounds $SrVO_3$ and $LaTiO_3$ that are situated on the metallic and insulating side of the Mott transition, respectively. They are *prototypical* in the sense that their rather simple electron configuration of $3d^1$ grants a clean view on the correlation effect. At the same time this makes them well comparable to the most simple theoretical paradigm of the field, i.e. the single-band Hubbard model.

The samples are produced by state-of-the-art thin film epitaxy which is combined with a careful characterization of the structural and chemical properties. Thin film structures provide in general several advantages over bulk crystals. First, the thin film properties are easier to tune and in the used setup the surfaces can be directly analyzed *in situ*, i.e. without breaking vacuum conditions. The latter is especially useful since the materials under investigation tend to over-oxidize which can strongly obscure the view on the electronic properties. Thanks to this strategy hitherto unachieved sample qualities are realized and the impact of extrinsic chemical effects is strongly suppressed. Second, the synthesis of a material as a thin film is a crucial requirement for the development of any future device applications. Third, thin films offer new ways of tuning the electronic state of materials. In the case of the correlated metal $SrVO_3$, a reduction of the film thickness down to only several unit cells results in a crossover into the Mott insulating phase. Hence, the Mott transition can be controlled by an easily accessible additional external parameter. Another way to drive the Mott transition is chemical doping of $LaTiO_3$. But in this case the other way around, from the insulating into the metallic phase. In this case the material's tendency to over-oxidize is harnessed to render $LaTiO_3$ metallic by simply increasing the oxygen growth pressure.

For both materials thin film epitaxy is not only used to observe the Mott transition but also to manipulate the electronic state. Going even one step further one can think of using these achievements for the design of future devices that harness correlation effects for their functionality—a field that is often referred to as Mottronics. For such a perspective we can draw parallels to the accomplishments of semiconductor technology. Before we can expect functional devices, fundamental research is crucial to understand and describe the underlying physics, i.e. in our case the correlation effects in TMOs. Furthermore, sample quality and tunability is another integral point and drastic advances in the material science are yet required to ready TMOs for technological applications. This dissertation tackles these points by means of spectroscopic investigation of prototypical correlated electron materials.

Outline of the Thesis

In Chapter 2 the main experimental methods for sample fabrication and characterization are briefly introduced. Then the theoretical framework of electron correlations is set in Chapter 3 by a presentation of different approaches to describe the Mott transition arranged in historic order. The chapter continues with an overview over relevant prototypical materials. In Chapter 4 the afore mentioned thickness induced phase transition in thin $SrVO_3$ films is closely investigated. A complementary view is given in Chapter 5 by studying the band-filling induced Mott transition in excess oxygen doped $LaTiO_3$. The following Chapters 6 and 7 provide a deeper look into the electronic structure of both materials by resonant and angle-resolved photoemission.

2 Thin Film Growth and Characterization Techniques

Naturally, experimental studies in solid state physics rely on samples and techniques to gain insights into intriguing phenomena such as electron correlation effects. To set the basis for the investigations of these effects, several experimental methods are introduced in the following. The samples of interest for this thesis are transition metal oxide thin films, which are grown by pulsed laser deposition. To optimize the growth process, the structural properties of the films are characterized by several techniques such as high and low energy electron diffraction, atomic force microscopy, and x-ray diffraction. Furthermore, the electronic properties of the samples and especially the footprints of electron correlation effects are analyzed by photoelectron spectroscopy and other x-ray based electron spectroscopies.

2.1 Pulsed Laser Deposition

Pulsed laser deposition (PLD) became popular in the late 1980s, when it was successfully used to grow high-T_c superconductor thin films based on cuprate compounds [1, 2]. The main advantage of PLD over other epitaxy techniques, e.g., molecular beam epitaxy is the roughly stoichiometric material transfer from a target compound to the substrate surface. This is especially beneficial for the growth of multicomponent compounds—as in the case of cuprates—, since polycrystalline targets can be obtained rather easily by a solid state reaction. For the same reason, PLD is now widely used to grow ternary transition metal oxides, i.e. the materials of interest here.

To elaborate more on the thin film fabrication by PLD, a typical state-of-the-art PLD setup, as is used in our case, is sketched in Fig. 2.1 (a). The target material is evaporated by means of a pulsed excimer laser that is focussed on the target surface. The laser operates at a wavelength of $\lambda = 248\,\mathrm{nm}$ with a pulse duration in the $10\,\mathrm{ns}$ range, repetition rates up to $100\,\mathrm{Hz}$, and typical laser fluences of about $1\,\mathrm{J/cm^2}$ on the target surface [2, 3]. Provided that the absorption coefficient of the target is large enough, the laser light is absorbed in a small volume inducing ablation of material and a subsequent heating by incoming laser light, which results in the formation of a plasma plume (see Fig. 2.1 (b)) [4]. The plasma propagates perpendicular to the target surface toward the substrate with a kinetic energy of the particles as high as $100\,\mathrm{eV}$ [5]. Throughout the experiments the laser, target, and substrate were aligned in a central ablation geometry, i.e. the plasma plume impinged at the center of the substrate at an angle of $90°$ as sketched in Fig. 2.1 (a).
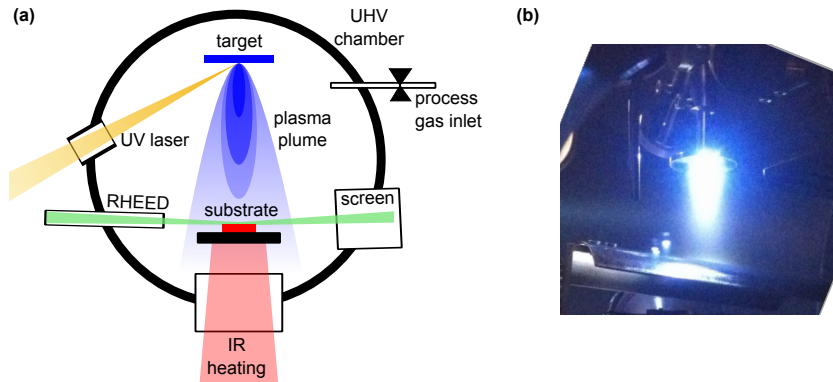
Fig. 2.1: (a) Sketch of the PLD growth setup. (b) Photograph of the plasma plume taken in the used setup in Würzburg.

As the plasma propagates from target to substrate, it can interact with the process gas allowing to manipulate the growth process in two ways. First, a gas atmosphere, e.g., oxygen which is often used for oxide materials, allows to change the chemical composition of the plasma and of the thin film directly [6]. Second, scattering of the plasma particles with the background gas results in a deceleration of particles and a change of their angular distribution, which can change the ratio of elements impinging on the substrate. In general, the latter effect is especially strong for elements with significantly different atomic masses [4, 6].

When the ablated material arrives on the substrate, thermal energy is required to allow for a rearrangement of the particles into a coherent lattice. This energy is provided by heating the substrate to the temperature T_s, which is realized in the present set-up by an infrared (IR) laser directed to the back side of the sample holder. Changing T_s influences the microscopic processes taking place during the formation of the thin film, namely adsorption, surface diffusion, nucleation at clusters or defects, and re-evaporation [7]. Depending on these processes and material specific properties of the involved compounds, different growth modes emerge. The relevant cases for this work are island (Volmer-Weber) and layer-by-layer (Franck-van-der-Merwe) growth. In the former growth mode, nucleated clusters at the surface grow into larger islands. In the latter case, single unit cell high layers form and are completely closed before the next layer starts to grow [7]. Such a layer-by-layer growth mode therefore allows for macroscopically large homogeneous areas and a control of the film thickness at unit cell precision. Thus, the growth parameters are usually chosen to favor the Franck-van-der-Merwe growth mode.

For the thin film growth in this work the main control parameters boil down to the laser fluence Φ, the oxygen growth pressure p_{O2}, and the substrate temperature T_s. They are not independent from each other, but throughout the experiments some general trends have evolved and it is instructive to briefly summarize them here.

The laser fluence can have a strong impact on the cation stoichiometry, however, this depends on the target material and has to be checked in each individual case. For

instance no strong dependence of the film properties on this parameter is detected for LaTiO$_3$, whereas an optimization of the laser fluence turned out to be crucial for the growth of SrVO$_3$ thin films. As will be discussed in chapters 4 and 5, the relevant oxygen growth pressures for the materials of interest are below 10^{-5} mbar. In this pressure regime scattering events between target and process gas play only a minor role and the impact of this parameter is mainly of chemical nature, i.e. p_{O2} essentially tunes the oxygen content of the films. For the substrate temperature, a minimal value of about 500 to 600°C is identified to achieve a coherently ordered lattice, lower temperatures result in disordered thin films.

2.2 Structural characterization

With optimized growth parameters, PLD allows for the fabrication of thin films of high structural quality with unit cell precision, as exemplified in the work of Scheiderer *et al.* [8] on LaAlO$_3$ thin films on SrTiO$_3$ substrates. To judge the quality of the prepared layers, however, several standard techniques to characterize their structural properties are required. Such methods are briefly introduced in the following from an application-oriented point of view.

2.2.1 High and Low Energy Electron Diffraction

The wave nature of electrons qualifies them as a probe in diffraction experiments, of which reflection high energy electron diffraction (RHEED) and low energy electron diffraction (LEED) have been employed throughout this thesis. In both techniques the probing depth of the electron beam is limited to the very first unit cells by the strong inelastic scattering of the electrons within the crystal. Due to this surface sensitivity, the techniques are perfectly suited to investigate the surface structure of thin films, for which the reciprocal space collapses to rods that are oriented along the normal of the two-dimensional surface.

Probing these reciprocal space rods can be realized by elastic scattering of the electrons described by the kinematic scattering theory. Here, Bragg reflexes emerge when the Laue condition is fulfilled, i.e. the change in wave vector $\Delta\vec{K}$ between in- ($\vec{k}_{in}$) and outgoing ($\vec{k}_{out}$) beam equals a reciprocal lattice vector $\vec{G}$.

It is helpful to visualize the condition for constructive interference by a simple geometrical considerations, widely known as the Ewald construction. To this end the tip of the incoming wave vector $\vec{k}_{in}$ is aligned to a reciprocal space rod at the sample surface and a sphere with radius $|\vec{k}_{in}|$ ($= |\vec{k}_{out}|$) is drawn around the tail of $\vec{k}_{in}$. When the sphere's surface intersects a reciprocal space rod, the Laue condition is satisfied since an outgoing wave vector $\vec{k}_{out}$—with tail at the sphere center and tip at the intersection point—is found, so that a reciprocal space vector $\vec{G}$ equals the transferred wave vector $\Delta\vec{K}$. Following these concepts, the RHEED and LEED diffraction patterns map the reciprocal space in different geometries, which we now discuss together with further experimental details.
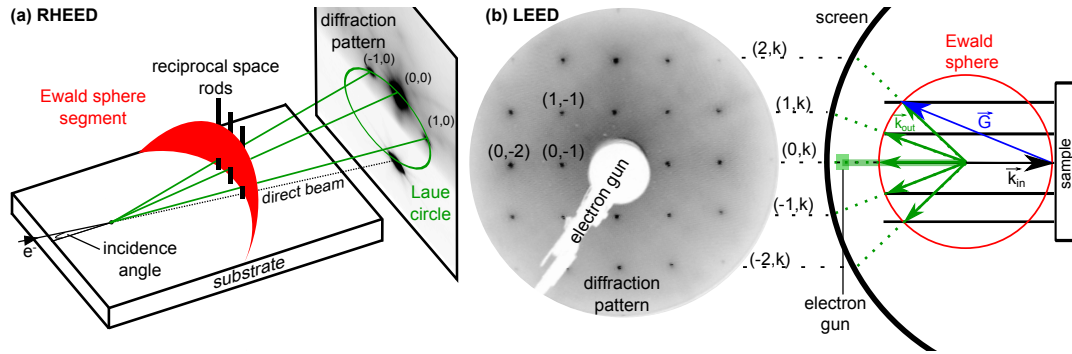
Fig. 2.2: (a) Sketch of the Ewald construction for a RHEED experiment including an actual interference pattern from the SrTiO$_3$ (001) surface. (b) Corresponding set-up of a LEED measurement. The exemplary data is obtained at an electron energy of 140 eV from a thin LaAlO$_3$ film grown on the SrTiO$_3$ (001) surface.

Reflection High Energy Electron Diffraction

The RHEED set-up is accommodated in the PLD chamber as sketched in Fig. 2.1 (a). For a better visualization of how the sample's reciprocal space is connected to the diffraction pattern, an Ewald construction is sketched in Fig. 2.2 (a). The incidence angle of the impinging electron beam is about two degrees, i.e. close to grazing incidence, and the kinetic energy of the electrons is 30 keV. The high kinetic energy enables the electrons to penetrate through a process gas atmosphere that is frequently required for PLD growth as mentioned above.

A typical diffraction pattern obtained from the (001) surface of the prototypical transition metal perovskite substrate SrTiO$_3$ is included in Fig. 2.2 (a). Due to the grazing incidence, a part of the electron beam passes by the substrate and is visible on the fluorescence screen, labeled as direct beam. The diffraction pattern itself usually consists of the specular reflection spot, i.e. the (0,0) Bragg peak, and the higher order (1,0) and (-1,0) spots that are all situated on the so called Laue circle. Note that Bragg peaks of second or even higher order can be observed in principle but require an increase of the incidence angle, which in turn reduces the surface sensitivity of the measurement.

Sharp spots in the diffraction pattern already signal a well ordered and atomically flat surface. When defects are introduced on the surface, the number of coherent scatterers is reduced and the reciprocal space rods broaden in the lateral directions (see Fig. 2.2 (a) for orientation). This causes a smearing-out of the diffraction patterns in direction of the surface normal, which is frequently used to judge the quality of thin films after PLD growth. Another typical feature of RHEED patterns are spots that are not situated along the Laue circle but are arranged differently, e.g., in a rectangular manner. Such deviating patterns usually signal the presence of islands on the surface. Due to the high kinetic energy of the electrons, the beam can penetrate through clusters as wide as 10 nm and the diffraction pattern obtained in such a transmission geometry is distinctively different from the pattern of a flat surface described above [9].

Due to the peculiar grazing incidence geometry of the RHEED experiment, diffraction patterns—and thereby information about the structural properties of the surface—can be obtained during the thin film growth process. Beyond qualitative arguments such as a smearing out of the Bragg peaks into streaks or the appearance of transmission spots as described above, the evolution of the specular spot intensity is used to monitor the film thickness with unit cell precision. Within a simple step density model, the surface roughness during the growth process is modulated periodically in a layer-by-layer growth mode, which is reflected by the intensity of the coherent diffraction signal [9, 10]. Initially the substrate surface is atomically flat, but as material is deposited on the surface, clusters with a height of a single unit cell form and the intensity of the Bragg peak is reduced due to diffuse scattering. When the relative coverage of the surface exceeds 50% the intensity recovers and peaks for a fully closed layer before the second unit cell is grown. Therefore, the detection of regular RHEED intensity oscillations during thin film growth signals a layer-by-layer growth mode and allows for a real time control of the film thickness with unit cell precision.

In general, the step density model describes the RHEED intensity oscillations very well, however, effects beyond this model such as phase shifts between the diffraction intensity and surface roughness oscillations have also been reported recently [11]. Therefore, further characterization by, e.g., atomic force microscopy (AFM) is required to check whether the film surface is fully closed when the growth process is stopped at an intensity maximum of the specular RHEED spot. Still, even when a phase shift is present the time required for one intensity oscillations always corresponds to the growth of one layer. Note that a layer corresponds to a thickness of a unit cell here, since the elements of a multicomponent film are co-supplied by evaporation from a single target compound.

Low Energy Electron Diffraction

While the gracing incidence geometry of RHEED allows for measurements during thin film growth, the insights into the surface's reciprocal space are heavily distorted by this perspective. More straightforward diffraction patterns, reflecting the 2D surface symmetry are obtained by LEED in a perpendicular incidence geometry as depicted in Fig. 2.2 (b). To avoid surface contamination, the samples are transferred under UHV conditions from the growth chamber into the LEED measurement chamber. The typical electron energies used here span from approx. 20 up to 200 eV. The detection of a LEED pattern already indicates a coherently ordered surface and—as in RHEED—the sharpness of the diffraction spots is a measure for the structural quality. Structural reconstructions of the thin film surface manifest in additional spots and signal an altered surface symmetry due to, e.g., adsorbed atoms. Throughout this thesis, reconstructions of the thin film surface are referred to the square surface lattice of the underlying (pseudo-)cubic perovskite substrate.

2.2.2 Atomic Force Microscopy

As mentioned above, regular RHEED intensity oscillations indicate a layer-by-layer growth mode but some ambiguity remains whether the top layer is fully or only partially closed. Atomic force microscopy (AFM) provides suitable information about the surface morphology that can eliminate these uncertainties. In the present case the AFM measurements are performed with a Bruker Dimension Icon apparatus operated in tapping mode imaging and—in contrast to the *in situ* electron diffraction experiments—in air.

The technique uses a cantilever with a sharp tip as a probe. The tip interacts with the microscopic force field of the sample's surface. The probe is scanned laterally across the surface where changes in the topography cause a detuning of the oscillation by the altered force field, which is detected by a deviating amplitude of the cantilever oscillation in our case. The probe's height is then regulated back to the initial conditions by means of a piezo crystal, which allows a point-by-point mapping of a height profile across the surface [12]. In this way, the apparatus reaches a height resolution in the Ångström range, which allows to map the single unit cell high steps of about 4 Å for the materials of interest here. Every substrate was checked by AFM before usage for thin film growth to guarantee an atomically flat step-and-terrace surface.

2.2.3 X-ray Diffraction

The characterization techniques described so far focus on the structural properties of the surface, whereas complementary x-ray diffraction (XRD) measurements provide bulk sensitive information about the crystal structure. X-rays typically penetrate several micrometers deep into a crystal, therefore the three dimensional reciprocal space of the thin films and the substrate is probed rather than only the reciprocal space rods of the surface as in electron diffraction [13]. For the experiments, a Bruker D8 Discovery apparatus is used that employs the Cu K_α line as a source of photons with a wavelength of $\lambda = 1.54$ Å. A weak satellite line from the Cu K_β transition gives rise to additional signals in the diffraction patterns, which are labeled as K_β throughout the thesis. Due to the bulk sensitivity of XRD, no sizable diffraction signal is obtained from ultrathin films of only several unit cells thickness. Depending on the cross sections of the x-ray diffraction process—that scales with the square of the atomic number of an element— the film thickness has to be chosen accordingly. As inferred from experience with the apparatus and the materials investigated here, thin films should be 20 uc thick at least.

The interference conditions that induce the diffraction pattern are again well described by the Laue condition and different measurement modes are employed to probe certain sections of the reciprocal space. The out-of-plane lattice constant, i.e. lattice spacing along the surface normal, is usually investigated in so-called $\omega - 2\Theta$ scans. In this mode the incidence and escape angle of the x-rays are kept equal to keep the transferred momentum $\Delta\vec{K}$ directed along the surface normal and thus scanning along the (00l)-direction in k-space. These scans already provide first insights into the structural phase of thin films and their epitaxial relation to the substrate. Furthermore, the limited number of scattering planes perpendicular to the surface normal in thin films induces

several side maxima, which are in this context often referred to as Laue oscillations. Similar to optical interference patterns of N-slit structures, the Laue oscillations allow to determine the number of coherently ordered scatterers along the surface normal, i.e. the film thickness in unit cells, thereby providing a complementary characterization to the RHEED growth monitoring.

To investigate the strain state of thin films, i.e. whether or not the film has adopted the in-plane lattice constants of the substrate, the inspection of $\Delta\vec{K}$ vectors with an in-plane component is required. This is realized by scanning the escape angle for different fixed incidence angles, which allows to construct a two dimensional reciprocal space map (RSM) with an in- and out-of-plane axis. In the present work, RSMs were collected around the (103) Bragg reflex of the (pseudo-)cubic perovskite substrates.

2.3 Photoelectron Spectroscopy

Photoelectron Spectroscopy (PES) is one of the most powerful and versatile techniques to investigate the occupied part of a material's electronic structure. It relies on the photoelectric effect, i.e. the emission of electrons upon irradiation of a solid with light, discovered by Hertz in 1887 [14]. Einstein's explanation of this effect in 1905 revealed the quantized nature of light [15]. Beginning in the 1950's, the photoelectric effect was harnessed by Kai Siegbahn who developed instruments and methods to analyze the binding energies of electrons in a material by using light in the x-ray regime—now known as electron spectroscopy for chemical analysis (ESCA) [16]. Ever since, the technique has been refined further and state-of-the-art PES experiments not only identify the core levels of materials that are characteristic for the respective elements and their chemical environment, the technique is also employed to map the dispersions of valence band Bloch states in crystals [17]. In this section, a brief introduction into the PES technique is given with special attention to the method's capability to catch the footprints of electron correlations. The section is based on several reviews and textbooks to which the interested reader is referred for further study [17–19].

Three Step Model

Photoemission is a photon-in electron-out process that can be described by a one-step transition. The incoming photon excites an electron from its initial state, i.e. a core level or valence Bloch state, into a final state wave function. These final states are often referred to as *time reversed LEED states* since they are free electron like in the vacuum, penetrate into the solid in a damped way, and match the unoccupied Bloch states in the sample—similar to an electron diffraction experiment, but with the source of electrons inside the sample [20]. For didactic reasons, however, the final state is simplified by dividing the PES process into three steps at this point: excitation of the electron from an initial state into an unoccupied Bloch state (final state) (1), travel to the surface under consideration of scattering events (2), and transmission through the surface into the vacuum (3) [21]. Before going into the details of each step of this
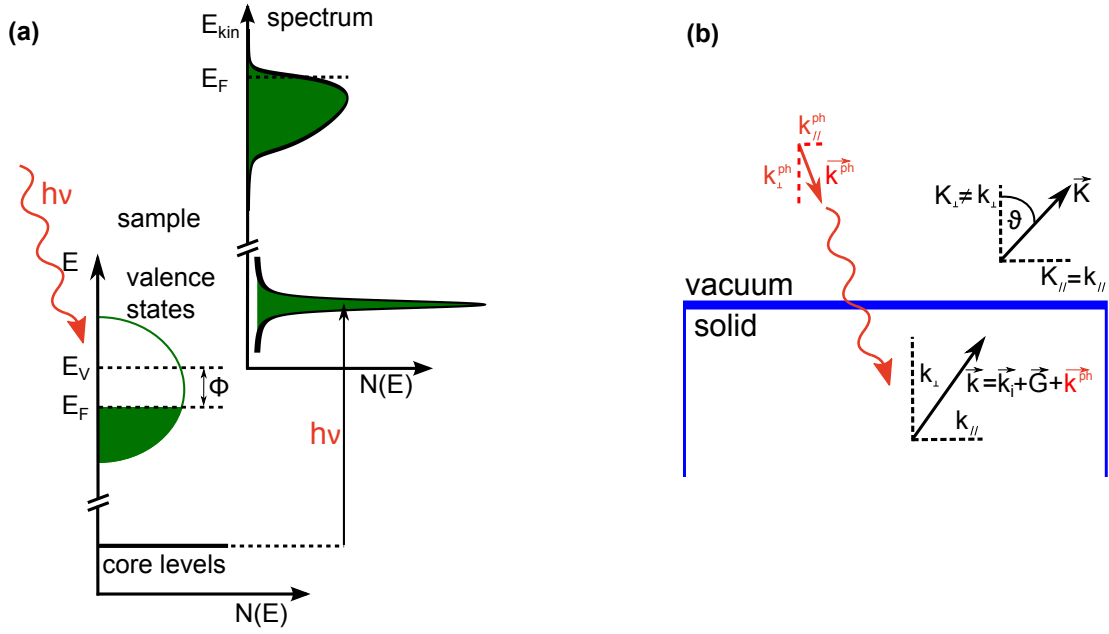
Fig. 2.3: Energetics (a) and kinematics (b) of the photoemission process, with the electron momentum $\vec{k}_i$ in the initial (Bloch) state, the momentum $\vec{k}$ after excitation but still inside the solid and the momentum $\vec{K}$ in vacuum.

model, simple arguments based on energy and momentum conservation are brought forward that already allow to understand the basic concept of PES.

Energetics and Kinematics

As sketched in the energy diagram depicted in Fig. 2.3 (a) the kinetic energy E_{kin} of the photoelectron in vacuum is connected to the binding energy E_B in the initial state and the photon energy $h\nu$ by

$$E_{kin} \; = \; h\nu \; - \; |E_B| \; - \; \Phi, \tag{2.1}$$

where Φ is the material's work function. Based on this simple relation, the measurement of the kinetic energy spectrum in a PES experiment essentially allows to map the occupied density of states of a solid. The core levels appear as broadened peaks in the spectrum that are usually described by a Voigt lineshape. The Lorentzian contribution is thereby caused by the finite lifetime of the core hole, whereas the instrumental resolution enters as a Gaussian distribution. More complex line shapes are possible, one example being screening of the core hole by metallic valence electrons. Such a screening manifests itself as an asymmetry on the high binding energy side in the spectrum, which is phenomenologically described by the *Doniach-Šunjić* function and can be used as an indication of conduction electrons in the sample [22]. The valence band states are also subject to these broadening effects and are cutoff by the Fermi distribution at the Fermi level E_F.

Complementary to the energetics, angle-resolved photoemission spectroscopy (ARPES) harnesses momentum conservation to measure the electronic dispersion of the valence band. To do so, PES spectra are measured for a series of emission angles ϑ, which can be realized by tilting the sample surface with respect to the analyzer.[1] Dispersing bands/excitations are then reflected by dispersing peaks or structures in these spectra. The geometrical situation (see 2.3 (b)) suggests to express the photoelectrons' momenta in vacuum $\vec{K}$ by its components parallel ($K_\parallel$) and perpendicular ($K_\perp$) to the sample surface. For these components the relations

$$\hbar K_\parallel = \sqrt{2mE_{kin}} \sin\vartheta \quad \text{and} \quad \hbar K_\perp = \sqrt{2mE_{kin}} \cos\vartheta \tag{2.2}$$

hold, where m is the free electron mass. Additionally to the photoelectrons' momenta in vacuum $\vec{K}$, the photoelectrons' momenta in the solid $\vec{k}$ and the electrons' momenta in the initial (Bloch) state $\vec{k}_i$ are introduced.

The momenta $\vec{K}$ are not identical to $\vec{k}_i$, but closely related to it. Let us first inspect the parallel component $K_\parallel$, because it is conserved in the transition from the solid into the vacuum (step 3 of the above mentioned three step model). Taking the photon momentum $\vec{k}_{ph}$ (orientation as sketched in Fig. 2.3 (b)) and a momentum transfer from the lattice by a reciprocal lattice vector $\vec{G}$ into account, one finds

$$k_{i,\parallel} = K_\parallel - k_\parallel^{ph} - G_\parallel = \frac{1}{\hbar} \sqrt{2mE_{kin}} \sin\vartheta - k_\parallel^{ph} - G_\parallel. \tag{2.3}$$

In the VUV regime ($h\nu$ below $\approx 100\,\text{eV}$) the photon momentum typically amounts only to several percent of the Brillouin zone (BZ) extension and can therefore be neglected [17]. Higher photon energies are employed in the course of this thesis though and therefore $\vec{k}_{ph}$ is explicitly included here.

In contrast to the parallel component, $K_\perp$ is not conserved at the solid-vacuum interface since the translational invariance fails in this direction. Further information about the dispersion relation of the final state is required to determine $k_{i,\perp}$, which is, however, not available in general. A pragmatic solution to this problem is to assume a free-electron like dispersion of the final states originating at an energy V_0 below the vacuum level. V_0 is also often referred to as *inner potential*, since one can picture it as a potential step at the surface. Based on this assumption together with equation 2.2 one finds [17]:

$$k_{i,\perp} = \frac{1}{\hbar} \sqrt{2m(E_{kin} \cos^2\vartheta + V_0)} - k_\perp^{ph} - G_\perp. \tag{2.4}$$

In experiment, values for V_0 are usually obtained by scanning $K_\perp$ across several BZs. The periodicity of the PES signal together with the lattice constant then allows to estimate a reasonable inner potential.

---

[1]State-of-the-art ARPES setups use a hemispherical analyzer that allows the parallel detection of the electron energy over a several degree wide angular range of ϑ.

Many Body Description

As we have just seen, the energy and momentum conservation relations already allow to connect a measured spectrum to the initial state properties to a great extent. However, a full quantum mechanical description that takes the many body nature of the initial and final states into account is required to catch the peculiar properties of correlated electron systems that are the scope of this thesis. Let us therefore evaluate the transition rate for the photoinduced excitation from the N-electron initial or ground state ($|i\rangle$) into a certain final state $|f\rangle$ composed of the remaining (N-1)-electron system and the photoelectron. Following Fermi's Golden rule we find:

$$w_{i \to f} = \frac{2\pi}{\hbar} \; |\left\langle \Psi_f^N \left| \mathcal{H}_{per} \right| \Psi_i^N \right\rangle|^2 \; \delta(E_f - E_i - h\nu), \tag{2.5}$$

with photon energy $h\nu$ and E_f (E_i) the energy of the final (initial) state. The perturbation $\mathcal{H}_{per}$ is in our case the electromagnetic field of the impinging photons, which can be introduced in the Hamiltonian by the canonical replacement $\vec{p} \to \vec{p} - e\vec{A}$ within a semi-classical description, where $\vec{A}$ is the electromagnetic vector potential. The unperturbed part of the Hamiltonian can be separated, which leaves

$$\mathcal{H}_{per} = -\frac{e}{2m} \left(\vec{A} \cdot \vec{p} + \vec{p} \cdot \vec{A} \right) + \frac{e^2}{2m} \vec{A}^2. \tag{2.6}$$

It is convenient to proceed within the second quantization formalism, where $c_{\vec{k}_j}^\dagger$ ($c_{\vec{k}_j}$) is the creation (annihilation) operator for an electron in state $\vec{k}_j$. $\mathcal{H}_{per}$ then takes the form:

$$\mathcal{H}_{per} \;=\; \sum_{m,n} \left\langle \vec{k}_m \left| \mathcal{H}_{per} \right| \vec{k}_n \right\rangle \; c_{\vec{k}_m}^\dagger \; c_{\vec{k}_n} \;=\; \sum_{m,n} M_{m,n} \; c_{\vec{k}_m}^\dagger \; c_{\vec{k}_n}. \tag{2.7}$$

Note that momentum conservation is taken into account here by the single-particle matrix element $M_{m,n}$, whereas energy conservation is given by the δ-function in equation 2.5.

A further simplification is possible within the so-called *sudden approximation*. In this limit, the kinetic energy of the photoelectron is large enough that it does not interact with the remaining (N-1) electron system. In other words, relaxation effects can be neglected since the photoelectron decouples instantaneously from the system. Typically, these assumptions are fulfilled for kinetic energies of the photoelectron above $10\,\text{eV}$, which is the case for all measurements presented in this thesis [23]. Within the sudden approximation the final state factorizes into a photoelectron in state $\vec{k}_f$ and an (N-1) electron system with a set of quantum numbers s and energy E_s^{N-1}:

$$|f\rangle = c_{\vec{k}_f}^\dagger \left| \Psi_s^{N-1} \right\rangle. \tag{2.8}$$

The initial state is the N-electron ground state (at temperature $T = 0$) and in analogy to the final state we express it by $\left| \Psi_0^N \right\rangle$ with energy E_0^N. Inserting these expressions into equation 2.5 and summation over all quantum numbers s yields the photoemission intensity:

$$I(\vec{k}_f, E_{kin}) = \frac{2\pi}{\hbar} \sum_s \left| \sum_{m,n} M_{m,n} \left\langle \Psi_s^{N-1} \left| c_{\vec{k}_f} c_{\vec{k}_m}^\dagger c_{\vec{k}_n} \right| \Psi_0^N \right\rangle \right|^2 \delta(E_{kin} + E_s^{N-1} - E_0^N - h\nu).$$
(2.9)

This relation can be further simplified since the initial state $\left| \Psi_0^N \right\rangle$ does not contain electrons in state $\vec{k}_f$. Therefore, the creation operator $c_{\vec{k}_m}^\dagger$ has to match this state, i.e. $c_{\vec{k}_f} c_{\vec{k}_m}^\dagger = \delta_{fm}$. Furthermore, the chemical potential $\mu = E_0^N - E_0^{N-1}$ is introduced and the abbreviation $\epsilon = E_{kin} - h\nu - \mu$ is used, which yields:

$$\begin{aligned} I(\vec{k}_f, \epsilon) &= \frac{2\pi}{\hbar} \sum_s \left| \sum_n M_{f,n} \left\langle \Psi_s^{N-1} \left| c_{\vec{k}_n} \right| \Psi_0^N \right\rangle \right|^2 \delta(\epsilon + E_s^{N-1} - E_0^{N-1}) \\ &= \frac{2\pi}{\hbar} \sum_n \left| M_{f,n} \right|^2 \cdot A^<(\vec{k}_n, \epsilon). \end{aligned}$$
(2.10)

Here, the electron removal spectral function $A^<(\vec{k}, \epsilon)$ is introduced, that is directly measured by PES as long as $M_{f,i}$ is only slowly varrying in the investigated parameter range (which is usually the case). The spectral function is the excitation spectrum generated upon removal of one electron from the N-electron system. For non-interacting electron systems, the initial state can be expressed by a product of single particle wave functions, hence $c_{\vec{k}_n} \left| \Psi_0^N \right\rangle$ results in an eigenstate of the (N-1) electron system and $A^<(\vec{k}, \epsilon)$ gives a single δ-function at an energy ϵ and momentum $\vec{k}_f$. Such systems are also straightforwardly described by the energetics and kinematics outlined above, however, if electron interactions are present this simple picture breaks down.

In an interacting system, the initial state does not simply factorize in single particle wave functions and $c_{\vec{k}_n} \left| \Psi_0^N \right\rangle$ is in general *not* an eigenstate of the remaining system, but is projected onto the $\left| \Psi_s^{N-1} \right\rangle$ basis. Therefore, multiple peaks may arise that can be detected in the photoemission spectrum. Measuring such spectra gives direct insight into the many body physics of interacting electron systems making PES one of the most powerful experimental techniques in this field.

To complement the experimental data available by PES, a comparison to theory is helpful. Usually, theoretical descriptions of many body effects are formulated in a Green's function approach:

$$G(\vec{k}, \epsilon) = \frac{1}{\epsilon - \epsilon_{\vec{k}}^0 - \Sigma(\vec{k}, \epsilon)},$$
(2.11)

with the complex self energy $\Sigma(\vec{k}, \epsilon) = \Sigma'(\vec{k}, \epsilon) + i\Sigma''(\vec{k}, \epsilon)$ containing correlation effects.

Such Green's functions are closely connected to the experimentally observable spectral function by [17]:

$$A^<(\vec{k}, \epsilon) = -\frac{1}{\pi} Im\, G(\vec{k}, \epsilon - i0^+) \cdot f(\epsilon, T) = -\frac{1}{\pi} \frac{\Sigma''(\vec{k}, \epsilon) \cdot f(\epsilon, T)}{\left(\epsilon - \epsilon_{\vec{k}}^0 - \Sigma'(\vec{k}, \epsilon)\right)^2 + \Sigma''(\vec{k}, \epsilon)^2}.$$

(2.12)

The Fermi-Dirac distribution $f(\epsilon, T)$ is introduced here since only the electron removal part of the spectral function is probed by PES. In this relation the imaginary part Σ'' of the self energy takes the role of a line width and the real part Σ' shifts the energy position. Therefore, PES in principle can measure the self energy, which in turn characterizes the many body physics in correlated electron systems.

Probing Depth

Having elaborated on the many body physics involved in the photoexcitation, we inspect the propagation of the photoelectron to the surface, i.e. step 2 of the three step model. On its way through the crystal the photoelectron is subject to inelastic scattering, e.g., by the excitation of plasmons. To account for these processes a Beer-Lambert-type damping of the elastic signal, i.e. the intensity of electrons that did not suffer an energy loss (I_0), is introduced:

$$I(z) = I_0 \cdot \exp\left(-\frac{z}{\lambda_0 \cos\vartheta}\right) = I_0 \cdot \exp\left(-\frac{z}{\lambda_{eff}}\right),$$

(2.13)

with z the distance of the emitting atom to the surface, ϑ the detection angle (see Fig. 2.3), and λ_0 (λ_{eff}) the (effective) inelastic mean free path (IMFP) of the photoelectron. Here, the trajectory of the electron in the solid is assumed to be a straight line of length $z/\cos\vartheta$, which is quite successfully employed to describe emission angle dependent experimental data [8, 24, 25]. Note that for grazing emission geometries ($\vartheta \gtrsim 60°$) elastic scattering events become important and this simple geometric argument breaks down [26]. But since only moderate emission angles below 60° are of interest throughout this thesis, equation 2.13 suffices to describe the measurements. However, values for λ_0 are yet required for quantitative considerations of the probing depth.

As briefly mentioned above, the energy losses of photoelectrons are mainly due to the excitation of plasmons. It turns out in experiment that the resulting IMFP for various materials exhibits a general trend as depicted in the *universal curve* in Fig. 2.4 (a) [27]. For kinetic energies above $\approx 50\,\mathrm{eV}$ this universal curve is quite well described by the semi-empirical formula developed by Tanuma, Powell, and Penn that is often referred to as $TPP - 2M$ relation [29, 30]:

$$\lambda_0 = \frac{E_{kin}}{E_p^2 \left(\beta\, ln(\gamma E_{kin}) - (C/E_{kin}) + (D/E_{kin}^2)\right)}.$$
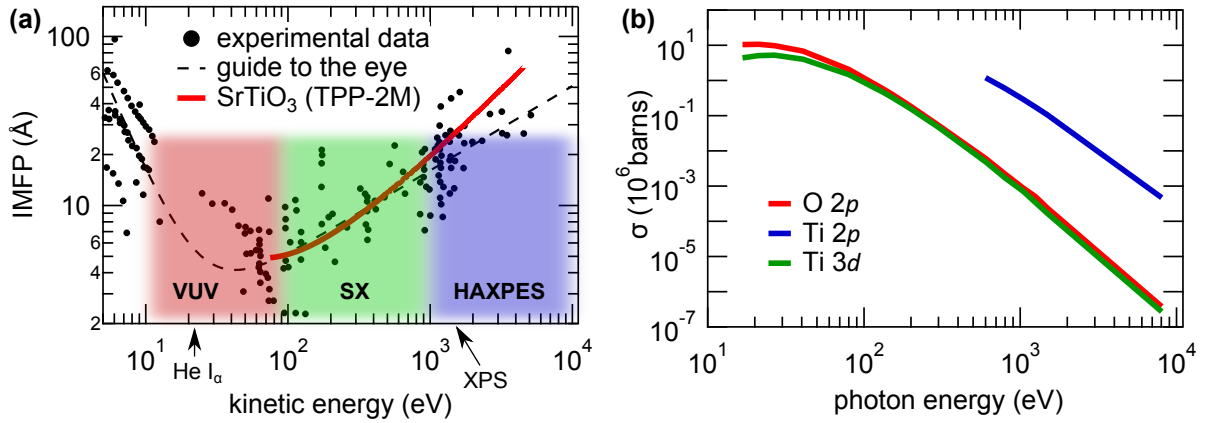
(2.14)

Fig. 2.4: (a) Kinetic energy dependent values of the inelastic mean free path λ_0 in various materials (black dots) exhibit a general trend that is highlighted by the dashed line (data taken from Seah *et al.* [27]). For comparison, λ_0 of $SrTiO_3$ as calculated by the TPP-2M relation is included (red line). Different spectral ranges are highlighted by the colored areas and the He I_α and Al K_α lines are marked by arrows. See text for details. (b) Energy dependent photoabsorption cross sections as tabulated by Yeh and Lindau [28] for several relevant orbitals.

Here, the plasmon energy is given by $E_p = 28.8(N_V \rho/M)^{1/2}$ and depends on the number of valence electrons N_V, the material's density ρ, and the atomic weight M. Furthermore, the parameters β, γ, C, and D are material specific parameters that also depend on N_V, ρ, and M. In the following chapters the IMFP is used to quantify the surface sensitivity of measurements, to this end λ_0 is calculated by the $TPP - 2M$ relation, i.e. equation 2.14.

Let us come back to the shape of the universal curve. For photoelectrons with a kinetic energy of approx. 20...100 eV, λ_0 is minimal with absolute values around 4 Å (see Fig. 2.4 (a)). Hence, photoemission measurements in this energy range are extremely surface sensitive. To obtain more bulk sensitive spectra the universal curve suggests either to decrease or increase the photoelectron's energy. The former can be achieved by using laser light excitation, however, the universality of λ_0 for low energies is still under debate and a strong impact of the final state dispersion in this energy range complicates this approach. Therefore, the hard x-ray regime is employed within this thesis to increase the PES probing depth.

To illustrate the variation in the surface sensitivity for the experiments with different light sources employed in the course of this thesis—ranging from the vacuum ultraviolet (VUV) up to the hard x-ray regime (HAXPES)—a specific example is discussed. Consider the excitation of a valence band electron at a certain photon energy. Since the binding energy of the electron is rather small, the kinetic energy of the electron is approx. equal to the photon energy therefore giving an upper limit of the IMFP for all excited electrons. In this way the probing depth for the different light sources is estimated and the kinetic energy range is highlighted by different colored areas in Fig. 2.4 (a).

Furthermore, this estimate quantifies the surface sensitivity when we consider $SrTiO_3$ as a concrete example material. In the VUV, a helium gas discharge lamp provides photons with an energy of 21.2 eV and is widely available in laboratories. The corresponding IMFP is comparable to the atomic distances, i.e. only the topmost atomic layers of a crystal are probed. The relative share of the signal emanating from the first unit cell ($I_{surface}$) to the overall signal (I_{total}) is then determined by using equation 2.13 and a summation over all layers. Be $\lambda_0 = 4$ Å and the lattice constant $c = 4$ Å , then[2]:

$$I_{rel} = I_{surface} : I_{total} = 1 : \sum_{j=0}^{\infty} \exp\left(-\frac{j \cdot c}{\lambda_0}\right) = 1 - \exp\left(-\frac{c}{\lambda_0}\right) \approx 63\%. \quad (2.15)$$

In the soft x-ray regime (SX) at photon energies of about 500 eV, one finds $\lambda_0 = 1.2$ nm and the first layer contributes 28% to the signal. For XPS with an Al K_α laboratory source ($E_{ph} \approx 1.5$ keV), λ_0 amounts to 2.7 nm and $I_{rel} = 14\%$. In the HAXPES regime at photon energies of 3 keV, λ_0 is further increased to about 4.7 nm and the share of the surface layer signal is reduced to only 8 %. These results demonstrate how the different spectral ranges can be used to drastically change the surface sensitivity in PES experiments.

The downside of high photon energies, however, are weak cross sections for the photoemission process as depicted in Fig. 2.4 (b). For instance, increasing the photon energy from about 100 to 3000 eV results in a drop of about 6 orders of magnitude for O $2p$ or Ti $3d$ cross sections. Therefore, bulk sensitive measurements in the HAXPES regime require high-flux light sources, e.g., endstation I09 at the third generation synchrotron Diamond Light Source.

We have just seen that inelastic scattering of photoelectrons limits the probing depth in PES experiments. Another aspect of the scattering events is their impact on the line shape of the measured spectra, e.g., core level lines. Electrons that have lost energy in step (2) of the PES process generate a background signal on the low kinetic energy side of the spectrum. To disentangle the elastic from the inelastic signal in the experimental data the shape and magnitude of this background has to be determined. A standard method to do so was introduced by Shirley [31]. Assuming that the background intensity at a kinetic energy E in the spectrum is proportional to the total number of electrons at higher kinetic energies one arrives at the iterative relation:

$$I_c^{n+1}(E) = I_m^0(E) - I_{BG}(E_1) \left(\frac{\int_E^{E_2} I_c^n(E')dE'}{\int_{E_1}^{E_2} I_c^n(E')dE'}\right). \quad (2.16)$$

Here, $I_c(E)$ denotes the corrected spectrum, n is the iteration index, $I_m^0(E)$ is the measured spectrum, and $I_{BG}(E_1)$ is the desired background level on the low kinetic energy side of the spectrum. Note that the spectrum covers the energy range from E_1

---

[2]The value for λ_0 is assumed to be comparable to the lattice constant for the VUV example. For the higher kinetic energies in the SXPES, XPS, and HAXPES regime the $TPP - 2M$ relation is used for $SrTiO_3$ to calculate λ_0.

to E_2 and $E_2 > E_1$. Practice has shown that five iterations already suffice to obtain convergence. The Shirley background is a coarse simplification, but determining the actual inelastic signal requires detailed information such as the energy loss spectrum of the investigated line in the material of interest or the surface morphology. The Shirley background is a pragmatic solution if such information is not available and has therefore been employed on several occasions throughout the thesis to remove the contribution from inelastically scattered electrons.

2.4 Resonant Photoemission Spectroscopy

In the considerations on PES so far, the photon energy $h\nu$ was essentially discussed as an offset for the kinetic energy of the photoelectron with consequences on, e.g., the probing depth. However, more elaborate measurements are possible due to the availability of light sources with tunable photon energies over a wide spectral range at synchrotron radiation facilities. For instance, setting the photon energy to an x-ray absorption edge opens other photoemission channels that can lead to interference effects. Such conditions allow not only for chemical contrast—given by the investigated absorption edge—, but also for a sizable intensity enhancement of the photoemission signal. Here, we will concentrate on valence band photoemission from $3d$ states at photon energies close to the $2p \rightarrow 3d$ x-ray absorption threshold, i.e. the L-edge.

The transitions involved in an L-edge resonant photoemission experiment at an ion with $3d^1$ configuration are sketched in Fig. 2.5 (a). The two channels that lead to the emission of a photoelectron in the state $\varepsilon_{\vec{k}}$ are:

$$2p^6d^1 + h\nu \rightarrow 2p^6d^0 + \varepsilon_{\vec{k}} \quad \text{(direct photoemission)} \quad (2.17)$$
$$2p^6d^1 + h\nu \rightarrow 2p^5d^2 \rightarrow 2p^6d^0 + \varepsilon_{\vec{k}} \quad \text{(coherent Auger decay)}. \quad (2.18)$$

Note that the initial and final state are undistinguishable for both channels giving rise to quantum mechanical interference. If the coherence is lost in the intermediate state (here, $2p^5d^2$), the final states of the two channels differ and an incoherent Auger decay occurs which does not interfere with the direct PES channel.

A theoretical description of such an interference was first introduced by Fano in 1961 who investigated inelastic electron scattering by He atoms, which turns out to involve similar processes as resonant photoemission [32]. In both techniques, the problem boils down to the coupling of a continuum of states to a discrete state—in our case the continuum of free electron final states of the photoelectron $\varepsilon_{\vec{k}}$ and the discrete intermediate state $2p^5d^2$. Fano's description, and especially the connection to resonant photoemission, is briefly reviewed in the following based on references [32–36] that are also recommended for further reading.

The system consisting of a discrete state $|\varphi\rangle$ with energy E_φ and a continuum of states $|\psi_{E'}\rangle$ (energy E') is described by:

$$\langle \varphi \,|\, \mathcal{H} \,|\, \varphi \rangle = E_\varphi \ , \quad \langle \psi_{E''} \,|\, \mathcal{H} \,|\, \psi_{E'} \rangle = E'\delta(E'' - E') \ , \quad \langle \varphi \,|\, \mathcal{H} \,|\, \psi_{E'} \rangle = V_{E'}, \quad (2.19)$$
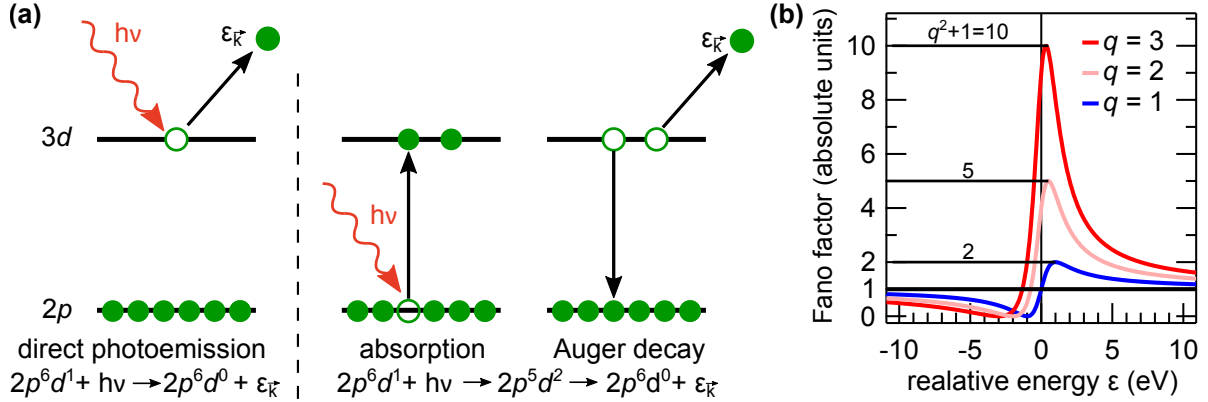
Fig. 2.5: (a) Processes involved in a resonant photoemission measurement at an L absorption edge. The left side depicts direct photoemission from the $3d$ states. On the right side the two step process of absorption followed by an Auger decay is displayed. Note that for both channels the initial and final state is identical. (b) Fano profile for different values of the parameter q, see text for details. The maximal Fano factor is $q^2 + 1$ as highlighted by the horizontal lines.

where $V_{E'}$ accounts for the coupling of $|\varphi\rangle$ and $|\psi_{E'}\rangle$ via the Auger decay channel. Note that it is understood that E_φ is within the energy range of the continuous spectrum E'. The corresponding eigenstates have the form:

$$\Psi_E = a\varphi + \int dE' \, b_{E'} \, \psi_{E'}, \qquad (2.20)$$

and the coefficients a and $b_{E'}$ can be determined by using the properties of equations 2.19. For a complete derivation, however, the reader is referred to Ref. [32]. Here, we focus on the ratio between a transition from an initial state $|i\rangle$ into the continuum $|\psi_{E'}\rangle$ without discrete states being involved and the transition into $|\Psi_{E'}\rangle$, i.e. into an eigenstate of the coupled system. The ratio f of the transition probabilities for these two cases is the Fano factor and given by:

$$f = \frac{|\langle \Psi_E | T | i\rangle|^2}{|\langle \psi_E | T | i\rangle|^2} = \frac{(q+\epsilon)^2}{(1+\epsilon^2)}, \qquad (2.21)$$

where T is the transition operator, ϵ a reduced energy variable for which the resonance energy is located at 0, and q a parameter determining the shape of the resonance. The resulting line shape of $f(\epsilon)$ is plotted for different values of q in Fig. 2.5 (b). Far away from the resonance, i.e. in the limit $\epsilon \to \pm\infty$, the discrete state has no influence and f approaches 1. The maximal enhancement is given by $q^2 + 1$ and is located at positive ϵ close to $\epsilon = 0$. Destructive interference is also present at negative ϵ. However, the complete suppression, i.e. $f = 0$, as shown in Fig. 2.5 is only found in our simple model of *one* discrete state coupled to *one* continuum of states and is usually not present when more states are involved [32].

Coming back to resonant photoemission the photocurrent can be expressed by the following expression [35, 37]:

$$I(E, h\nu) \propto \sum_f \left| \langle f \,|\, \mathcal{H}_R \,|\, i \rangle + \sum_m \frac{\langle f \,|\, \mathcal{H}_C \,|\, m \rangle \langle m \,|\, \mathcal{H}_R \,|\, i \rangle}{E_i + h\nu - E_m - i\Gamma_m/2} \right|^2 \delta(E - E_i - h\nu), \quad (2.22)$$

where $|i\rangle$ is the initial, $|f\rangle$ the final, and $|m\rangle$ the intermediate state with a lifetime-width Γ_m. Furthermore, $\mathcal{H}_R$ and $\mathcal{H}_C$ denote the radiative (photoabsorption) and Coulomb (Auger) part of the excitation, respectively. The first term in equation 2.22 represents the direct photoemission, whereas the second term accounts for the Auger decay channel. Evaluating the squared sum yields a mixed term between the two channels inducing the interference.

In the Fano framework with one core-hole excitation, the photoemission intensity can be expressed as [38]:

$$I(h\nu, \varepsilon_{\vec{k}}) \propto |\langle f \,|\, \mathcal{H}_R \,|\, i \rangle|^2 \cdot \frac{(q + \epsilon)^2}{(1 + \epsilon^2)}, \quad (2.23)$$

where the reduced energy $\epsilon = (h\nu - h\nu_0)/(\pi V_A^2)$ with the resonance energy $h\nu_0$ and the matrix element for the Auger decay V_A. The parameter q can be connected to the matrix elements of the involved processes. In our example of resonant photoemission at an L-edge as discussed above (see Fig. 2.5 (a)), one finds [38–40]:

$$q = \frac{\langle 3d \,|\, \mathcal{H}_R \,|\, 2p \rangle}{\pi V_A \langle \varepsilon_{\vec{k}} \,|\, \mathcal{H}_R \,|\, 3d \rangle}, \quad (2.24)$$

with the matrix elements for the x-ray absorption process in the numerator and for the Auger decay (V_A) as well as the direct photoemission in the denominator.

3 Mott Physics—Theoretical Concepts and Prototypical Examples

In the early 1920s the seminal works of Bethe, Bloch, and Sommerfeld pioneered the concept of electronic bands by considering the movement of electrons in the periodic arrangement of atoms in a crystal lattice [41–43]. One of the most important points of band theory is the distinction between metals and insulators: in insulators the bands are either completely filled or empty, whereas in metals the valence band is only partially filled. Following this concept, the conductivity of many materials has been described correctly.

However, band theory relies on weak electron-electron interactions, which is not a good approximation for materials with localized valence orbitals such as the $3d$ shell in transition metal oxides. As reported by de Boer and Verwey at a conference in Bristol in 1937, the materials of this group are often only poor conductors—if not even insulators—despite their partially filled d bands and are therefore at variance with band theory [44, 45]. One typical example in their report is NiO with a $3d^8$ electron configuration that exhibits insulating behavior in experiment [45]. In the following discussion Peierls pointed out that electrostatic interactions between the electrons can prevent them from moving, giving rise to the insulating behavior [44, 46].

This debate raised the interest in the mechanisms behind the insulating nature of such transition metal oxides and especially the question of how a transition from a metallic into an insulating phase in such systems can be described. In 1949 Mott gave an answer by considering a toy model, which we will briefly elaborate on here [45, 47, 48].

Let us consider a chain of N periodically arranged hydrogen atoms (each in the $1s$ state) whose electronic properties are described by a band. The dispersion of this band within a tight binding model is depicted in Fig. 3.1 (a) and follows a $E(k) \propto -4\,t\,\cos(k{\cdot}a)$ relation, where a is the lattice constant and t the transfer integral. The band hosts $2N$ states. Therefore, the band is half filled as indicated by the dashed horizontal line in Fig. 3.1 (a). Following the classification from band theory as outlined above, the chain is identified as a metal due to its partial band filling.

When the distance a between the atoms is now enlarged, smaller values for t are obtained and the band narrows as sketched in Fig. 3.1 (b). This leads to an increase of the effective mass but the band remains half filled and—strictly speaking—metallic behavior is expected. It is not only against common sense that even the limit of large a still yields a metallic conductor, but in this picture the conductivity is also expected to decrease in a continuous way upon increasing the lattice constant. In real systems, however, a sharp transition between metals and insulators is detected and not only a
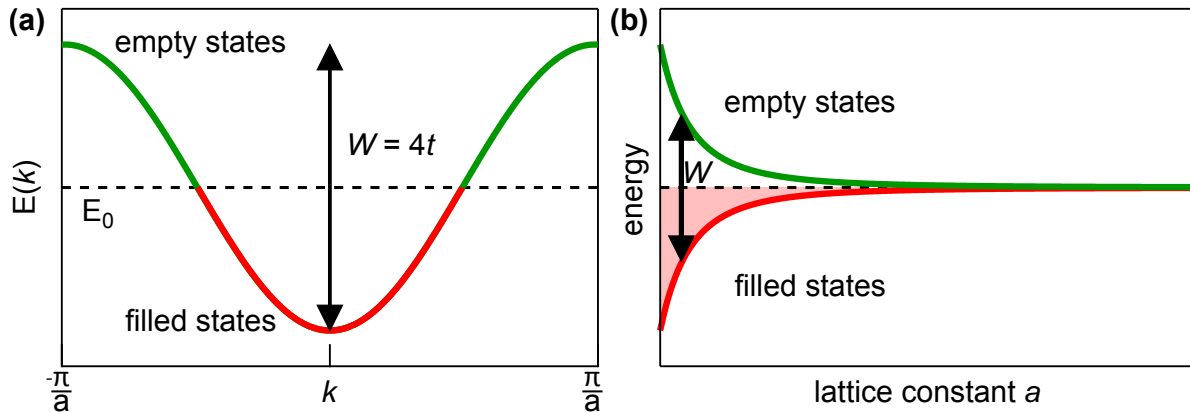
Fig. 3.1: Electronic properties of a hypothetical chain of hydrogen atoms disregarding short range Coulomb interactions between the electrons. (a) Dispersion relation from a tight binding model. The bandwidth W is proportional to the transfer integral ($W = 4t$) and the band is half filled (red line). The Fermi level is indicated by the dashed line. (b) Evolution of the bandwidth for increasing lattice constants a. Even though the band narrows it remains half filled as indicated by the red shaded area. Plot after [48].

continuous variation of the conductivity. For instance, Mott mentions the example of insulating NiO compared to monovalent metals like sodium with smaller lattice constants [45]. So the question remains: how can a sharp metal-insulator transition be described?

   Mott considered a model taking screening into account, but still lacking important aspects, e.g, short range Coulomb interactions. For metallic transport the electrons need to hop along the chain, which requires an electron to overcome the attractive potential of the proton. This is possible when the density of mobile electrons is high enough to screen the positive charge. For the screened Coulomb potential Mott used the Thomas-Fermi approximation [48]:

$$V_{eff} = -\frac{e^2}{r} e^{-qr}, \quad \text{where} \quad q^2 = \frac{4\,n^{1/3}}{a_H}, \tag{3.1}$$

with the screening constant q, the carrier density n, and the Bohr radius a_H. Since the potential is exponentially damped the transition from localized electrons (due to insufficient screening) to a metal is quite sharp giving rise to a discontinuous metal-insulator transition. The critical value can be estimated by:

$$q \cdot a_H \approx 1 \Rightarrow n^{-1/3} \approx 4\,a_H. \tag{3.2}$$

Note that the lattice constant a is included here by the carrier *density*. Even though the screening argument predicts an abrupt metal-insulator transition, it is a very crude approximation and many microscopic details, e.g. short range Coulomb interactions, are missing. We therefore turn to the Hubbard Model for a more elaborate description of materials with strong electron correlations.
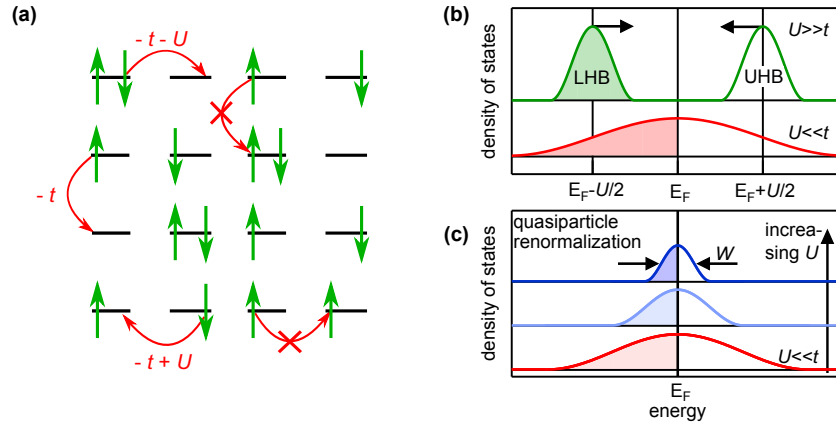
Fig. 3.2: (a) Sketch illustrating the energetics of the Hubbard Hamiltonian. The black lines symbolize the different sites in a lattice. (b) Phase transition as suggested by Hubbard. Starting from the exact solution in the atomic limit ($U \gg t$) one finds a gapped spectrum with the lower and upper Hubbard band. An extrapolation towards smaller U eventually leads to a collapse of the gap between the features resulting in a single partially filled band. (c) Quasiparticle renormalization after Brinkman and Rice. Coming from the weak correlation limit, the band narrows since the effective mass increases with U. When a critical value U_c is reached, the effective mass diverges and induces an insulating phase, see text for details.

3.1 Hubbard Model and Mott transition

Again motivated by the characteristics of transition metal oxides that exhibit both band-like and atomic like features, Hubbard developed a theoretical description of electron correlation effects in narrow energy bands [49]. Even though this description is nowadays known as the Hubbard model, similar theories were also independently developed by Gutzwiller [50] and Kanamori [51] in the same year. The model considers a single band with two possible states per electron (up and down spins) and restricts the Coulomb interaction between the electrons to an on-site problem, which leads to the Hamiltonian:

$$\mathcal{H}_{Hubbard} = \mathcal{T} + \mathcal{U} = -t \sum_{<ij>,\sigma} \left(c_{i,\sigma}^{\dagger} c_{j,\sigma} + c_{j,\sigma}^{\dagger} c_{i,\sigma} \right) + U \sum_{i} n_{i,\uparrow} n_{i,\downarrow}, \qquad (3.3)$$

where $\mathcal{T}$ is the kinetic energy part describing the motion of electrons as in a tight binding Hamiltonian and $\mathcal{U}$ accounts for the intra-atomic Coulomb interactions. In the second equality, t is the transfer integral, U the on-site Coulomb repulsion, i and j are indices for the lattice sites, and the bracket in the first sum ($< i, j >$) denotes the summation over nearest neighbors only. Furthermore, σ indicates the spin state that is either up ($\uparrow$) or down ($\downarrow$). Again, $c_{i,\sigma}^{\dagger}$ and $c_{i,\sigma}$ are the creation and annihilation operators for electrons at site i in spin state σ, and lastly the number operator $n_{i,\sigma} = c_{i,\sigma}^{\dagger} c_{i,\sigma}$ counts the electrons according to the respective indices.

One may imagine the energetics described by the Hubbard Hamiltonian by hopping processes of the electrons on a lattice as sketched in Fig. 3.2 (a). Movement of an

electron to a neighboring site is associated with an energy gain of $-t$, whereas the Coulomb repulsion U has to be paid when the electron hops on a site that is already occupied by an electron (with different spin). Even though this is an over-simplified description, it captures the interplay between the kinetic energy and the Coulomb term which is the essence of the Hubbard model and determines whether the electrons are mobile or localized. To familiarize ourselves more with the consequences of electron correlations, we turn to several special cases and limits that are briefly discussed in the following.

Atomic Limit—Hubbard transition

In the atomic limit, i.e. at zero bandwidth, an exact solution of the Hubbard model was already presented in Hubbards original paper [49]. He found that the electronic density of states splits into two energy levels: E_0 and $E_0 + U$, where E_0 is the binding energy of the electron in the isolated atom. Suppose, electrons are added starting with the empty system. Initially the chemical potential μ is equal to E_0 until this level hosts one electron per site. Then, the chemical potential jumps to $\mu = E_0 + U$ giving rise to a gapped spectrum. Note that each of these energy levels hosts only *one* electron per atom and not the *two* electrons as in a regular electron band.

Starting from this limit, approximate solutions for the case of finite bandwidth can be found. The motion of the electrons gives rise to a finite width of the energy levels, therefore the ratio between the separation of the energy levels and their width determines whether the spectrum remains gapped or not. This situation is sketched in Fig. 3.2 (b) for the case of half filling, i.e. one electron per site. In the strong correlation limit $U >> t$ (but at finite bandwidth t), the spectrum splits in the so-called upper and lower Hubbard bands (UHB and LHB). The terminology "bands" is usually used, but may be confusing since the LHB and UHB are not conventional Bloch states, which becomes clear when one recalls that each of them hosts only one electron per atom.

Since the LHB is fully occupied and the UHB empty, the system is an insulator. The electrons are fully localized and every site is occupied by one electron. Decreasing U brings the LHB and UHB closer together and increasing t broadens the features until they eventually overlap, the gap collapses, and a single conventional band forms [52]. Such a situation is depicted in the lower part of Fig. 3.2 (b) and it is clear that this half filled band gives rise to metallic behavior. Comparing this insulator-to-metal transition as obtained from starting in the atomic limit of the Hubbard model to the transition described by Mott, one realizes that the LHB and UHB approach and finally overlap in a continuous way at variance with the rather sudden transition described in the previous section. Hubbard comments that this might be due to neglected interactions between electrons on different sites [52]. Another footprint of the Hubbard-type transition outlined here, is that the Fermi surface volume is initially small when LHB and UHB merge, violating Luttinger's theorem, i.e. the proportionality between the Fermi surface volume and the electron density [46].

Renormalized Fermi Liquid—The Brinkman Rice Transition

In contrast to Hubbard, Brinkman and Rice approached the metal-to-insulator transition from the opposite limit, i.e. they described the electron system at half filling starting from the non-interacting limit [53]. The electron correlation effects are introduced by reducing the double occupancy of sites by means of a variational parameter in the many body wave function that itself is composed of single-particle states. Following this approach the authors find that the system is described by a strongly renormalized Fermi liquid.

Let us briefly specify the term Fermi liquid here. In a non-interacting state, the many electron system can be described by a product of one-electron wave functions and the spectral function (see section 2.3) consists of δ-functions for the electron addition and removal part. When electron interactions are now switched on adiabatically the single electron wave functions are not longer eigenstates of the system and therefore exhibit now a finite lifetime. One can imagine the correlated Fermi sea by *quasiparticles* that are electrons dressed by excitations. The former δ-functions of the non-interacting case are broadened due to the finite lifetime and are subject to a renormalized energy scale of the dispersion and hence an altered effective mass m_{eff} [17, 54].

Coming back to Brinkman's and Rice's description of electron interactions, the authors find that the effective mass of the quasiparticles increases for larger values of the on-site Coulomb interaction U and eventually diverges as a critical value U_c is approached. Due to this divergence the number of doubly occupied sites in the system goes to zero at the critical value signalling the localization of the electrons and thereby the metal-to-insulator transition [53, 55]. The trend is sketched in Fig. 3.2 (c) and one realizes that the quasiparticle peak narrows for larger values of U or rather for larger band masses. In the literature, the renormalization of the quasiparticle properties is often described by the parameter $Z \propto (U_c - U)$, which approaches zero at the transition. Two exemplary properties are the effective mass m_{eff} being proportional to Z^{-1} and the energy scale of the quasiparticle, i.e. its bandwidth W, that scales with Z [55].

In this picture the Fermi surface of the system is built in from the start in the metallic phase and conserved up to the transition point, satisfying the Luttinger theorem. However, compared to the atomic limit described in the previous section, the high energy excitations, i.e. the Hubbard bands, are completely absent. In conclusion, one can adapt Hubbards description in the atomic limit and the Brinkmann and Rice framework in the metallic limit, but to describe all features of the correlation driven metal-to-insulator transition a unified theory is required.

Limit of Infinite Dimensions—Dynamical Mean Field Theory

Complementary to the different limits of the energetics in the Hubbard Hamiltonian, dynamical mean field theory (DMFT) gives also a solution for intermediate coupling strength, however, only in the limit of systems with infinite dimensions d. For $d = \infty$ the coordination number of an atom in the lattice diverges and spatial fluctuations are suppressed and the many body system effectively breaks down to a single site problem.

To catch the kinematics of the system a dynamic description is required, which can be realized by coupling to a bath of non-interacting excitations. This approach was pursued by Metzner and Vollhardt in 1989. They showed that an exact solution of the Hubbard model can be obtained in the $d = \infty$ limit setting the foundation for the so-called DMFT which is one of the most powerful tools to describe strongly correlated electron systems [46, 56].

As mentioned above, DMFT treats the Hubbard model by the interaction of a single site or impurity with a bath. To solve the impurity problem various sophisticated numerical techniques have been developed to date that allow to compute the spectral function not only in the limits of strong or weak correlations but all across the Mott transition. For further details on the DMFT technique the reader is referred to the review articles by Georges *et al.* [55] and Imada *et al.* [46]. Here, we will focus on the evolution of the angle-integrated spectral function $A(\omega)$ as obtained by DMFT.

Let us first inspect the results for different values of the on-site correlation strength U depicted in Fig. 3.3 (a), which is usually referred to as the *bandwidth* controlled Mott transition. In the large U limit, the spectrum is reminiscent of the gapped spectrum as suggested by Hubbard with a fully occupied LHB and an empty UHB. Upon lowering U, a quasiparticle emerges at the chemical potential that is initially very sharp but broadens for lower correlation strengths. At the same time the gap between the Hubbard bands closes and they lose spectral weight in favor of the quasiparticle feature. Thus the spectral function changes from a clearly gapped and insulating spectrum towards a metallic situation, thereby describing an insulator-to-metal transition. This transition contains the footprints of both the Hubbard transition as well as the Brinkman-Rice transition, i.e. the collapse of the Hubbard gap and the renormalization of the quasiparticle, and is therefore in a way unifying these models.

Additionally to the bandwidth controlled Mott transition discussed so far, a Mott insulator can also be rendered metallic by changing its band filling. To motivate this *filling* controlled Mott transition consider again a system in which each site is occupied by one electron. We can again argue in the cartoon-like framework of Fig. 3.2 (a) and realize that moving any electron to a neighboring site results in a double occupation and therefore costs the Coulomb energy U. When we now reduce the number of electrons in the system, empty sites are created and electrons can hop onto these sites without the energy costs associated with a double occupation. Following this reasoning, it is clear that reducing the band filling tips the energetics of the Hubbard model in favor of the metallic phase. Note that the same arguments hold for increasing the filling since hopping away from a doubly occupied site releases the Coulomb energy U.

A more refined view on the filling controlled transition is gained by DMFT results on the evolution of the spectral function for different p doping levels x of a system that is Mott insulating at half filling depicted in Fig. 3.3 (b). Without doping, i.e. $x = 0$, the well known gapped situation with LHB and UHB is reproduced. Upon p doping the chemical potential jumps toward the leading edge of the LHB and a sharp quasiparticle develops at this position. Note that doping breaks the particle hole symmetry of the system, therefore the spectral function is no longer symmetric with respect to the chemical
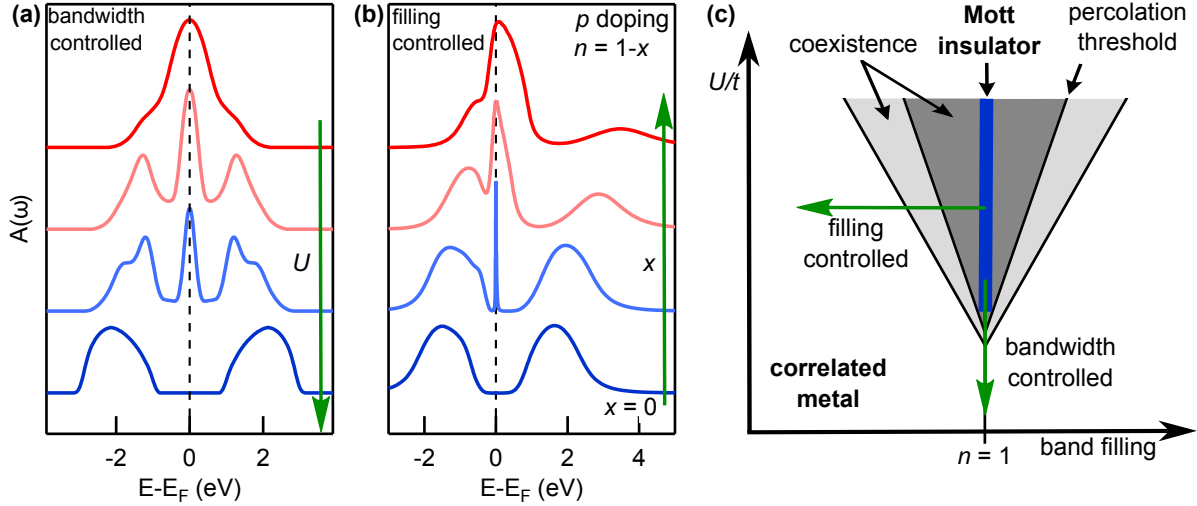
Fig. 3.3: (a-b) Evolution of the spectral function $A(\omega)$ across the bandwidth (a) and band filling (b) controlled Mott transition as simulated by DMFT. Plot adapted from [57] with data from [55] and [58]. (c) Sketch of the phase diagram in the plane of correlation strength U/t *vs.* band filling. The blue area denotes a pure Mott insulating phase, whereas the grey areas indicate a coexistence of Mott insulating and correlated metal patches.

potential as in the *bandwidth* controlled case (see Fig. 3.3 (a)). Further increasing the doping level induces a broadening of the quasiparticle and the feature gains in spectral weight at the expense of the Hubbard bands' spectral weight.

Phase Diagram for Mott Transitions

Before visiting the phase diagram of the bandwidth and filling controlled Mott transition let us briefly come back to the initial question about the nature of the insulator-to-metal transition. A closer inspection of the DMFT simulations reveals that the transition is of first order and hence the metallic and insulating phase coexist close to the transition line [59, 60]. This is for instance detected by a hysteresis effect of observables upon variation of U across the transition [55, 59]. The coexistence region is taken into account in the phase diagram sketched in Fig. 3.3 (c). The diagram maps the plane of correlation strength U/t and band filling around a filling of one electron per site ($n = 1$). The Mott insulating phase is marked by the blue line at $n = 1$. As discussed above, two paths can be pursued to drive the transition from the Mott insulating phase into the correlated metal phase: the bandwidth and filling controlled transition that are marked by the vertical and horizontal arrows, respectively. The grey areas indicate the coexistence of the two phases, i.e. correlated metal and Mott insulator, and the region is subdivided in light and dark grey to differentiate between situation where the metallic regions percolate or not [60, 61]. This schematic phase diagram is employed throughout the thesis in more or less detailed representations depending on the effects that are described. Note that the phase diagram is not intended to capture the exact shape of the transition lines but rather to catch the main trends involved.

3.2 Prototypical Materials: $3d^1$ Perovskites

Even though modern numerical methods like DMFT can describe the Hubbard model in certain limits, experimental studies are crucial to investigate the physics of strongly correlated electron systems. As already mentioned above, electron correlations are strong in materials with narrow energy bands such as in NiO—the archetypical example for an insulating material at nominally partial band filling brought forward by de Boer and Verwey [44]. For this reason compounds with a $3d$ valence band are especially suited to investigate Mott physics and a subclass of such materials is at the focus of this thesis, namely ternary transition metal oxides with a $3d^1$ configuration and a perovskite related structure. These materials are not only prototypical Mott compounds, but also ready to be integrated in thin film structures allowing for further tuning of their properties. To clarify these statements, a brief introduction to the material class is given.

Ternary Transition Metal Oxides of Formula $AB\mathbf{O}_3$

A large variety of ternary transition metal oxides with the composition $AB\mathrm{O}_3$ exists, where A and B are cations and the anion is oxygen (O). Many of these compounds crystallize in a perovskite related structure with comparable lattice constants roughly around $4\,\text{Å}$. The ideal, i.e. cubic, perovskite structure is depicted in Fig. 3.4 (a). The A cations (colored in red) occupy the corners of a cube, B cations (blue) are body-centered whereas the oxygen anions (black) are located on face-centered positions. As highlighted in Fig. 3.4 (a) the oxygen ions form an octahedron around the B cation.

Since the B cation usually hosts the $3d$ valence electrons that form the decisive d bands in the crystal, the consequences of the octahedral coordination on the $3d$ orbitals are inspected in Fig. 3.4 (b). The $3d$ shell can host ten electrons, which are all energetically degenerate in a spherical symmetry as in the atomic case. In the perovskite lattice an anisotropy is induced by the oxygen ligands that have a negative valence and impose a crystal field on the $3d$ orbitals that lifts the degeneracy. For the cubic perovskite case the orbitals with e_g symmetry, i.e. $d_{x^2-y^2}$ and d_{z^2}, are directed toward the ligand atoms which is not the case for the t_{2g} orbitals, i.e. d_{xy}, d_{yz} and d_{xz}. The e_g levels are therefore raised in energy whereas the t_{2g} orbitals are lowered with respect to the atomic case. The corresponding energy diagram is sketched in Fig. 3.4 (b) together with an exemplary arrangement of orbitals for the two cases.

As we have just seen from the crystal field splitting, the oxygen ligands have a strong impact on the $3d$ electrons. Besides the energetic rearrangement of the orbitals in the crystal field, the oxygen $2p$ states have to be considered for the hopping processes that were discussed in the framework of the Hubbard model above. Due to the relatively small overlap of the d orbitals of neighboring B cations an indirect electron transfer via the oxygen p orbitals is considered [46]. In principle this should be included in the Hubbard model which we only discussed for the case of a single band close to the Fermi level above (see equation 3.3). However, our simplified Hamiltonian is a good approximation for the $3d$ transition metal oxides when the degeneracy of the $3d$ orbitals is lifted so that only one band is close to the Fermi level [46].
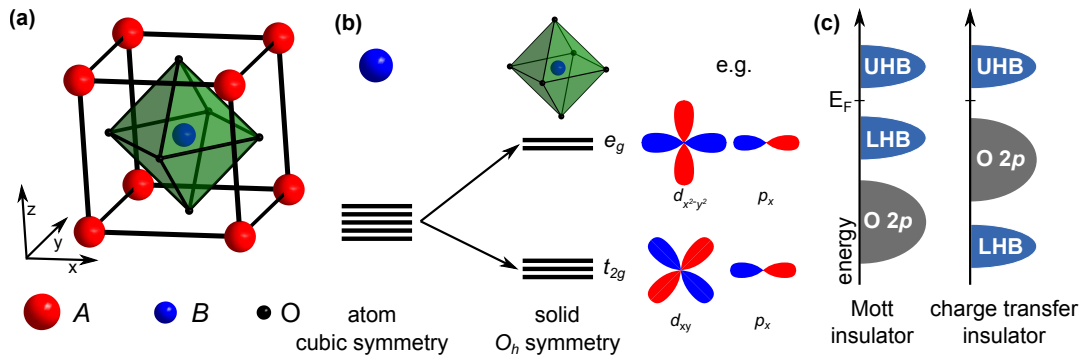
Fig. 3.4: (a) Unit cell of a cubic perovskite with chemical formula $AB\mathrm{O}_3$. (b) Crystal field splitting due to the octahedral (O_h) symmetry around the B-cation. The alignment of d and ligand p orbitals is sketched for two examples. (c) Depending on the alignment of the transition metal d states, i.e. LHB and UHB, and the oxygen $2p$ states, a strongly correlated transition metal oxide is classified as a Mott insualtor or charge transfer insulator.

In view on the energetic position of the ligand p states relative to the d bands some general trends exist in the series of early to late transition metal oxides. When going from titanium to copper as B cation the nuclear charge increases and therefore the chemical potential of the d electrons is lowered with respect to the oxygen p states [46]. Furthermore, the hybridization between the p and d orbitals is stronger when e_g levels are involved in the late transition metals. This becomes clear from the geometric arrangement of the orbitals as sketched in Fig. 3.4 (b) [46]. A stronger hybridization—as for instance in the cuprates compared to the titanates—pushes the oxygen $2p$ states closer to the Fermi level.

This brings us to a general classification of strongly correlated transition metal oxides based on the relative arrangement of the O $2p$ states and the LHB derived from the $3d$ transition metal states. As sketched in Fig. 3.4 (c), a Mott insulator has the $3d$ states in the vicinity of the Fermi level and the ligand states are well separated at higher binding energies. Here, the gap is determined by the separation of the LHB and UHB, i.e. by the on-site Coulomb interaction U. The oxygen $2p$ orbitals contribute only through virtual hopping processes and one may use our simplified single band Hubbard Hamiltonian as a good approximation.

When the order of the LHB and the oxygen states is interchanged (see Fig. 3.4 (c)) and the energy gap is between the UHB and the O $2p$ states, the material is called a *charge transfer insulator* since the excitation gap is no longer determined by U but by a charge transfer from the ligand to the transition metal [62]. As motivated above, the late transition metal cations such as Co, Ni and Cu lead to such a charge transfer configuration in their oxides. Note that the LHB and oxygen states can in general overlap, the clear separation in Fig. 3.4 (c) is due to didactical reasons only. To distinguish between Mott and charge transfer insulator the dominating character of the valence band edge has to be determined which is not always straight forward in experiment.

Since the interest of this thesis is to investigate Mott physics in prototypical materials, the focus is set to early transition metal oxides such as the titanates and vanadates. In these materials the oxygen states are indeed well separated from the $3d$ valence band as in the idealized sketch for the Mott insulator case in Fig. 3.4 (c). Therefore, the $d-p$ hybridization does not have to be taken into account explicitly and the clear features in the valence band allow for a straightforward characterization by photoemission spectroscopy.

Besides the discussed trend that is driven by the nuclear charge of the B-cation, the ionic radii of the cations vary in the ABO_3 compounds which can lead to distortions of the cubic perovskite structure that may alter their electronic properties. One such example is the series of $3d^1$ materials $SrVO_3$-$CaVO_3$-$LaTiO_3$-$YTiO_3$ (SVO-SVO-LTO-YTO) that exhibits a crossover from a correlated metal in the vanadates to a Mott insulator in the titanates.

The Series SrVO$_3$—CaVO$_3$—LaTiO$_3$—YTiO$_3$

Let us first discuss the distortions of the perovskite structure that are characteristic for this series. The cubic perovskite structure presented above requires a balance between the ionic radii R of its components, i.e. the A and B cations and the oxygen anion. Usually this is expressed by the so-called Goldschmidt tolerance factor t_G that is given by [63]:

$$t_G = \frac{R_A + R_O}{\sqrt{2}\,(R_B + R_O)}.\tag{3.4}$$

In an ideal cubic perovskite the ratio between the distances of the A and B cations to its neighboring anion AO to BO equals $\sqrt{2}$ to 1 (see, e.g., Fig. 3.4 (a)), which corresponds to a tolerance factor of $t_G = 1$. In the case of $SrVO_3$ the tolerance factor is very close to this ideal value and the material adopts the cubic perovskite lattice. Going along the series, however, the value of t_G gradually decreases due to the smaller A-cations and the larger titanium cation compared to vanadium [64].

The smaller t_G values promote an orthorhombic distortion of the lattice into the $GdFeO_3$-type structure, in which the oxygen octahedra are tilted compared to the cubic case. With the cubic perovskite unit cell in mind (see Fig. 3.5 (a)), the tilts are described by rotations around the three main axes of the octahedron as sketched in Fig. 3.5 (b). Among the various possible tilt combinations, the $GdFeO_3$-type structure adopts the $(a^+b^-b^-)$ tilt system, i.e. a axis rotations of neighboring octahedra are in phase, whereas the directions of rotations around the b and c axes are alternating at a constant amplitude [65, 66]. The resulting $GdFeO_3$ structure is sketched in Fig. 3.5 (c), in which the distorted perovskite is represented by eight blocks of the former cubic unit cell to clarify the tilt system. An alternative representation is the orthorhombic unit cell (black lines) as depicted in Fig. 3.5 (d). For clarification a (pseudo-) cubic unit cell is highlighted by the blue lines. The comparison makes clear that the orthorhombic unit cell is enlarged by factors of $(2 \times \sqrt{2} \times \sqrt{2})$ with respect to the cubic case.
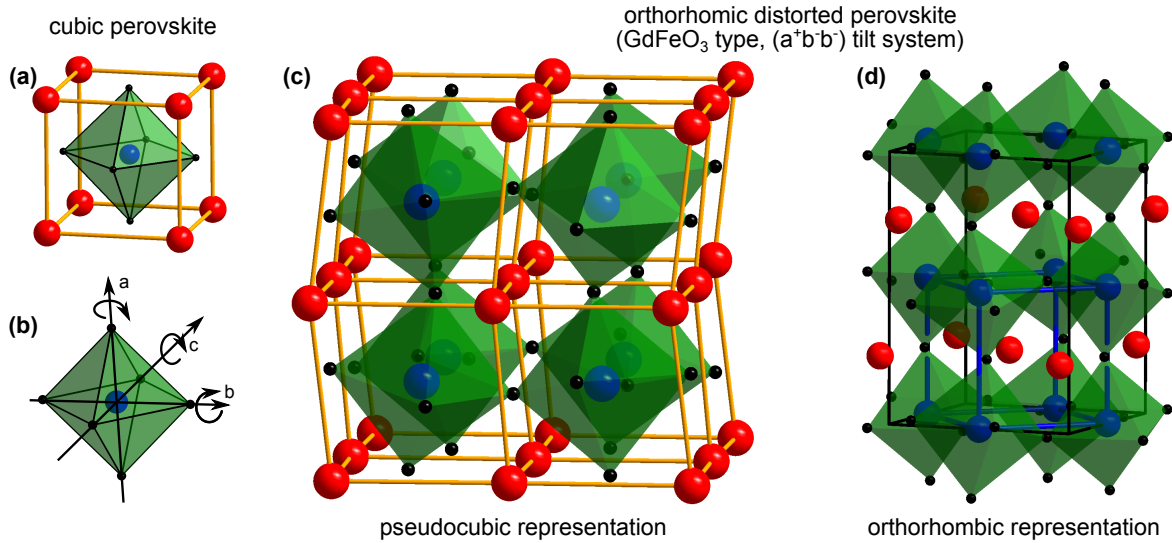
Fig. 3.5: (a) Unit cell of the cubic perovskite. (b) Definition of axes for octahedron tilts. (c) Orthorhombic distorted perovskite structure with in phase octahedron tilts about the a axis and out of phase tilts about the remaining axes built up from eight former cubic unit cells. (d) Orthorhombic unit cell (black lines) of the same structure depicted together with the pseudoubic unit cell (blue lines).

Inspecting the B-O-B bond angle in Fig. 3.5 (c) compared to the cubic perovskite depicted in panel (a) of the same figure, one finds a decreased value that is characteristic for the distortion. In our example the bonding angle decreases from $180°$ in SVO to $160°$ (CVO), to $155°$ (LTO), down to $140°$ (YTO) as the series progresses [67, 68].

In early reports on the metal-to-insulator transition in this series, it has been argued that the decreased bond angles induce smaller effective $3d$ band widths leading to the experimentally observed enhancement of the effective mass from about $2.7\,m_0$ to $3.6\,m_0$ in the vanadates and the opening of a gap of 0.2 and $1\,\text{eV}$ in LTO and YTO, respectively [67, 69, 70]. Due to the threefold degeneracy of the t_{2g} levels in the octahedral crystal field the metal-to-insulator transition was described by a simplified degenerate Hubbard model [67]. In this framework the degeneracy is taken into account by an effective value U_{eff} that is in general smaller than U of the corresponding single band model [46, 67]. Following these arguments the Mott transition in the d^1 series from SVO to YTO is classified as bandwidth controlled, i.e. is located at a vertical path in the electronic phase diagram sketched in Fig. 3.3 (c).

More recently, Pavarini *et al.* have pointed out that the GdFeO$_3$ distortion also induces a small splitting of the t_{2g} levels [71]. When this splitting is large enough to lift the orbital degeneracy the Mott insulator is stabilized, since the critical value for the transition into the insulating phase $(U/t)_c$ is smaller in a single band situation [72–74]. Using local density approximation (LDA), the authors predict for LTO (YTO) a splitting of the t_{2g} levels in which the lowest lying level is separated by 140 (200) meV from the middle one and by $200(330)\,\text{meV}$ from the highest level [71]. Note that although the octahedron

is tilted in the $GdFeO_3$ structure, its O_h symmetry remains nearly perfect. The origin of the splitting is rather due to altered distances of the A- to the B-cations and to the oxygen anions [71] (see also Fig. 3.5 (c)).

Even though the calculated splitting is one order of magnitude smaller than the (single electron) bandwidth W[1], the relevant energy scale for lifting the degeneracy in this case is the *renormalized* bandwidth ZW that can be considerably smaller. This has been taken into account by Pavarini *et al.* [71] by means of LDA+DMFT, which gives the following results: in the vanadates the degeneracy is not lifted and the occupancy of every t_{2g} orbital is approximately 1/3. In the titanates, however, only *one* orbital per site is nearly fully occupied. Hence, the $GdFeO_3$ distortion does not only decrease the t_{2g} bandwidth but also lifts the orbital degeneracy which stabilizes the Mott insulating phase in the titanates [71]. In the mean time, experimental evidence for this splitting has been provided by Haverkort *et al.* who performed x-ray absorption measurements on LTO single crystals and identified a t_{2g} splitting in the range of 0.12 to 0.30 eV [75]. In summary, one may still label the Mott transition in the series as bandwidth controlled since the path in the electronic phase diagram remains in a way vertical. However, the situation is more complex than the mere modification of the $3d$ bandwidth by the bond angle.

The series of $3d^1$ materials is a good example for the drastic impact of electron correlations on the electronic properties of a material. As we have seen, correlation effects dominate the physics in these materials and tune them from a metallic phase in the vanadates into insulators in the titanates. Furthermore, the materials' rather simple d^1 configuration qualifies them as prototypical Mott systems, which is why single crystals of these compounds have been studied for decades to get insights into Mott physics and to put theoretical models and methods to the test.

For these reasons two members of the series are investigated more closely in the following chapters, namely SVO as a prototypical correlated metal and LTO as a Mott insulator. The experiments are performed on thin films rather than single crystals.

Modern epitaxy methods such as pulsed laser deposition (PLD, see chapter 2.1) allow the fabrication of thin films with high structural quality and atomically flat surfaces. The used experimental setup is furthermore designed to analyze the films' electronic structure by means of *in situ* photoelectron spectroscopy, i.e. without exposure to air. This approach has crucial advantages compared to preceding single crystal studies that often suffer from contaminated surfaces or ambiguities from surface preparation methods such as filing or cleaving. Furthermore, the film thickness is also introduced as a new tuning parameter to manipulate the electronic structure. As will be investigated in the following chapter, scaling the thickness down to only several unit cells to reduce the dimensionality of the material is a way to trigger the transition into the Mott insulating phase in otherwise metallic SVO.

---

[1]$W \approx 2.8$ and 2.1 eV in SVO and LTO, respectively [71]

4 Thickness Controlled Mott Transition in Thin SrVO$_3$ Films

Bulk SrVO$_3$ (SVO) is a correlated metal and with its simple cubic perovskite crystal structure as well as the uncomplicated electronic configuration of one $3d$ electron per vanadium site, the material qualifies as a prototypical reference system to study electron correlation effects in transition metal oxides (TMOs). From the experimental side the system has been intensively studied by photoelectron spectroscopy (PES) to capture the hallmarks of electron-electron correlations, namely the coherent quasi-particle peak and the incoherent lower Hubbard band. Starting in the 1990s with PES measurements on polycrystalline samples, spectra that catch these features became available [67, 76]. Sparked by this experimental data and the prototypical properties of SVO, the material emerged as a benchmark system for *ab initio* calculations of correlated systems [77–82].

More recently, advances in thin film deposition techniques made high quality samples available and added the layer thickness of SVO as another parameter to manipulate the material's electronic properties [83–87]. Yoshimatsu *et al.* reported a surprising modification of the electronic properties induced by this additional degree of freedom: upon decreasing the thickness of SVO films grown on the (001) surface of SrTiO$_3$ (STO) substrates to a few unit cells, a crossover into the Mott insulating phase emerges [84]. Although this phase transition is referred to as *dimensional crossover* by the authors, it is associated with the reduced hopping perpendicular to the film surface. This corresponds to a change in the effective *bandwith*, therefore the electronic phase transition from a correlated metal to a Mott insulator triggered by the reduction of the film thickness can be understood as a *bandwidth controlled* Mott transition.

From the material science point of view the advances in sample quality make SVO thin films attractive as highly conductive bottom electrodes with high electron mobilities and low resistivities [86]. Due to their optical transparency these films were recently also proposed as transparent conductors offering an alternative material to indium tin oxide (ITO), which is currently used in industry, but suffers from the increasing costs of the scarce indium [87, 88]. Furthermore, the strong electron correlation effects in SVO may even be harnessed in a new class of electronic devices—often referred to as *Mottronics*. Dynamical mean field theory (DMFT) based calculations suggest that Mott insulating SVO thin films with a thickness close to the transition into the correlated metal phase can be rendered metallic by an external electric field [59]. These simulations demonstrate that SVO thin films are a promising channel material for the realization of a Mott transistor that employs the electronic phase transition between Mott insulator and correlated metal to switch between an OFF- and ON-state.

The background of SVO as a prototypical correlated metal and the exciting developments initiated by the fabrication of the material as thin films animate further material optimization and investigation of its structural and electronic properties, which is the scope of this chapter. In the following the thin film fabrication by pulsed laser deposition (PLD) is discussed before turning to the thickness induced Mott transition. A closer inspection by *in situ* XPS reveals an over-oxidation of the sample surface that is overcome by capping the SVO thin films with STO. These fully stoichiometric STO/SVO/STO heterostructures then allow to disentangle the extrinsic modifications induced by surface over-oxidation from the intrinsic electronic properties of ultrathin SVO layers.

4.1 Optimization of SrVO$_3$ Thin Film Epitaxy by Pulsed Laser Deposition

As outlined in section 2.1 PLD is well suited for thin film growth of ternary oxide materials such as SVO and allows for a unit cell precision in film thickness. We therefore employ this technique for the fabrication of SVO thin films. One of the main challenges in the preparation of this material is the multivalent character of the vanadium cations, which results in a zoo of different compounds in the Sr-V-O phase diagram. Since vanadium is tetravalent in SrVO$_3$, special care has to be taken to avoid an oxidation toward the thermodynamically favored V^{5+} oxidation state. The tendency to over-oxidize is reflected in the typical growth parameters reported in literature: most groups fabricate SVO thin films in a low oxygen background of $p_{O2} \approx 10^{-7}$ mbar or even in vacuum. The typical substrate temperatures range from about $700\,°C$ to $900\,°C$ and a laser fluence of about $1\,J/cm^2$ is usually used to ablate material from polycrystalline SrVO$_{3+x}$ targets [83, 84, 89–91].

Since these parameters may delicately depend on the exact geometry of the used PLD setup or on variations in the composition and density of the target, an optimization of the thin film growth process is required before detailed investigations of the thin SVO films can be performed. The used target is a polycrystalline SrVO$_{3+x}$ pellet supplied by SurfaceNet (Germany). All SVO thin films are deposited on the TiO$_2$-terminated (001) surface of STO substrates, the surface termination procedure is described in [92]. Every substrate used for epitaxy was checked by atomic force microscopy (AFM) before growth and exhibits an atomically flat surface with terrace steps of single unit cell height. In the following, we will first analyze the impact of the substrate temperature T_s on the structural properties of the SVO films. The optimization procedure then continues with a variation of the laser fluence before the impact of an oxygen background gas on the vanadium valence is studied.

4.1.1 Substrate Temperature

Consistent with the typical fabrication parameters for SVO thin films mentioned above, the laser fluence Φ is set to $1.3\,J/cm^2$ at a laser repetition rate of $1\,Hz$. The ablation
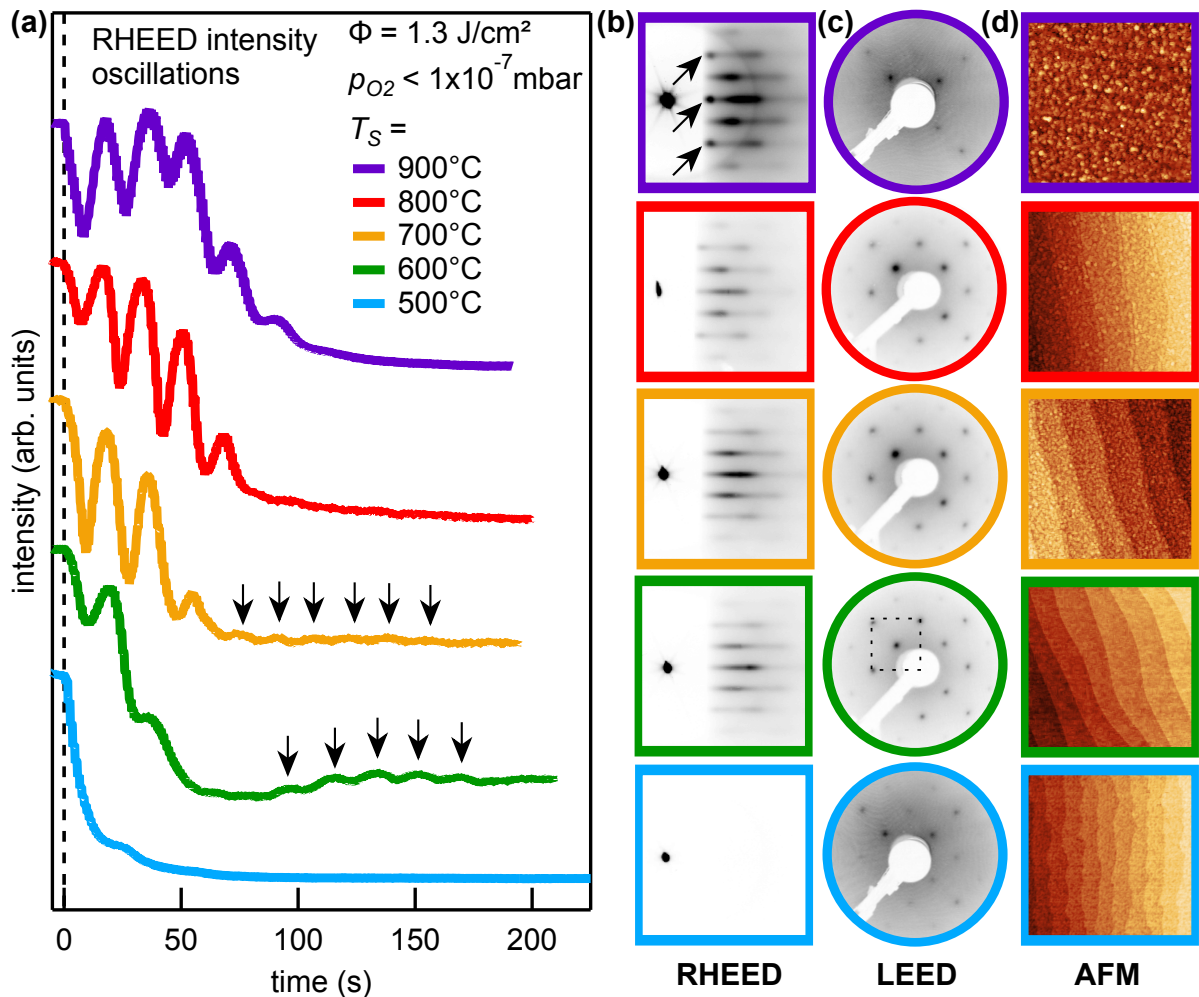
Fig. 4.1: Structural characterization of thin SVO films grown at various temperatures of the STO substrate. (a) Intensity oscillations of the specular RHEED reflex. Laser ablation starts at $t = 0$ s. The initial oscillations become clearer with increasing temperature, but in all cases except $T_s = 600\,°C$ the overall intensity is damped with progressing ablation time. The green line ($T_s = 600\,°C$) shows an upturn at t $\approx$ 75 s followed by regular intensity oscillations (highlighted by arrows) that indicate layer-by-layer growth. (b) Corresponding post-growth RHEED patterns of the SVO film. No coherent diffraction signal is observed for $T_s = 500\,°C$ suggesting a disordered film surface. For the highest growth temperature additional signals (marked by arrows) emerge that are typical for surfaces covered with crystalline islands. (c) LEED patterns of the SVO film surface taken with an electron energy of 80 eV. All patterns exhibit a $\sqrt{2} \times \sqrt{2}$ R(45°) reconstruction with respect to the cubic perovskite unit cell of STO that is exemplarily marked by the dashed square. The clearest diffraction signal is observed for $T_s = 600\,°C$. (d) *Ex situ* AFM measurements of the film surface topography. A crossover from atomically flat films to island covered surfaces with increasing T_s is detected. Image size is 2μm $\times$ 2μm.

is performed in vacuum, i.e. no process gas is injected into the PLD growth chamber. Prior to the actual film growth, an annealing step in vacuum was performed at 500 °C for 30 min to desorb adsorbates from sample holder and substrate. Due to the elevated growth temperatures the residual gas pressure in the PLD system increases from a base pressure in the 10^{-10} mbar range at room temperature to a value in the high 10^{-8} mbar range at growth temperature. The actual oxygen partial pressure during ablation is therefore indicated with the upper limit of $p_{O2} < 1 \times 10^{-7}$ mbar.

To cover the relevant range for the substrate temperature T_s, SVO films are grown from $T_s = 500$ °C to 900 °C in steps of 50 °C, with a targeted film thickness of 10 uc. The resulting structural characterization data obtained by RHEED, LEED and AFM is depicted in Fig. 4.1. For clarity, only every second temperature step is displayed, which suffices to capture the trends in this set of samples.

Let us first examine the RHEED intensity of the specular reflex during the growth process which is depicted in Fig. 4.1 (a). The evolution of the intensity can be roughly categorized in three regimes: low, mid and high substrate temperature. For the lowest temperature of 500 °C the RHEED intesity rapidly decreases and essentially decays exponentially without any sizable modulations. In the mid temperature regime ($T_s = 600 - 700$°C) intensity oscillations indicative of a layer-by-layer growth mode are detected. The oscillations are initially strongly pronounced and then fade, but not completely as marked by the arrows in Fig. 4.1 (a). In the high temperature regime the first few oscillations are even clearer, but eventually completely vanish after four to five repetitions with no further detectable intensity maxima.

The RHEED intensity evolution can be understood by analyzing the post-growth RHEED and LEED diffraction patterns of the SVO films as displayed in Fig. 4.1 (b) and (c). In the low temperature regime no coherent diffraction pattern is detected in RHEED and only a weak pattern with a noisy background is observed in LEED. This suggests that the substrate temperature is insufficient to allow for a well ordered SVO film. For the mid T_s regime a clear diffraction pattern is observed indicative of a well ordered surface. Note that the LEED pattern corresponds to a $\sqrt{2} \times \sqrt{2}$ R(45°) surface reconstruction with respect to the STO unit cell. Its microscopic origin will be discussed later, for now we take the LEED pattern as a measure for the structural quality. At the highest T$_s$ of 900 °C the RHEED pattern exhibits additional reflexes (marked by arrows in Fig. 4.1 (b)) that are typical for surfaces covered with islands.

These results show that substrate temperatures of 500 °C or lower lead to disordered SVO thin films, whereas too high temperatures (T$_s > 800$°C) result in surfaces covered by islands. This interpretation is complemented by AFM measurements depicted in Fig. 4.1 (d). Upon increasing T_s the surface morphology changes from atomically flat with steps of one unit cell in height to rough and island-like. At the highest substrate temperature, these islands are approximately 1-2 nm in height and 50-100 nm in diameter.

Based on these results, we conclude this section by identifying the mid temperature regime, i.e. $T_s = 600 - 700$ °C, as optimal growth window for SVO.

4.1.2 Laser Fluence

Another important parameter for the PLD process is the laser fluence Φ used for material ablation from the target. As discussed in section 2.1, the employed laser fluence may have an impact on the plasma kinetics or the evaporation processes. Therefore the cation stoichiometry of the grown SVO film may be affected by a variation of Φ calling for another iteration of the optimization process.

Before doing so, a related study is briefly presented. In SVO films grown by molecular beam epitaxy (MBE) on $(LaAlO_3)_{0.3}(Sr_2AlTaO_6)_{0.7}$ (LSAT) substrates, a strong impact of the cation stoichiometry on the out-of-plane (oop) lattice constant of the grown material was reported [86]. Films of different cation ratios were fabricated and the minimal oop lattice constant was found to correlate with a maximum in the residual resistivity ratio (RRR) in temperature dependent transport measurements. Since higher RRRs usually indicate a smaller amount of defects in a crystal, the maximum RRR was used to identify the stoichiometric cation ratio in this study.

The approach sketched above is straightforward for MBE grown films since this technique readily allows for a systematic variation of the cation ratio by changing the respective ion fluxes, i.e. strontium and vanadium in the case of SVO. In our case, the connection between laser fluence and cation stoichiometry is more indirect and may not give access to the whole range of possible stoichiometries.

To optimize the laser fluence Φ, a set of samples was fabricated at different values of Φ and characterized by x-ray diffraction (XRD). A sizable diffraction signal of the film is assured by increasing the targeted thickness (as determined by the RHEED intensity oscillations) to 50 uc for $\Phi=1.3$ J/cm^2 and 75 uc for all other samples. Upon decreasing Φ below the hitherto used value of 1.3 J/cm^2, the amount of ablated material per laser pulse is reduced resulting in an unreasonably long duration of the growth process. This effect is compensated by increasing the repetition rate from 1 Hz, which was used at $\Phi=1.3$ J/cm^2, up to 10 Hz for $\Phi=0.35$ J/cm^2. No differences in the thin film properties are detected for samples fabricated at the same laser fluence but at different repetition rates, therefore all variations of the film properties are directly related to the laser fluence. Another detail enters the considerations here, since the manipulator of the PLD setup was exchanged in the course of the experiments, which caused an increase of the target to substrate distance from $d_t \approx 50$ mm to 54 mm. An increase of d_t potentially changes the growth rate and the kinetics of material arriving at the substrate, which are both also linked to the laser fluence. To connect the two geometries, a sample prepared at the new and increased target distance is also included here for comparison, but the dependency of the thin film properties on the laser fluence is presented for the old geometry.

The substrate temperature is set in the optimal range between 600°C and 700°C as determined in the previous section and the ablation is performed in vacuum. The resulting ω—2Θ XRD scans around the STO and SVO (002) Bragg-reflexes of the whole sample set are depicted in Fig. 4.2 (a). The SVO (002) reflex clearly shifts toward higher diffraction angles, i.e. smaller oop lattice constants, with decreasing laser fluence Φ. To
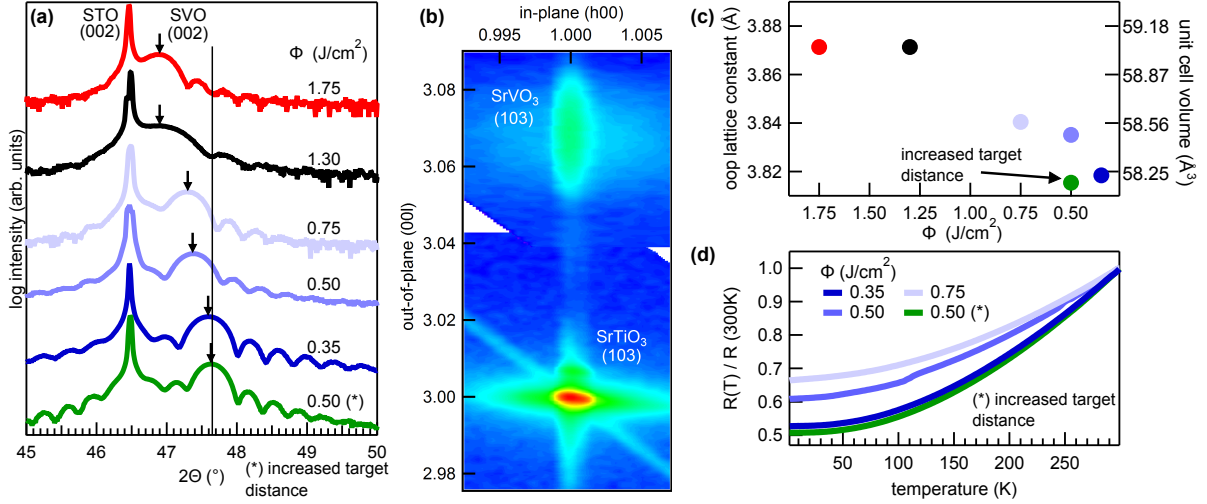
Fig. 4.2: Characterization of SVO thin films fabricated with various laser fluences. (a) $\omega - 2\Theta$-scans around the (002) reflex of the STO substrate and SVO film. As the laser fluence is decreased, the Laue intensity oscillations appear more clearly and the SVO reflex shifts to higher diffraction angles approaching the value reported by Yoshimatsu *et al.* [84] that is indicated by the vertical solid line. (b) Recioprocal space map for $\Phi = 0.35 \, \text{J/cm}^2$ indicating that the SVO films are fully strained to the substrate, i.e. exhibit the same in-plane lattice constant. (c) Out-of-plane lattice constants and unit cell volumes evaluated from the scans presented in (a). (d) Temperature dependent resistivity measurements for a subset of samples.

compare the data on an absolute scale, the value reported in literature for SVO films grown on STO substrates is included in Fig. 4.2 (a) by the straight vertical line [84]. This comparison is in favor of the samples fabricated with the lowest laser fluences, since they virtually coincide with the literature value. Furthermore, the Laue intensity oscillations centered around the SVO (002) reflex become clearer in this regime, suggesting an increase of the crystalline quality as Φ is reduced. Lower laser fluences are not accessible, since the growth rate slows down in a highly non linear manner in this regime and the unrealistic long time required for growth cannot be compensated by the repetition rate any longer. For the increased target distance ($d_t = 54 \, \text{mm}$), the lowest applicable laser fluence is $0.5 \, \text{J/cm}^2$ resulting in samples that compare well to SVO films grown with $\Phi = 0.35 \, \text{J/cm}^2$ in the initial geometry.

In order to link the oop lattice constant to the unit cell volume, reciprocal space maps (RSM) of the substrate and film (103) reflex are measured. All SVO thin films are fully strained to the STO substrate, i.e. film and substrate exhibit the same in-plane lattice constant, making the oop lattice constant a direct measure for the unit cell volume. Exemplarily for the whole sample set, the RSM of the film grown at $\Phi = 0.35 \, \text{J/cm}^2$ is depicted in Fig. 4.2 (b). The resulting oop lattice constants and unit cell volumes of the SVO thin films are plotted in Fig. 4.2 (c). The relative decrease of the unit cell volume amounts to approx. 1.4% taking the highest and lowest values into account. This reduction of the unit cell volume is likely related to a smaller lattice defect concentration, which again favors the low Φ regime in view of optimizing the growth conditions [86].
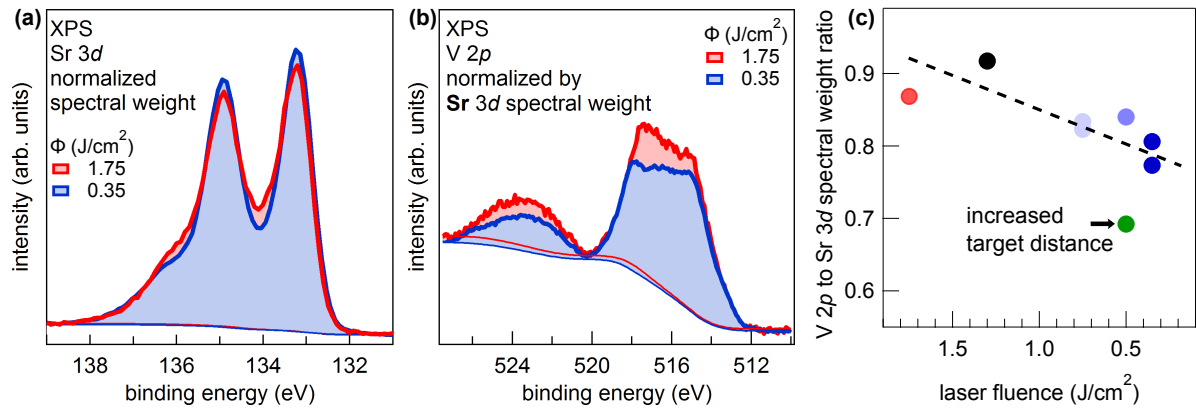
Fig. 4.3: Impact of laser fluence on the SVO cation stoichiometry. (a) Sr $3d$ core level spectra for the lowest and highest laser fluence of the same sample set as presented in Fig. 4.1. The colored area represents the extracted spectral weight and was obtained by subracting a shirley background. (b) The corresponding V $2p$ line normalized by the Sr $3d$ spectral weight indicates an increase in relative vanadium content for higher laser fluence. (c) V $2p$ to Sr $3d$ spectral weight ratio for the whole sample set. The dashed line is a guide to the eye.

Complementary data that is sensitive to the amount of structural defects is obtained by temperature dependent resistivity measurements, which are displayed in Fig. 4.2 (d). The measurements are performed in a van-der-Pauw configuration that induces uncertainties in the absolute resistivity values due to inevitable variations of the contact geometry. These effects are compensated by normalizing the data to the room temperature resistivity, thereby giving access to the RRR. As expected from the structural characterization above, the samples with the smallest SVO unit cell volume exhibit the highest values for the RRR and therefore the lowest defect density. The maximum RRR obtained here is approx. 2 and compares well to other studies [89, 93]. Significantly higher RRRs are yet reported only for MBE grown samples [86].

Having identified the lowest achievable laser fluence as the best growth regime, the question remains which type of off-stoichiometry—a relative vanadium or strontium excess—is present in samples prepared at higher laser fluences. To tackle this question, V $2p$ and Sr $3d$ core level spectra are measured by x-ray photoelectron spectroscopy (XPS). Due to the tendency of SVO to over-oxidize, the data is taken *in situ*, i.e. the samples are kept in ultrahigh vacuum after PLD growth. The resulting spectra are normalized to the Sr $3d$ spectral weight that was obtained under consideration of a shirley type background. For reasons of clarity, only the spectra for the lowest and highest Φ are depicted in Fig. 4.3 (a) and (b) and the corresponding spectral weight of the core-levels is highlighted by colored areas.

As expected from the normalization employed here, the spectral weight of the Sr $3d$ peak is equal for both samples in Fig. 4.3 (a). In the V $2p$ spectra displayed in Fig. 4.3 (b), however, the spectral weight is clearly increased for the sample fabricated at $\Phi = 1.75\,\mathrm{J/cm^2}$ indicating an increase of the relative vanadium to strontium content. For a quantitative analysis the V $2p$ to Sr $3d$ spectral weight ratio is evaluated for the

whole sample set and plotted against the laser fluence in Fig. 4.3 (c). A clear trend is detected: films grown with higher laser fluence exhibit a larger share of vanadium cations. The structural defects detected for SVO thin films fabricated with high laser fluence are therefore likely induced by a deviation of the cation ratio toward vanadium excess. Note that the spectral weight ratio evaluated here is a measure for the relative vanadium to strontium ratio, but the absolute values do not directly correspond to the stoichiometry. However, based on the complementary characterization by XRD (lowest unit cell volume) and temperature dependent resistivity measurements (highest RRR), the low Φ limit is identified to result to be closest to the optimal cation ratio.

In summary, the optimal laser fluence is determined to $0.35\,\mathrm{J/cm^2}$ in the old PLD geometry ($d_t \approx 50\,\mathrm{mm}$) and to $0.50\,\mathrm{J/cm^2}$ for $d_t = 54\,\mathrm{mm}$. In experiment, it has proven valuable to keep track of the number of laser pulses required to grow one unit cell, i.e. one RHEED intensity oscillation. Extrinsic influences such as changes of the transmission of the laser entry window are compensated by this method. The optimized laser fluences correspond to about 150 pulses per unit cell, for both geometries.

4.1.3 Oxygen Growth Pressure

As mentioned in the opening paragraph of this section, most groups fabricate SVO thin films in very low oxygen growth pressure or even in vacuum to avoid an over-oxidation of the multivalent vanadium ions. However, these thermodynamic conditions favor the formation of oxygen vacancies in STO, rendering the normally insulating substrate metallic [94, 95]. A conducting substrate complicates a characterization of the heterostructure by transport experiments and may impede the fabrication of future devices based on SVO/STO. Therefore, the impact of the oxygen growth pressure on the film properties is systematically analyzed. A structural characterization is again realized by RHEED, LEED and AFM and the electronic properties are studied by XPS and ultaviolet photoelectron spectroscopy (UPS).

The sample set studied here consists of four samples fabricated with the already optimized substrate temperature ($T_s = 650\,°\mathrm{C}$) and laser fluence ($\Phi = 0.5\,\mathrm{J/cm^2}$ at $d_t = 54\,\mathrm{mm}$) with a film thickness of approx. 75 uc. The laser repetition rate is set to $10\,\mathrm{Hz}$ and the oxygen growth pressure is varied from vacuum ($p_{O2} < 5 \times 10^{-8}\,\mathrm{mbar}$) up to $p_{O2} = 1 \times 10^{-5}\,\mathrm{mbar}$.

The structural characterization is depicted in Fig. 4.4. Let us first discuss the RHEED intensity oscillations for the three lowest growth pressures, that are depicted in Fig. 4.4 (a). Due to the optimization of T_s and Φ, the quality of the oscillations is clearly increased compared to the first experiments presented in Fig. 4.1. After an initial decrease in intensity, the signal almost fully recovers with well pronounced and regular oscillations for more than 50 repetitions. The situation is different for the highest oxygen growth pressure of the set ($p_{O2} = 1 \times 10^{-5}\,\mathrm{mbar}$): after about 200 s the intensity is strongly damped and the oscillations fade.

The cause of this behavior becomes evident from the RHEED patterns displayed in Fig. 4.4 (b). For the lower two oxygen pressures, RHEED patterns of the SVO film
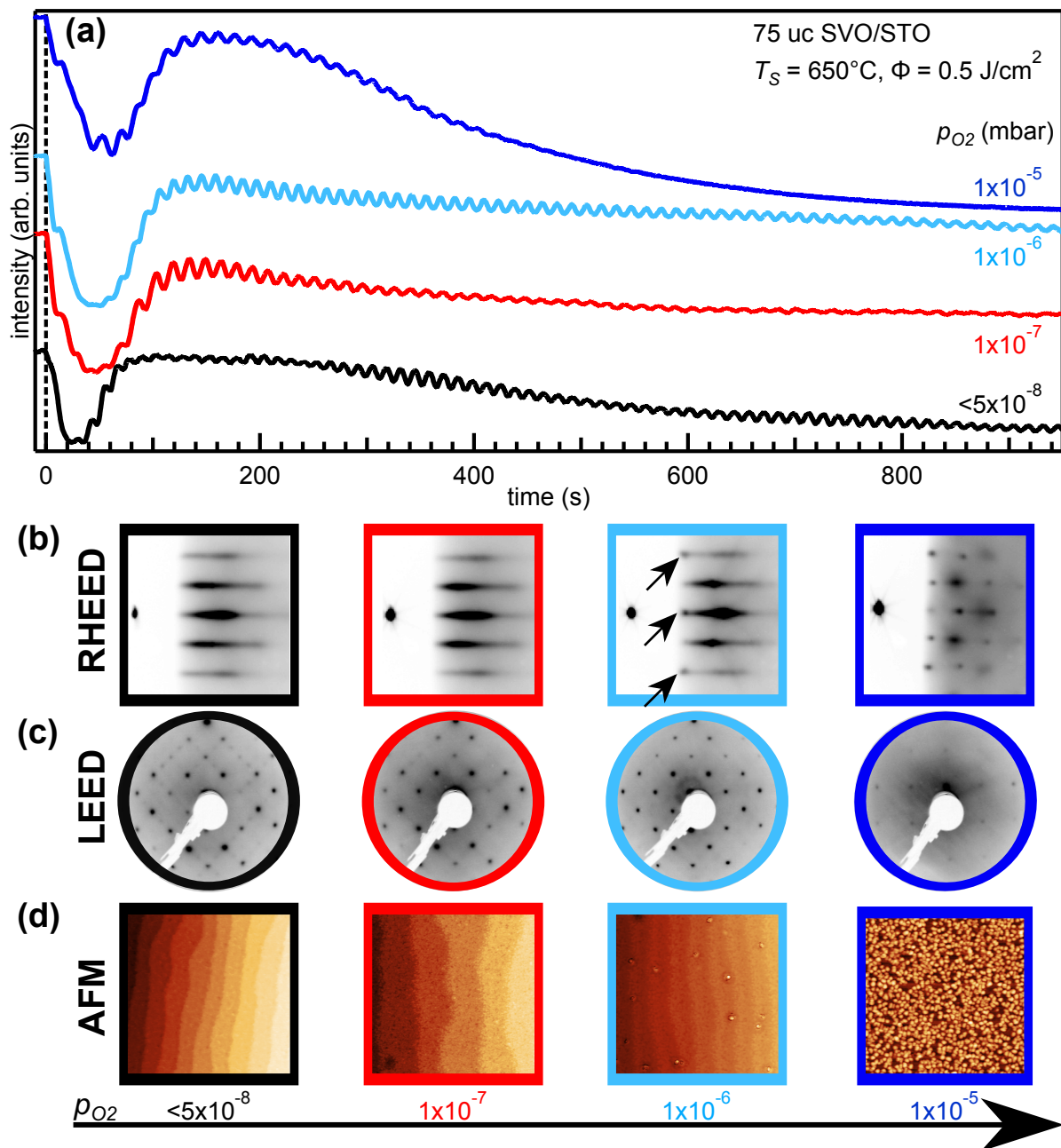
Fig. 4.4: Structural characterization of SVO thin films fabricated in various oxygen growth pressures. (a) RHEED intensity oscillations. Ablation starts at $t = 0$ and continues beyond the time frame shown. (b) RHEED diffraction pattern of the SVO thin film surface after growth. As the oxygen growth pressure is increased to 1×10^{-6} mbar or higher, additional diffraction spots (marked by arrows) appear and signal island formation at the surface. (c) Corresponding LEED patterns, measured at an electron energy of 110 eV. (d) Topography of the sample surface measured by AFM. The image size is $2\,\mu$m $\times 2\,\mu$m, each visible terrace step is one unit cell in height. The islands detected for the highest growth pressure are up to 10 nm high and approx. 50 nm in lateral extent.

surface are observed which are typical for well ordered and atomically flat surfaces. Using higher oxygen pressures induces the formation of crystalline clusters as indicated by the altered RHEED pattern, obvious for $p_{O2} = 1 \times 10^{-5}$ mbar and marked by arrows in the $p_{O2} = 1 \times 10^{-6}$ mbar case.

In LEED the diffraction pattern for the film grown in the highest oxygen pressure is barely visible indicating structural disorder. The other SVO thin films again exhibit a clear pattern indicating high structural quality. Note that the microscopic origin of this reconstruction will be discussed in the course of chapter 4, for now we take the quality of the LEED pattern as a measure of the crystalline quality of the sample surface.

To complement the structural characterization, the surface morphology of the SVO thin films is inspected by AFM. The resulting data is depicted in Fig. 4.4 (d) and confirms the interpretation of the RHEED patterns: for the lower two growth pressures an atomically flat SVO film surface with a terrace-step-height corresponding to a single unit cell is detected, whereas the highest oxygen growth pressure ($p_{O2} = 1 \times 10^{-5}$ mbar) leads to the formation of islands with up to 10 nm height and approx. 50 nm lateral extent at the film surface. The intermediate pressure of $p_{O2} = 1 \times 10^{-6}$ mbar represents a transition regime which is dominated by a flat surface but already shows indications of cluster formation.

All of the films in this sample set are about 75 uc (30 nm) thick and thereby substantially thicker than the ones studied in the course of the growth temperature optimization (see Fig. 4.1). It is remarkable that even for such thick SVO films an atomically flat surface is preserved, which demonstrates the well controlled layer-by-layer growth mode achieved for SVO thin films.

Turning from the structural characterization to the electronic properties, the V $2p$ core-level and the V $3d$ valence band spectra are analyzed. These spectra were obtained before removing the samples from the UHV system, i.e. *in situ*, to collect data that is not obscured by any additional oxidation due to air-exposure. In principle, the core-level spectra allow the determination of the vanadium valence, but the $3d^1$ configuration in SVO is expected to induce a complex line shape arising from the interaction of the $3d$ valence electron and the $2p$ core hole. Since SVO is in the metallic phase here, additional structures in the spectrum stem from non local screening of the core hole by the conduction electrons [96, 97]. The intensity of such screened structures are reported to depend on the employed photon energy and thus complicate the comparison of measured data with literature [98]. The vanadium valence therefore cannot be determined in a quantitative way from the V $2p$ core level.

Nonetheless, the spectra displayed in Fig. 4.5 (a) reveal a clear trend that is analyzed in a qualitative way by comparing the data with literature. An SVO reference spectrum is taken from Eguchi *et al.* [96] that was measured on an UHV cleaved $SrV^{4+}O_3$ single crystal at a photon energy of about 8 keV. As a second reference, the binding energy of V^{5+} ions in V_2O_5 as reported by Silversmith *et al.* [99] is indicated by the dashed line in Fig. 4.5 (a). The spectrum obtained for the SVO film fabricated in vacuum (black line in Fig. 4.5 (a)) resembles the reference spectrum with an additional feature on the high binding energy side at about 518-519 eV. As the oxygen growth pressure is increased,
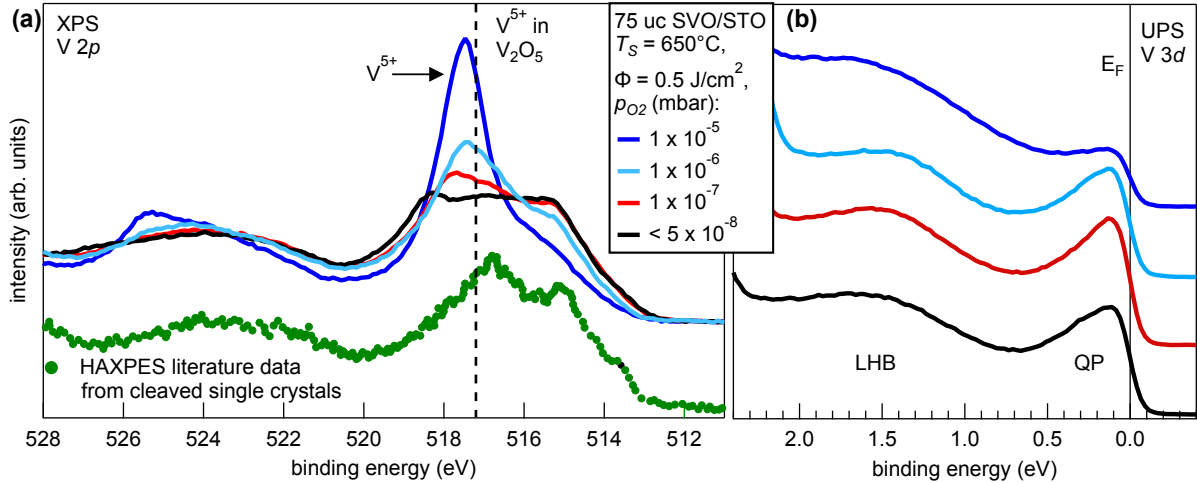
Fig. 4.5: Spectroscopic characterization on the impact of oxygen growth pressure on SVO thin films. (a) *In situ* XPS measurements of the V $2p$ core level spectrum shows the formation of pentavalent vanadium upon increasing p_{O2}. For comparison the binding energy of V^{5+} ions in V_2O_5 and a HAXPES (h$\nu \approx 8$ keV) reference spectrum measured on UHV-cleaved SVO single crystals is included. The data is taken from Silversmith *et al.* [99] and Eguchi *et al.* [96] respectively. (b) Corresponding V $3d$ spectra obtained by UPS. The sample fabricated at $p_{O2} = 1 \times 10^{-5}$ mbar exhibits a distinctly different spectral shape, all other spectra are almost identical.

this feature gains in intensity and shifts to smaller binding energies. Due to the expected over-oxidation and the comparison to V_2O_5, this feature is assigned to V^{5+}-ions. The V^{5+}-signal dominates the $2p$ spectrum for an oxygen growth pressure of 1×10^{-5} mbar making a strong over-oxidation evident that probably causes the cluster formation on the surface discussed above.

The assessment of the electronic properties is complemented by the V $3d$ valence band spectra depicted in Fig. 4.5 (b). For all samples, two distinct features are observed close to the Fermi level and are attributed to the quasiparticle peak (QP) and lower Hubbard band (LHB). The spectral line shape consisting of these two features is almost identical for the lower three oxygen growth pressures while the highest p_{O2} leads to a suppressed QP.

It is surprising that the V $3d$ states are rather robust against over-oxidation. For instance, a sizable V^{5+} contribution is detected for $p_{O2} = 1 \times 10^{-6}$ mbar in the V $2p$ spectrum, but the QP remains well pronounced. A possible reason for this behavior is a separation into d^1 (V^{4+}) and d^0 (V^{5+}) areas in this SVO film. In such a configuration the d^0 areas give rise to the V^{5+} signal in the core level spectrum but at the same time do not contribute to the valence band because of an empty $3d$ shell, as suggested by Takizawa *et al.* [83].

In conclusion, an oxygen growth pressure of 1×10^{-7} mbar or lower should be employed to fabricate SVO thin films. The analysis of the V $2p$ spectrum even suggests to minimize the oxygen pressure. As mentioned above, certain applications cannot tolerate an oxygen

vacancy doped, i.e. conducting, STO substrate. For such cases the intermediate regime in the 1×10^{-6} mbar range might be a valuable trade-off between film quality and oxygen vacancy doping in the substrate. However, the cluster formation detected for growth in an 1×10^{-5} mbar oxygen sets a hard upper limit for the growth pressure.

4.1.4 Growth Phase Diagram

The results of the optimization procedure carried out for the SVO thin film epitaxy are summarized in a growth phase diagram in the plane of laser fluence Φ and substrate temperature T_s depicted in Fig. 4.6. Black and green stars indicate the fabricated samples in the two PLD geometries, i.e. with target distance $d_t \approx 50$ mm and $d_t = 54$ mm, respectively. The oxygen growth pressure should be kept below 10^{-6} mbar, with the lowest pressures yielding the smallest V^{5+} content and higher pressures leading to strongly over-oxidized SVO films.

The growth window with respect to the substrate temperature is located between 600°C and 700°C. Lower temperatures result in disordered SVO thin films, whereas a higher T_s favors the formation of clusters on the otherwise atomically flat film surfaces.

The optimized laser fluence is 0.50 J/cm^2 (0.35 J/cm^2) for d$_t$ = 54 mm ($d_t \approx 50$ mm, geometry before replacement of the manipulator), which corresponds to a growth speed of $\approx$150 laser pulses per unit cell. Smaller values for Φ are not possible due to the drastic decrease of the growth rate for these very low laser fluences, which is referred to as *deposition limit* in Fig. 4.6. Samples fabricated with higher laser fluences exhibit deviation of the relative cation ratio toward vanadium excess as detected by XPS.
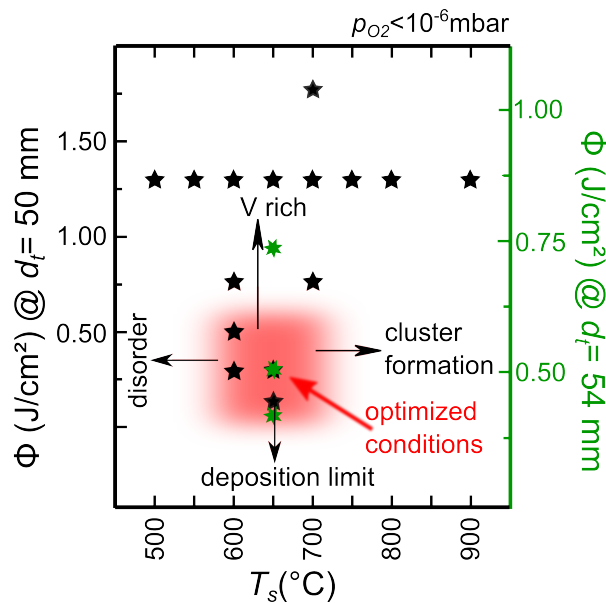

Fig. 4.6: SVO thin film growth phase diagram summarizing the optimized conditions and detected trends. Black stars indicate samples fabricated at a target distance of about $d_t \approx 50$ mm, green stars correspond to $d_t = 54$ mm.

4.2 Characterization of Ultrathin SrVO$_3$/SrTiO$_3$ Structures

Having identified the optimal growth conditions and established a layer-by-layer growth mode for SVO, we now turn to analyze the electronic properties of ultrathin films that approach the two-dimensional limit. First, the vanadium $3d$ valence states are inspected for films with various thicknesses to pinpoint each sample's electronic phase, i.e. correlated metal or Mott insulator. Then, the chemical environment of surface vanadium ions is investigated by emission angle dependent XPS since the surface layer accounts for a large proportion of the ultrathin films and may strongly impact their electronic properties.

4.2.1 Metal-to-Insulator Transition in the Two-Dimensional Limit

The V $3d$ valence states of SVO are conveniently inspected by means of UPS operating with He I_α (photon energy of h$\nu \approx 21$ eV). The cross section for photoemission for V $3d$ electrons in this photon energy range is significantly higher than for Al K_α-XPS (h$\nu \approx$ 1.5 keV) allowing for high count rates. The trade-off is the reduction of the probing depth to only a few uc, which means that even for thick SVO films the obtained spectra may not purely reflect the bulk properties of SVO, but may be altered by surface effects.

The resulting spectra for a set of samples with SVO thicknesses ranging from 2 to 6 uc are depicted in Fig. 4.7 (a). In the following the samples are referred to as x uc SVO/STO, x denoting the SVO film thickness in unit cells. As references, a Nb:STO substrate ($x = 0$) and a 75 uc thick SVO film (bulk SVO) are included as well.

The spectra consist of O $2p$ and V $3d$ states that are well separated. On the high binding energy side, the O $2p$ spectral shape changes as the SVO thickness is increased from 2 to 6 uc. As is clear from the comparison to the Nb:STO reference, these changes are an artifact stemming from the finite probing depth of the experiment. For the thinnest SVO films an O $2p$ signal emitted from the STO substrate is picked up and the resulting line shape is a superposition of the STO and SVO spectrum. At a film thickness of 5 to 6 uc the changes saturate and the spectral shape is identical to the 75 uc thick film that serves as a bulk reference.

The situation is clearer for the V $3d$ states located near the Fermi level, since the STO substrate does not contribute any signal in this energy range. For clarity, this region is depicted in more detail in Fig. 4.7 (b). The bulk reference sample exhibits the well known two peak structure of LHB and QP peak with a clear Fermi cutoff signalling the correlated metal phase. Upon decreasing the SVO thickness, spectral weight is transferred from the QP to the LHB and eventually the QP is completely supressed at $x = 2$ with only the LHB remaining. The onset of this LHB is at about 100 meV below the Fermi level, giving a lower boundary for the Mott gap between the onsets of lower and upper Hubbard band. The size of the Mott gap indicates that the 2 uc thick SVO film is well within the Mott insulating phase.
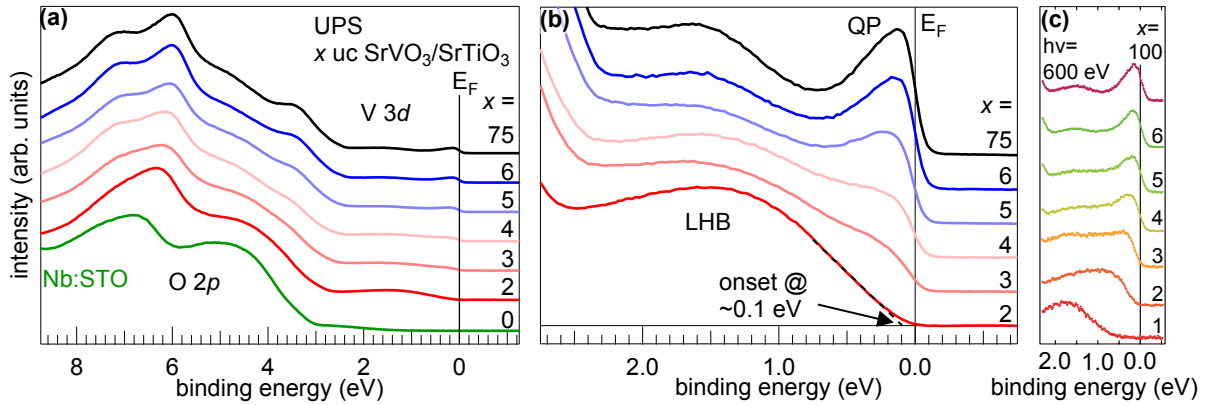
Fig. 4.7: Valence states of SVO films on STO with various thicknesses. (a) Spectra measured with He I_α (h$\nu \approx 21$ eV) in a wide binding energy range. (b) Near E$_F$ region: thick SVO films exhibit a Fermi cutoff and the typical two peak structure for a correlated metal consisting of QP and LHB. The QP spectral weight at the Fermi level gradually vanishes as the film thickness is decreased. At $x = 2$ uc exclusively a LHB is detected indicating the crossover into the Mott insulating phase. (c) The data from Yoshimatsu *et al.* [84] (figure adopted) exhibit the same characteristics of the thickness induced Mott transition.

Adding a single unit cell to the thickness already changes this clear situation: for $x = 3$, neither a sizable energy gap is observed nor a clear Fermi cutoff. The structure closest to the Fermi level resembles the QP of thicker SVO films, but without a Fermi cutoff this sample is situated in a crossover region in the electronic phase diagram [84]. The clear onset of the correlated metal phase is then detected at $x = 4$ and the QP intensity further increases until saturation in a bulk like lineshape at 6 uc SVO thickness.

As mentioned above, this thickness induced Mott transition was reported before by Yoshimatsu *et al.* [84]. In order to connect our data set to this precedent study their results are also depicted in Fig. 4.7 (c), which allows a direct comparison to our findings. Even though the photon energy—and thereby the probing depth—is significantly different in the two experiments, the main characteristics of the transitions are identical: a Fermi cutoff is observed for SVO films thicker than 3 uc and the evolution of the V $3d$ spectral shape saturates at $x = 6$, i.e. the spectrum already resembles the SVO bulk reference.

The origin of this Mott transition is ascribed to a reduction of the electron hopping perpendicular to the film surface (z-direction), which is fully suppressed in the two-dimensional limit [84]. With view on the Mott phase diagram introduced in chapter 3, we capture the reduced z-hopping by replacing the bandwidth t by an effective bandwidth t_{eff}. Within such a simplified phenomenological approach, we can argue that the reduced film thickness decreases t_{eff} and thereby alters the ratio between on-site Coulomb repulsion U and t_{eff} in favor of the Mott insulating phase, i.e. larger $\frac{U}{t_{eff}}$ values in the Mott phase diagram. Decreasing the SVO film thickness therefore causes the crossover into the Mott insulating phase when a critical value $(\frac{U}{t_{eff}})_c$ is reached (see schematic diagram in Fig. 4.8). Thus one can classify the transition as bandwidth con-

trolled. Note that the V 3d states are located within the bandgap of the STO substrates (see Fig. 4.7 (a)), the valence electrons are therefore fully confined to the SVO film.

More refined versions of this explanation take the V 3d crystal field into account. Due to the cubic perovskite structure of bulk SVO, the t_{2g} levels are three fold degenerate. Such a degeneracy is thought to increase the critical value of $(\frac{U}{t_{eff}})_c$ that is required for the transition from a correlated metal into the Mott insulating phase by a factor of $\sqrt{N_d}$, where N_d denotes the orbital degeneracy [100]. Hence, the three fold degeneracy in bulk SVO shifts the critical value in favor of the metallic phase.

It appears intuitive that the symmetry of the crystal field is lowered when the two-dimensional limit is approached. Indeed, recent DMFT simulations predict a sizable splitting of the t_{2g} levels in the surface layer of a 2 uc SVO/STO structure [59]. The splitting amounts to 0.18 eV between the xy (lower level) and the orbitals with an out of plane component (yz and xz) inducing an orbital polarization, i.e. preferred occupation of the xy levels. The authors of this study identify the lifting of the degeneracy in the t_{2g} levels as the origin of the Mott transition rather than the mere reduction of hopping in z-direction.

Another approach to explain the transition is based on the detection of quantum well states in SVO films with a layer thickness of 5 to 10 uc by Yoshimatsu *et al.* [85]. The confinement of the V 3d states causes an orbital-selective quantization of the xz and yz states whereas the xy orbital is not affected by the reduced film thickness. Similar to the textbook example of confined electrons, the xz and yz states form quantum well states and the film thickness determines the number of filled subbands. For the thinnest films of 1 and 2 uc thickness, all xz and yz subbands are located above the Fermi level, leaving only the xy band occupied which again lifts the degeneracy of the t_{2g} levels in favor of the Mott insulating phase.

Fig. 4.8: Electronic phase diagram plotting U/t_{eff} *vs.* band filling. Upon approaching the two-dimensional limit (x=1) the electron hopping perpendicular to the film surface is suppressed corresponding to a reduction of t_{eff} compared to bulk SVO.

Let us conclude that even though the splitting of the t_{2g} levels is likely involved in the dimensional crossover in ultrathin SVO films, we can describe this Mott transition in our simplified phase diagram as *bandwidth* controlled. On the insulating side of the transition, the unoccupied xz and yz states are not available for electron hopping, thereby reducing the effective bandwidth.

Complementary to the spectroscopic data presented above, a temperature dependent resistivity study by Gu *et al.* on SVO thin films grown on LSAT substrates finds a similar dimensional crossover [93]. The details are, however, distinctly different: whereas a Mott gap is detected below 3 uc SVO thickness in spectroscopy, insulating behavior is reported
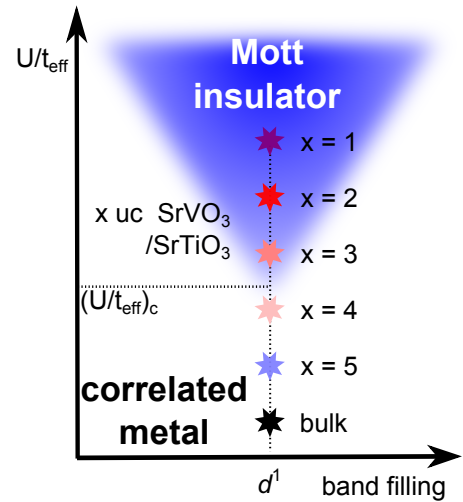
up to 7 to 8 uc thick SVO films in this transport study. The substrate choice of LSAT over STO is likely not causing the change of the crossover-thickness since the lattice constants of these substrates are very similar (3.846 and 3.905 Å, respectively). One more striking difference is the sample handling: while the spectroscopy experiments are performed *in situ*, the samples are exposed to air for electrical contacting in transport measurements. As inferred from the growth study in different oxygen background pressures presented in section 4.1.3, such an air exposure probably causes an over-oxidation of the SVO films and may effectively reduce the active SrV^{4+}O$_3$ film thickness due to the emergence of an insulating dead layer at the surface. Such a scenario explains the delayed onset of metallic behavior detected in transport experiments.

4.2.2 Over-Oxidation at the SrVO$_3$ Film Surface

To catch a possible over-oxidation and its impact on the dimensional crossover in ultra-thin SVO films, the V $2p$ spectrum is measured *in situ* and after storage of a sample in air (*ex situ*). As depicted in Fig. 4.9 (a), the spectrum is strongly altered with V^{5+} being the dominating valency after exposure to air signalling electron loss in the V $3d$ states. The valency shift is likely attributed to the inclusion of excess oxygen ions from air into the surface of the SVO film. The thickness of this surface layer is at least several nm, since the inelastic mean free electron path λ amounts to approx. 2 nm in this measurement. These findings confirm that samples handled in air suffer from an uncontrolled over-oxidation as suspected for the transport study discussed above—putting their results in doubt.

Surface over-oxidation may not only be a problem when samples are exposed to air, since the thermodynamically most stable valence in vanadium is 5+ and the SVO film surface offers various adsorption sites for additional oxygen ions. Therefore, the V $2p$ spectrum is measured at various electron emission angles ϑ, i.e. at different effective probing depths, on a 75 uc thick SVO film that was transferred in UHV from the PLD chamber into the XPS spectrometer (same experimental conditions as for the measurements of the V $3d$ valence states depicted in Fig. 4.7). The resulting spectra are plotted in Fig. 4.9 (b) and exhibit a clear V^{5+} signal, which gains intensity in more surface sensitive measurement geometries, i.e. at larger angles ϑ. In light of the complex line shape of the V^{4+} $2p$ spectrum and the lack of a comparable reference spectrum, a quantitative analysis of this depth profile is not feasible. A coarse estimation, however, suggests that the V^{5+} signal is confined to the first few unit cells of the SVO surface.

Complementary structural information to these measurements is provided by LEED, the corresponding diffraction pattern is depicted in Fig. 4.9 (c). As briefly mentioned in section 4.1.3, the observed pattern is a $\sqrt{2} \times \sqrt{2}$ R(45°) reconstruction with respect to the cubic perovskite unit cell. The associated unit cells in reciprocal and direct space are marked in the pattern and in the structural model below by green and black squares for the cubic perovskite and the reconstruction, respectively. This surface reconstruction is also reported in the literature and a recent scanning tunneling microscopy (STM) study by Okada *et al.* [91] identifies adsorbed oxygen ions as its microscopic origin [83, 85].
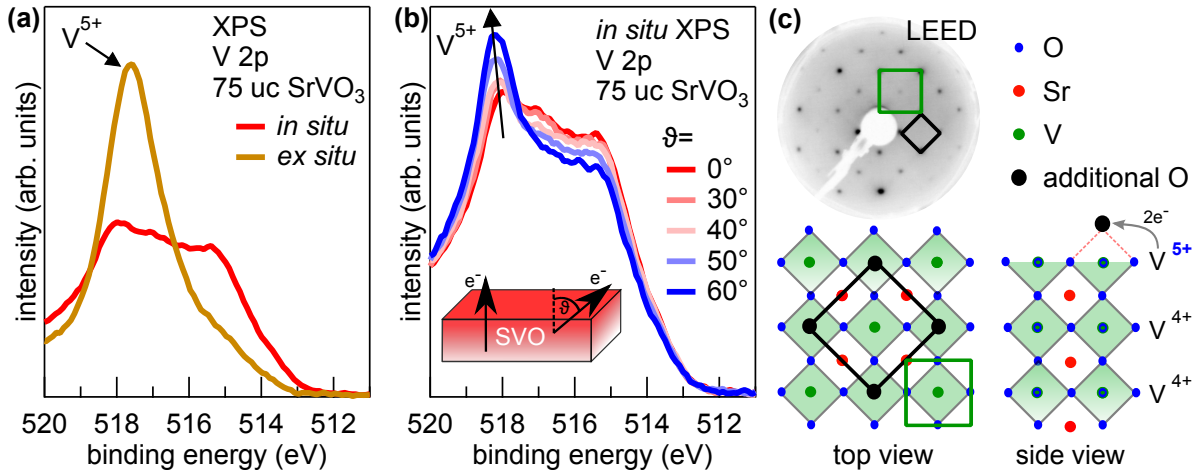
Fig. 4.9: Surface characterization of SVO films. (a) V $2p_{3/2}$ spectra measured *in situ* and after exposure to air (*ex situ*). (b) *In situ* XPS at different electron emission angles ϑ detects a V^{5+} signal that emanates from the surface, even without exposure to air. (c) Typical LEED patterns exhibit a $\sqrt{2} \times \sqrt{2}$ R(45°) surface reconstruction consistent with the adsorption of excess oxygen ions on apical sites recently detected in an STM study [91]. The corresponding structural model of ordered additional oxygen ions that drain electrons from the SVO film generating V^{5+}-ions at the surface is depicted in the lower part. The green and black squares refer to the surface unit cell of the cubic perovskite and the reconstruction, respectively.

They find that additional oxygen ions occupy half of the apical sites above the surface vanadium ions, thereby closing the VO_6 octahedron as sketched in the lower right part of Fig. 4.9 (c) [91]. This microscopic picture matches the over-oxidation detected in the V $2p$ core level since every excess oxygen ion drains two electrons from the SVO films, thereby generating two vanadium ions of valency 5+.

With a view on the dimensional crossover in SVO, such surface effects may play a decisive role since the film thickness is decreased to only several uc. We therefore now turn to the analysis of the V $2p$ core level and the LEED patterns measured on SVO/STO samples with thicknesses across the bandwidth controlled Mott transition.

4.2.3 Evolution of the Vanadium Valence with Film Thickness

In the course of the UPS measurements performed to analyze the Mott transition in ultrathin SVO films (see Fig 4.7 (a) & (b)), additional XPS and LEED data were taken on the identical samples. The resulting V $2p_{3/2}$ spectra are depicted in Fig. 4.10 (a) and exhibit a systematic trend: the intensity of the V^{5+} signal scales with the film thickness and saturates at 5 to 6 uc at the same level as the bulk-like reference, i.e. 75 uc SVO/STO. This means that the average vanadium valence appears to change in the same thickness range in which the dimensional crossover occurs. Note that some subtle changes in the spectra may also be caused by a change of the V^{4+} line shape of the $2p$ core level across the phase transition, since the afore mentioned non-local screening channels are only available in the metallic phase [96, 97].

To back up the analysis of the V $2p$ spectrum the corresponding LEED patterns are added to the consideration. As pointed out in the previous section, the $\sqrt{2} \times \sqrt{2}$ R(45°) surface reconstruction is caused by excess oxygen adsorbed at the sample surface and is therefore a qualitative indicator for the presence of over-oxidized V^{5+} ions. The diffraction patterns are displayed in Fig. 4.10 (b) and the cubic perovskite unit cell expected for pristine SVO is marked by dashed squares. The surface reconstruction is present on all samples, see for instance the exemplary reflex highlighted by arrows. Upon closer inspection it is, however, apparent that the intensity of the reflexes belonging to the reconstruction lose intensity with respect to the intrinsic spots, i.e. the 1×1 pattern, for thinner SVO films. This trend is likely connected to the proportion of the surface which is covered with excess oxygen, to be more specific it is the relative area on which the adsorption occurs in a structurally ordered way. In principle it is possible that additional oxygen ions occupy the apical sites in a random manner, giving no coherent diffraction signal at all. But since the trend detected in the LEED patterns corroborates the interpretation of the V $2p$ spectrum, we can draw the following conclusion: V^{5+} ions are present on the surface of ultrathin SVO films and the relative coverage gradually decreases when the SVO film thickness is smaller than 5 uc.

The link between film thickness and coverage may be exemplified by considering the amount of electrons that is drained from the SVO film by the excess oxygen ions. A full coverage by the $\sqrt{2} \times \sqrt{2}$ R(45°) reconstruction induces one V^{5+} ion per surface unit cell. A thick film provides a large reservoir of $3d$ electrons and therefore the *average* change of the vanadium valence is negligible. As the film thickness is decreased the relative share of the V^{5+} ions generated by the reconstruction increases. For instance at $x = 2$ uc, half of the vanadium ions are rendered from tetra- to pentavalent at a full coverage by the reconstruction, which may not be energetically favorable and hence a lower coverage develops.

It is surprising that the change in V^{5+} content correlates with the dimensional crossover and puts some doubt on the established interpretations as a purely *bandwidth* controlled Mott transition. The transition might be assisted by a change in *band filling*.

However, the question arises whether the surface V^{5+} ions actually dope the V $3d$ band in a homogeneous way or if a separation into patches of d^0 and d^1 filling occurs. Such an electronic inhomogeneity is widely reported for transition metal oxides [101–105]. The most relevant comparison can be made to the two-dimensional electron system (2DES) found on the bare surface of STO. Here, the formation of oxygen *vacancies* leads to an electron doping of the Ti $3d$ band, the doping, however, is not homogeneous but induces highly doped and undoped patches [101]. In the present case of the SVO surface, the excess oxygen on the surface drains electrons from the V $3d$ band (p doping) and could—in analogy to the STO 2DES—induce patches of d^0 filling that give no contribution to the V $3d$ spectrum at all, while at the same time inducing a V^{5+} signal in the $2p$ core level spectrum.

On the other hand, the additional oxygen at the SVO surface has a large impact on the average number of V $3d$ electrons in these ultrathin films. An estimation presuming that every second apical site is occupied with an excess oxygen ion each accepting two
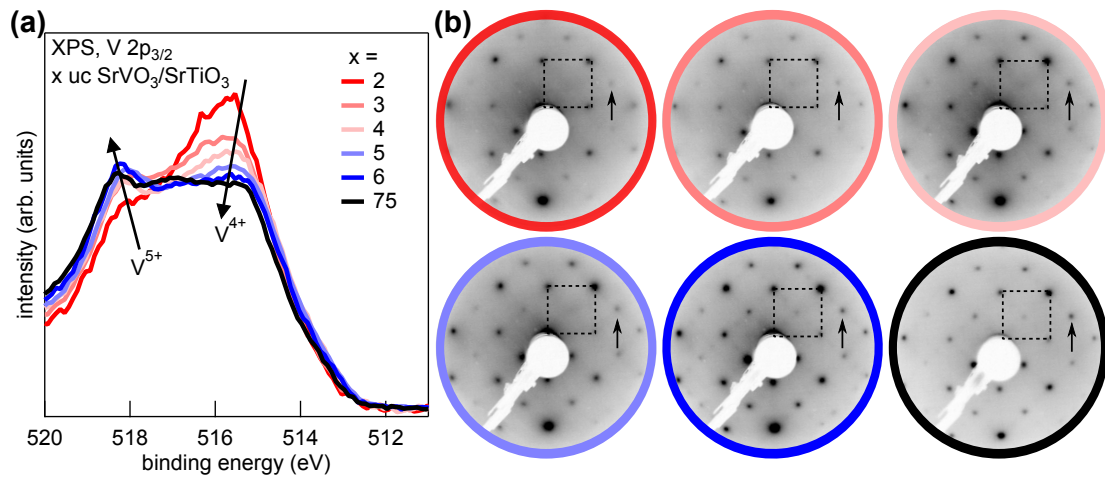
Fig. 4.10: Surface over-oxidation of ultrathin SVO films. (a) V $2p_{3/2}$ spectra of SVO films with thicknesses relevant to the Mott transition. A clear V^{5+} signal is detected that decreases for thinner layers. (b) Corresponding LEED patterns with the cubic perovskite unit cell marked by dashed squares. The surface reconstruction is present on every sample (see exemplary reflex indicated by the arrows), but less pronounced at smaller SVO thicknesses.

electrons yields a loss of 20 % of the $3d$ electrons for a 5 uc SVO/STO sample and even 50 % for a 2 uc thin film. Even if the electron loss is not an homogeneous p doping, these strong extrinsic chemical effects may disguise the intrinsic origin of the metal-to-insulator transition. This raises the question how the over-oxidation can be avoided and tetravalent vanadium can be stabilized at the SVO surface, which will be addressed in the following section.

4.3 Surface Passivation by SrTiO$_3$ Capping

The SVO thin films discussed above are already handled *in situ*, further reducing the exposure to oxygen is not possible. Therefore, it is necessary to reconsider the sample design to avoid the loss from vanadium $3d$ electrons to excess oxygen at the thin film surface. Besides the surface, the SVO films exhibit an interface to the underlying STO substrate. The chemical situation at this bottom interface is straightforward: the strontium cations are present on both sides and in oxidation state +2. The vanadium cations are replaced by titanium in the substrate—both have a valence of +4. The STO substrate therefore mimics the structural and chemical environment of bulk SVO and due to its large band gap confines the V $3d$ electrons to the film.

This motivates to consider an STO layer on top of the SVO film instead of the bare VO$_2$-terminated surface, as depicted in Fig. 4.11 (a). For the bare surface two electrons are lost to each adsorbed oxygen ion, i.e., one layer of V^{5+}O$_2$ is generated when every second apical oxygen site is occupied. In the STO capped case all apical sites are occupied by oxygen ions, but electrons are also supplied by the strontium and titanium cations of the capping layer, stabilizing the V^{4+} valence.
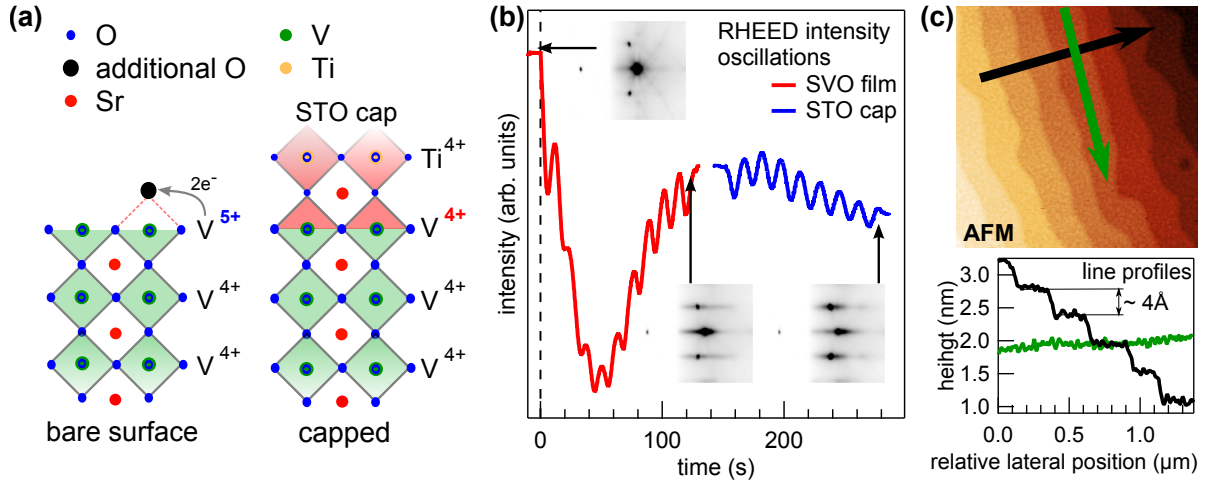
Fig. 4.11: (a) Comparison of the vanadium valence of a bare SVO film surface and an STO capped sample. (b) Structural characterization by RHEED indicates a layer-by-layer growth of the STO capping. (c) AFM measurements reveal an atomically flat surface of the STO cap. Image size is $2\,\mu$m $\times\ 2\,\mu$m. The height profiles depicted in the lower part of the figure are taken along the lines indicated by the arrows.

Experimentally, such a capping layer is grown by PLD at the same substrate temperature and oxygen pressure as the SVO film itself (see section 4.1 and Fig. 4.6). The STO material is ablated from a single crystalline target with a laser fluence of $1.3\,\mathrm{J/cm^2}$ at a repetition rate of $1\,\mathrm{Hz}$. The resulting regular RHEED intensity oscillations are plotted in Fig. 4.11 (b) together with the corresponding diffraction patterns. The characterization by RHEED suggests a layer-by-layer growth mode resulting in an atomically flat STO surface. This interpretation is confirmed by an AFM measurement of the same sample and is depicted in Fig. 4.11. The faint granular structures visible on top of the step-and-terrace like surface are probably induced by excess material deposited on the sample after completion of the topmost closed layer. The line profiles indicate that the surface is still atomically flat and the STO capping layer fully covers the SVO film.

Having established the fabrication of an epitaxial STO capping layer, we now turn back to the V $2p$ core level spectrum to evaluate the impact of the modified sample design on the vanadium valence.

4.3.1 Stabilization of Tetravalent Vanadium

To compare the vanadium valence of a bare film to an STO capped one, two $50\,\mathrm{uc}$ thick SVO/STO samples are fabricated at identical conditions and only one is equipped with a $4\,\mathrm{uc}$ thick STO capping layer. These samples are transferred to beamline I09 of the Diamond Light Source by means of a vacuum suitcase ($p < 10^{-9}\,\mathrm{mbar}$). The endstation allows for a broader spectrum of photon energies hν and thereby for a larger variation in probing depth. Measurements of the V $2p_{3/2}$ core level are performed at h$\nu = 700\,\mathrm{eV}$ and $3\,\mathrm{keV}$ at various electron detection angles ϑ.
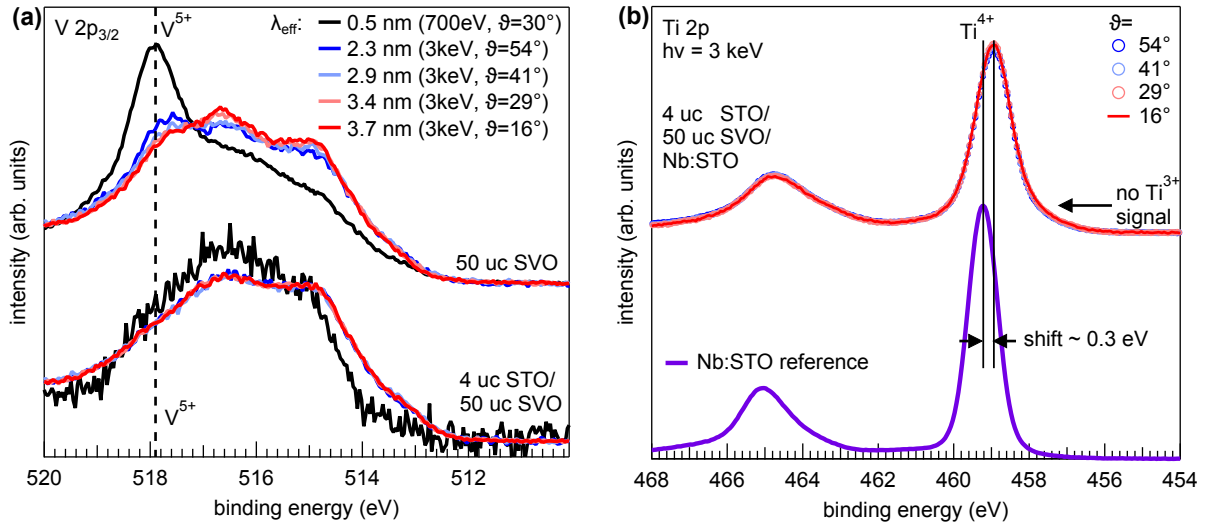
Fig. 4.12: (a) V $2p_{3/2}$ core level spectra of 50 uc thick SVO films with a bare surface and capped by 4 uc STO measured with different probing depths as indicated by λ_{eff}. The V^{5+} signal detected on the bare film is absent in the STO capped sample. (b) Ti $2p$ lines obtained from the 4 uc STO/50 uc SVO structure exhibit no emission angle dependence. The line shape is typical for tetravalent titanium as is clear from the comparison to the STO bulk reference.

The results are depicted in Fig. 4.12 (a) and for clarity the corresponding effective inelastic mean free path $\lambda_{eff} = \lambda \times \cos \vartheta$ is indicated for each spectrum. As expected, a clear V^{5+} signal is detected on the bare SVO surface. In line with the surface character of the over-oxidation, this signal is more pronounced for smaller values of λ_{eff}.

The situation is different for the capped sample: no sizable V^{5+} signal or probing depth dependence is detected. The change in line shape between the black curve ($\lambda_{eff} = 0.5$ nm) and the remaining spectra is likely attributed to the fact that the afore mentioned non local screening channels are less pronounced at low photon energies and not to a variation of the vanadium valency [96, 97]. All spectra obtained at 3 keV coincide despite the different emission angles ϑ employed during the measurements which demonstrates the homogeneity of the vanadium valence. Even though the intrinsic V^{4+} line shape is not known, these experiments strongly suggest that the chemical surface effects detected for the bare SVO surface are completely suppressed by the STO capping layer and that tetravalent vanadium is stabilized throughout the SVO film.

In order to mimic the chemical environment of bulk SVO, it is crucial that the STO capping layer consists essentially of Ti^{4+} ions. Since STO tends to form oxygen vacancies, the low oxygen pressures used during epitaxy of the capping may result in a sizable amount of oxygen vacancies that in turn create Ti^{3+}-ions [101, 106]. Such trivalent titanium ions could induce a finite filling of the Ti $3d$ band in the STO cap that overlap with the V $3d$ states in SVO and could again obscure our view on the dimensional crossover in ultrathin SVO films. Therefore, the Ti $2p$ line of the 4 uc STO/50 uc SVO sample is carefully characterized as depicted in Fig. 4.12 (b). Let us first draw the comparison to the bulk $SrTi^{4+}O_3$ reference: besides an energy shift of approx. 0.3 eV, the

line shape of the spectra is almost identical and no additional feature arising from Ti^{3+}-ions is detected. Hence, the STO capping consists exclusively of tetravalent titanium ions. We further note that the spectra measured at different electron emission angles ϑ all coincide, the Ti $2p$ binding energy is therefore constant throughout the capping layer and no asymmetry develops in more surface or interface sensitive geometries—ruling out a strong band bending at the surface or interface of the STO layer.

Two conclusions can be drawn from these results. First, the STO capping layer does not contain a sizable amount of oxygen vacancies and the samples match the idealized design presented in Fig. 4.11 (a). Second, no electrons are transferred from the SVO film with d^1 configuration to the STO capping layer. In analogy to the band alignment between substrate and film, we will show in the following that the V $3d$ states are located in the STO bandgap at this top interface of film and cap. We will quantify this finding on the band alignment at the STO/SVO interface in the following section.

4.3.2 Band Alignment at the SrTiO$_3$/SrVO$_3$ Interface

Before discussing the valence band offsets at the interface between STO capping layer and SVO film, we note that the absence of any emission angle dependence in the V $2p$ and Ti $2p$ spectra measured on the 4 uc STO/50 uc SVO structure (see Fig. 4.12) already indicates that the bands on both sides of the interface are flat, i.e. no band bending occurs. To complete the view on the band alignment at the top interface we will now determine the offset between STO and SVO valence bands.

A band alignment analysis usually requires measurements on three samples: both bulk constituents (here a 50 uc thick SVO film and an STO substrate) as reference points and the heterostructure with layer thicknesses that matches the probing depth of the experiment. The band alignment can be accessed by a decomposition of the heterostructure's valence band into a superposition of the corresponding reference spectra while allowing for an energy shift of the references. As an alternative method the core level binding energies can be evaluated relative to the valence band onset position [107, 108]. In the case of STO/SVO, the core level based method is not suited since both layers contain oxygen and strontium therefore giving no proper contrast for the data evaluation. Furthermore, the V $2p$ line is disqualified as well due to the inherent surface oxidation present on the bare SVO film which is required as a bulk reference. This leaves only the Ti $2p$ core level, which can serve as a comparison of STO as capping layer and bulk material, but alone is not sufficient to deduce the valence band offset between STO and SVO.

We therefore first concentrate on the valence band decomposition method. The relevant data is depicted in Fig. 4.13 (a). The heterostructure's valence band is fitted by the superposition of the SVO and STO bulk reference data with the relative intensities and the binding energy as free parameters. One may argue that the spectral shape of the O $2p$ states in STO and SVO is very similar putting the sensitivity of this method in doubt. Therefore, the V $3d$ states that are only present in SVO are included in the fit, making it very reliable. The resulting O $2p$ band onsets are then determined by a linear fit to the leading edge (see dashed lines in Fig. 4.13 (a)) and the onset of the STO
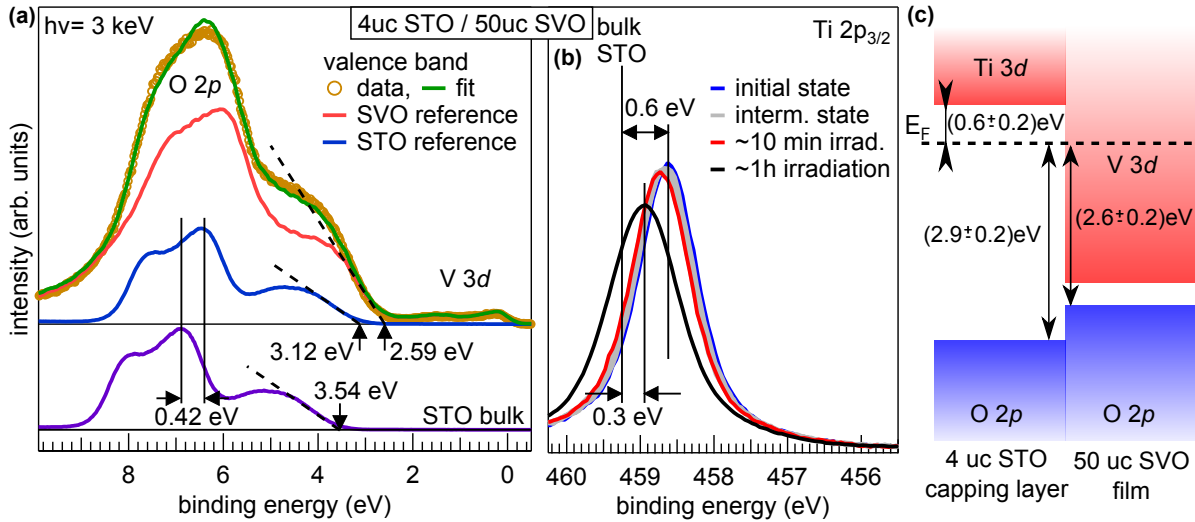
Fig. 4.13: Band alignment at the STO cap/SVO film interface. (a) Valence band decomposition of a spectrum measured on a 4 uc STO/50 uc SVO structure into its SVO and STO components. The onsets of the O 2p bands are indicated by vertical arrows. (b) Beam induced shift of the Ti 2p spectrum observed on the same heterostructure. (c) The resulting band alignment shows that the V 3d states are located well within the STO bandgap.

component is found at a higher binding energy than the one of the SVO film (approx. 0.5 eV difference, see Fig. 4.13 (a)).

We can now compare the obtained energy positions of the valence band offsets in the heterostructure to the bulk references. The SVO states in the heterostructure exhibit the same binding energy as the bulk reference, i.e. the bare 50 uc thick SVO film (not shown). The STO states of the capping layer are, however, shifted by about 0.4 eV toward the Fermi level compared to the bulk STO crystal as depicted in the lower part of Fig. 4.13 (a).

The size of this shift allows us to deduce the energetic location of the empty Ti 3d states above the Fermi level. In bulk STO, the Fermi energy is pinned by defects—or by intentional niobium doping—at the onset of the Ti 3d states. The bulk STO band gap size is therefore determined from the O 2p valence band onset to 3.54 eV, which matches well with the literature values [101, 109]. Since the gap size is fixed, the Ti 3d states in the STO capping layer are pushed approx. 0.4 eV above the Fermi level in the heterostructure. Note that a similar situation was also found at the bottom interface between STO substrate and SVO film by Yoshimatsu et al. [85].

The shift of the Fermi energy into the STO band gap also causes the reduced binding energy of the Ti 2p line in the STO capping compared to the bulk reference which was already mentioned in the previous section and in Fig. 4.12 (b). In the core level, the binding energy shift amounts to 0.3 eV which fits the valence band analysis quite well. However, upon closer inspection of the Ti 2p line, changes in the spectrum are detected that correlate with the irradiation time during the PES experiment. Figure 4.13 (b) depicts these changes: initially the binding energy difference to the bulk reference is

0.6 eV but gradually decreases to 0.3 eV as the measurement is repeated on the same sample spot. One reason for this behavior could be a charging effect due to the band insulator situation in the capping layer. However, one expects such effects on shorter timescales than observed here. Another possible cause is the x-ray beam induced formation of oxygen vacancies frequently observed in STO [101]. Such oxygen vacancies form a positive background charge that pushes all states to higher binding energies as observed in our experiment. However, no Ti^{3+} signal is observed that is expected in such a scenario. On the basis of the available data we cannot pinpoint the origin of these beam induced changes, the effect is therefore treated as a systematic error which is minimized by the measurement on a fresh sample spot. Hence, we take the shift of 0.6 eV obtained from the initial Ti $2p$ line (blue curve in Fig. 4.13 (b)) as intrinsic value. Note that the beam induced changes to the spectra do not affect the qualitative result: for all measurements—even with beam damage present—the Fermi level is located in the STO band gap.

Let us conclude the band alignment analysis with the band diagram sketch displayed in Fig. 4.13 (c), for which the measurement on the fresh spot was taken to extract the absolute values. The situation is reminiscent of a type I interface (straddling gap) in semiconductors with the Fermi level well inside the STO gap and crossing the V $3d$ states. The occupied part of the vanadium conduction band is located within the band gap of the STO capping layer therefore spatially confining the V $3d$ electrons to the SVO film.

4.3.3 Protection against Over-Oxidation in Air

As mentioned above, bare SVO films suffer from over-oxidation when they are exposed to air. Having developed an STO capping layer to prevent the adsorption of excess oxygen in vacuum, it is now intuitive to examine if such a capping layer can also be used to protect the films from over-oxidation in air, thereby facilitating sample handling in ambient conditions.

A very thick STO capping layer is of course expected to do the job, but would disqualify the samples for further characterization with surface sensitive techniques such as XPS. We therefore search the minimal STO thickness that is required for a full passivation. To this end SVO thin films with a thickness of the capping layer of 0,4 and 8 uc are fabricated. These structures are then transferred from the growth chamber into the spectrometer under UHV to record the V $2p$ line (labeled *in situ*). After this measurement the samples are exposed to air for at least several days and then reinserted into the vacuum system to repeat the measurement (*ex situ*).

The resulting spectra are plotted in Fig. 4.14. Without any capping layer, the spectrum measured *ex situ* is dominated by the V^{5+} signal which demonstrates that—on the scale of the probing depth this measurement (several nanometers)—the film surface is almost completely oxidized to V^{5+}. Please note that the small V^{5+} signal detected *in situ* arises from the surface adsorption of excess oxygen that occurs even in vacuum as already discussed in detail above.
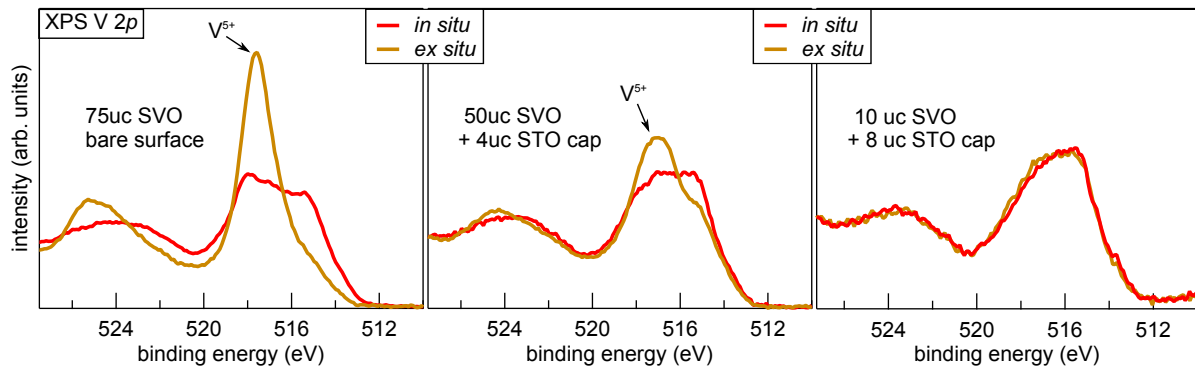
Fig. 4.14: Comparison of V $2p$ spectra measured before and after exposure to air, i.e. *in* and *ex situ*, on SVO thin films with different thicknesses of the STO capping layer. Note that the capping layers are grown directly after the SVO films and before the XPS experiments. The oxidation toward V^{5+} in air is partially suppressed with a 4 uc STO cap and almost completely prevented at an STO thickness of 8 uc.

The changes of the spectral line shape are weaker when a 4 uc STO capping layer is added and a smaller V^{5+} line is detected in the *ex situ* measurement. Further increasing the cap thickness to 8 uc then fully stabilizes the V $2p$ spectrum, i.e. both measurements on this structure yield the same line shape and no post fabrication oxidation is detected. Therefore, a thickness of 8 uc is identified as a lower limit for the STO capping to fully passivate SVO thin films.

The passivation of the SVO surface by an STO capping layer solves two problems that arise on the bare film surface. The first issue is the adsorption of excess oxygen that occurs despite handling the samples in vacuum. The STO layer blocks the adsorption sites and therefore this surface effect is avoided. Increasing the thickness of the capping to at least 8 uc furthermore conveniently avoids an over-oxidation in air.

4.4 Disentangling Over-Oxidation versus Intrinsic Properties

Having established the stabilization of tetravalent vanadium in STO/SVO/STO structures, we can now investigate fully stoichiometric ultrathin SVO layers and disentangle the extrinsic chemical effects caused by over-oxidation from the intrinsic electronic properties. Before discussing the intrinsic V $3d$ bulk valence band spectrum, the dimensional crossover is reinspected on capped SVO structures. These structures also allow for sample handling in air and thereby give access to resistivity measurements that complement the view on the metal-to-insulator transition.

4.4.1 Thickness Induced Mott Transition in Capped SrVO$_3$ Layers

Let us initially focus on the electronic transport properties of ultrathin SVO layers. To this end a set of SVO layers with varying thickness is fabricated on STO substrates and passivated by a 10 uc thick STO cap. In the following these structures are denoted 10 uc STO / x uc SVO / STO. For comparison a 75 uc thick SVO film (without any capping layer) is included as a bulk reference in the sample set. All samples are measured in a van-der-Pauw geometry and electrical contacts are realized by ultrasonic wire bonding with aluminum wires.

The resulting temperature dependent sheet resistivity, i.e. the resistivity of the whole SVO layer per unit area, $R_s(T)$ is plotted in Fig. 4.15 (a). We first note that the overall trend is reminiscent of the metal-to-insulator transition in the bare SVO films: the thinnest films exhibit a high resistivity with a negative temperature gradient signalling insulating behavior, whereas the sheet resistivity of the bulk reference sample is about six orders of magnitude smaller and has a positive temperature gradient characteristic for a metal.

The activated behavior ($dR_s/dT < 0$) for the $x = 3, 4, 6$ samples can be reproduced by an Arrhenius-type temperature dependence of the form $R_s \propto \exp\frac{\Delta}{2k_bT}$ which is exemplarily demonstrated for the thinnest SVO layer by an Arrhenius-plot depicted in Fig. 4.15 (b). As expected in such a plot, a linear relationship is found for the logarithmic sheet resistivity and reciprocal temperature—but only in the limited range between 160 K and 225 K. At higher temperatures the resistivity strongly deviates to smaller values, which is most likely caused by leak conductance in the STO substrate. As mentioned above, STO tends to form oxygen vacancies at the thermodynamic conditions used for the SVO epitaxy that can render the insulating substrate conducting.

Admittedly, we know from the band alignment analysis carried out in section 4.3.2 that the Fermi level in the capping layer is pinned well inside the band gap of STO probably preventing electronic transport upon oxygen vacancy doping. For symmetry reasons the same argument holds for the STO substrate at the bottom interface with the SVO film, but not deeper in the substrate. Therefore, the leak conductivity is expected to stem from an oxygen vacancy doped region deep within the STO substrate. This extrinsic contribution is taken into account by only fitting the linear part of the data in the Arrhenius plot which yields a Mott gap of $\Delta = 140$ meV for an SVO layer thickness of $x = 3$.

The Arrhenius fits (colored dotted lines) and the data (colored symbols) are overlayed in Fig. 4.15 (a) for the $x = 3, 4, 6$ structures; the size of the respective Mott gap is indicated. As the thickness is increased, the Mott gap reduces to $\Delta = 32$ meV at 4 uc SVO, $\Delta = 1$ meV for $x = 6$, and eventually collapses for thicker SVO layers.

The collapse of the Mott gap induces characteristic changes in the temperate dependence of the sheet resistivity which is better visible in a close-up of the $R_s(T)$ curves for the $x = 10, 12$ samples depicted in Fig. 4.15 (c). At room temperature both samples exhibit a positive temperature gradient, but upon cooling an upturn to activated behavior is detected. The positions of the resulting minima are highlighted by arrows in Fig. 4.15
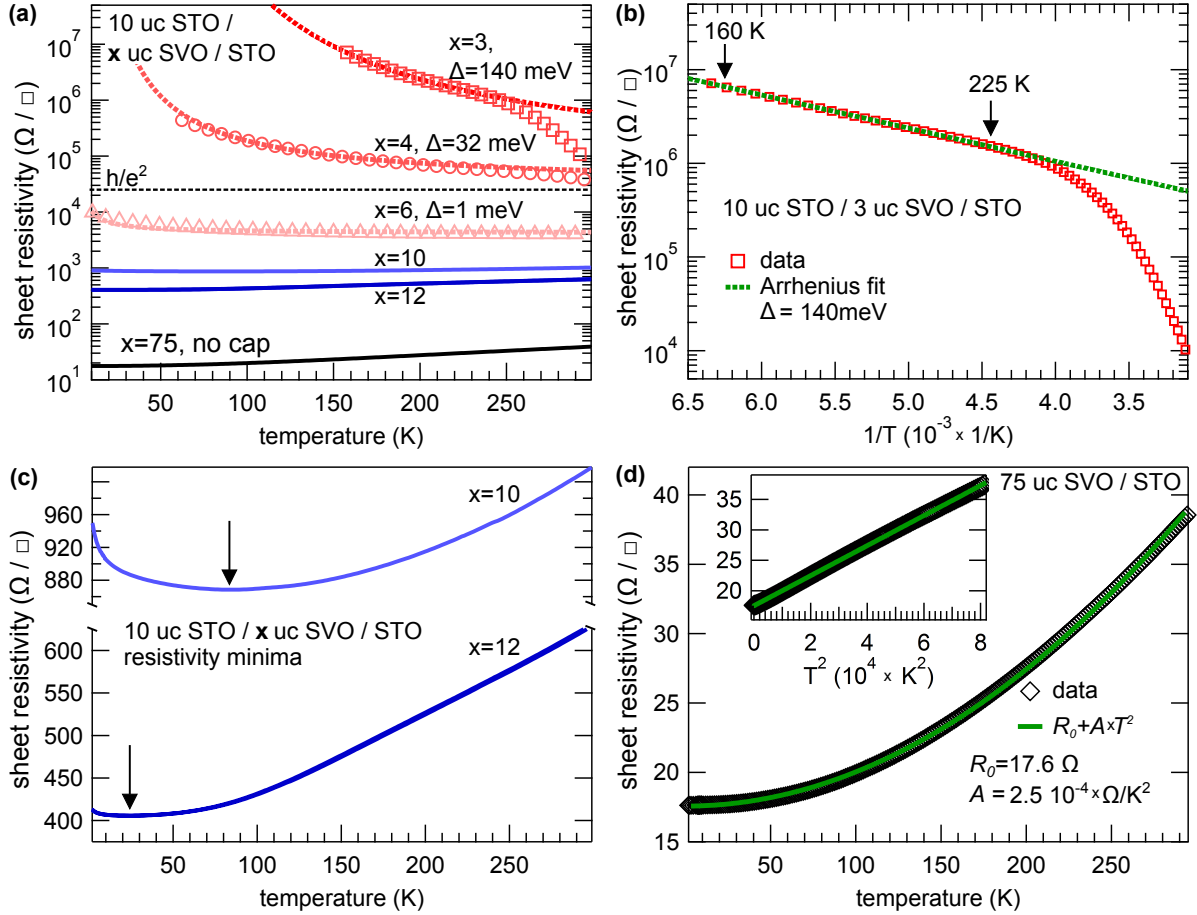
Fig. 4.15: Transport properties of ultrathin SVO layers in 10 uc STO / x uc SVO / STO structures. (a) Temperature dependent sheet resistivity for various SVO thicknesses. For $x = 3$, 4 and 6 the data (colored symbols) reveals an activated behavior that is fitted (colored dotted lines) by the Arrhenius law, the resulting activation energies Δ are indicated. Thicker SVO layers ($x = 10$, 12) exhibit only a weak temperature dependence. A 75 uc SVO / STO sample (without STO capping) is included as a bulk reference. The black dotted line highlights the value of h/e^2 as a guide to the eye. (b) Arrhenius plot, i.e. logarithmic resistivity *vs.* reciprocal temperature for the x = 3 structure. The deviation from the linear dependence at high T most likely stems from leak conductance in the substrate. (c) A close-up view for the $x = 10$, 12 data reveals minima of the temperature dependent resistivity. (d) The bulk reference sample exhibits a quadratic temperature dependence. Same data is plotted against T^2 in the inset.

(c) with the minimum for the $x = 12$ structure located at lower temperatures than the one for $x = 10$. The appearance of such upturns is also reported in related systems, e.g. doped calcium titanates [110], doped calcium vanadates [111], or SrIrO$_3$ thin films [112] and is usually attributed to the vicinity of the Mott transition or disorder.

Further increasing the SVO layer thickness finally leads us to the SVO bulk reference sample. Again, the shape of the temperature dependent resistivity is inspected in a close-up which is depicted in Fig. 4.15 (d). As clear from the inset, the resistivity follows a T^2 law in the whole temperature range. The data is well fitted by the function $R_s(T) = R_0 + A \times T^2$ yielding a residual resistivity value of $R_0 = 17.6\,\Omega/\square$ and $A = 2.5 \times 10^{-4}\,\Omega/(\square K^2)$, both coefficients are in line with the literature values reported for bulk SVO [113].

Having discussed the characteristic shape of $R_s(T)$ for each sample we can now turn back to the dimensional crossover from correlated metal to Mott insulator which immediately raises the question: At which SVO layer thickness occurs the transition? Based on the temperature dependence of R_s one can argue that samples which exhibit an Arrhenius-type resistivity curve, i.e. the $x = 3, 4, 6$ structures, are situated in the Mott insulating phase. Thicker SVO samples then exhibit a positive, i.e. metallic temperature gradient, around room temperature, which turns negative at low temperatures for $x = 10$ and 12, while it persists in the whole range for the bulk reference. Such samples are usually assigned to the correlated metal phase, placing the critical thickness for the onset of metallicity between 6 and 10 uc layer thickness.

Another classification can be performed by considering the resistance value of $\frac{h}{e^2} \approx 26\,\mathrm{k\Omega}$ corresponding to the limit $k_F l_e \approx 1$ in two dimensional systems that marks the crossover from weak to strong localization, where k_F is the Fermi wave vector and l_e the mean free path [112, 114]. For instance, Groenendijk *et al.* followed this line of argument to characterize the metal-to-insulator transition in thin SrIrO$_3$ films [112]. The value of $\frac{h}{e^2}$ is highlighted in Fig. 4.15 (a) and surprisingly gives another result than the precedent qualitative discussion: in this classification the $x = 6$ structure is in the correlated metal phase and not a Mott insulator as assigned before. This seemingly contradictory interpretations can be unified when higher temperatures outside our measurement range are taken into account. For the $x = 6$ SVO layer the Mott gap is almost closed (Δ amounts only to $1\,\mathrm{meV}$) which makes it likely that—similar to the $x = 10, 12$ samples— a resistivity minimum is present, but here at temperatures above $300\,\mathrm{K}$. Hence, the crossover from metallic to insulating-like electronic transport is located between 6 and $4\,\mathrm{uc}$ SVO thickness.

We conclude the discussion of the transport measurements by converting the sheet resistivity to the specific resistivity ρ by accounting for the thickness of each layer, the resulting $\rho(T)$ curves are plotted in Fig. 4.16.

Even though the transport measurements allow for a complementary characterization of the electronic properties, the distinction between Mott insulating and correlated metal behavior is not straightforward. Furthermore, a direct comparison to the properties of bare SVO films is not possible since the dimensional crossover in these samples is only characterized by photoemission. However, UPS measurements on the capped layers
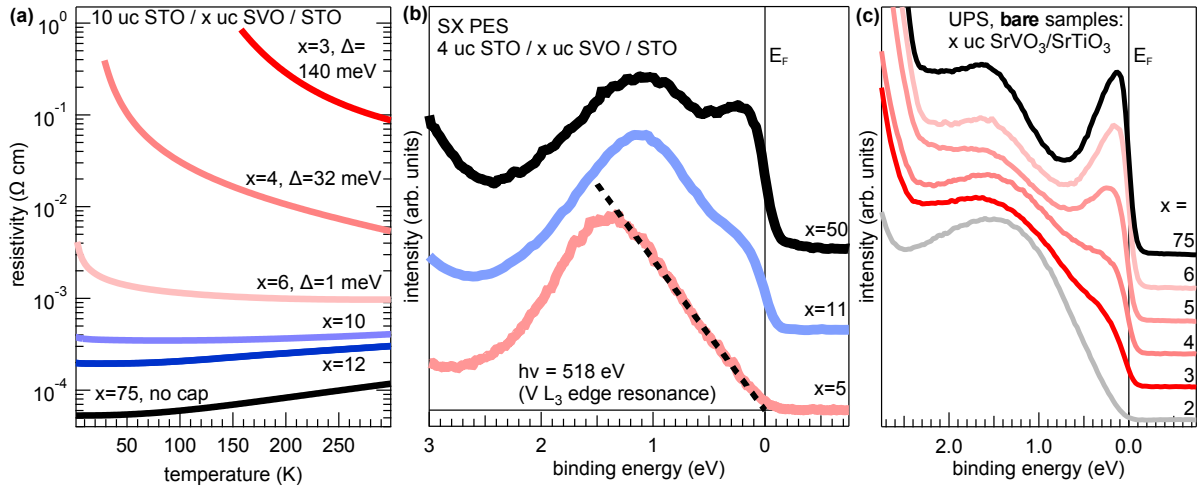
Fig. 4.16: (a) Temperature dependent resistivity data of ultrathin SVO layers capped with STO. (b) Corresponding V 3d spectra of capped SVO films measured at the V L edge resonance ($h\nu$=518 eV). The dashed line marks the onset of the LHB in the 5 uc thick SVO layer. (c) For comparison the spectra obtained from uncapped SVO ultrathin films with various thicknesses are shown again (see also Fig. 4.7).

do not allow to access the V 3d spectra of the buried SVO film since this technique is extremely surface sensitive. To overcome this obstacle, the capped SVO layers are investigated by soft x-ray photoemission (SOXPES) allowing for an increased probing depth up to several nm.

For the SOXPES experiments the thickness of the STO capping is reduced to 4 uc and the photon energy is tuned to the V L absorption edge. This resonant condition strongly and selectively enhances the V 3d photoemission signal. The inelastic mean free path λ amounts to 1.3 nm at this photon energy ($h\nu = 518$ eV). Note that other buried interfaces were already successfully investigated by this approach and motivated the choice of the capping thickness in our case [106, 115, 116].

Even though a 4 uc thick STO capping layer successfully avoids the adsorption of excess oxygen on apical sites at the surface as demonstrated in section 4.3.1, it is not sufficient to fully block an over-oxidation upon exposure to air (see, e.g., Fig. 4.14). Therefore, the samples must be transferred to the synchrotron in vacuum by means of an UHV suitcase which restricts the amount of samples that can be investigated.

The sample set consists of three 4 uc STO/x uc SVO/STO structures with $x = 5, 11, 50$ covering the three regimes identified in the transport measurements, i.e. Arrhenius-type, appearance of a resistivity minimum, and the T^2 behavior. The corresponding V 3d spectra are depicted in Fig. 4.16 (b) and fit the transport data quite well. For $x = 5$ a single V 3d feature is detected and identified as the LHB.[1] Its onset is very close to the Fermi level (≈ 1 meV) but no Fermi cutoff or QP is observed which clearly indicates a Mott insulating phase. In the $x = 11$ structure a QP and a Fermi cutoff is observed,

---

[1] Measurements across the whole photon energy range of the V L_3 edge were performed to exclude the appearance of a QP signal for the $x = 5$ sample. No such signal was detected.

both findings signal a metallic phase. The QP further gains in intensity in the thickest SVO layer, which is used as a bulk reference.

Let us now compare the V $3d$ spectra of the capped samples to the bare SVO films that are depicted in Fig. 4.16 (b) and (c), respectively. The overall QP intensity is lower in the capped case and the appearance of the Fermi edge is delayed to larger thicknesses. These findings are best exemplified in the spectra of the 5 uc thick SVO layers: for the bare SVO/STO film the QP peak is clearly visible while this feature is completely missing in the spectrum of the capped structure.

Having presented the differences in the electronic structure of capped and bare SVO thin films, the question of the origin causing these discrepancies arises. We have seen in section 4.3 that the STO capping layer is required to stabilize tetravalent vanadium in ultrathin SVO films. The electronic properties of the capped structures are therefore identified as the intrinsic case, whereas the dimensional crossover in the bare SVO films appears to be modified by the over-oxidation at the surface. As already discussed above, it is in principle not clear whether this over-oxidation causes a p doping of the V $3d^1$ band or just leads to the formation of areas with d^0 configuration. The fact that the metal-to-insulator transition is affected by the capping layer points to the former case, i.e. the filling of the $3d$ band in bare SVO films is affected by the excess oxygen—at least to some extent.

Such p doping does in turn alter the location of the bare SVO films in the electronic phase diagram as sketched in Fig. 4.17. Due to the surface over-oxidation the uncapped films are located at band fillings smaller than d^1. Decreasing the film thickness will still increase the correlation strength U/t_{eff} and the transition into the Mott insulating phase at $x = 3$ corresponds to a critical value of $(U/t_{eff})_{c2}$—but not at a band filling of d^1. The *in situ* XPS and LEED measurements discussed in section 4.10 furthermore suggest that the amount of excess oxygen on the bare SVO surface increases with the film thickness, i.e. the band filling depends on the film thickness. This means that the phase transition may be assisted by the chemical surface effects and is not purely band*width* induced, therefore the corresponding path in the electronic phase diagram (see Fig. 4.17) is not vertical.
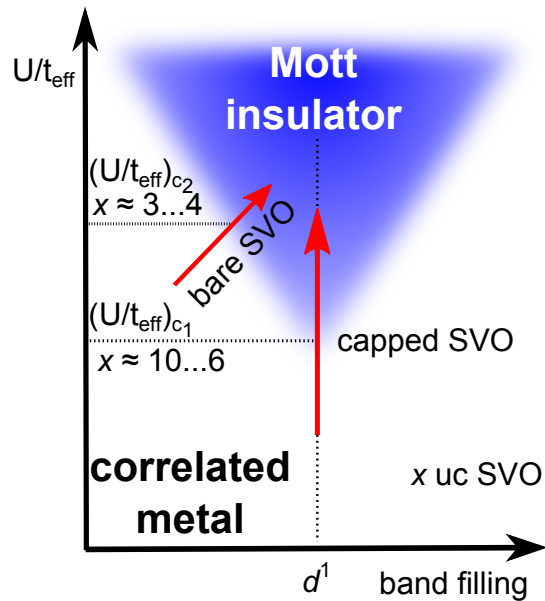

Fig. 4.17: Schematic phase diagram including the observed transition from correlated metal to Mott insulator upon decreasing the layer thickness for capped and bare SVO films.

In the capped STO/SVO/STO structures the transition follows the vertical dotted line that indicates d^1 filling, since these samples were identified as stoichiometric SVO. Our results show correlated metal behavior down to a SVO layer thickness x of about 10 to 6 uc, thinner layers are in the Mott insulating phase. As is clear from the phase diagram, the critical correlation strength $(U/t_{eff})_{c1}$ in this case is smaller than in the bare SVO case, i.e. $(U/t_{eff})_{c2}$. The order of $(U/t_{eff})_{c1} < (U/t_{eff})_{c2}$ is quite intuitive since approaching integer band filling—here d^1 configuration—as done for the stoichiometric capped samples favors the Mott insulating phase. Or putting it the other way around: doping away from integer filling destabilizes the Mott insulating phase.

Going from the correlation strength to the SVO layer thickness, which is the parameter that is tuned in our experiments, it is surprising that the phase transition occurs around a thickness as large as 6 uc. Taking up again the considerations of reduced hopping in z direction, one would naively not expect major changes to the effective band width t_{eff} in this range, e.g. upon increasing x from 5 to 6. This line of argument is more plausible in the bare SVO case, because the transition occurs closer to the two-dimensional case. Our findings disentangle the chemical properties, i.e. surface over-oxidation, from the intrinsic mechanisms at play and the capped samples therefore provide a better connection to theory calculations that rely on fully stoichiometric models. The results demonstrate the complexity of the dimensional crossover in thin SVO layers and provide new experimental insights to spark future *ab initio* calculations that are required to pinpoint the microscopic details behind the metal-to-insulator transition in thin SVO layers.

4.4.2 Intrinsic Valence Band Spectrum

Besides the metal-to-insulator transition in ultrathin SVO films, the bulk V $3d$ valence band spectrum is an important aspect in this material system. As mentioned in the introductory section of this chapter, bulk SVO is a benchmark system for DMFT calculations. Therefore reliable experimental data of the V $3d$ *bulk* spectrum is required as reference for these calculations.

This is not a straightforward task as pointed out by Sekiyama *et al.* [78]: the electron correlation effects are found to be enhanced at the sample surface which disqualifies PES experiments in the UV range to obtain *bulk* spectra due to the insufficient probing depth of only several Å in such experiments [29]. The authors have overcome this obstacle by measurements in the soft x-ray regime and other studies further extended the probing depth by hard x-ray (HAXPES) and laser PES. The intrinsic line shape of the V $3d$ spectrum is, however, still under debate [78, 97, 117].

The afore mentioned experiments were carried out on cleaved single crystals with an unclear surface termination. Thin films offer a higher structural quality of the surface and a controlled surface termination, however, a recent study on SVO films adds another aspect to the discussion about the intrinsic V $3d$ line shape. Backes *et al.* [90] report that the intense x-ray beam available at third generation synchrotron light sources can induce oxygen *vacancies* in the SVO lattice. These vacancies add spectral weight of
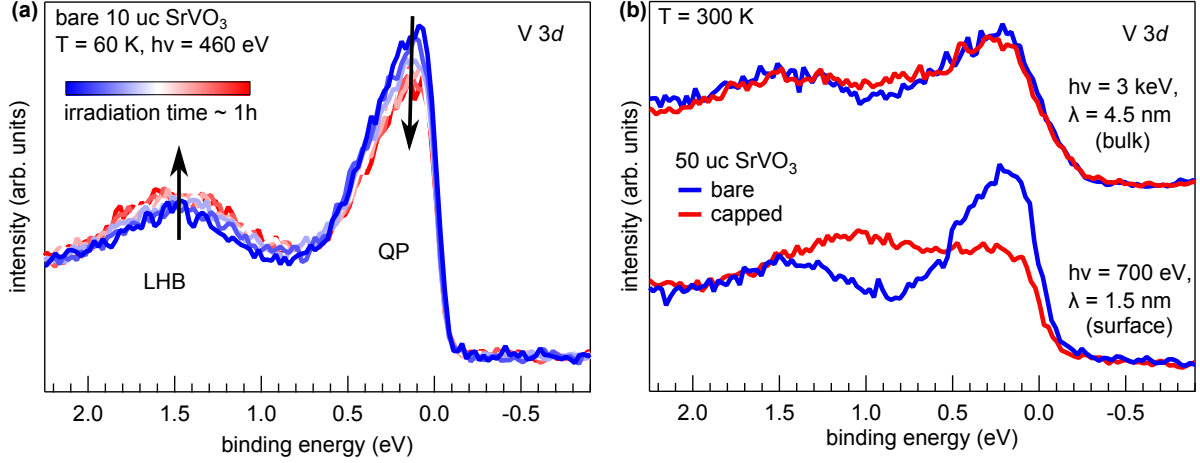
Fig. 4.18: (a) Irradiation induced changes in the V 3d spectrum suggest a desorption of excess oxygen from the bare SVO surface. (b) V 3d spectra obtained from capped and bare SVO films. The lineshape is similar in bulk sensitive measurements (hν=3 keV), but differ in a more surface sensitive experiment (hν=700 eV) due to the surface over-oxidation on the bare SVO surface and enhanced electron correlation effects close to the SVO/STO interface in capped structures.

V 3d character in the same binding energy region where the LHB is situated. This is surprising against the background of the material's—and especially its surface's— tendency to over-oxidize.

Therefore, we test our samples for such an oxygen vacancy formation scenario. To this end, a 10 uc thick SVO film (no capping) was transferred under vacuum to endstation I09 at the third generation synchrotron Diamond Light Source, which provides a photon beam intensity comparable to the one used by Backes *et al.* ($\approx 10^9 \frac{\text{photons}}{\mu\text{m}^2\,\text{s}}$) [90]. For comparability the measurements depicted in Fig. 4.18 (a) were performed at low temperature ($T = 60\,K$) along the <100> direction in k-space. Since the beamline cannot operate at the same photon energies as reported by Backes *et al.* (h$\nu = 33$ eV), higher photon energies in the SX regime are used and the V L edge resonance is employed to gain intensity. The varied experimental conditions compared to ref. [90] result in a different probing depth and a different k-space volume that is probed. We can nonetheless track the changes in the spectrum that would signal the formation of oxygen vacancies.

The resulting data is depicted in Fig. 4.18 (a) and is normalized by the integral V 3d spectral weight to highlight the evolution of the line shape as the irradiation time increases. In contrast to Backes *et. al*, we observe only minor changes and not a major increase of the LHB signal.

The results of Backes *et al.* are therefore not reproduced here. Based on the detailed investigation of the bare SVO surface, however, another microscopic mechanism to explain our data is presented: desorption of excess oxygen from the surface. This situation would approach the stoichiometric d^1 filling with increasing irradiation time and hence decrease the spectral weight ratio between QP and LHB.

It is not clear why Backes *et al.* observe much stronger changes of the spectral line shape, however, note that their samples are transferred in air and then annealed in vacuum to recover a clean surface. It is not stated whether the over-oxidation caused by air-exposure (see also section 4.14) is fully reversible. Other phases than $SrVO_3$ might also be present on the surface and give a contribution to the spectrum. For instance the formation of $Sr_3V_2O_8$ clusters was recently reported for a post growth oxygen treatment of SVO thin films [89].

In order to avoid such ambiguities about the stoichiometry at the SVO film surface, we again turn to the STO capped films to investigate the intrinsic V $3d$ line shape. To this end spectra are measured on 50 uc thick SVO layers capped with 4 uc STO and for comparison also on the bare surface as depicted in Fig. 4.18 (b). The spectra are again normalized to their integral spectral weight. The experiments are performed at $h\nu = 3$ keV and 700 eV to vary the inelastic mean free photoelectron path from 4.5 nm to 1.5 nm, respectively.

The bulk sensitive V $3d$ spectra ($h\nu = 3$ keV) are almost identical for both samples, which shows that the probing depth is already large enough to avoid a contribution from the over-oxidized surface of the bare sample to the spectrum. Note also, that the employed photon energy of 3 keV is high enough to supress a possible impact of enhanced electron correlations at the surface [78]. Hence, we assign these spectra as V $3d$ bulk and extract the characteristic parameters by fitting the data with a superposition of two Voigt profiles multiplied with a Fermi cutoff (fit not shown). The resulting spectral weight ratio of the LHB to the QP feature is about 1.7.

When we now turn to more surface sensitive measurements at $h\nu = 700$ eV, two effects can cause changes to the V $3d$ spectrum: the extrinsic over-oxidation and enhanced electron correlations at the surface. While the over-oxidation is expected at the bare surface, the capped SVO layer is fully stoichiometric. We therefore again measure on the capped and bare samples to disentangle the contributions to the spectrum.

Due to the different instrumental resolution, electron analyzer lens mode and probed k-space volume, the spectra cannot be directly compared to the bulk sensitive ones ($h\nu = 3$ keV). However, we can draw a comparison between the two samples measured at $h\nu = 700$ eV. In contrast to the bulk sensitive spectra, a very different spectral shape for the capped and bare SVO surface is detected. In the bare case, the QP intensity is clearly stronger, hence the bare surface is deeper in the metallic phase [78, 97, 118]. This demonstrates that the over-oxidation on the bare SVO film has a drastic impact on the electronic properties of the surface, i.e. the first few nanometers. Doping is active and drives the bare SVO film surface further away from the Mott insulating phase confirming the scenario sketched in Fig. 4.17 for the metal-to-insulator transition in ultrathin films.

5 Band-Filling Controlled Mott Transition in Thin LaTiO$_{3+x}$ Films

After studying the *bandwidth* controlled Mott transition in ultrathin films of SrVO$_3$ (SVO)—a correlated metal in bulk—,we now turn to the Mott insulator LaTiO$_3$ (LTO). The material is the first insulating compound in the prototypical $3d^1$ perovskite series SrVO$_3$—CaVO$_3$—LaTiO$_3$—YTiO$_3$ (see chapter 3) and exhibits a rather small gap between lower and upper Hubbard band of approx. $0.2\,\text{eV}$ [67, 71, 119].

The small gap of LTO indicates that the material is already close to the transition into the correlated metal phase, which makes it an ideal candidate to study the *band filling* induced Mott transition by detuning the occupation of the $3d$ band away from integer filling. Such a modification of the electronic configuration is usually achieved by chemical doping. In the particular case of LTO the La^{3+} cation can be substituted by Sr^{2+} or excess oxygen can be incorporated into the lattice [120–122].

Both methods deplete electrons, i.e. act as p doping, however, the latter method is not always intended: nominally stoichiometric samples often suffer from an uncontrolled excess oxygen content in experiment. The tendency to over-oxidize in LTO is even more pronounced than in the case of SVO and has lead to conflicting reports on the electronic transport properties of stoichiometric LaTiO$_3$ in the abundant literature available on this prototypical material [120–125].

We will tackle this problem by studying LTO thin films fabricated by pulsed laser deposition (PLD) in this chapter. To do so, the titanium valence—and thereby the Ti $3d$ band filling—is carefully monitored by *in situ* photoelectron spectroscopy, which allows us to adjust the growth conditions for the thin films and eventually stabilize fully stoichiometric LaTiO$_3$.

Having gained control of the oxygen stoichiometry, *controlled* oxygen excess doping is then employed to trigger the phase transition into the correlated metal phase. This filling induced Mott transition is then further characterized by transport measurements which reveal a several orders of magnitude high change of the resistivity. The strong impact of the electronic phase transition on the transport properties together with the tunability of the doping level by means of the oxygen content make LaTiO$_{3+x}$ thin films an exciting channel material for future electron correlation based devices—often referred to as Mottronics—, which will be discussed by the end of the chapter.

Before discussing the thin film epitaxy, we first visit the bulk crystal structures of LaTiO$_3$ and related oxygen-rich phases to identify possible structural changes induced by over-oxidation in bulk crystals.
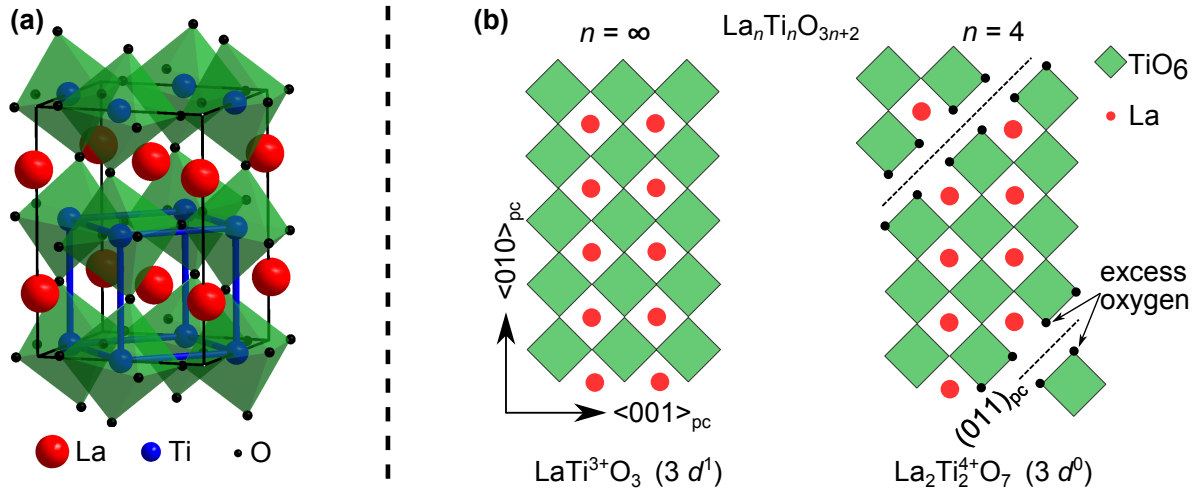
Fig. 5.1: (a) The GdFeO$_3$-type crystal structure of bulk LaTiO$_3$ with the orthorhombic and pseudocubic perovskite unit cell highlighted by black and blue lines, respectively. (b) Simplified sketch of the $n = \infty$ and $n = 4$ endmembers of the La$_n$Ti$_n$O$_{3n+2}$ layered perovskite series (for details see text).

5.1 Bulk Crystal Structure

The structural phase diagram of La-Ti-O compounds is quite rich due to the multivalent character of the titanium cations, among them are Ruddlesden-Popper and other more exotic phases with cation ratios deviating from 1:1 [126–128]. However, we are interested in LaTiO$_3$ and related phases with higher oxygen content at a *constant* cation ratio, which brings us to the homologous series La$_n$Ti$_n$O$_{3n+2}$. Bulk LTO is the $n = \infty$ endmember of this series and exhibits an orthorhombic distorted perovskite structure (GdFeO$_3$-type) as depicted in Fig. 5.1 (a). For the sake of clarity the pseudocubic (pc) notation is employed here, with the unit cell highlighted in blue in Fig. 5.1 (a).

In the layered perovskite series La$_n$Ti$_n$O$_{3n+2}$, excess oxygen ions are hosted on the $(011)_{pc}$-planes and the index n denotes the distance in unit cells of these planes that ranges from $n = \infty$ to $n = 4$. The structures of the two endmembers LaTiO$_3$ ($n = \infty$) and La$_2$Ti$_2$O$_7$ ($n = 4$) are sketched in Fig. 5.1 (b), the former consists of trivalent titanium corresponding to a $3d^1$ configuration and the latter of Ti^{4+}-ions with an empty $3d$ band. Due to the noble gas configuration of tetravalent titanium, the oxygen-rich phases are energetically favored complicating the stabilization of the LaTiO$_3$ phase.

For the thin film growth of La$_2$Ti$_2$O$_7$ on (110)-oriented SrTiO$_3$ substrates, it has even been shown that oxygen can diffuse from the surface into the film during or after the growth process. In this geometry the excess oxygen planes are parallel to the surface, therefore oxygen ions are expected to diffuse along structural defects [129]. For the more conventional (001) substrate orientation—also used in our study—the $(011)_{pc}$ excess oxygen planes cross the surface and additional oxygen can move along these planes deep into the film rendering them highly susceptible to over-oxidation.

We note in passing that the layered perovskite series is not reported for the Sr-V-O material systems. Due to the different cation radii, the structure of the Sr$_2$V$_2$O$_7$ phase drastically differs from a perovskite, e.g., the vanadium cation has a tetrahedral coordination instead of the octahedral one of titanium in LaTiO$_{3+x}$ [130]. This suggests that the SrVO$_3$ phase does not allow for incorporation of additional oxygen, but will rather turn amorphous or form islands of oxygen rich phases upon over-oxidation, which is in line with our observations on the SrVO$_3$ thin film epitaxy at high oxygen growth pressures in section 4.1.3 of the previous chapter.

These considerations make clear that the fabrication of fully stoichiometric LaTiO$_3$ is challenging on the one hand, but the special properties of the LaTiO$_{3+x}$ lattice can be harnessed for p doping by oxygen excess, which on the other hand makes the material a fascinating playground for studying electron correlation effects at variable band filling. Let us therefore now investigate the epitaxy of LaTiO$_{3+x}$ thin films by PLD.

5.2 Fabrication of LaTiO$_{3+x}$ Thin Films on SrTiO$_3$ Substrates

For the growth of LTO thin films, (001)-oriented STO substrates are widely used [125, 131–135]. This is probably due to the small lattice mismatch of about 1.6% and the well established procedure for the preparation of atomically flat and clean TiO$_2$-terminated surfaces. In order to connect our experiments to the growth studies in literature, we commence our growth study also on STO substrates.

The typical growth parameters for LTO thin films fabricated by PLD are an elevated substrate temperature of $T_s = 600...1000\,°\mathrm{C}$, oxygen growth pressures p_{O2} lower than 10^{-4} mbar, and a laser fluence of $\Phi = 1...2\,\mathrm{J/cm^2}$ [125, 131–135]. Polycristalline LaTiO$_{3+x}$ target material is commercially available and was supplied by SurfaceNet GmbH (Germany). Since the oxygen growth pressure is decisive for the oxygen stoichiometry—the most critical parameter for LTO epitaxy—we concentrate on the influence of p_{O2} on the thin film properties in this section. Note that no sizable influence of different laser fluences on the growth process was detected and that Φ was set to $1.5\,\mathrm{J/cm^2}$ in accordance with the reported values in literature.

As in the case of SVO thin film growth, a degas of sample holder and substrate was performed at $500\,°\mathrm{C}$ for 30 min to achieve a pressure in the low 10^{-8} mbar range even at high substrate temperatures. Note that the base pressure of the system is in the low 10^{-10} mbar range. During the growth process itself, the substrates were held at $T_s = 800°\mathrm{C}$. Higher temperatures cause a drastic increase of the residual gas pressure and significantly lower temperatures lead to disordered films.

In order to systematically analyze the effects of over-oxidation, a set of LTO thin films is fabricated at these growth parameters in oxygen growth pressures ranging from 10^{-5} mbar down to the pressure of 2×10^{-8} mbar. A film thickness of 40 uc is chosen to ensure a sizable diffraction signal in XRD measurements and to avoid a substrate contribution to the XPS signal.
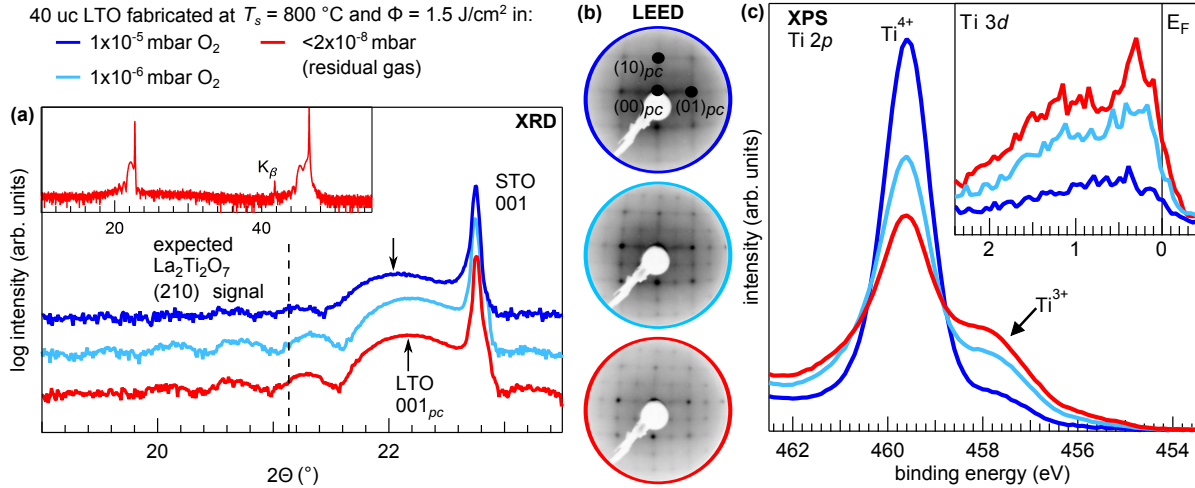
Fig. 5.2: Characterization of LTO films grown on STO substrates in various oxygen growth pressures. (a) XRD scans indicate phase pure LTO films, Bragg peaks of the oxygen rich La$_2$Ti$_2$O$_7$ phase or other Ti oxides are absent (see also inset). K$_\beta$ in the inset denotes the satellite line caused by the Cu K$_\beta$ part of the x-ray source. (b) LEED patterns reflect the structural quality of the surface, which improves as p_{O2} is reduced. (c) Ti $2p$ spectra reveal a strong over-oxidation toward Ti^{4+} for all films. The corresponding Ti $3d$ valence band spectra plotted in the inset are normalized to the integral Ti $2p$ spectral weight.

The corresponding structural characterization of these films by XRD and LEED is presented in Fig. 5.2 (a) and (b). It reveals a general trend: upon decreasing the oxygen growth pressure, the structural quality of the LTO thin films increases. This manifests itself in the clearer Laue intensity oscillations in XRD and the higher overall contrast as well as the smaller widths of the Bragg peaks in LEED. Also note that the $(001)_{pc}$ reflex in XRD of the LTO film shifts to smaller angles, i.e. higher lattice constants, for growth in 1×10^{-5} mbar, as indicated by the arrows in Fig. 5.2 (a). The absence of the La$_2$Ti$_2$O$_7$ diffraction signal that is expected around $2\Theta = 21.15°$ and any other diffraction peaks from binary titanium oxides as reported by refs. [131] and [136] suggests that the films are phase pure LaTiO$_3$. Note that the 2×2 surface reconstruction with respect to the pc unit cell observed in LEED is in line with the orthorhombic distorted GdFeO$_3$-type unit cell as depicted in Fig. 5.1 (a).

Complementary characterization of the electronic properties is realized by *in situ* XPS, i.e. with keeping the samples in UHV. As is clear from the Ti $2p$ line depicted in Fig. 5.2 (c) all samples suffer from a strong over-oxidation. The Ti^{3+} signal increases for lower oxygen growth pressures, but even for fabrication in vacuum ($p < 2 \times 10^{-8}$ mbar) the tetravalent signal is dominating. The over-oxidation does also affect the Ti $3d$ valence states which are displayed in the inset of Fig. 5.2 (c). These spectra are normalized to the integral spectral weight of the Ti $2p$ core level, so the Ti $3d$ intensity is a relative measure of the band filling. As expected, the band filling increases as the average valence shifts toward Ti^{3+}. Even though an absolute value for the filling cannot be assigned, the Fermi cutoff observed for all three LTO films indicates that the samples are not in the Mott insulating phase as expected for the stoichiometric compound.

The apparent contradiction between the phase purity suggested by XRD and the strong over-oxidation revealed by XPS can be resolved by taking the oxygen rich bulk phases into account. Similar to the $La_2Ti_2O_7$ phase, additional oxygen ions can be incorporated in the lattice by breaking the shared corners of the TiO_6 octahedron but—in contrast to $La_2Ti_2O_7$— only locally and in a random manner. Such a scenario for a $LaTiO_{3+x}$ structure is sketched in Fig. 5.3. Due to the random arrangement of the excess oxygen ions diffraction techniques are insensitive to this kind of over-oxidation explaining the absence of any additional Bragg peak in the XRD characterization presented above.

Fig. 5.3: Proposed structure for $LaTiO_{3+x}$ films. Excess oxygen is hosted on randomly distributed interstitial sites.

Similar to the $LaTiO_{3+x}$ structure proposed here, excess oxygen hosted on interstitial sites was recently identified to cause over-oxidation in the related d^1-material $NdTiO_3$ upon exposure to air [137]. It is therefore to be expected that this kind of over-oxidation is an important aspect for many titanate materials with a perovskite structure. A characterization merely based on diffraction techniques—as in previous studies [138]—may be misleading and a direct characterization of the titanium valence or the Ti $3d$ band filling is vital for the evaluation of the oxygen stoichiometry.

Furthermore, our results provide a different view on oxide heterostructures, in which LTO is frequently integrated as an electron donor layer [139–141]. It is usually argued that the detection of tetravalent titanium in LTO indicates an electron transfer to the adjacent layer in such structures. However, the Ti^{4+} signal—or at least a part of it— might simply arise from an over-oxidation as in our LTO/STO samples. Therefore, special care about the titanium valence should be exercised before assuming a charge transfer in such structures.

In summary, our combined XRD, LEED and *in situ* XPS analysis of LTO/STO samples reveals that the films are strongly over-oxidized. Since we used the typical parameters reported in literature, our findings imply that many preceding studies on STO based thin films suffer from a similar uncontrolled oxygen stoichiometry that obscures the material's electronic properties [132, 138–141]. The question remains how this over-oxidation can be avoided, which will be the scope of the following section.

5.3 Gaining Control of the Oxygen Stoichiometry

We have seen that in LTO/STO structures, the tetravalent titanium signal is strongly dominating the Ti $2p$ spectrum, which shows that the over-oxidation is not limited to the very surface. It rather penetrates at least several nm deep into the film as estimated from the probing depth of the XPS experiment. Therefore, the supply of oxygen during
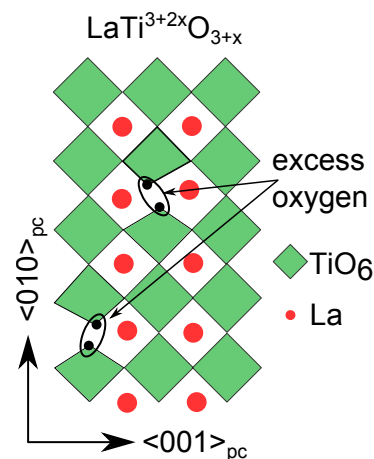
the film growth has to be minimized before one can think of investigating the chemical environment of the surface, e.g., excess oxygen ions adsorbed on apical sites as on the SVO surface (see chapter 4).

In general there are three sources of oxygen in the PLD process: the background atmosphere, the target, and the substrate. The oxygen content in the background atmosphere has already been minimized by performing the ablation *in vacuo*. The stoichiometry of target material cannot be modified in a controlled way and even if the oxygen content in the target is reduced, air exposure or high oxygen pressures in the PLD chamber—which are frequently required for other material systems—could induce an uncontrolled re-oxidation of the target material. Efforts toward an oxygen deficient LTO target are therefore not promising, which leaves the substrate as the remaining source of oxygen during epitaxy.

5.3.1 Avoiding Oxygen Out-Diffusion from the Substrate

As outlined above, the choice of STO substrates was mainly motivated by the fact that it is commonly used to grow LTO thin films. However, it was recently reported that the elevated temperatures during epitaxy allow for a substantial oxygen diffusion between substrate and film [142]. Furthermore, STO is especially prone to the formation of oxygen vacancies at such high temperatures and low oxygen pressures and exhibits a high oxygen diffusion coefficient [142–145]. Therefore, a strong oxygen out-diffusion from STO into the LTO film is expected during the growth process putting the substrate choice into doubt.

To test this hypothesis an epitaxial LaAlO$_{3-x}$ buffer layer is introduced between STO substrate and LTO film to block the oxygen out-diffusion. The buffer layer was grown at the same conditions as the LTO layer (T$_s$ = 800°C, vacuum) and the LAO material was ablated from a single crystalline target with a laser fluence of Φ = 1.3 J/cm^2 at a repetition rate f = 1 Hz. As depicted in Fig. 5.4 (a), the amount of trivalent titanium is clearly increased in this sample (black curve), which supports the oxygen out-diffusion hypothesis. A further reduction of the Ti^{4+} content is achieved by replacing the STO substrate with DyScO$_3$ (DSO). In these DSO based samples the Ti^{3+} signal now dominates the spectrum indicating that the oxygen out-diffusion is absent—or at least strongly suppressed—for these substrates as sketched in Fig. 5.4 (b). Note that the DSO (001)$_{pc}$ surface, i.e. (110) in orthorhombic notation, was treated by annealing in oxygen and subsequent etching in NaOH to achieve an atomically flat ScO$_2$ surface termination as described in detail elsewhere [146, 147].

The change of the titanium valence is accompanied by an improvement of the structural properties of the LTO films as is clear from the RHEED and LEED results displayed in Fig. 5.4 (c). Whereas the RHEED intensity oscillations are strongly damped for LTO growth directly on STO, growth on DSO substrates yields well pronounced and regular oscillations indicating a layer-by-layer growth mode. A similar trend is observed in the RHEED and LEED patterns measured on the LTO film surface. For LTO/STO, the Bragg peaks are connected by blurry lines in LEED and the RHEED pattern exhibits
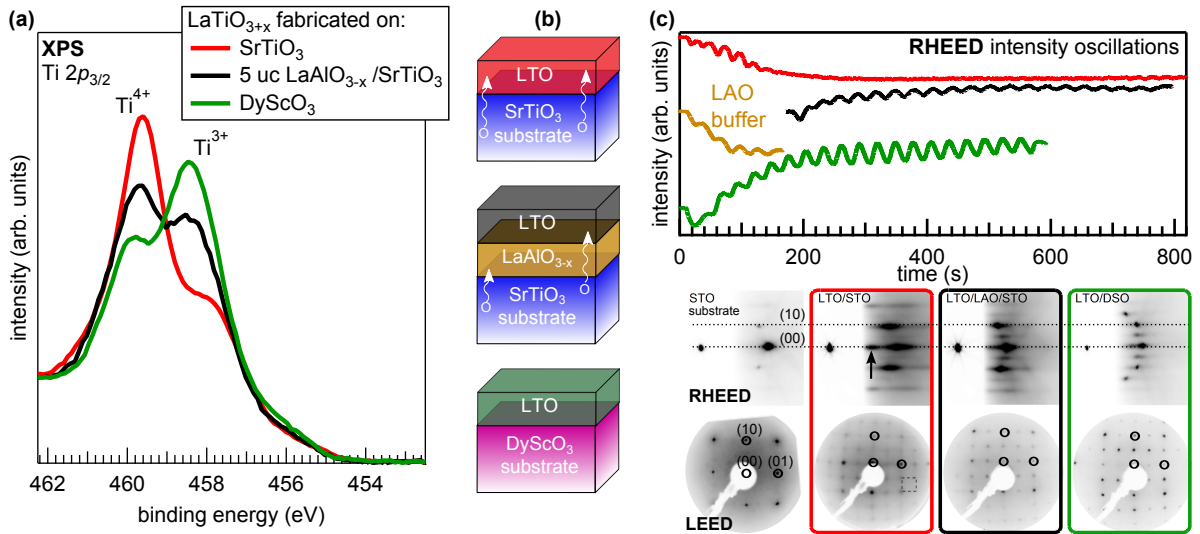
Fig. 5.4: Characterization of LTO films grown on STO, on LAO-buffered STO, and on DSO substrates. (a) *In situ* XPS measurements of the Ti $2p_{3/2}$ line. (b) Schematic oxygen out-diffusion processes for the different sample layouts. (c) Corresponding RHEED intensity oscillations together with the RHEED and LEED diffraction patterns. The dashed horizontal lines are a guide to the eye, the dashed square highlights the streaks between Bragg peaks for LTO/STO, and the arrow points to an additional diffraction spot.

an additional diffraction spot indicating cluster formation on the film surface. Both features are absent for growth on DSO and the contrast of the patterns is significantly increased, which suggests an atomically flat surface of high structural quality. As in the case of the titanium valence, the LTO/LAO/STO sample takes an intermediate role.

Surprisingly, the oxygen growth pressure p_{O2} has to be increased for growth on DSO substrates. The highest Ti^{3+} signal and best structural properties are achieved at $p_{O2} = 5 \times 10^{-8}$ mbar and not in vacuum as for STO based samples. The XPS measurements of the Ti $2p$ line and the LEED patterns for LTO/DSO structures fabricated in various oxygen pressures are depicted in Fig. 5.5 (a) and (b), respectively. The film grown in vacuum shows a sizable Ti^{2+} signal and at the same time an enhanced Ti^{4+} line. Furthermore, the intensity of the corresponding LEED pattern is very weak indicating a low structural quality. Without a sizable oxygen out-diffusion from the substrate, additional oxygen needs to be supplied to reach the optimal oxidation conditions for LTO growth. These conditions are reached at $p_{O2} = 5 \times 10^{-8}$ mbar, here the clearest LEED pattern and lowest Ti^{4+} signal is detected. Higher oxygen growth pressures, in turn, lead to an increase of the tetravalent titanium content and a blurring of the LEED pattern.

Up to now, the titanium valence in the LTO thin films was tentatively connected to the oxygen content since it scales with the oxygen growth pressure. However, other structural defects such as cation vacancies in the thin films could offer an alternative explanation for the presence of tetravalent titanium. In such a scenario, every missing cation—be it lanthanum or titanium—generates three Ti^{4+}-ions.
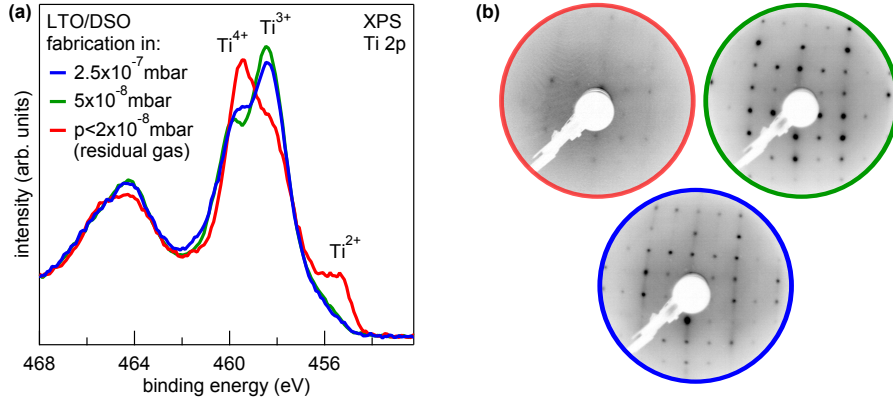
Fig. 5.5: Optimization of the oxygen growth pressure p_{O2} for epitaxy of LTO films on DSO substrates. (a) The Ti 2p spectrum exhibits the highest Ti^{3+} content for $p_{O2} = 5 \times 10^{-8}$ mbar, lower pressures lead to a Ti^{2+} signal, and higher pressures to an increase of the Ti^{4+} line. (b) The quality of the corresponding LEED patterns scales with the Ti^{3+} signal.

To clarify the microscopic situation in the LTO films, the spectral weight of the Ti 2p, La 4d and O 1s core levels is evaluated allowing for an insight into the stoichiometry. The sample set consist of three LTO/STO structures grown at different oxygen growth pressures and films fabricated on LAO-buffered STO, and DSO substrates.

The spectral weight is extracted by integrating from the low to the high binding energy background of the respective core levels. To account for the strong changes of the line shape induced by the different titanium valencies in the Ti 2p spectrum, the high binding energy integration limit was set to the location of the minimum around 468.5 eV for this core level. The resulting spectral weight ratios are depicted in Fig. 5.6 (a) and the core levels—all normalized by the Ti 2p spectral weight—are plotted in Fig. 5.6 (b).

This analysis clearly shows that the La to Ti stoichiometry is constant for the whole sample set, essentially ruling out the cation vacancy scenario. In fact, a clear connection between the oxygen stoichiometry and the titanium valence is revealed, which corroborates the microscopic picture of excess oxygen ions on interstitial sites drawn above (see Fig. 5.3). For LTO/STO structures, excess oxygen ions are randomly distributed throughout the film leading to an enhanced oxygen content compared to films fabricated on DSO substrates.

Even though a reliable calibration of the absolute stoichiometry is not possible due to uncertainties in the cross sections of the photoemission process, it can be demonstrated that the remaining Ti^{4+} signal in LTO films grown on DSO substrates originates entirely from the surface, which is discussed in detail in the following section.

5.3.2 Oxidation State of the Surface

We have seen that using DSO substrates for the LTO thin film growth allows to drastically decrease the Ti^{4+} content. The remaining over-oxidation is of a different nature
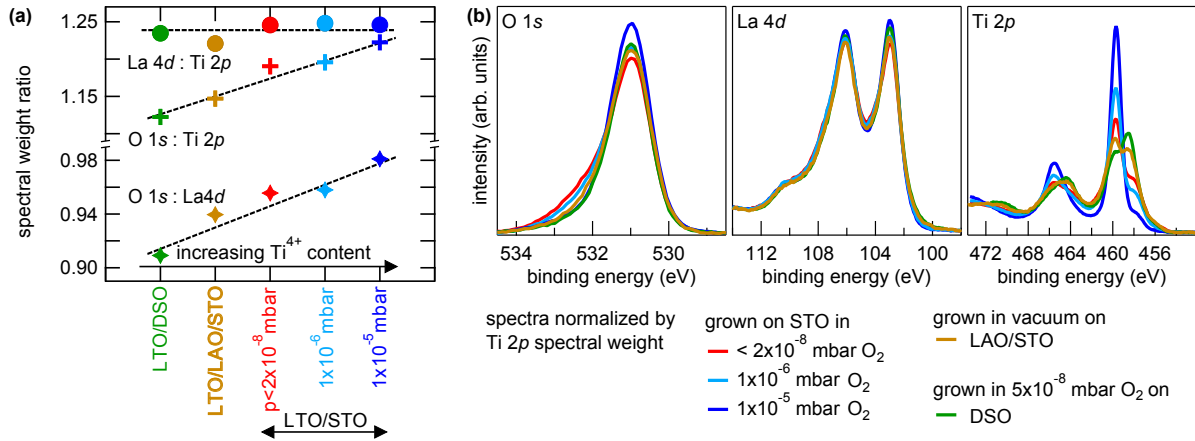
Fig. 5.6: Stoichiometry analysis of LTO thin films with varying Ti^{4+} content. (a) Spectral weight ratios of the La $4d$, Ti $2p$, and O $1s$ core levels reveal a constant cation ratio and an increasing oxygen content. (b) Corresponding core level spectra, all normalized by the Ti $2p$ spectral weight.

than in LTO/STO as revealed by angle-dependent XPS measurements of the Ti $2p$ spectrum depicted in Fig. 5.7. Increasing the emission angle ϑ toward grazing emission—thereby decreasing the effective inelastic mean free path $\lambda_{eff} = \lambda_0 \cos\vartheta$—results in a strong enhancement of the Ti^{4+} component. This demonstrates that the tetravalent titanium signal is emitted from a strongly confined surface layer on the length scale of the inelastic mean free path $\lambda_0 = 18.9\,\text{Å}$.

As on the SVO surface, additional oxygen ions can adsorb on apical sites above the surface titanium ions and complete the oxygen octahedron [91]. This situation is sketched in Fig. 5.7 (b), every additional oxygen ion removes two electrons from the Ti $3d$ band causing the oxidation from tri- to tetravalent in two titanium ions. Note that the TiO_2 surface termination of the LTO film is assumed here, based on the ScO_2 termination of the DSO substrate and the layer-by-layer growth mode inferred from the regular RHEED intensity oscillations (see Fig. 5.4 (c)).

To avoid the surface oxidation, a capping layer can be employed, however—in contrast to SVO thin films—STO is not a suited capping material here. While STO consists of Sr^{2+} and Ti^{4+}, the cations in bulk LTO are both in oxidation state +3. Therefore, a material which is epitaxially compatible and at the same time exhibits exclusively trivalent cations is required to mimic the chemical environment of stoichiometric LTO. These points are fulfilled for $LaAlO_3$ as sketched in Fig. 5.7 (c). With the capping layer, the surface oxygen octahedron is closed and the LAO-cations supply their share of electrons to the anions thereby avoiding electron depletion from the Ti^{3+}-ions.

To verify these considerations in experiment, an LTO/DSO sample is capped with $4\,\text{uc}$ of LAO at $T_s = 700\,^\circ\text{C}$, $p_{O2} = 5 \times 10^{-8}\,\text{mbar}$, and the identical laser parameters as used for the growth of the LAO buffer layer. The resulting Ti $2p$ spectrum is included in Fig. 5.7 (a) and indeed no sizable Ti^{4+} signal is detected anymore, which indicates a fully stoichiometric $LaTi^{3+}O_3$ film.
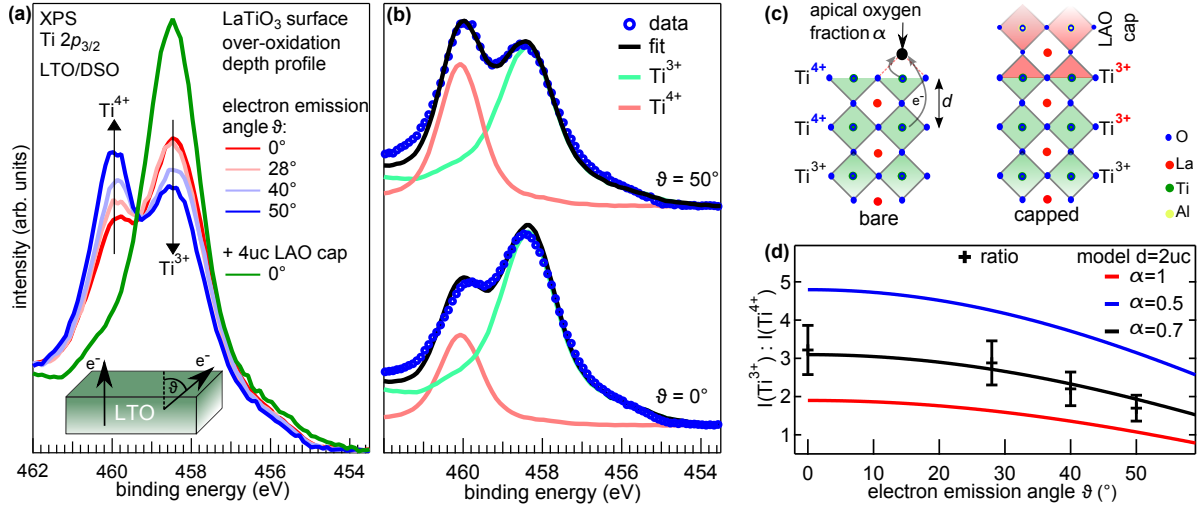
Fig. 5.7: (a) XPS measurements of the Ti $2p_{3/2}$ line measured on a bare LTO film at various emission angles ϑ together with data from an LAO-capped LTO film. (b) Exemplary fits with tri- and tetravalent reference spectra of the data presented in (a). (c) Microscopic model of the bare and capped LTO film surface. (d) Spectral weight ratio $I(Ti^{3+}) : I(Ti^{4+})$ plotted against ϑ. The quantitative comparison with the microscopic model yields a coverage $\alpha \approx 75\%$ and an extension d of 2 uc.

The pure Ti^{3+} spectrum not only demonstrates the correct titanium valence, but can also serve as a reference spectrum to fit the angle dependent XPS data from the *bare* surface in order to quantify the surface over-oxidation. Note that a Ti^{4+} reference is readily available from LTO/STO samples fabricated in high oxygen pressures. As is clear from the exemplary fits depicted in Fig. 5.7 (b), a superposition of the reference spectra with variable intensities as free parameters reproduces the data very well. The spectral weight ratio of the Ti^{3+}- to the Ti^{4+}-component is extracted by this fitting routine. The resulting intensity ratio is plotted against the emission angle ϑ in Fig. 5.7 (d). This data allows a quantitative comparison to the microscopic model sketched in Fig. 5.7 (c), which is briefly elaborated on in the following.

Let us assume that the surface coverage α with additional oxygen anions on apical sites—each depleting *two* electrons from titanium ions—induces an homogeneously over-oxidized surface layer of extension of d uc and a relative Ti^{4+}-content $x = \frac{2\alpha}{d}$. Considering the exponential damping caused by inelastic scattering of the photoelectrons in the sample, the Ti^{3+} to Ti^{4+} intensity ratio is then given by:

$$\frac{I(Ti^{3+})}{I(Ti^{4+})} = \frac{\sum_{j=0}^{d-1} \left(1 - \frac{2\alpha}{d}\right) e^{-\frac{j \cdot c}{\lambda_0 cos\vartheta}} + \sum_{j=d}^{\infty} e^{-\frac{j \cdot c}{\lambda_0 cos\vartheta}}}{\sum_{j=0}^{d-1} \frac{2\alpha}{d} e^{-\frac{j \cdot c}{\lambda_0 cos\vartheta}}}. \tag{5.1}$$

As is clear from Fig. 5.7 (d), the model reproduces the experimental values very well and a fit yields $\alpha = 0.7$ and $d = 2$ as best values. For orientation, the half and full coverage case for $d = 2$ are also plotted. Note that an extension d of the surface layer of
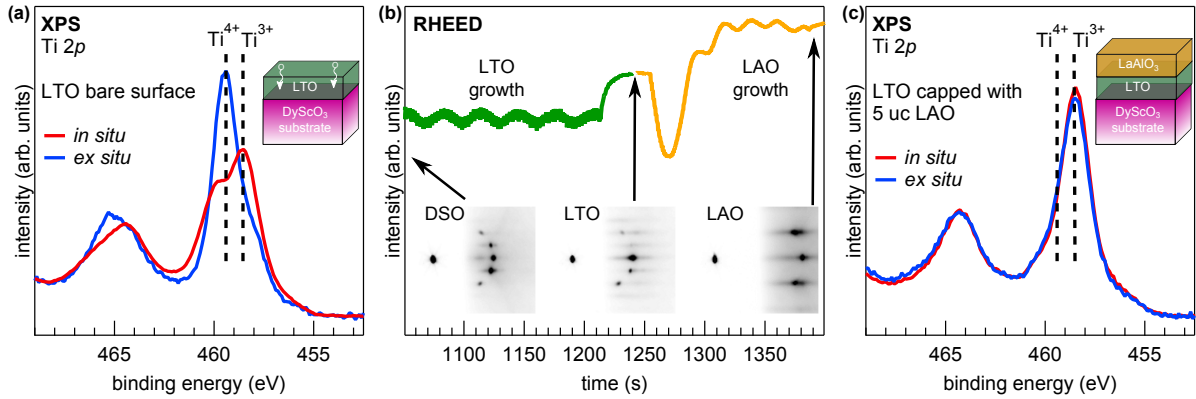
Fig. 5.8: Surface passivation of LTO thin films by an LAO capping layer. (a) Ti 2p before (*in situ*) and after (*ex situ*) air exposure of a bare, i.e. uncapped, LTO / DSO sample. (b) RHEED intensity oscillation and patterns characterizing the growth of the LAO capping layer. (c) Ti 2p spectra of an LTO film capped with 5 uc of LAO measured *in* and *ex situ*. No sizable changes are detected after exposure to air.

only one unit cell would require a coverage $\alpha > 1$ to match the experimental data and is therefore unreasonable. Larger values of d are possible, but result in higher $\mathcal{X}^2$ values of the fits. The exact coverage α may delicately depend on the experimental conditions, i.e. the base pressure in the vacuum system and the storage time between film fabrication and XPS measurement. However, a full coverage ($\alpha = 1$) is the upper limit for this kind of over-oxidation, which corresponds to an intensity ratio of $I(Ti^{3+}) : I(Ti^{4+}) \approx 2$ at normal emission ($\vartheta = 0°$) in the XPS experiment.

These quantitative considerations demonstrate that LTO films grown on DSO substrates are already stoichiometric in the bulk and only the very surface is affected by an over-oxidation caused by adsorbed oxygen ions. An LAO capping layer is successfully employed to protect the surface from this oxidation and we will now investigate if this capping layer can also passivate the samples to enable a sample handling in air.

5.3.3 Surface Passivation by a LaAlO$_3$ Capping Layer

Due to the material's strong tendency to over-oxidize, the LTO surface is not expected to be stable against exposure to air. This is tested by measuring the Ti 2p core level spectrum of an LTO/DSO sample directly after growth without exposing it to air, i.e. *in situ*. The sample is then removed from the vacuum system and stored in air for at least several days before the measurement is repeated (referred to as *ex situ*). The resulting spectra are plotted in Fig. 5.8 (a) and it is clear that the average valency strongly increases toward Ti^{4+}.

As mentioned above, a similar behavior was recently reported for thin NdTi^{3+}O$_3$ films. Samples exposed to air are also found to exhibit a Ti^{4+} surface layer that penetrates at least several nm into the film [137]. The authors suggest that oxygen from air diffuses into NdTiO$_3$ films and occupies interstitial sites. They support this statement with

first-principle simulations that indeed show an energy gain when additional oxygen is incorporated into the lattice. These results can be transferred to our LTO case: upon exposure to air oxygen diffuses into the films to occupy interstitial sites as sketched in the inset of Fig. 5.8 (a).

To passivate the LTO surface against over-oxidation in air, an LAO capping layer of 5 uc thickness is grown on top of the LTO film. The structural characterization of this sample by RHEED is depicted in Fig. 5.8 (b). In this plot, the ablation of LTO material starts at $t = 0$, but only the part relevant for the capping is shown. Regular intensity oscillations indicate a layer-by-layer growth mode for both LTO and LAO, and the diffraction patterns suggest atomically flat surfaces, i.e. no additional spots arising from transmission through clusters are detected.

This capped sample is again examined *in* and *ex situ* by XPS, the resulting Ti $2p$ spectra are plotted in Fig. 5.8 (c). In the capped case no changes after exposure to air are detected in the spectrum which demonstrates that the 5 uc thick LAO capping layer fully passivates the LTO surface. Note that the Ti^{4+} signal is absent for both measurements, the LAO capping avoids over-oxidation in two ways: it blocks the adsorption sites for excess oxygen ions at the LTO surface and prevents oxygen from air to diffuse into the LTO film.

5.3.4 Characterization of Fully Stoichiometric LaTiO$_3$ Thin Films

Having gained control of the oxygen content, the structural and electronic properties of fully stoichiometric LTO thin films can be investigated.

Let us first concentrate on the structure of the thin films, which is investigated by XRD on a 5 uc LAO/100 uc LTO/DSO sample to ensure a sizable diffraction signal of the titanate layer. A reciprocal space map around the $(103)_{pc}$ Bragg peak of film and substrate is depicted in Fig. 5.9 (a) together with an intensity profile along the q_z direction through these reflexes. The film peak is located at the same q_x value as the substrate which indicates that LTO is fully strained to DSO, i.e. film and substrate exhibit the same in-plane lattice constant. The out-of-plane lattice constant c of the strained LTO layer is determined to $c = 4.02$ Å. Besides the two Bragg reflexes, Laue intensity oscillations (marked by arrows) around the LTO peak are detected up to the 6th order demonstrating the high structural quality of the film. The spacing between these oscillations corresponds to a layer thickness of 97 uc, closely matching the 100 uc targeted by RHEED growth monitoring.

Besides the structural properties, transport measurements are crucial to characterize the electronic phase of the LaTiO$_3$ films, i.e. Mott insulator or correlated metal. As discussed above, diffraction techniques are not sensitive to excess oxygen hosted on interstitial sites that can potentially dope the material. Therefore, complementary temperature dependent resistivity measurements are performed on a 5 uc LAO/40 uc LTO/DSO sample. The LTO layer is contacted by Al wire bonding in a van-der-Pauw geometry, which is performed in air making the surface-passivation by the LAO capping layer crucial for these experiments. The resulting temperature dependent resistivity

$\rho(T)$ curve is depicted in Fig. 5.9 (b) and is obtained by multiplying the measured sheet resistance with the LTO layer thickness. For the whole temperature range an activated behavior, i.e. a negative temperature gradient $d\rho/dT$, is observed which signals an insulating phase. Measurements at lower temperatures are not possible since the resistance exceeds the measurement limit in the $1\,\text{M}\Omega$ range (corresponding to a resistivity of $\approx 1\,\Omega\,\text{cm}$ in this case).

As is clear from the inset of Fig. 5.9 (b) the resistivity follows an Arrhenius law since the data is linear in the $\log(\rho(T))\,vs.\,1/T$-plot. Therefore, the temperature dependence is fitted by a $\rho(T) \propto \exp\frac{\Delta}{2k_bT}$ law (see red line in the inset), which yields a Mott gap Δ of $0.2\,\text{eV}$. The size of the Mott gap determined here closely matches the value found by optical conductivity measurements on bulk crystals [70, 119] and also fits DMFT results that report a small but sizable gap of the order of several $100\,\text{meV}$ [71]. The insulating transport behavior and the size of the Mott gap detected here is another indicator for the correct stoichiometry of the LTO films. Earlier studies report a significantly smaller Mott gap ($< 10\,\text{meV}$) [121, 124] or even metallic behavior [122, 123], which is likely due to uncontrolled over-oxidation.

Further characterization of the electronic phase is realized by XPS measurements of the valence band states on a $5\,\text{uc}\,\text{LAO}/40\,\text{uc}\,\text{LTO}/\text{DSO}$ structure, the resulting spectrum is depicted in Fig. 5.9 (c). Note that the O $2p$ part of the spectrum is generated by photoelectrons emitted from the LAO capping and the LTO film, with a contribution of about $50\,\%$ each. The Ti $3d$ part emerges exclusively from the LTO layer. The Ti $3d$ states form a single feature that does not exhibit a Fermi edge and is therefore identified as the LHB. Hence, the LTO thin film is in the Mott insulating phase. The gap size cannot be determined here, since photoemission probes only the occupied part of the density of states. However, the onset of the LHB gives a lower limit for the Mott gap and is estimated by fitting the leading edge close to the Fermi level as shown in the inset of Fig. 5.9 (c). The resulting value of $50\,\text{meV}$ has a rather large error bar owing to the low count rate and low energy resolution (approx. $0.4\,\text{eV}$) in this experiment.

The detailed characterization of the LTO thin films above shows that the samples are fully stoichiometric and exhibit Mott insulating behavior. They therefore provide a valuable reference for spectroscopy. Hence, the Ti $2p$ core level line and the Ti L x-ray absorption edge of a stoichiometric $LaTi^{3+}O_3$ film together with spectra obtained from $SrTi^{4+}O_3$ crystals are presented in Fig. 5.9 (d) and (e), respectively.

Let us first discuss the $2p$ line which is measured at a photon energy of $3\,\text{keV}$ on a $5\,\text{uc}\,\text{LAO}/40\,\text{uc}\,\text{LTO}/\text{DSO}$ structure. The spectra of both compounds exhibit a similar line shape, but in the trivalent case the core level is shifted by $1.1\,\text{eV}$ toward lower binding energies and significantly broadened compared to its tetravalent counterpart. The shift arises from the additional screening of the core charge by the $3d$ electron, usually referred to as a *chemical* shift. The increased width of the features is caused by interactions of the remaining Ti $2p$ photoemission core hole with the Ti $3d$ electron.

A recent publication by Lin *et al.* [135] reports a different Ti $2p$ line shape for LTO. They find a strong d^0 (Ti^{4+}) component and argue that this is an intrinsic feature caused by final state effects of the photoemission process. The absence of this feature in our
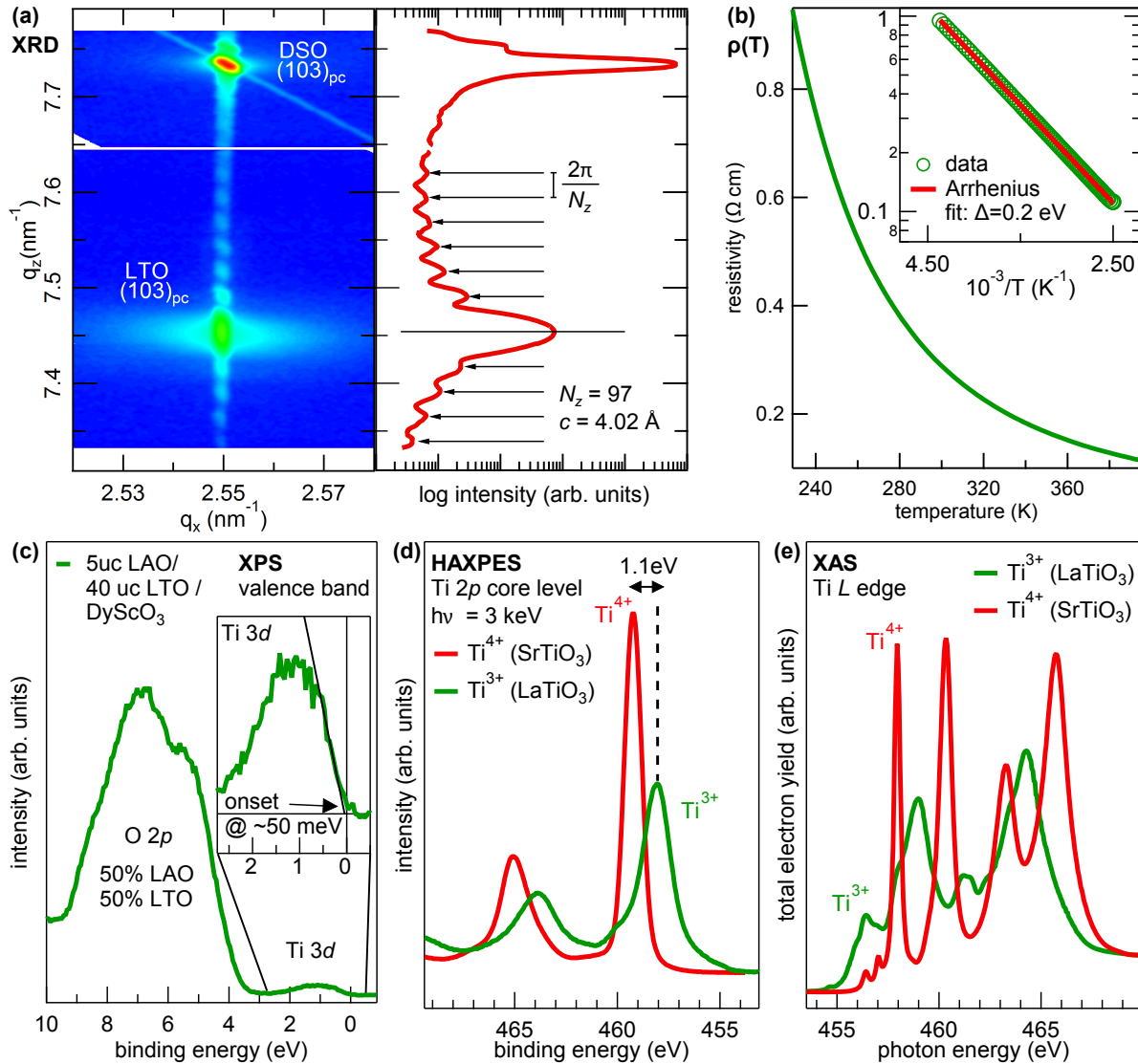
Fig. 5.9: Characterization of stoichiometric LaTiO$_3$ thin films. (a) XRD of a 5 uc LAO/100 uc LTO/DSO structure. Reciprocal space map around the (103)$_{pc}$ Bragg reflex (left panel) together with a line profile in q$_z$ direction through the peaks (right panel). The film is fully strained to the substrate and exhibits an out-of-plane lattice constant of $c = 4.02$ Å. The Laue intensity oscillations are marked by arrows and yield a film thickness of 97 uc. (b) Temperature dependent resistivity $\rho(T)$ of a 40 uc LTO thin film capped with 5 uc LAO. The inset reveals a linear behavior in an Arrhenius plot for the whole temperature range and a gap size Δ of 0.2 eV. (c) Valence band spectra measured by XPS on a 5 uc LAO / 40 uc LTO/DSO sample. The Ti 3d states close to the Fermi level are identified as the LHB with an onset at approx. 50 meV. (d,e) Ti 2p photoemission and Ti L absorption spectra for Ti^{3+} and Ti^{4+} obtained from LTO and STO, respectively. Note that the sample used for XAS was not equipped with any capping layer while the HAXPES measurement was performed on a 5 uc LAO/40 uc LTO/DSO sample.

measurements, however, clearly proofs that such a final state effect is not at play in this core level spectrum and that the d^0 satellite structure in their study is of chemical origin. This interpretation is further supported by HAXPES measurements of the Ti $2p$ line in LTO and YTiO$_3$ single crystals by Chang *et al.* [148] that are in line with our findings, i.e. no additional features in the Ti^{3+} spectrum are observed.

The Ti L absorption edge is another spectroscopic feature to judge the titanium valence (see Fig. 5.9 (e)). Note that for this measurement, the LTO thin film was not equipped with an LAO capping layer, but the film was transferred under UHV conditions to endstation I09 at Diamond Light Source. Hence, the very surface may be contaminated by Ti^{4+}. Comparing the spectrum to reliable literature data obtained from cleaved LTO single crystals reported by Haverkort *et al.* [75], however, indicates that it exclusively consists of a Ti^{3+} signal. Furthermore, no admixture of a tetravalent feature can be found in the spectrum—best visible in the energy range around $460\,\mathrm{eV}$. The Ti^{4+} features are likely absent here due to the increased probing depth of the XAS measurement in total electron yield mode, which is employed here, compared to XPS of the Ti $2p$ core level discussed earlier (see Fig. 5.7 (a)) [149]. Another reason is the intense x-ray beam at the synchrotron which was found to induce a loss of oxygen in related materials [101, 106]. In the case of LTO the oxygen adsorbates at the surface may desorb upon irradiation—at least to some extent.

Coming back to the comparison of the tri- and tetravalent absorption spectrum depicted in Fig. 5.9 (e), it is evident that the line shapes and energy positions are distinctly different allowing to clearly distinguish between the two valencies. Nonetheless, the complex over-oxidation mechanisms in LTO frequently lead to a misinterpretation of these spectra. For instance Disa *et al.* [140] fabricated superlattices of LTO and LaNiO$_3$ to trigger an electron transfer from the Ti to the Ni $3d$ band across the heterointerface. The charge transfer is monitored by XAS measurements on the Ti L edge and indeed a purely tetravalent line is detected in the superlattice seemingly confirming the intended charge transfer. However, their reference measurement on a thick LTO film yields a very similar spectrum and misses the characteristic features of trivalent titanium of a stoichiometric LaTi^{3+}O$_3$ film. Therefore, uncontrolled over-oxidation is most likely involved here—putting the electron transfer results into doubt.

This example shows that reliable spectroscopic references for fully stoichiometric LTO are crucial to rule out extrinsic chemical effects. The key aspect to gain control of the oxygen stoichiometry in LTO thin films is the substrate choice as shown in the detailed growth study presented here. As a next step, we now employ a *controlled* over-oxidation since it is a promising way of p doping the material, which could trigger the band filling induced Mott transition.

5.4 Mott Transition Induced by Excess Oxygen Doping

For orientation, let us briefly inspect the electronic phase diagram sketched in Fig. 5.10. The dimensional crossover of SVO ultrathin films (see chapter 4) is included and indicated by along a vertical line at a band filling of d^1. The effective bandwidth decreases

with the film thickness and the material is rendered from correlated metal (bulk) into a
Mott insulator. In the present case of the Mott insulator LaTiO$_3$, however, the material
can be driven into the correlated metal phase via p doping at a constant film thickness.

In view of the material's strong tendency to over-
oxidize, it is intuitive to use the (excess) oxygen stoi-
chiometry as a way of p doping. As demonstrated above,
excess oxygen ions are readily hosted on interstitial sites
in the LTO lattice. From an experimental point of view,
the oxygen growth pressure offers a well accessible han-
dle to increase the oxygen content in the thin films,
which is easier to realize as for instance a substitution of
La^{3+} with Sr^{2+} cations. Furthermore, even when doping
is realized via cations, the problem of uncontrolled over-
oxidation remains and can impede a controlled tuning
of the band filling. For these reasons, we pursue oxygen
excess doping to reduce the Ti $3d$ band filling in LTO
thin films.

Before investigating the transport properties of
LaTiO$_{3+x}$ thin films, spectroscopic methods are used to
check whether a sample fabrication in elevated oxygen
growth pressures is an effective way of p doping. Va-
lence band photoemission is employed to assign the elec-
tronic phase—Mott insulator or correlated metal—and
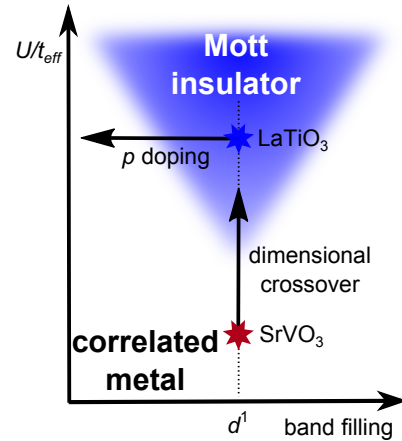the doping level is estimated from core level spectroscopy.

Fig. 5.10: The dimensional
crossover in thin SVO films and
the band filling induced Mott
transition sketched in an elec-
tronic phase diagram.

5.4.1 Ti $3d$ Valence Band States

The valence band states of LTO/DSO structures without an LAO capping. i.e. the bare
surface, are investigated by resonant photoemission (ResPES) at the Ti L absorption
threshold that strongly and selectively enhances the Ti $3d$ photoemission signal. Mea-
surements are performed at endstation I09 at the Diamond Light Source and the samples
are again transferred in UHV conditions to prevent oxidation in air. The inelastic mean
free path λ_0 amounts to $10.6\,\text{Å}$ in these measurements and is therefore high enough to
probe the bulk of the LTO films below the over-oxidized surface layer. Assuming a two
unit cell thick surface layer, the contribution of the bulk signal to the overall signal is
approx. 50%. Note that the resonance processes of the photoemission signal is discussed
in detail throughout the next chapter. For now, the ResPES technique is simply used
to enhance the Ti $3d$ intensity.

Two samples are investigated and the oxygen growth pressure was chosen to result in
a stoichiometric film (LaTiO$_3$) and in an over-oxidized (LaTiO$_{3+x}$) one. The resulting
spectra are depicted in Fig. 5.11 (a). The stoichiometric sample (blue line) exhibits a
single Ti $3d$ feature with an onset at $42\,\text{meV}$ identified as the LHB. This is in line with
the XPS measurements of stoichiometric capped samples (see Fig. 5.9 (c)).
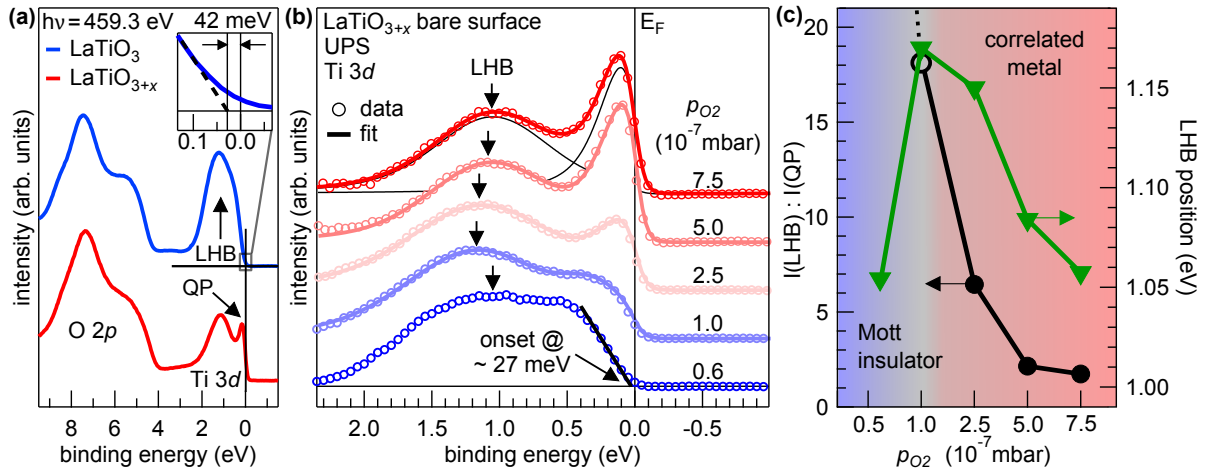
Fig. 5.11: Band filling induced Mott transition triggered by oxygen excess doping as observed by photoemission measurements on the *bare* film surface of LaTiO$_{3+x}$. (a) Resonant photoemission of a stoichiometric (LaTiO$_3$) and a p doped (LaTiO$_{3+x}$) sample. (b) UPS measurements of films fabricated in various oxygen growth pressures p_{O2} show the crossover from Mott insulating to correlated metal upon doping. The LHB and QP component of the fit are shown exemplarily for the highest p_{O2}. (c) Spectral weight ratio between LHB and QP together with the LHB position plotted against p_{O2}. Data is evaluated from the spectra presented in (b), see text for details.

Surprisingly, no Fermi cutoff or QP feature is detected despite the over-oxidized surface layer that is also probed here, which means that no metallic charge carriers are induced by the surface oxidation. The most plausible microscopic scenario to explain this behavior is a separation into areas with an empty d band that do not contribute to the Ti $3d$ spectrum at all, and subjacent or adjacent stoichiometric areas with d^1 configuration that give rise to the LHB. This is reminiscent of the SVO surface and as discussed in that context, such phase separations are also observed on related materials such as STO [101], manganites [102–104], or high-T_C cuprates [105].

The excess oxygen doped LaTiO$_{3+x}$ film on the other hand, clearly exhibits the typical two peak structure of a correlated metal, consisting of QP and LHB. The appearance of the QP feature with a Fermi cutoff demonstrates that the fabrication of LTO films in elevated oxygen growth pressures is a suitable method to reduce the band filling, i.e. for p doping, and to drive the Mott transition into the correlated metal phase.

Since the over-oxidized surface layer on the bare film surface does not induce metallic states and seems to gives no signal in the Ti $3d$ region of the valence band, lab based UPS measurements are employed to extend the study by analyzing more intermediate doping levels. To this end, LTO films are fabricated at various oxygen pressures ranging from 0.6 up to 7.5×10^{-7} mbar. Note that a slightly enhanced substrate temperature of 900°C was employed for this sample set, the properties of these samples are, however, in line with the characterization presented in Fig. 5.9. The resulting *in situ* UPS measurements are depicted in Fig. 5.11 (b). To correct for the He I$_\beta$ and I$_\gamma$ emission lines, the satellite signals arising from O $2p$ emission are subtracted.

The stoichiometric sample fabricated at $p_{02} = 6 \times 10^{-8}$ mbar exhibits a LHB with an onset at 27 meV. Increasing the pressure to 1×10^{-7} mbar leads to the emergence of a second feature close to the Fermi level reminiscent of the QP feature that does, however, not exhibit a clear Fermi edge. The assignment to the Mott insulating or correlated metal phase in this case is therefore not clear, a coexistence of both phases may be present or defects impede the formation of coherent states. The situation is clearer when p_{O2} is further increased: a Fermi cutoff is detected and the QP peak gains intensity.

To track the hallmarks of the Mott transition, the spectra are fitted by two Voigt profiles and a Fermi cutoff function (see Fig. 5.11 (b), fit components exemplarily shown for the highest p_{O2}). The resulting position of the LHB is indicated by arrows. For the stoichiometric sample no fit was performed, for this spectrum the arrow highlights the center of mass of the LHB. Besides the position of the LHB, the intensity ratio between LHB and QP is also extracted from this fit and both are plotted against the oxygen growth pressure in Fig. 5.11 (c).

Let us fist discuss the intensity ratio I(LHB):I(QP) plotted on the left axis, which diverges in the stoichiometric sample since no QP is observed, i.e. I(QP) $= 0$. At $p_{O2} = 1 \times 10^{-7}$ mbar, the feature close to the Fermi level is tentatively assigned to a QP-like feature (indicated by the open circle) and the ratio takes a high value around 20 that indicates strong electron correlations and the proximity to the Mott insulating phase. Going to higher p_{O2} the intensity ratio between LHB and QP strongly decreases down to approx. 1.7—a value comparable to bulk SVO, a prototypical correlated metal. This finding demonstrates that the electronic phase of LTO films can be tuned all the way from the Mott insulating phase deep into the correlated metal phase by adjusting the oxygen growth pressure.

Another systematic trend across the Mott transition is identified in the LHB position. Coming from the correlated metal phase, the LHB subsequently shifts to higher energies before it jumps back toward the Fermi level in the Mott insulating sample. The jump may be an artifact of the different determination of the LHB position, i.e. the position of the fitted Voigt line and the center of mass in the metallic and insulating phase, respectively. Furthermore, the position of the Fermi level is not well defined in the insulating phase and may be pinned by defect states somewhere in the Mott gap—and not in the middle of it. In the correlated metal phase, however, the location of the Fermi level is dictated by the coherent spectral weight of the QP peak. Therefore, the abrupt change of the LHB position observed for the Mott insualting sample is likely correlated to a jump of the Fermi level.

The detected changes of the valence band spectra follow systematic trends that can be correlated with the growth pressure. However, the results have to be taken with a grain of salt because the measurements are performed with a very surface sensitive technique, i.e. UPS, on the *bare* surface of LTO. We have seen that the over-oxidized surface layer does not contribute to the Ti $3d$ spectrum in the stoichiometric case, but some indirect influence may be at work. Therefore, a complementary characterization of the band filling induced Mott transition in LaTiO$_{3+x}$ films by transport measurements is
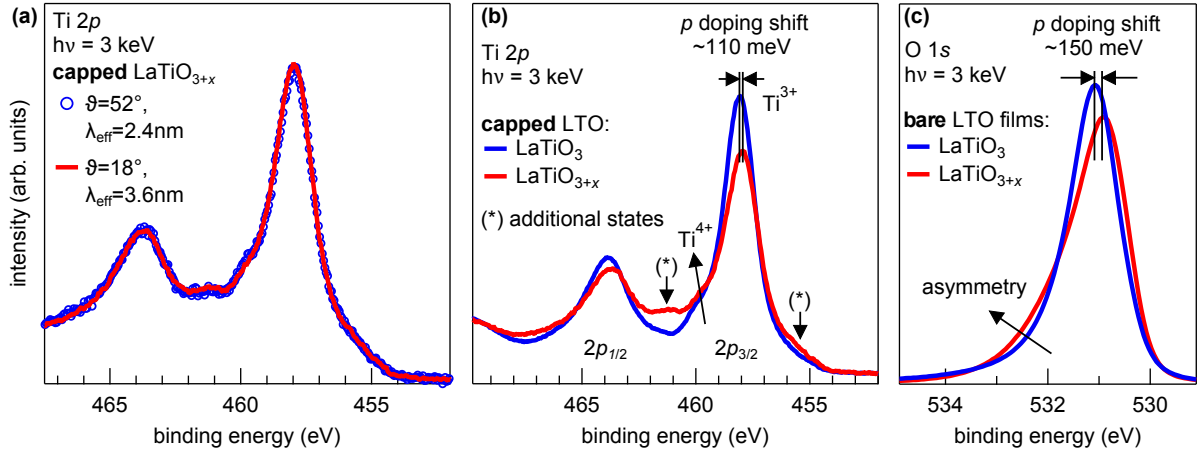
Fig. 5.12: (a) Ti $2p$ core level spectrum measured at different emission angles ϑ on a 5 uc LAO/40 uc LTO/DSO sample grown in $p_{O2} = 5 \times 10^{-7}$ mbar. The spectra are virtually identical, which indicates a homogeneous doping. (b) The comparison to the stoichiometric case (LaTiO$_3$) reveals a p doping shift, a sizable Ti^{4+} signal, and additional features for the LaTiO$_{3+x}$ sample. See text for details. (c) The doping shift is also detected on bare LTO films with similar doping levels, best seen in the O $1s$ line displayed here. This sharp core level line also allows to detect an asymmetry that is typical for the metallic phase.

presented in the course of this chapter. Before doing so, however, core level spectroscopy is employed to estimate the critical doping level that is required to render LTO metallic.

5.4.2 Estimation of the Doping Level

Several footprints of the oxygen excess doping and the band filling induced Mott transition can be found in the core levels, which are best investigated by HAXPES to enhance the bulk sensitivity. The following measurements are performed at a photon energy of 3 keV at endstation I09 of the Diamond Light Source. The two samples under investigation are stoichiometric and insulating (LaTiO$_3$) as well as p doped and metallic (LaTiO$_{3+x}$, $p_{O2} = 5 \times 10^{-7}$ mbar) thin films. Both LAO-capped and bare structures are investigated, the former are transferred in air to the synchrotron while the latter are shipped in the vacuum suitcase.

Let us first inspect the Ti $2p$ line of the doped capped sample. To check whether the oxygen excess doping is homogeneous in growth direction, i.e. along the surface normal, the spectrum of the LaTiO$_{3+x}$ film is measured at various electron emission angles ϑ as depicted in Fig. 5.12 (a). The corresponding effective inelastic mean free path of the photoelectrons (λ_{eff}) is also indicated in the figure and no discernable difference between the two spectra measured in different geometries is detected. This demonstrates that the oxygen excess doping in the LTO films is indeed homogeneous, at least on the length scale of this experiment, i.e. approx. the upper 10 uc.

The line shape of the Ti $2p$ spectrum of the doped sample is best studied in comparison to the spectrum of a stoichiometric LTO thin film, therefore both spectra are normalized

by their integral spectral weight and depicted in Fig. 5.12 (b). The plot shows that doping induces complex changes to the line shape, including several new features. The most prominent one is located at a binding energy of approx. 461 eV and highlighted by the symbol (*). This energy is too high for the $2p_{3/2}$ emission line of tetravalent titanium which is usually located around 459.5 eV (see for instance Fig. 5.7 (a) (d) and Fig. 5.9 (d)). Furthermore, the Ti^{4+} signal caused by oxygen excess doping is already accounted for by the shoulder feature between 459 and 460 eV, therefore the origin of the additional peak is of a different kind.

One possibility are additional photoemission final states due to screening of the core hole by delocalized conduction electrons—often referred to as *well screened final states* or *non local screening* [98, 150, 151]. This effect is not active in (Mott) insulating phases due to the full localization of the electrons, but can contribute to the spectrum in the (correlated) metal phase, which fits our observations. Moreover, such well screened (WS) final states have already been observed in the $2p$ line of related $3d$ materials such as La$_{1-x}$Sr$_x$MnO$_3$ [98], V$_2$O$_3$ [150, 151], VO$_2$ [96], Ti$_2$O$_3$ [148, 152], and—as already mentioned in the previous chapter—SrVO$_3$[96]. In these materials the WS final states appear at approx. 3 eV lower binding energies than the main line suggesting that the additional spectral weight detected at 461 eV is the WS satellite of the Ti$^{3+}2p_{1/2}$ line. In our case the binding energy difference between main and satellite line is 2.4 eV, therefore the WS final state of the Ti$^{3+}2p_{3/2}$ peak should be located at a binding energy of 455.5 eV and indeed the doped sample exhibits an increased spectral weight here compared to the stoichiometric LTO film. For these reasons we tentatively assign the additional features detected for the doped case in Fig. 5.12 (b) to WS final states, which therefore contribute to the trivalent and not to the tetravalent signal.

Besides these changes in the line shape, the $2p$ spectrum of the doped sample is also shifted by 110 meV toward lower binding energies with respect to the stoichiometric case as highlighted by the horizontal arrows in Fig. 5.12 (b).

For a better observation of the shift, the sharp and less complex O $1s$ line is inspected (see Fig. 5.12 (c)). To do so, bare LTO films are measured to avoid a contribution of the LAO capping layer to the signal. As clear from Fig. 5.12 (c), the O $1s$ core level exhibits only a single line and is almost fully symmetric in the stoichiometric sample. Upon oxygen excess doping the core level shifts by 150 meV to lower binding energies and an asymmetry on the high binding energy side develops. Such a shift is characteristic for p doping since electrons are removed from the system and is consistent with the incorporation of additional oxygen. The asymmetry resembles a Doniach-Šunjić-type line shape reflecting the metallic character of the doped sample. Note that a similar change from symmetric to asymmetric lineshape in the O $1s$ core level is also reported for the temperature driven Mott transition in Cr:V$_2$O$_3$ [150].

Having discussed the qualitative changes in the core level spectra that are induced by doping, the question naturally arises: What is the critical doping level required to trigger the band filling induced Mott transition?

To answer this question—or at least give an upper limit for the critical doping level—the Ti $2p$ spectrum of the doped sample (see Fig. 5.12 (b)) is fitted by six Voigt profiles
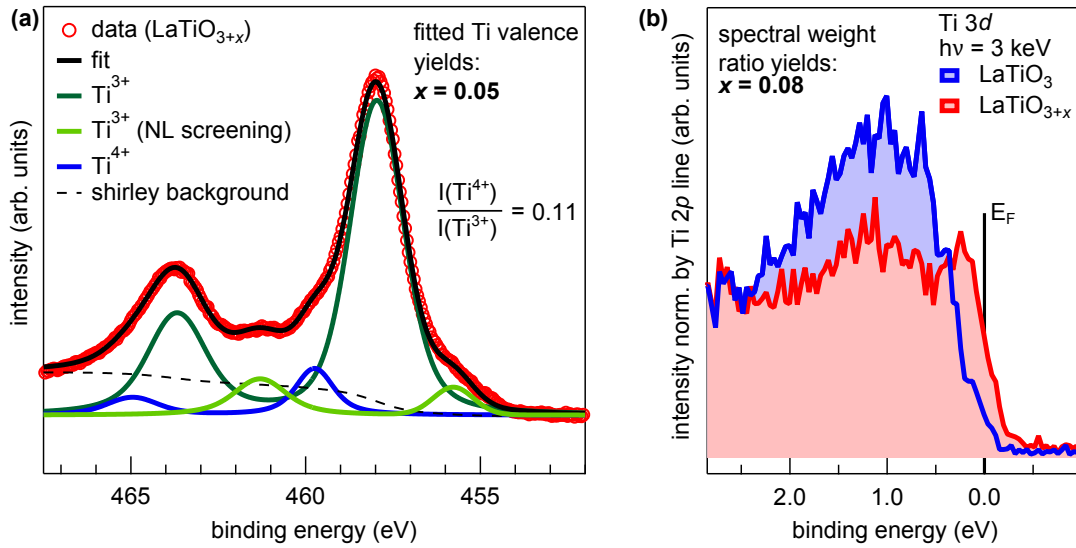
Fig. 5.13: (a) To determine the titanium valence of the doped sample ($LaTiO_{3+x}$), its Ti $2p$ spectrum is fitted by six Voigt profiles which yields a good agreement with the data. The resulting intensity ratio between tri- and tetravalent signals is 11% which corresponds to an excess oxygen doping level x of approx. 0.05. (b) Ti $3d$ valence band spectra normalized by their Ti $2p$ core level lines give a complementary estimate of the doping level of $x = 0.08$.

and a Shirley-type background as depicted in Fig. 5.13 (a). The peaks represent the Ti^{3+} $2p_{3/2}$ and $2p_{1/2}$ main lines and their WS satellite lines as discussed above. For the Ti^{4+} signal, only the main lines are included in the model since their possible satellites— if present—are expected to have very low intensities and are not visible in the data. The resulting fit reproduces the measured data very well and yields an intensity ratio $I(Ti^{4+}):(I(Ti^{3+})+I(Ti^{4+}))= 0.1$. This corresponds to an average titanium valence of $+3.1$, a band filling of $d^{0.9}$, and a stoichiometry of $LaTiO_{3.05}$. We refer to the doping level as $x = 0.05$ following the notation $LaTiO_{3+x}$. Fitting the Ti $2p$ core level may not be a very reliable method to determine the doping level since the attribution of the additional states (see again Fig. 5.12 (b)) to WS satellites has yet to be verified. Furthermore, the different Voigt profiles heavily overlap, which makes the fit not very robust.

We therefore corroborate our findings by directly evaluating the Ti $3d$ spectral weight. To this end the valence band spectrum of the stoichiometric and the doped sample are normalized by their integral Ti $2p$ spectral weight. The resulting Ti $3d$ spectra are plotted in Fig. 5.13 (b). Due to the chosen normalization, the Ti $3d$ spectral weight is a relative measure for the band filling and it turns out to be clearly reduced in the p doped case. To provide absolute numbers for the doping level, the stoichiometric sample is taken as a reference with $3d^1$ occupation. Then, the ratio of the red and blue colored areas in Fig. 5.13 (b) is evaluated which gives a filling of $d^{0.83}$ for the doped sample. In turn, this filling corresponds to an average titanium valency of $+3.17$ and a stoichiometry of $LaTiO_{3.08}$.

These values suggest a higher doping level as inferred from the Ti 2p core level fit and we will briefly discuss the discrepancy. Besides the uncertainties involved in the core level analysis that can lead to this deviation, the valence band spectra suffer from an extremely low cross section of the photoemission process in the used energy range. The resulting large noise level (see Fig. 5.13 (b)) gives rise to a sizable errorbar for the determination of the spectral weight. Furthermore, the change of the Ti 2p line shape upon doping (see Fig 5.12 (b)) causes uncertainties in the determination of the integral spectral weight of the core level, which is used as a normalization reference. Another systematic error might arise from remaining dispersion effects in the Ti 3d spectrum. The data is collected in an emission angle range from $\vartheta = 10°$ to $50°$, but only in a narrow angular range of $\approx 0.3°$ perpendicular to the analyzer slit. Since these capped samples have been transferred in air to the synchrotron, an alignment of the measurement geometry via LEED was not possible. Even though the dispersion effects are expected to be small at the high photon energies 3 keV, the QP intensity might depend on the sample orientation, which is not well defined, here.

In summary, we can conclude that the determined doping level of the LaTiO$_{3+x}$ sample suffers from several ambiguities. Therefore, the results are cross checked with literature on the critical doping level in bulk LTO. In such studies, the use of single crystals has the advantage that the oxygen content can be accessed by thermogravimetric analysis. The technique monitors the crystal's weight gain upon oxidation toward the tetravalent compound LaTiO$_{3.5}$ to obtain the oxygen content of the initial compound. It is, however, not sensitive enough to be employed for thin films. The onset of the metallic phase in single crystals can again be checked by transport or spectroscopy and the reported critical band filling range from $d^{0.96}$ to $d^{0.92}$ [153–157]. Complementary studies on Sr doped LTO report a critical value of $d^{0.95}$, which is in line with the oxygen excess doping experiments [120, 157, 158].

The comparison to these single crystal studies are in line with the upper boundary for the critical doping level, i.e. lower boundary for the band filling, determined above for the thin films of $d^{0.83-0.9}$. These quantitative considerations show that stoichiometric LTO is already close to the transition into the correlated metal phase. A reduction of the band filling by only several percent is sufficient to drive the Mott transition, which drastically changes its electronic properties. To gain further insight into the filling induced Mott transition in this material, we now turn to a complementary characterization by transport measurements.

5.4.3 Transport Properties

To analyze the transport behavior of oxygen excess doped LTO thin films, a set of samples is fabricated at various oxygen growth pressures p_{O2}. The pressure ranges from $p_{O2} = 5.0 \times 10^{-8}$ mbar up to 7.5×10^{-7} mbar, resulting in stoichiometric Mott insulating films for the lowest, and strongly p doped samples for the highest growth pressure. As monitored by RHEED, the LTO film thickness is set to 40 uc and the films are equipped with a 5 uc thick LAO capping to prevent oxidation in air. All samples are measured in
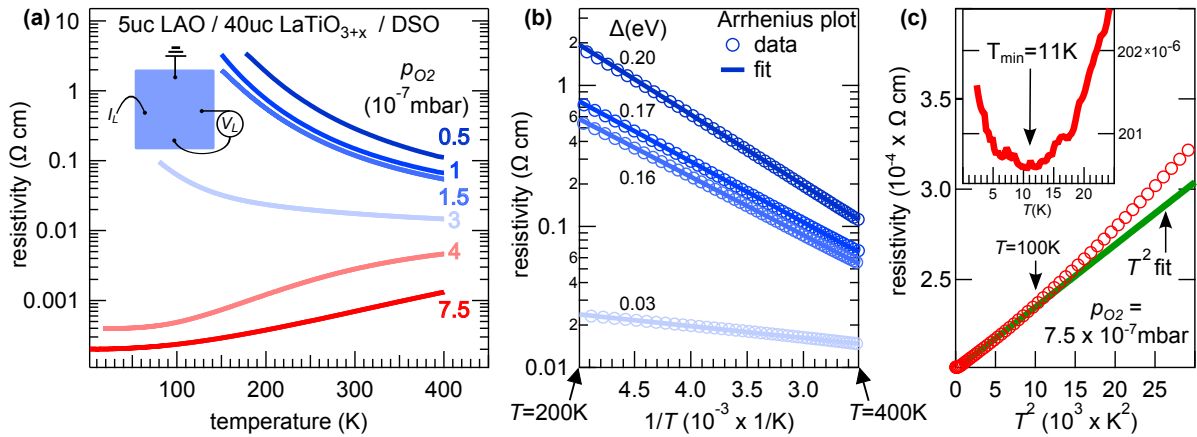
Fig. 5.14: (a) Temperature dependent resistivity measurements for a set of LaTiO$_{3+x}$ films fabricated at various p_{O2}. (b) Arrhenius plot for the samples that exhibit an activated behavior (color code consistent to (a)). (c) Closer inspection of the temperature dependence of the resistivity of the sample with highest doping level reveals a minimum at low temperatures (see inset) and a deviation from a T^2 behavior toward room temperature.

a square van-der-Pauw geometry and the electrical contact to the LTO films is realized by ultrasonic wire bonding with Al wires. A DyScO$_3$ substrate that has been annealed in vacuum to mimic the thermodynamic conditions during the LTO fabrication process was tested to check for possible leak currents through the substrate. The resulting resistivity of this substrate was above the measurement limit, thereby excluding any substrate contribution to the conductivity measurements of the LTO films.

The resulting temperature dependent resistivity $\rho(T)$ data is plotted in Fig. 5.14 (a). A clear crossover from an activated behavior (negative $d\rho/dT$) toward a metallic temperature dependence (positive $d\rho/dT$) is detected as p_{O2} is increased. The insulator-to-metal transition occurs between $p_{O2} = 3$ and 4×10^{-7} mbar, which is close to the emergence of the QP feature detected on the bare surface with UPS at $p_{O2} = 2.5 \times 10^{-7}$ mbar (see Fig. 5.11 (b)). The crossover signals the Mott transition and a drastic impact on the resistivity is revealed. Comparing the endmembers of this doping series, i.e. the stoichiometric sample and the one with the highest p doping level, a change of resistivity by about a factor of 100 at room temperature and even several orders of magnitude more at cryogenic temperatures is observed.

To check whether the activated behavior of the blue curves in Fig. 5.14 (a) follows an Arrhenius law, the data is depicted again in a log ρ *vs.* $1/T$ plot in Fig. 5.14 (b) (color code consistent to Fig. 5.14 (a)). As is clear from the linear behavior in the Arrhenius plot, the data is well described by a $\rho \propto \exp{(-\Delta/2k_B T)}$ relation over a wide temperature range from 200 to 400 K. The corresponding gaps Δ are determined by a fit and are indicated in Fig. 5.15 (b). For the stoichiometric case ($p_{O2} = 5 \times 10^{-8}$ mbar), Δ amounts to 200 meV and higher oxygen growth pressures lead to a reduction of the gap size. The smallest gap detected is 30 meV for $p_{O2} = 3 \times 10^{-7}$ mbar, which is a sizable value and the sample is therefore assigned to the insulating phase.

Turning to the metallic side of the transition, the resistivity of the sample with the highest doping level is inspected more closely. As depicted in the inset of Fig. 5.14 (c), an upturn is detected at temperatures below $\approx 15\,\mathrm{K}$. Such an upturn at low temperatures has also been observed in p doped LTO single crystals and is typical for doping levels close to the transition into the Mott insulating regime [122, 123, 153, 154, 156]. Furthermore, the temperature dependence deviates from a simple T^2 relation above 100 K as depicted in the main panel of Fig. 5.14 (c). Such a deviation has also been observed in single crystal studies for doping levels close to the Mott insulating phase [120, 153]. Higher doping levels, i.e. smaller band fillings, are reported to result in a pure T^2 behavior up to room temperature [120, 158]. Note, however, that other groups also report a $\rho \propto T^{3/2}$ relation [156], which shows that the temperature dependence is not straightforward to interpret.

Further insight into the transport properties of the LaTiO$_{3+x}$ thin films is gained by measuring the Hall effect. The realization of this experiment has turned out problematic since samples frequently suffered from macroscopic cracks or did even break apart during the measurements. After several runs, a correlation between sample damage and sweeping of the magnetic field at low temperatures was identified. Such a behavior is also reported in literature for DyScO$_3$ crystals: due to a magnetocrystalline anisotropy, samples physically crack or rotate when a magnetic field of a few tesla is applied at cryogenic temperatures [159]. Therefore, the Hall effect measurements in our case were restricted to a maximum B-field of $\pm 1\,\mathrm{T}$ and a minimum temperature of 50 K which allowed for non-destructive measurements.

As mentioned before, the measurements are performed in a square van-der-Pauw geometry but for the Hall effect measurements the contacts are rearranged as sketched in the inset of Fig. 5.15 (a). In the main part of this figure, the data obtained at 50 K from the LTO film fabricated at $p_{O2} = 7.5 \times 10^{-7}\,\mathrm{mbar}$ is presented. The Hall resistivity ρ_H is plotted against the magnetic field and a clear linear dependence is detected. The negative sign of the slope corresponds to electrons as charge carriers and a linear fit yields a value of $-2.5 \times 10^{-2}\,\mu\Omega\,\mathrm{cm}\,\mathrm{T}^{-1}$ for the slope, i.e. the Hall constant R_H.

Motivated by the linear behavior of $\rho_H(B)$, we employ the simple relation between Hall constant and charge carrier density n:

$$R_H = \frac{-1}{n\,e}, \tag{5.2}$$

where e is the elementary charge. The small Hall constant measured here is due to the high charge carrier density close to half band filling in LTO. For comparison, the B-field dependence of the Hall resistance in LAO/STO structures is several orders of magnitude higher since its two dimensional electron system (2DES) has an almost empty Ti $3d$ band, i.e. a $d^{0+\delta}$ configuration.

Another peculiarity of the data is the large offset of the Hall resistivity, since it should in principle be zero at zero field. This is most likely owed to the van-der-Pauw geometry: due to deviations from a strictly square arrangement of the contacts a part of the longitudinal resistivity is picked up and offsets the data by approx. $13\,\mu\Omega\,\mathrm{cm}$.
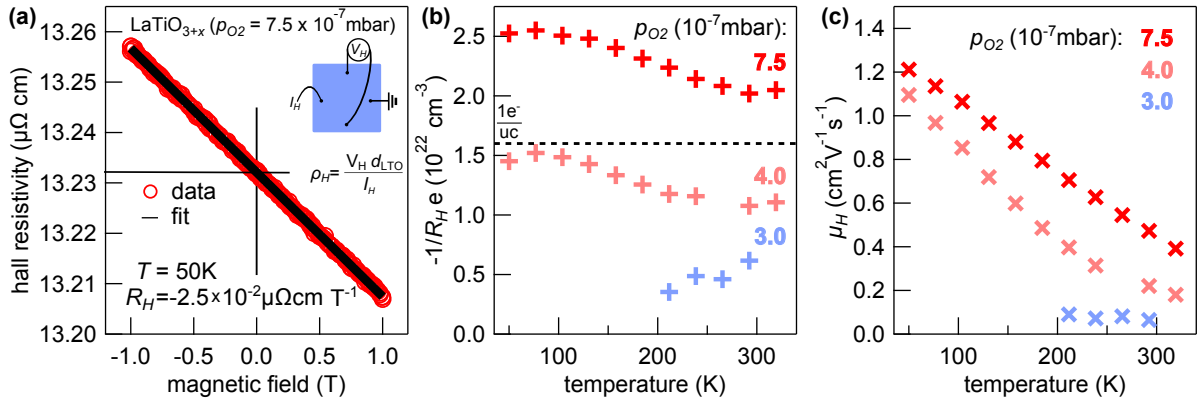
Fig. 5.15: (a) The Hall resistivity measured in van-der-Pauw geometry for the highest doping level of the sample set. (b) Inverse Hall constant as function of temperature for three doping levels (indicated by p_{O2}). The expected charge carrier density for one electron per unit cell is marked by the dashed line. (c) Corresponding mobility values.

Therefore a high sensitivity is required to catch the Hall effect since the relative changes induced by the B-field sweep with respect to the absolute resistivity is only 10^{-3} for this sample and temperature. The relative contribution of the Hall effect to the measured signal decreases further for samples with a higher longitudinal resistivity (see Fig. 5.14 (a)) and eventually the sensitivity of the measurement becomes insufficient. For this reason reliable Hall effect data is only obtained from the three samples with the lowest resistivity.

Using equation 5.2, the carrier density n is evaluated from the Hall constant R_H. The resulting data is plotted in Fig. 5.15 (b) together with the expected value for stoichiometric LTO, i.e. one electron per unit cell. The carrier density is in the expected order of magnitude of about $10^{22}\,\mathrm{cm}^{-3}$ and only a minor temperature dependence is detected. However, the absolute value for the highest excess oxygen doping level, i.e. the sample grown at $p_{O2} = 7.5 \times 10^{-7}$ mbar, exceeds the one electron per unit cell limit by about a factor of 2, which is at variance with the p doping scenario. The reason for this quantitative discrepancy is most likely connected to the van-der-Pauw geometry. As discussed above the contact arrangement is not perfectly square, which also has an impact on the Hall constant [160]. Furthermore, the contacts are not placed on the edge of the sample but within a distance of approx. 1 mm at a sample size of 5×5 mm, which causes an overestimation of the charge carrier density as discussed by Bierwagen *et al.* [161]. A quantitatively reliable measurement of the charge carrier density requires a Hall bar geometry, for which microstructuring techniques have yet to be developed for this material system.

Let us therefore dismiss the absolute value of the charge carrier density and rather investigate the trends for different doping levels. Naively, one would expect that the Hall constant gives a straightforward measure for the charge carrier density, which can in turn be used to determine the band filling and doping level. In our case, the charge carrier density is expected to *decrease* for higher oxygen growth pressures, since p doping

is performed as confirmed by the spectroscopic investigations presented above. The trend observed in Fig. 5.15 (b) is, however, the other way around: higher oxygen growth pressures lead to an increase of the charge carrier density, i.e. higher values of $-1/(R_H e)$.

A plausible explanation for this behavior is the separation into undoped and doped regions throughout the LTO film, which is expected to occur across the band filling controlled Mott transition [46, 55, 60, 61, 156]. When sample homogeneity breaks down, a simple interpretation of the Hall data is not possible anymore, since it is a major assumption required for the relation between Hall resistivity, Hall constant, and charge carrier density [160]. For instance, inhomogeneities can lead to strong distortions of the potential distribution generated by driving a current through the sample and probed by the Hall voltage V_H.

Nonetheless, we can try to capture the trend observed in Fig. 5.15 (b) by assuming a simplistic model consisting of undoped and doped regions. The undoped areas of fully localized electrons do not contribute to the Hall effect and we assume that they have no impact on the potential. Only the remaining doped regions give rise to the observed Hall effect. Even though the d^1 regions are taken as dead islands, their presence has an impact on the absolute value of the Hall constant. As noted in the inset of Fig. 5.15 (a), the film thickness d_{LTO} is used to convert the measured resistance into the Hall resistivity. However, when the thickness is effectively reduced to d'_{LTO} since only a part of the sample volume is active a smaller Hall resistivity and a smaller value for R'_H is obtained. Therefore, the Hall constant is overestimated above and in turn the charge carrier density is underestimated in an inhomogeneous system.

These considerations explain the trend in Fig. 5.15 (b). As the p doping level is decreased for lower p_{O2}, the Mott insulating phase is approached and the areas with fully localized electrons gain in volume, which leads to smaller values for $-1/(R_H e)$ even if the *average* density of 3d electrons may increase.

Having determined the Hall constant R_H and the resistivity ρ of the LTO films, the mobility μ of the charge carriers can be determined by $\mu = R_H / \rho$. Again, inhomogeneities may have an impact here and obscure the values calculated for the mobility. However, when μ is traced back to the measured values, i.e. the Hall voltage V_H and the longitudinal voltage V_L, one realizes that the sample thickness d_{LTO} cancels out:

$$\mu = \frac{R_H}{\rho} = \left(\frac{d_{LTO}}{I} \frac{dV_H}{dB} \right) : \left(\frac{\pi}{\ln 2} \frac{V_L}{I_L} d_{LTO} \right) = \frac{\ln 2}{\pi} \frac{dV_H}{dB} \frac{I_L}{I_H V_L}. \tag{5.3}$$

In this relation, the prefactor stems from the square arrangement of the contacts in the van-der-Pauw geometry [160], B is the magnetic field applied during the Hall effect measurements, and I_H and I_L are the excitation currents used during the Hall effect and resistivity measurements, respectively.

The resulting mobility values are plotted against the measurement temperature in Fig. 5.15 (c). The absolute values are of the order of 10^0 cm^2/Vs, hence several orders of magnitude smaller than for instance in the LaAlO$_3$/SrTiO$_3$ 2DES [106, 162]. One reason for these low mobilities are the strong electron correlations present in LTO causing an enhancement of the effective band mass compared to non-correlated materials as

$LaAlO_3/SrTiO_3$. On the other hand, high mobilities of the order of $10^3 cm^2/Vs$ are also reported for MBE grown $SrVO_3$ films, which is a *correlated* metal [86]. Therefore, scattering at structural defects probably plays a sizable role in limiting the electron mobility here.

Even though the low mobility of the LTO thin films may not exclusively be caused by electron correlation effects, a clear trend is observed upon comparing the different doping levels. As p_{O2} is reduced, i.e. the band filling is increased, the mobility strongly decreases. This is in line with the band filling induced Mott transition: as the Mott insulating phase is approached, the insulating behavior is caused by a critical enhancement of the band mass—hence a suppression of the mobility.

Note that an interpretation purely based on structural defects would suggest an opposite trend at variance with the experimental data. With a higher degree of oxygen excess doping, more structural defects, i.e. excess oxygen ions on interstitial sites, are incorporated in the lattice and the mobility should *decrease* with p_{O2}.

In summary, the transport characterization confirms that the band filling induced Mott transition can be controlled by excess oxygen doping in LTO thin films. The transition causes a strong change in resistivity of several orders of magnitude and a crossover from activated to metallic transport is detected in temperature dependent resistivity measurements. Hall measurements suggest an enhancement of the band mass as the Mott insulating phase is approached from the correlated metal side. Furthermore, the charge carrier density is found to be of the order of one electron per unit cell and indications for a phase separation in undoped areas with a d^1 configuration and doped d^{1-x} regions are found. Based upon these findings and the spectroscopic investigations discussed above, we discuss the electronic phase diagram of excess oxygen doped $LaTiO_{3+x}$ thin films in the following section.

5.4.4 Electronic Phase Diagram

To trace the band filling induced Mott transition in LTO thin films, a refined version of the simplified phase diagram depicted in Fig. 5.10 is required. As discussed in more detail in chapter 3 and mentioned in the preceding section, theoretical studies suggest an electronic phase separation when the band filling of a Mott insulator is detuned from integer filling [46, 60, 61]. Based on these studies, a refined version of the electronic phase diagram for the case of p doping in LTO is sketched in Fig. 5.16. Uur experimental findings are discussed within this framework. Please note in passing that the antiferromagnetic ordering of stoichiometric $LaTiO_3$ is also expected to vanish upon doping and the material becomes paramagnetic. However, we focus on the electronic properties here.

The microscopic situation is clear for the stoichiometric case. All electrons are fully localized and the material is in the Mott insulating phase. As the band filling is reduced from d^1 to an *average* band filling of $d^{1-\delta}$, i.e. a doping level of δ, metallic patches with a *local* doping level of δ_2 are formed [60, 61]. For small doping levels, these metallic puddles—if present—do not percolate which impedes conducting transport in
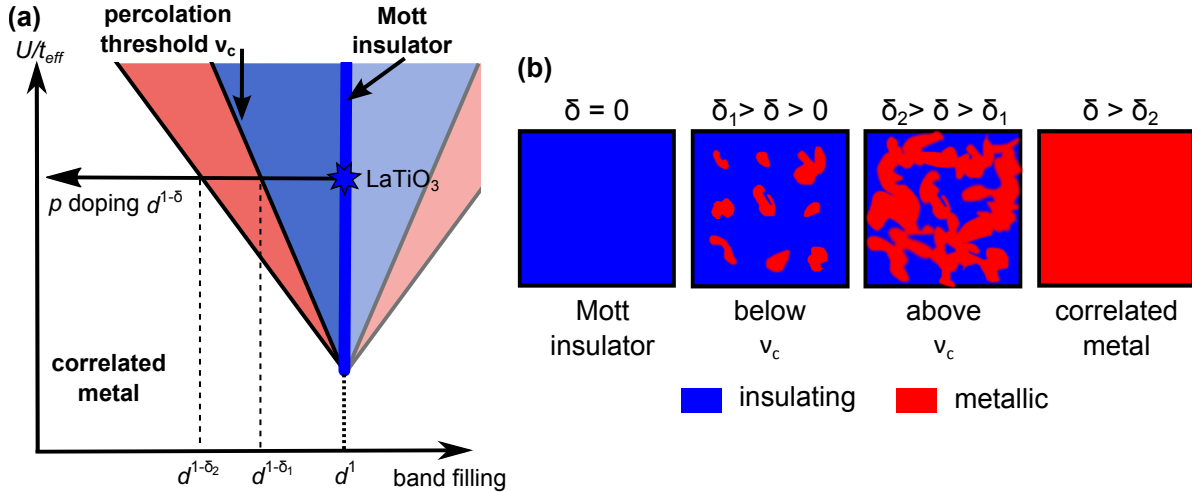
Fig. 5.16: (a) Refined electronic phase diagram for the band filling induced Mott transition taking spatial phase separations into doped metallic and stoichiometric insulating patches into account. (b) Corresponding sketch visualizing the phase separation for the different doping levels across the insulator-to-metal transition.

the resistivity measurements. The samples that exhibit an activated transport behavior ($p_{O2} \leq 3 \times 10^{-7}$ mbar) are expected to be in this regime.

In photoemission, no conducting path over the whole sample is required to detect a metal like spectrum, i.e. a QP peak with a Fermi cutoff, since the signal averages over the probed area. Therefore, the metallic islands are expected to give rise to a QP peak in the UPS measurements—provided that the island size and the degree of chemical disorder in the sample allows for the formation of a coherent state at the Fermi level. Furthermore, the signal emanating from the conducting patches is superimposed by the spectrum originating from the insulating regions. A QP peak from a small volume fraction may therefore not be detected in experiment due to the dominating LHB-type spectrum of the rest of the sample. As clear from Fig. 5.11 (b), a QP feature with a Fermi cutoff is observed for oxygen growth pressures of $p_{O2} = 2.5 \times 10^{-7}$ mbar and higher, which indicates the presence of metallic patches but not necessarily a coherent charge transport over macroscopic distances.

Going to higher average doping levels, the volume fraction of metallic puddles increases and eventually a conducting path forms at an average band filling of $d^{1-\delta_1}$. In three dimensions the percolation threshold ν_c beyond which the metallic patches are expected to touch is about 0.3 for a cubic system, i.e. about 30% of the sample volume is required to be metallic [60]. As inferred from the temperature dependent resistivity behavior (see Fig. 5.14 (a)), a metallic path is obtained for oxygen growth pressures $p_{O2} \geq 4 \times 10^{-7}$ mbar. Based on earlier single crystal studies and the estimation of the doping level carried out above, the corresponding critical doping level δ_1 is about 0.05 [110, 120, 157, 158]. Taking this value for δ_1 together with the three dimensional percolation limit ν_c, the local doping level of the metallic patches δ_2 is estimated by $\delta_2 = \delta_1/\nu_c \approx 0.17$.

The volume of the insulating puddles reduces further as the doping level is increased until the system has a homogeneous band filling of $d^{1-\delta_2}$ and the correlated metal phase is reached.

Whether or not insulating islands are still present in the samples with the highest doping level ($p_{O2} = 7.5 \times 10^{-7}$ mbar) investigated above is not clear, since no direct detection is given by the photoemission or transport measurements discussed here. However, the trends observed for the Hall constant in the previous chapter suggest an inhomogeneous sample, but further proof by spatially resolved techniques are required for a more detailed investigation of the phase separation across the filling induced Mott transition in thin LTO films.

5.5 LaTiO$_3$ as a Channel Material in Future Mottronics Devices?

As discussed by Scheiderer *et al.* in the publication *Tailoring Materials for Mottronics: Excess Oxygen Doping of a Prototypical Mott Insulator* [25], the tunability of the oxygen stoichiometry achieved in LTO thin films motivate their use in future devices that harness the unique electronic properties induced by electron correlation effects, often referred to as Mottronics [163, 164]. One particularly striking example of the field is the Mott transistor that employs the electronic phase transition from Mott insulator (OFF-state) to correlated metal (ON-state) as a switch rather than the mere manipulation of the carrier density in conventional semiconductor devices.

Similar to chemical doping by excess oxygen as described above and as sketched in Fig. 5.17 (a), the band filling induced Mott transition may also be triggered by applying an external electric field to a Mott insulator, thereby rendering all the previously localized electrons mobile in the ON-state. This allows for advanced transistor operation with potentially large ON/OFF ratios as well as fast switching speeds [165–170]. Furthermore, Mott materials evade a major miniaturization limit of conventional semiconductors set by the extremely small number of carriers within one nanoscale semiconductor device [164, 171]. As sketched in Fig. 5.17 (b), the carrier density in a Mott system is many orders of magnitude higher than in semiconductors, hence the size of a device can be drastically reduced at a constant number of carriers per device. Together with the carrier density, the typical length scales in the materials change as well. For instance the Thomas-Fermi screening length $\lambda_{TF} \propto n^{1/6}$ amounts to about 10 nm...100 nm in semiconductors and is of the order of Ångströms in Mott materials [54, 172].

The downside of the high charge carrier density, however, is the need for high electric fields to significantly change the band filling. The use of LTO as a channel material is advantageous here, since a change of only several percent of the filling is required to trigger the phase transition as demonstrated in the oxygen excess doping study above. Nonetheless, reducing the band filling from d^1 to $d^{0.95}$ corresponds to a difference in the charge density of $\Delta n \approx 8 \times 10^{20}$ cm^{-3} in bulk LTO and $\Delta n_{2d} \approx 3 \times 10^{13}$ cm^{-2} for a single two-dimensional layer. To judge whether this can be realized in a field effect
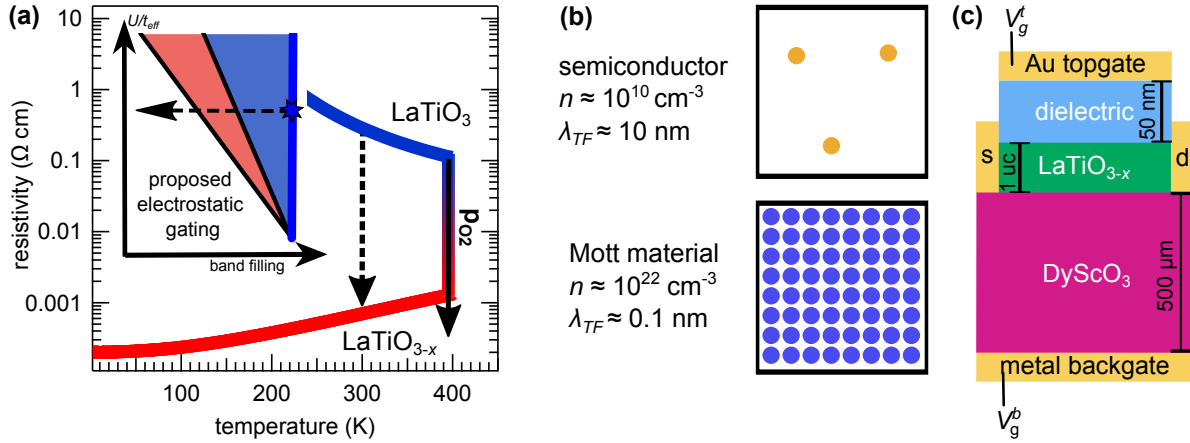
Fig. 5.17: (a) Path in the electronic phase diagram of LTO expected for electrostatic gating used in a Mott transistor together with the resistivity data from chemical doping, which demonstrates the strength of the band filling induced Mott transition. (b) Some characteristic properties of semiconductors and Mott materials. The small carrier densities in semiconductors complicate the miniaturization of devices since the number of carriers within one device approaches unity in state of the art nanostructures. Due to their high carrier densities, the use of Mott materials may resolve these limitations. (c) Sketch of a structure including back and top gate bias labeled V_g^b and V_g^t, respectively, and source (s) and drain (d).

device, we consider a simple structure as sketched in Fig. 5.17 (c) and calculate the corresponding gate voltages and capacitance within a plate capacitor model. Note, that the LTO film thickness is chosen to be a single unit cell, to approximately match the Thomas-Fermi screening length. In thicker films, only the first layers adjacent to the dielectric are expected to be affected by the external gate field [172].

The simplest geometry to realize in experiment is using the insulating DyScO$_3$ substrate as dielectric and a metallic back gate electrode. Using the simple plate capacitor model the gate bias is estimated by:

$$V_g = \frac{\Delta n_{2d}\, e\, d}{\epsilon\, \epsilon_0},\qquad(5.4)$$

where Δn_{2d} is the displaced charge density in the single layer LTO channel, e the elementary charge, d the thickness of the dielectric, ϵ the relative permittivity of DyScO$_3$ and ϵ_0 the vacuum permittivity. In the back gate geometry, the typical substrate thickness d is 500 μm, ϵ is approx. 25 [173], and we assume a 5% change of band filling. This yields a back gate voltage V_g^b of the order of 10^5 V, which is an unrealistic high value and hence disqualifies this setup.

As clear from equation 5.4, a thinner dielectric allows for lower gate voltages. Such thin dielectrics can be realized by coating the LTO film surface with a typically several 10 nm thick dielectric material such as SiO$_2$ ($\epsilon \approx 4$) [174]. This configuration is referred to as top gate geometry. Using equation 5.4 and $d = 50$ nm, the required top gate bias V_g^t to

alter the carrier density by 5% is estimated to be about 70 V. Even though 70 V is a quite large value for the top gate voltage, detectable results are already expected for smaller voltages V_g^b in the range of several volts since the transition causes a drastic change of resistivity—especially at low temperatures. Therefore, the fabrication of structures equipped with a top gate are promising to test an LTO based Mott transistor, but requires further developments in microstructuring.

Other strategies could follow more exotic techniques to achieve high electric fields such as liquid ion gating, which has been used to demonstrate Mott transistor operation in the related compounds VO_2 and $NdNiO_3$ [172, 175]. However, the technique may not be suitable for scalable electronics.

Recently, an alternative approach to harness the Mott transition in devices at moderate electric fields has been suggested. Dynamical mean field theory-based calculations have demonstrated that Mott materials in the insulating phase, but already near the transition, are highly sensitive to external parameters such as electric fields [59, 176]. Due to the tunability of its position in the electronic phase diagram, LTO is a suited material to test these predictions. It was demonstrated above that oxygen excess doping can be employed to tune the band filling to the possible operating point close to the Mott transition. Furthermore, the material's band width can be tuned by strain engineering. For instance, the use of other rare earth scandate substrates allows to change the in-plane lattice constant, while preserving the chemical properties [177].

Turning from the high controllability of the material's position in the electronic phase diagram to its perovskite crystal structure, one realizes that many functional compounds are epitaxially compatible to LTO. For instance the highly conductive $SrRuO_3$ or $SrVO_3$ and the high-ϵ $SrTiO_3$ can be employed as electrode and dielectric, respectively, allowing to design all oxide devices.

In summary, the considerations of using LTO as a channel material in Mottronics motivate further research toward the fabrication of an actual device. In this work, it has been demonstrated how to gain control of the oxygen stoichiometry in LTO thin films, which is an important achievement to control the material's electronic properties. Furthermore, oxygen excess doping was found to trigger the band filling induced Mott transition. It has been shown that the crossover from Mott insulator to correlated metal causes a strong decrease in resistivity of several orders of magnitude qualifying this phase transition for future transistor operation.

6 Resonant Photoemission of $3d^1$ Transition Metal Oxides

In the recent past the resonant photoemission (ResPES) technique became fashionable to investigate the electronic structure of buried interface states, such as the two dimensional electron system (2DES) at the oxide interface $LaAlO_3/SrTiO_3$ [38, 106, 115]. As discussed in section 2.4, the resonance between direct photoemission and Auger decay channel—in the case of LAO/STO Ti $3d^1$ emission and LMM Auger—can strongly enhance the photoemission intensity. Harnessing these resonant conditions is an elegant way to probe interface states with soft x-ray photoemission despite the limited probing depth in this regime. Note that an enhancement of the probing depth by the use of high-energy photons is not effective here, since the photoemsission cross section of the Ti $3d$ states decreases drastically with the photon energy (cf. Fig. 2.4). Furthermore, high-energy photoemission usually suffers from phonon broadening impeding angular resolved measurements that are, in turn, possible in the soft x-ray regime [115, 178].

For these reasons, the ResPES technique is widely used to investigate the electronic structure of the buried Ti $3d^1$ states. However, in these experiments no signal is detected when the photon energy is tuned away from the resonance due to the strong damping of the signal by the capping layer. The lack of an OFF-resonance (OFF-res) reference spectrum then inhibits a full characterization of the resonance behavior. For instance it is not clear how strong the resonant enhancement in the measurements on LAO/STO actually is. As discussed in section 2.4 the intensity enhancement is one of the key characteristics of ResPES and is closely connected to the Fano factor q. It is apparent that data from more prototypical and better characterized materials is required to gain a deeper understanding of the ResPES process. For the case of L edge resonance in $3d^1$ materials, the $LaTiO_3$ (LTO) and $SrVO_3$ (SVO) thin film samples presented in the preceding chapters are perfectly suited to do the job. Furthermore, ResPES measurements on LTO and SVO grant a deeper insight into the materials' electronic structure.

The chapter is structured as follows: first, the resonance behavior of stoichiometric Mott insulating LTO is presented before a p-doped metallic sample ($LaTiO_{3+x}$) is analyzed. Then, a complementary dataset on SVO thin films is presented, which are likewise investigated in the Mott insulating and correlated metal phase.

All measurements have been performed at beamline I09 at Diamond Light Source on thin films without capping layers. To prevent oxidation in air the samples have been transferred by means of a UHV suitcase. The photoemission data is normalized by the integration time which turned out to be quite accurate due to the stable photon flux.
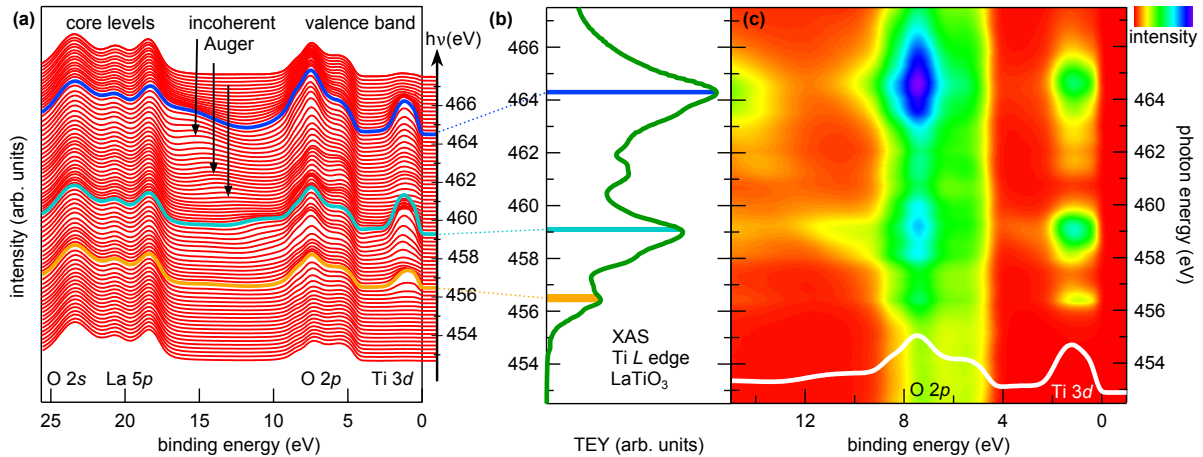
Fig. 6.1: (a) Series of spectra measured on a stoichiometric LTO thin film at various photon energies hν across the Ti L absorption edge. The highlighted spectra indicate the main resonances. (b) Left side: x-ray absorption spectrum of the Ti L edge. The resonances of panel (a) are included by colored lines. Right side: valence band spectra of (a) presented in a false color map. For orientation, the spectrum taken at h$\nu = 459.1$ eV is included in the lower part (white line).

6.1 Stoichiometric LaTiO$_3$

The stoichiometric 20 uc thick LaTiO$_3$ film has been fabricated by PLD on a DyScO$_3$ substrate. For a detailed characterization of these films the reader is referred to section 5.3. However, we recall here that the very film surface is subject to over-oxidation due to excess oxygen ions located at apical sites (see section 5.3.2).

To catch the resonance of the titanium related parts of the valence band, spectra are taken at various photon energies across the Ti L absorption edge in steps of 200 meV. A small contribution from the second order light (h$\nu \approx 920$ eV) resulted in a signal from the Ti $2p$ core level in the measurement window. This artifact was corrected by subtracting a core level reference spectrum scaled to the proper kinetic energy and intensity for each spectrum.

The resulting data is depicted in Fig. 6.1 (a) in which the y-axis indicates the intensity, while the offset of each spectrum with respect to the lowest lying one gives the corresponding photon energy (arrow on the right side). The main features of the spectra are labeled. The shallow core levels O $2s$ and La $5p$ are located on the high binding energy side and show no sizable modulation with the photon energy. The intensity of the valence band features of O $2p$ and Ti $3d$ character on the other hand are strongly enhanced as is clear from the highlighted colored spectra. An additional feature is highlighted by the black arrows at binding energies around 15 eV. Since this signal is not located at constant binding energy, it is most likely related to an Auger decay not participating in the resonance and is therefore termed *incoherent* Auger (cf. section 2.4). The incoherent Auger will be examined more closely below. First, the valence band resonance is inspected.
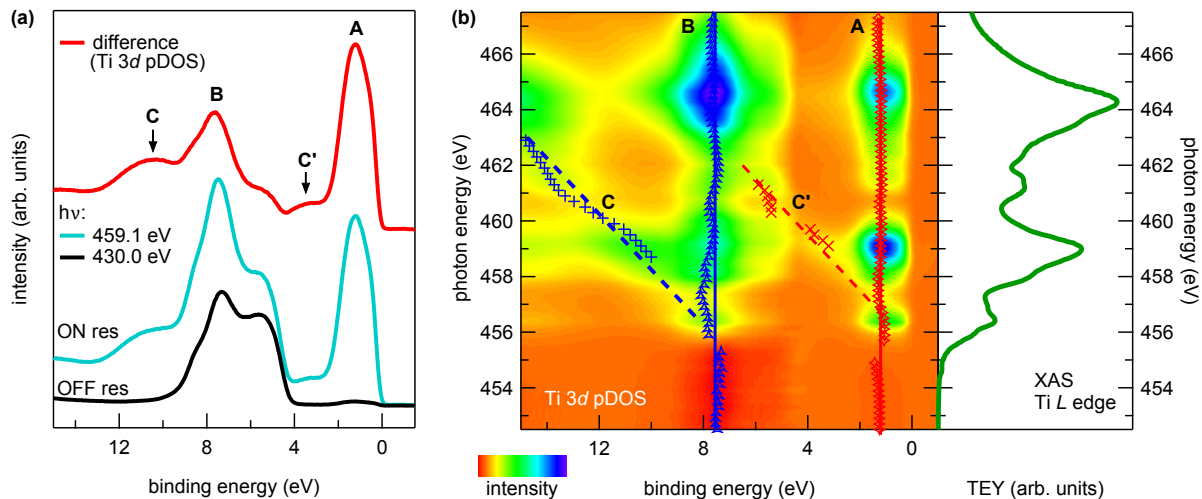
Fig. 6.2: (a) Valence band spectrum measured on the resonance (ON-res, $h\nu = 459.1\,\text{eV}$) together with a reference taken well below the Ti L edge (OFF-res, $h\nu = 430.0\,\text{eV}$). The difference spectrum, i.e. (ON-res) - (OFF-res), directly probes the Ti $3d$ pDOS. The main features of the difference spectrum are labeled by A, B, C, and C′ (see text for details). (b) False color map after substraction of the OFF-res spectrum together with the corresponding absorption spectrum (right side). The symbols indicate the positions of the corresponding features as extracted from the difference spectra, the dashed and solid lines are guides to the eye.

As reference the Ti L edge x-ray absorption spectrum of the LTO film is plotted in the left panel of Fig. 6.1 (b). The photon energies of the highlighted high-intensity spectra of panel (a) are indicated by colored horizontal lines. From this comparison, it is clear that the resonance of the lower Hubbard band coincides with the maxima of the Ti^{3+} absorption. A better visualization of the connection between resonance behavior and absorption spectrum is possible by constructing a false color map of the ResPES data in the plane of binding energy vs. photon energy, in which the color represents the intensity. Such a map is depicted in the right panel of Fig. 6.1 (b) and we realize that the regions of highest intensities in the Ti $3d$ as well as in the O $2p$ feature are located at photon energies for which the absorption is maximal.

At first sight it is surprising that the O $2p$ feature resonates as well with the Ti L absorption. The microscopic origin for this behavior is the finite hybridization of the Ti $3d$ and O $2p$ states. Since the resonance exclusively affects Ti $3d$ states, only the $3d$ partial density of states (pDOS) is left when an OFF-res spectrum (measured at $h\nu = 430\,\text{eV}$) is subtracted from each spectrum. This is exemplarily shown in Fig. 6.2 (a). Besides the main feature A of the difference spectrum, which is straightforwardly identified as the LHB, another strong feature labeled as B is detected. Peak B is located within the energy range of the O $2p$ states at a binding energy of $7.6\,\text{eV}$ and reflects the covalency of the Ti-O bond [37, 38, 179].

The remaining small peaks C and C′ have a different origin, which becomes clear when spectra taken at different photon energies are considered. To this end, all difference
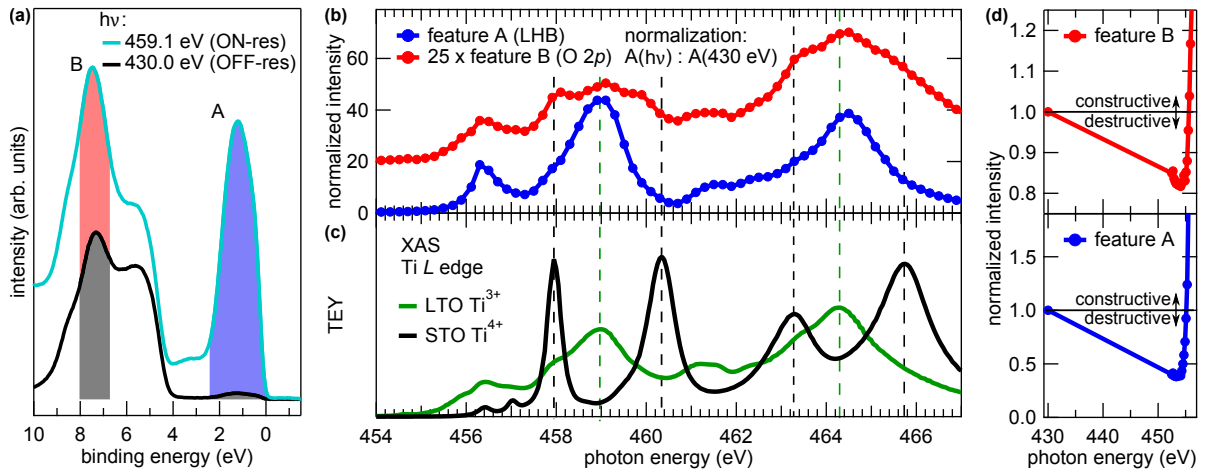
Fig. 6.3: (a) Integration areas (shaded areas) for the extraction of the spectral weight of feature A and B are exemplarily shown for the ON-res and OFF-res spectra. The latter is used as a reference for the normalization of the CIS curves. (b) CIS curves for feature A and B. (c) X-ray absorption spectra of tri- and tetravalent titanium serve as a reference. Dashed lines are guides to the eye. (d) CIS curves with focus on the pre-edge region reveal the destructive part of the Fano resonance.

spectra are compiled in a false color map that is depicted in Fig. 6.2 (b) together with the XAS reference spectrum. To keep track of the features, their peak positions are included in the map by markers. The binding energy of peaks A and B remains approximately constant for all photon energies, whereas features C and C' are rather located at lines of constant *kinetic* energies. This analysis confirms the tentative assignment of peaks C and C' as incoherent Auger signals from above. For clarity, dashed lines with a slope of 1 (constant kinetic energy) are included in Fig. 6.2 (b).

Having identified the origin of the main valence band features, their resonance behavior is inspected more closely. This is best done by extracting the *constant initial state* (CIS) curves that track the evolution of the intensity of a feature across the resonance. The spectral weight of the features A and B is determined by integration over the peaks as exemplarily shown in Fig. 6.3 (a). The resulting values are then normalized by their off-resonant counterparts highlighted by the black shaded areas in the same plot. In this way the relative intensity evolution across the absorption edge is determined. The resulting CIS curves for features A and B are plotted in Fig. 6.3 (b) together with the XAS spectra of tri- and tetravalent titanium that serve as reference in panel (c).

The maximum relative amplification of the LHB signal is about 45, which corresponds to a Fano factor of $q = 6.6$, i.e. the high q limit with small asymmetries of the resonance profile. Furthermore, the shape of feature A's (the LHB) CIS curve closely follows the LTO absorption spectrum, no additional structures or sizable energy shifts are detected. Turning to feature B, the CIS curve is multiplied by a factor of 25 for the sake of visibility in Fig. 6.3 (b). The maximal enhancement factor is about 2.8 and thereby significantly smaller than in the LHB case. Furthermore, the shape of the CIS curve

exhibits additional features at energies close to the Ti^{4+} absorption maxima as indicated by the dashed black lines in Fig. 6.3 (b) and (c).

The microscopic origin of these additional Ti^{4+}-features is likely related to the over-oxidation at the LTO surface. As mentioned above and discussed in detail in the preceding chapter, Ti^{4+}-ions are present on the thin film surface. Due to their $3d^0$ configuration, these ions do not contribute any signal close to the Fermi level, i.e. in the LHB region. For this reason the CIS curve of feature A is not affected by the over-oxidation. Due to the $2p$-$3d$ hybridization, the ions do, however, contribute to the spectral weight in the O $2p$ region which participates in the resonance process. In the materials of interest here, such hybridization effects are often described by charge transfers from the ligand to the transition metal ions. In terms of such a configuration interaction (CI) framework, the ground state for the tetravalent titanium ions may be expressed by $\alpha_0 \ket{3d^0 2p^6} + \alpha_1 \ket{3d^1 2p^5} + ...$, where the first term is usually dominating (weak hybridization). Apart from the first term, every configuration can participate in the resonant photoemission process, which gives rise to the additional structures in the CIS curve of feature B.

Finally, the CIS curves allow to detect another fignerprint of the Fano resonance. A closer inspection of the pre-edge region as depicted in Fig. 6.3 (d) reveals that the photoemission intensity is not only enhanced but also suppressed at certain energies. The CIS curves have been normalized by the OFF-res spectrum and hence they take a value of 1 at hν = 430 eV. In the pre-edge region the normalized intensity of features A and B drops below this value, hence the resonance is of destructive character before the enhancement sets in at the absorption threshold. Such a crossover from destructive to constructive interference as observed here is typical for the Fano resonance demonstrating the close connection of the ResPES technique to this theoretical description (see Fig. 2.5 (b) in section 2.4 for comparison).

6.2 Modified Resonance Behavior in Metallic LaTiO$_{3+x}$

The Fano description of the resonance usually employs a local picture of the electron configuration, i.e. only intrasite excitations. The question arises whether this simplification is justified when metallic valence band states are involved as, for instance, in the 2DES of the LAO/STO heterostructure. In this case the Ti $3d$ states form a delocalized conduction band which may change their resonance behavior across the Ti L edge. The LTO thin films are a suitable test system to investigate such changes since the electronic phase can be tuned from (Mott) insulating to metallic by excess oxygen doping as demonstrated in chapter 5. The stoichiometric and insulating compound has already been analyzed above and we now turn to the resonant photoemission data measured on a metallic 20 uc thick LaTiO$_{3+x}$ film. As for the measurements on the LaTiO$_3$ film, no capping layer was applied and the film was transferred by means of a vacuum suitcase. The step size of the photon energy was again set to 200 meV for the measurements.

The dataset is plotted in Fig. 6.4 (a) and the main features of the valence band are recognized, i.e. the O $2p$, Ti $3d$ states and the incoherent Auger signal. The most promi-
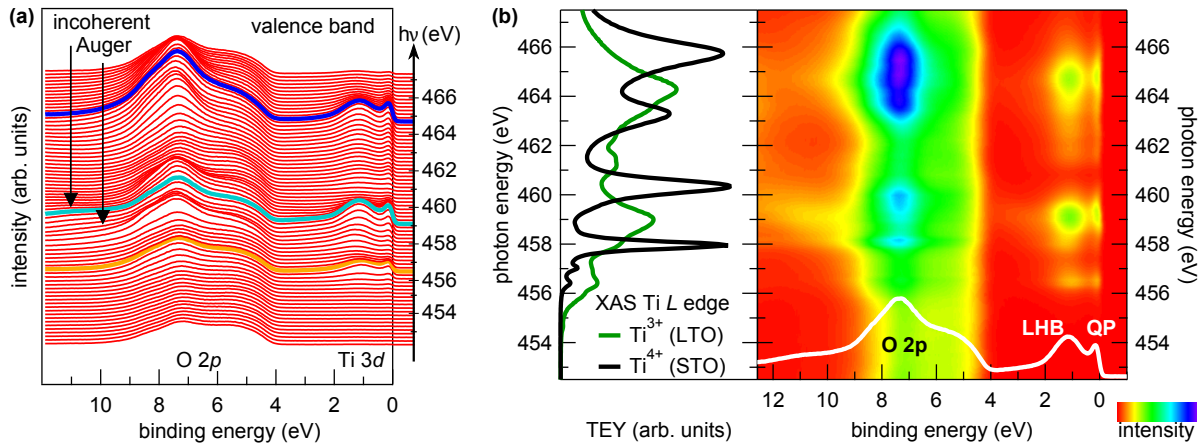
Fig. 6.4: (a) Ti L edge resonant photoemission data taken from an excess oxygen doped metallic LaTiO$_{3+x}$ thin film. The highlighted spectra indicate the main resonances. (b) Right panel: false color map representation of the spectra presented in panel (a). For clarity the spectrum taken at h$\nu = 459$ eV is included (white line) and the main features are labeled. For reference the absorption data of tri- and tetravalent titanium is shown in the panel to the left.

nent difference to the stoichiometric case is the two peak structure of the Ti $3d$ states verifying the correlated metal phase of the sample. Three main resonance maxima are detected and highlighted by colored lines. For a better comparison with absorption data the ResPES spectra are depicted in a false color map in Fig. 6.4 (b) together with XAS reference spectra of tri- and tetravalent titanium. Even though excess oxygen doping increases the amount of tetravalent titanium ions in the thin films, the Ti $3d$ states still resonate with the Ti^{3+} absorption. For the O $2p$ feature, however, the highest intensities (blue areas in Fig. 6.4 (b)) are clearly located at different photon energies that are more reminiscent of tetravalent titanium than Ti^{3+}. For a quantitative characterization of the resonances the corresponding CIS curves are extracted.

The ON- and OFF-res spectra are depicted in Fig. 6.5 (a) to clarify the spectral weight used to determine the CIS curves for the various features. Furthermore, the difference spectrum, i.e. the (OFF-ON)-res spectrum, is plotted as a direct probe for the partial density of Ti $3d$ states. As in the stoichiometric case, the Ti-O hybridization gives rise to a peak located at a binding energy of approx. 7.5 eV. Coming back to the extraction of the CIS curves, the used integration limits for the QP, LHB and O $2p$ features are highlighted by colored areas in Fig. 6.5 (a). Again, the OFF-res spectrum is taken as a normalization reference for the spectral weight to capture the relative resonance enhancement.

The resulting CIS curves are plotted in Fig. 6.5 (b) and for comparison various x-ray absorption spectra are depicted in panel (c) of the same figure. Let us first inspect the resonance profile of the O $2p$ feature that is multiplied by a factor of 25 for better visibility in Fig. 6.5 (b). As in the stoichiometric case, the CIS curve of this feature exhibits sharp features that correlate with the tetravalent XAS reference, best visible at photon energies of 458 and 460 eV (see dashed red line). However, in the doped case
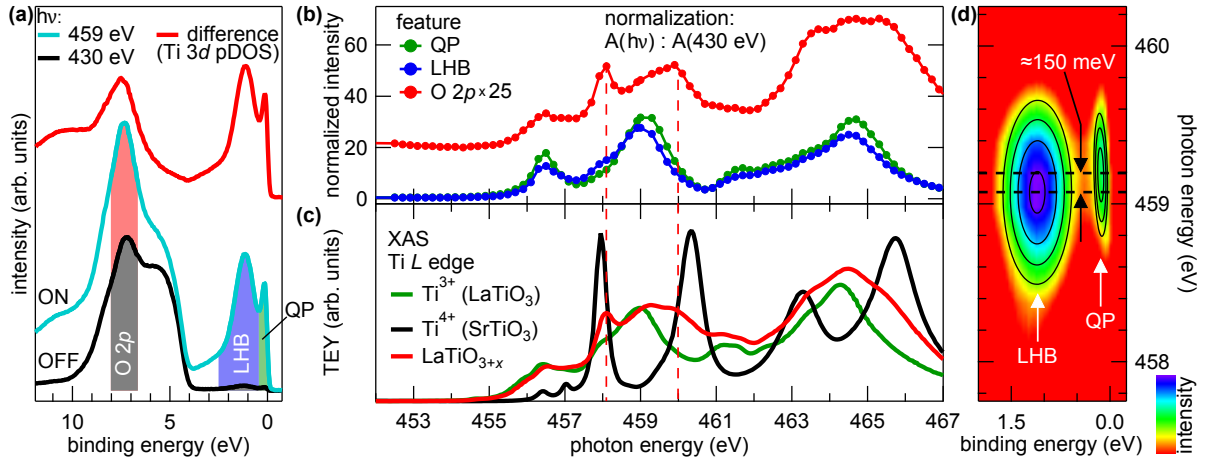
Fig. 6.5: (a) ON- and OFF-res spectra together with their difference spectrum which is a direct probe for the Ti $3d$ pDOS. The shaded areas indicate the integration areas used to extract the CIS curves for the various features. (b) CIS curves normalized by means of the OFF-res spectrum. (c) Ti L edge XAS reference data from tri- and tetravalent samples together with data from the LaTiO$_{3+x}$ sample under investigation. The dashed lines are guides to the eye. (d) Zoomed-in false color map revealing the delayed resonance of the QP feature with respect to the LHB. Contours are 2D Gaussian fits and the dashed lines are guides to the eye.

the tetravalent features are more pronounced since the average valency is further shifted toward Ti^{4+} by the excess oxygen doping. The overall lineshape of the resonance profile is a superposition of the Ti^{4+} and Ti^{3+} absorption, which is also the case for the XAS data of the LaTiO$_{3+x}$ film (red line in Fig. 6.5 (c)).

Turning to the resonance behavior of the Ti $3d$ states, it is apparent that the corresponding CIS curves adopt the lineshape of the Ti^{3+} absorption. The maximal intensity enhancement of the QP and LHB feature is found at photon energies slightly above 459 eV and amounts to 28 and 32, respectively. In order to compare the enhancement of the $3d$ states in the doped case to the stoichiometric case presented above, we take the average value of 30 for the maximal intensity enhancement of the two features. This yields a Fano factor of $q_{doped} = 5.4$ that is significantly smaller than in the stoichiometric case ($q_{stoichio} = 6.6$, see previous section). Note that the reduced q-value cannot be explained by the simple fact that the filling of the $3d$ band is smaller, because the CIS curves reflect the *relative* enhancement due to the used normalization. A more plausible reason for the weaker resonance in the metallic sample is a stronger tendency of the intermediate state to delocalize via the Ti $3d$ conduction band. For instance, consider the intermediate state $2p^5 3d^2$ at a specific site. When one $3d$ electron moves away from the site, the ResPES channel is lost and the de-excitation may occur via fluorescence or other incoherent processes.

Finally, a peculiarity of the QP resonance behavior is discussed. Close to the strongest resonance at $E_{ph} = 459$ eV it appears that the QP resonance is delayed compared to the LHB. Even though the effect is rather small, the delay is also detected at the second largest resonance around h$\nu \approx 465$ eV. A better visualization of the delay is granted by

the zoomed-in false color map depicted in Fig. 6.5 (d). The contours in this figure are obtained from 2D Gaussian fits around the resonances of QP and LHB and serve as a visualization reference. A shift of the QP feature to higher photon energies relative to the LHB is visible and amounts to approx. 150 meV. Since the small shift is comparable to the used step size of the photon energy in these measurement, further experimental data is yet required to corroborate this finding. To this end, we turn to complementary ResPES measurements on the related material SVO.

6.3 Resonance Behavior of Mott Insulating and Metallic SrVO$_3$ Thin Films

As demonstrated in chapter 4, SVO thin films exhibit a thickness induced transition from correlated metal (bulk) to Mott insulating in ultrathin films. Therefore, the material can not only give complementary data for the delayed resonance of the QP, but also give insights how the resonance behavior changes across the Mott transition. In contrast to the doping induced transition in LTO, the nominal vanadium valency, i.e. V^{4+}, remains constant since only the thickness of the SVO films is varied. However, there is a caveat: the surface of the uncapped SVO films suffers from over-oxidation toward pentavalent vanadium—especially in the case of thick films (cf. section 4.2.3).

Resonant photoemission experiments are performed on a Mott insulating and a metallic SVO thin film with thicknesses of 2 uc and 20 uc, respectively. Both films are grown on STO substrates. For the Mott insulating film a niobium doped substrate is used to prevent charging effects. No capping layer is applied and therefore the samples are transferred to endstation I09 of the Diamond Light Source by means of a UHV suitcase to prevent oxidation in air. Due to the limited availability of beamtime the measurements are limited to the first resonance at the V L_3 edge, which is usually sufficient to get the relevant information as we have just seen in the experiments on LTO.

Let us first discuss the spectra obtained from the Mott insulating 2 uc thick SVO film. Note that the inelastic mean free path of the photoelectrons amounts to approx. 1.2 nm for these measurements. Therefore, the STO substrate contributes a sizable signal to the O $2p$ valence band. Figure 6.6 summarizes the data. In panel (a) the ON- and OFF-resonance spectra are plotted together with their difference spectrum, i.e. the V $3d$ pDOS. The Mott insulating phase of the sample is straightforwardly verified by the missing QP peak and the absence of a Fermi cutoff. The V $3d$ pDOS exhibits similar features as the Ti $3d$ counterpart in LaTiO$_3$: a LHB close to the Fermi level, a peak located at 7.1 eV labeled as O $2p$, and an incoherent Auger signal at approx. 10 eV binding energy. Again, the colored areas in Fig. 6.6 (a) indicate the integration ranges used for the extraction of the CIS curves.

The photon energy dependence of the resonant spectra is best inspected in the false color map depicted in Fig. 6.6 (b). As expected, the incoherent Auger feature moves to higher binding energies as the photon energy is increased (see white arrows). The resonant enhancement is strongest for the LHB. Both features, i.e. LHB and O $2p$, res-
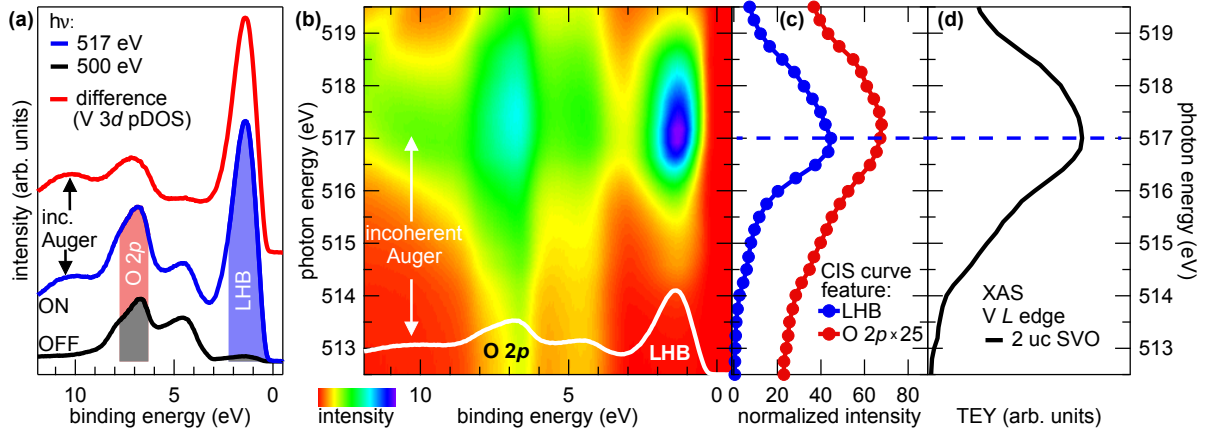
Fig. 6.6: Resonant photoemission data of a Mott insulating 2 uc thick SVO film. (a) ON- and OFF-resonance spectra together with the difference spectrum. The main features are labeled and the integration areas used for the extraction of the CIS curves are colored. (b) False color map of the ResPES data across the V L_3 absorption edge. For clarification the ON-res spectrum is included (white line). (c) Resulting CIS curves of the LHB and O $2p$ feature. The intensities are normalized by the spectral weight of the corresponding feature in the OFF-res spectrum. (d) V L_3 absorption edge measured on the sample under investigation. The dashed blue line is a guide to the eye to compare the XAS data to the CIS curves.

onate in the same photon energy range. This becomes apparent when the CIS curves and the XAS data are inspected in Fig. 6.6 (c) and (d), respectively. The CIS curves closely track the absorption spectrum and the maximal intensity enhancement factor is 45 and 2.7 for LHB and O $2p$, respectively. The Fano factor of the LHB resonance $q = 6.6$ matches the one determined for the Mott insulating LaTiO$_3$ sample, which shows that the resonance behavior of these similar materials compare very well—even in a quantitative way.

The data obtained on the metallic 20 uc thick SVO film is depicted in Fig. 6.7, whereby the figure is structured in the same way as for the 2 uc sample. The difference spectrum between ON- and OFF-resonance spectra in panel (a) reveals two major differences compared to the insulating case. First, the QP peak with Fermi cutoff signals the correlated metal phase of the sample. Second, a feature within the O $2p$ binding energy around 3.5 eV is pronounced more strongly. In order to distinguish between the two O $2p$-type features, the lower binding energy one is referred to as O $2p$ (B) whereas the feature at 7.1 eV is labeled O $2p$ (A). An overview over the photon energy dependence of the intensity of these features is given by the false color map depicted in panel (b).

The CIS curves of all four features, i.e. QP peak, LHB, O $2p$ (A) and (B), are plotted in Fig. 6.7 (c). Let us first inspect the O $2p$ related signals (reddish colored lines). The resonance of feature (B) roughly traces the absorption spectrum (see panel (d)) of nominally tetravalent vanadium. Feature (A), however, deviates from this lineshape which is most prominently visible around photon energies of 518.5 eV as highlighted by the black arrow in Fig. 6.7 (c). The additional structure is likely a consequence of the
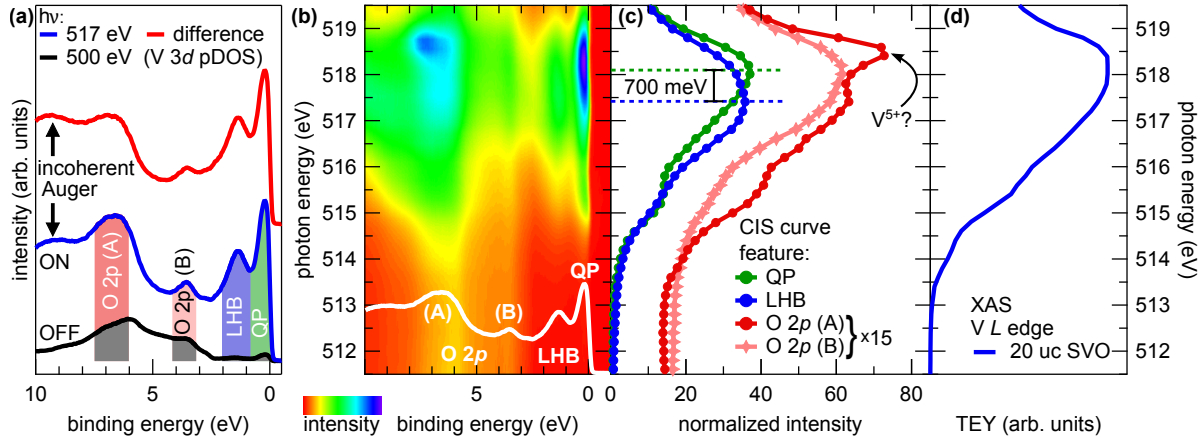
Fig. 6.7: Resonant photoemission data of a metallic 20 uc thick SVO film. (a) ON- and OFF-resonance spectra together with their difference spectrum. (b) ResPES map including the ON-res spectrum (white line). (c) CIS curves of all four features normalized to their OFF resonant spectral weight. The O $2p$(A) CIS curve exhibits a sharp feature that is reminiscent of pentavalent vanadium (see arrow). The QP resonance is delayed by approx. 700 meV with respect to the LHB as indicated by the dashed lines. (d) Complementary XAS data.

surface over-oxidation toward V^{5+}. Even though no pentavalent XAS reference spectrum is available for these measurements, the sharpness of the structure and its position at the high photon energy side of the CIS curve motivate a tentative assignment of this signal to V^{5+}-ions [180]. As in the case of excess oxygen doped LTO thin films, these over-oxidized V^{5+}-ions exhibit a $3d^0$ configuration and participate in the resonance process due to the hybridization of vanadium $3d$ and oxygen ligand $2p$ states. Note that the CIS curve of feature O $2p$ (B) does not show any sizable contribution from pentavalent vanadium and is therefore exclusively attributed to the V^{4+} cations of the remaining stoichiometric part of the sample.

Coming to the V $3d$ part of the valence band spectrum we first inspect the Fano factor q of this resonance. The maximum enhancement factor of the QP and the LHB signal is 37 and 36, respectively. Averaging these values yields $q_{metal} = 6.0$, which is smaller than in the Mott insulating SVO film ($q_{insulator} = 6.6$). So, as in the case of insulating and metallic LTO, the resonance effect is weaker in the metallic case. The shape of the CIS curves of both V $3d$ features is reminiscent of the V^{4+} absorption line (compare to Fig. 6.7 (d)). The QP resonance maximum is shifted by about 700 meV toward higher photon energies compared to the LHBs resonance peak (see Fig. 6.7 (c)). Since the resonance delay in SVO is of a sizable magnitude, it consolidates the findings drawn from metallic LaTiO$_{3+x}$, i.e. a QP can resonate at higher photon energies compared to its LHB.

A similar resonance delay has also been reported for ResPES measurements across the Ti L edge on LAO/STO heterostructures [106, 115, 179]. Here, the QP resonance is shifted by about 1 eV to higher photon energies compared to so-called in-gap states. These in-gap states are due to oxygen vacancies in the STO lattice that result in localized

Ti $3d$ states located approx. 1.3 eV below the Fermi level. It is tempting to confuse these in-gap states with a LHB, but this scenario has recently been ruled out by photoemission experiments that allow for an *in situ* tuning of the oxygen stoichiometry. These studies pinpoint oxygen defects as microscopic origin of the in-gap states in STO [101, 106]. In hindsight one may also support this finding by arguing that the QP and in-gap states resonate at different photon energies and are therefore different types of electronic states [107]. This line of argument is, however, not conclusive since even a QP and its LHB in a correlated metal may resonate at different energies as we have just experimentally demonstrated by the ResPES measurements on metallic SVO and LTO films.

Even though we have gathered experimental evidence for the QP resonance delay, the mechanism behind this effect is not easy to identify. In literature, ResPES data on controlled samples that may provide further insight into the resonance delay is only sparsely reported. Two ResPES studies at the M absorption edge ($3p \to 3d$ resonance) on transition metals report a broadened and delayed resonance for the metallic valence band states compared to the atomic case [181, 182]. These authors argue as follows. In the atomic case the resonance sets in at the $3p$ threshold. Going to a metallic solid, the formerly discrete energy levels of the intermediate state are now rendered into bands. This allows for a whole spectrum of intraband excitations that are often referred to as *shake up* transitions, which not only broaden the resonance but also account for the delay of the resonance maximum [181, 182]. Coming back to our experiments, we may adopt this simplistic view and assign the resonance of the LHB to the atomic case since its CIS curve closely traces the x-ray absorption line. The QP resonance is then broadened and delayed due to the shake up excitations in the conduction band. Following this interpretation we can speculate that the magnitude of the resonance delay may be used as an estimate for the spectral range of the intraband transition, i.e. the width of the conduction band. This means in our case that the conduction band in the doped LTO is narrower—or its width is renormalized more strongly due to electronic correlation—than in the metallic SVO thin film. The fact that the resonance delay in LAO/STO is even larger fits into this picture because the system is in the low filling limit, i.e. $d^{0+\delta}$, and therefore the conduction band renormalization is expected to be negligible.

Of course this is only a tentative interpretation of our results. To gain further insights into the microscopic processes involved, theoretical simulations of the ResPES process that take the material properties into account and fully consider electron correlation effects are required. The link between resonance delay and the effective width of the conduction band outlined above is of course speculative. However, it provides an outlook how ResPES data could be harnessed for the characterization of a material's electronic properties, once a deeper understanding of the resonance process is gained.

Besides the delayed QP resonance, the ResPES experiments on LTO and SVO thin films have revealed further findings from which the most important are briefly summarized in the following. First, the resonance of features located within the O $2p$ valence band binding energy range clearly shows the covalency between oxygen and B-cation in both materials, i.e. vanadium and titanium. Reference spectra for the V (Ti) $3d$ pDOS

are provided for SVO (LTO) in the correlated metal as well as in Mott insulating phase. This data is not easily accessible by other spectroscopic methods and may be of use for future theoretical simulations. Second, the maximal intensity enhancement of the L edge resonance for materials in a $3d^1$ configuration has been determined to a factor of about 40 to 50 in the insulating phase. For the metallic phase the resonance is found to be weaker by about 10 to 20%. These results provide a vital input for the ResPES measurements on LAO/STO, for which the absolute values of the resonant enhancement have not yet been accessible.

7 Probing the Band Structure of SrVO$_3$ and LaTiO$_{3+x}$ Thin Films

In the preceding chapters, photoemission has already provided vital insights into the electronic structure of the investigated samples. We now go one step further and add momentum resolution to study the band structure by means of angle-resolved photoelectron spectroscopy (ARPES) focussing on the Fermi surface tolopogy.

As already discussed throughout the introduction into Mott physics in chapter 3, the Mott transition into the insulating phase is expected to be induced by a divergence of the band mass and not a carrier freeze-out, i.e. a decreasing Fermi surface [46]. This means that in the case of the bandwidth induced Mott transition, the Luttinger volume enclosed by the Fermi surface should remain constant in the metallic phase before it vanishes for a Mott insulator (Brinkman and Rice framework). For the filling induced case the behavior is slightly modified since the Luttinger volume reflects the band filling that is varied to drive the transition. These statements can be put to test by ARPES measurements on the prototypical correlated metal SrVO$_3$ (SVO) and the doped Mott insulator LaTiO$_{3+x}$ (LTO). The focus of the investigations is set on the Fermi surface topology, but in addition the dispersion of the coherent quasiparticle is also studied to evaluate the band mass divergence mentioned above.

Coming from the physics that is to be investigated to the experimental details, some specifications of the samples and the used instrument are given. The SVO sample is a 50 unit cells (uc) thick film grown on a niobium doped SrTiO$_3$ (STO) substrate. The thin film was grown by pulsed laser deposition (PLD) under the optimized conditions described in chapter 4. The 20 uc thick LTO film is fabricated on a DyScO$_3$ substrate at an oxygen growth pressure of 5×10^{-7} mbar resulting in an excess oxygen doping level in the range of several percent, enough to reach the metallic phase (cf. section 5.4.4). No capping layers are used for both samples to avoid strong damping of the ARPES signal by any additional overlayers.

The ARPES measurements are carried out within a commissioning beamtime at the so-called K-branch of endstation I09 at the Diamond Light Source. To avoid oxidation in air, the samples are transferred by means of an UHV suitcase. The measurements are carried out in the soft x-ray (SX) regime from about 200 up to 600 eV which provides an enhanced probing depth to overcome the over-oxidized surface layer that is present in both samples despite handling in vacuum (see chapters 4 and 5 for details). Another advantage of these high photon energies with respect to vacuum ultraviolet (VUV) excitation sources, is the less severe broadening of the electron momentum along the surface normal, i.e. $k_\perp$ [183].

The chapter is structured as follows. First, a tight binding (TB) model for the cubic perovskite SVO (bulk) is introduced to provide an overview on the Fermi surface topology and band structure. Second, the experimental results obtained from the SVO thin film are presented and compared to the TB model. Third, the findings on the electronic structure of the doped Mott insulator LTO are discussed.

7.1 Tight Binding Model of Bulk SrVO$_3$

Before going into the details of the TB model, let us clarify that such a description does not account for short range correlation effects. Nonetheless, it provides the basic shape of the band structure and in the case of the Fermi surface it even gives a quantitative agreement. This becomes clear when we again recall the impact of correlation effects on an electronic band given by Brinkman and Rice (cf. chapter 3): the correlations induce a renormalization of the energy scale that is also often referred to as mass renormalization. Thus the texture of the bands, the Luttinger volume and Fermi surface topology remain unaffected. Following these considerations one can also extract quantitative values for the renormalization factor by comparing the TB model energy scale to the actually measured dispersion. For these reasons it is extremely useful to consider a TB model that describes the hypothetical case of an uncorrelated SrVO$_3$ crystal.

The TB model used here is adopted from Pavarini *et al.* [184] and is based on local density approximation (LDA) calculations. Let us recall the cubic perovskite structure of SVO that leads to three degenerate t_{2g} levels in which the $3d$ electron reside. Therefore, the electronic structure consists of three t_{2g} derived bands, i.e. d_{xy}, d_{yz}, and d_{zx}. Due to the symmetry of the system the three bands are equivalent in shape and nearly independent from each other [184]. In other words, the couplings within the TB model are restricted to the same orbitals, i.e. only intra-orbital hopping is relevant. This description gets clearer when we consider the concrete form of the d_{xy} band dispersion:

$$E_{d_{xy}}(\vec{k}) = \epsilon_{t_{2g}} + 2t_\pi \left(\cos \frac{k_x \pi}{a} + \cos \frac{k_y \pi}{a} \right) + 2\,t_\delta \, \cos \frac{k_z \pi}{a} + 4\,t'_\sigma \, \cos \frac{k_x \pi}{a} \cos \frac{k_y \pi}{a}. \quad (7.1)$$

Here, $\epsilon_{t_{2g}} = 625\,\mathrm{meV}$ is the t_{2g} energy with respect to the Fermi level, a is the SVO lattice constant and the various hopping amplitudes are denoted by t, which is further specified in the following. Before, however, note that the dispersion relation of the remaining d_{yz} and d_{zx} bands are obtained by simply interchanging the indices in equation 7.1, accordingly.

As mentioned above, only intra-orbital coupling is relevant here. To describe these processes we use the notation t_m^{xyz} that indicates hopping from site (000) to site (xyz) within orbital m. The most important nearest neighbor couplings are $t_\pi = t_{xy}^{100} = t_{yz}^{010} = t_{zx}^{001} = -281\,\mathrm{meV}$ and $t_\delta = t_{xy}^{001} = t_{yz}^{100} = t_{zx}^{010} = -33\,\mathrm{meV}$ that represent hopping in the orbital plane and perpendicular to it, respectively. Furthermore, the most important second-nearest neighbor term $t'_\sigma = t_{xy}^{110} = t_{yz}^{011} = t_{zx}^{101} = -96\,\mathrm{meV}$ is taken into account.
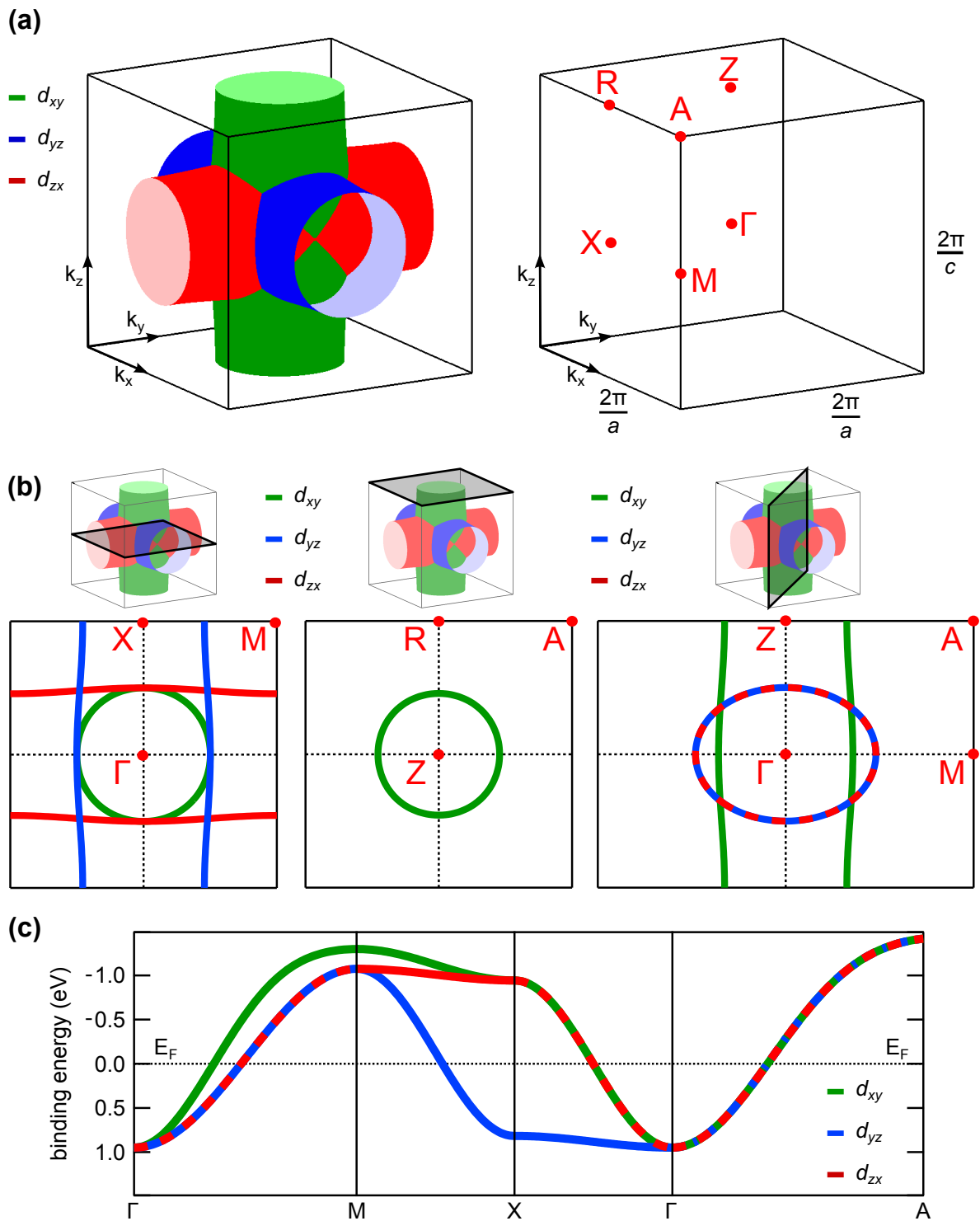
(a)

(b)

(c)

Fig. 7.1: Tight binding model for bulk SrVO₃. (a) Three-dimensional visualization of the Fermi surface (left) together with the notation of the high symmetry points within the BZ (right), see text for details. (b) Various 2D cuts through the Fermi surface as indicated by the grey shaded planes above each panel. (c) Band dispersion along all relevant high symmetry lines in the BZ.

The resulting band structure is depicted in Fig. 7.1. As is clear from panel (a) of the figure, the Fermi surface consists of three slightly warped cylinders that are derived from the three t_{2g} orbitals, each identical in shape. For a better orientation in reciprocal space, it is instructive to introduce some high symmetry points. The location of these points is found on the right hand side of Fig. 7.1 (a). At this point it may seem redundant to account for different in- and out-of-plane lattice constants a and c that introduce the additional symmetry points Z and R. However, in the course of the chapter strained SVO thin films are investigated that require such a notation. An estimate of the strained SVO films' unit cell deformation is provided by the experimental values of a and c obtained by x-ray diffraction (see Fig. 4.2) and one realizes that they differ by only about 2 %. Therefore, no qualitative difference in the band structure is expected, but for the sake of an accurate description we differentiate the in- and out-of-plane directions, whereby k_z is chosen to point along the surface normal of samples. The TB model used here, however, describes the cubic case, i.e. $a = c$, and every Z (R) point is equivalent to an X (M) point.

In Fig. 7.1 (b) various two-dimensional (2D) high symmetry cuts through the three-dimensional (3D) Fermi surface are presented. The location of these planes within the Brillouin zone (BZ) is highlighted by the grey shaded planes in the 3D plots above each panel. Furthermore, the high symmetry points are included by the red dots for better orientation. These high symmetry planes are plotted here, since they are well comparable to ARPES measurements that typically map 2D cuts through reciprocal space by variation of the electron emission angle and/or photon energy.

Turning from the Fermi surface topology to the band dispersion, we inspect Fig. 7.1 (c) in which the dispersion relation of all three t_{2g} bands is depicted. Note that only the cubic high symmetry points are considered here, the Z and R points are again equivalent to X and M within the TB model. It is instructive to verify that the crossing of the bands through the Fermi level (E_F) reproduces the location of the Fermi surface in reciprocal space by a comparison to Fig. 7.1 (a) and (b). Having done that one realizes an essential aspect of the dispersion relation: along the axis of a cylinder in the Fermi surface the band is flat, whereas perpendicular to this axis the bands disperse over approx. 2 eV. This becomes clear by tracing the dispersion relation along the ΓX direction and localizing this path in the left panel of Fig. 7.1 (b). While moving along the axis of the d_{yz} cylinder of the Fermi surface (colored in blue)—and at the same time perpendicular to the axis of the other two cylinders (red and green)—, the d_{yz} band remains flat and the remaining d_{xy} and d_{zx} bands strongly disperse.

7.2 Experimental Results from a SrVO$_3$ Thin Film

After this thorough introduction into the TB model of bulk SVO, let us now turn to the experimental results obtained from the 50 uc thick SVO film. First, the experimental details are specified. The measurement geometry is sketched in Fig. 7.2 (a). All measurements are performed at an incidence angle of 15° of the photon beam with respect to the sample surface. Data is taken in linear horizontal (LH) and linear vertical (LV)
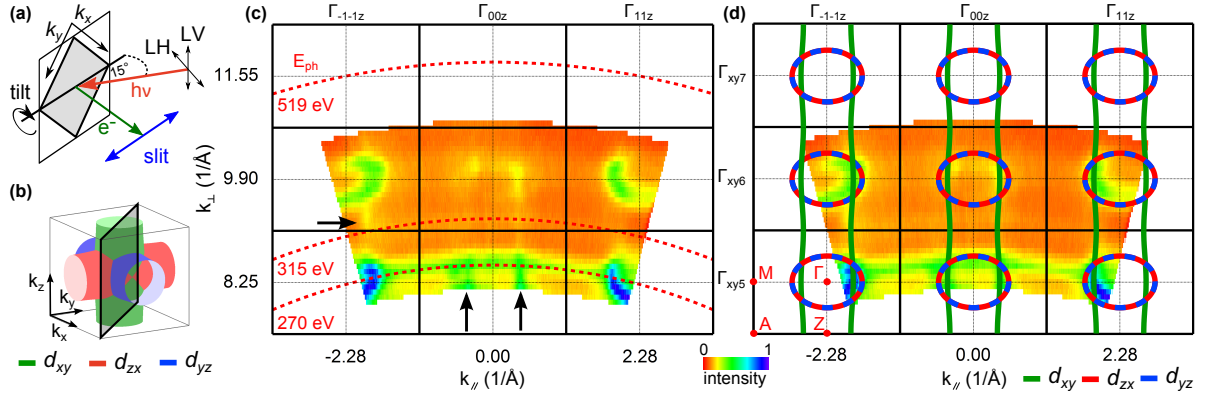
Fig. 7.2: (a) Measurement geometry. (b) TB Fermi surface with the cut probed by ARPES highlighted by the grey shaded plane. (c) Fermi surface map measured with LH polarized light. The bold lines indicate the BZ boundaries and the thin lines cross the centers. Various photon energies are included by the red dashed lines. (d) An overlay of data and TB model yields a good agreement of the Fermi surface topology and extension.

polarization. For the sake of clarity, however, only one polarization is presented for each measurement. Note that no major differences between LH and LV mode are detected, but only some minor intensity variations. In the following experiments, the 2D cuts through the reciprocal space are measured either by a variation of the photon energy to probe k_z, i.e. along the surface normal, or by tilting the sample to scan k along an in-plane axis. Furthermore, photoelectrons are detected along the slit direction probing an in-plane axis of k-space perpendicular to the tilt direction.

We will now inspect various Fermi surface maps that are obtained by integrating the measured intensity in an energy range of 100 meV around the Fermi level, i.e. $E_F \pm$ 50 meV. The first measurements are taken along the cut highlighted in Fig. 7.2 (b) by tuning the photon energy from 240 eV to 435 eV in steps of 5 eV. The resulting intensity distribution at the Fermi level is depicted in a false color plot in Fig. 7.2 (c). Before discussing the various structures visible in this map let us recall that the conversion from photon energy to $k_\perp$ (here k_z) requires a value for the inner potential V_0 (cf. chapter 2.3). The absolute location in k-space together with the distance of the structures around the 5th and 6th Γ point in k_z direction were evaluated and the resulting value $V_0 = 11$ eV matches the report from Takizawa et al. [83]. Having determined V_0, the measured intensity distribution for each photon energy and emission angle along the slit is presented in coordinates of $k_\perp$ and $k_\parallel$ that are oriented along the ΓZ and ΓM direction, respectively. The black bold lines that are overlayed in Fig. 7.2 (c) represent the BZ boundaries and the thin lines run through the centers.

One of the most prominent features of the intensity map is surprisingly located at constant photon energies, as is clear from the dashed red line labeled with 270 eV. The feature turns out to be an artifact that stems from the second order light. When the photon energy is scanned through $E_{ph} = 270$ eV, the corresponding second order light with an energy of $E_{ph} = 540$ eV gives rise to photoemission from the Sr $3p$ core level.

The kinetic energy of these photoelectrons coincides with the Fermi level of the first order light. Therefore, the feature at $E_{ph} = 270\,\mathrm{eV}$ is dismissed and we concentrate on the intrinsic Fermi surface structures.

The elliptic features around $\Gamma_{\pm 1 \pm 1\, 5}$ and $\Gamma_{\pm 1 \pm 1\, 6}$ arise from the cuts through the d_{yz} and d_{zx} cylinders of the Fermi surface as depicted in blue and red in Fig. 7.2 (b). Footprints of the remaining d_{xy} cylinder (colored in green) are also detected in form of vertical lines running parallel to $k_\perp$ as highlighted by the black arrows in Fig. 7.2 (c). Even though the d_{xy} features are fainter than the elliptic d_{yz} and d_{zx} ones, they are resolved by the measurement. Therefore, the ARPES data is in line with our expectations from the TB model. The agreement between model and measurement gets even clearer when we overlay the data with the expected contours as done in Fig. 7.2 (d). Note that the Fermi surface contour of the cubic TB model is morphed to match the Brioullin zone of the strained SVO film. The agreement of data and model in the graphic overlay not only confirms the expected topology, but also matches quantitatively and therefore suggests a Luttinger volume consistent with a filling of d^1.

In order to corroborate the quantitative agreement to the TB model further measurements in the k_x-k_y plane, i.e. a plane perpendicular to the one probed above, are performed at constant E_{ph} by tilting the sample. Doing so, it is intuitive to probe the high symmetry planes at the zone boundary and center for which the photon energies of $315\,\mathrm{eV}$ and $519\,\mathrm{eV}$ are employed, respectively (see dashed red lines in Fig. 7.2 (c)). As a convenient side effect, the V L-edge resonance is also active at $E_{ph} = 519\,\mathrm{eV}$, which is harnessed here to gain an intensity enhancement by a factor of approximately 40 (see Fig. 6.7 in the previous chapter).

The resulting intensity map through the Γ_{007} point is depicted in Fig. 7.3. The detected contours agree well with the TB model that is included in the plot by colored lines. For better visibility of the data the overlay is not plotted for the central zone. The orientation of the measurement plane with respect to the three cylinders of the Fermi surface is clarified in the lower sketch of Fig. 7.3 (b). At the top of this figure the location of the second measurement plane at the zone boundary is highlighted. The corresponding data is plotted in the upper panel of Fig. 7.3 (c). The low signal to noise ratio in this measurement is apparent, which is due to the missing resonant enhancement that accounts for a factor of about 40 lower intensities compared to the data presented in Fig. 7.3 (a). To allow for a better visualization of the Fermi surface contour the (negative) second derivative of the intensity map (chipped at a value of 0) is depicted in the lower panel of Fig. 7.3 (c). In this representation of the data one can clearly identify the circle that arises from cutting the d_{xy} cylinder of the Fermi surface.

In summary, the scans in the k_x vs. k_y plane confirm the quantitative agreement between TB model and data. Therefore, the Luttinger volume of the correlated metal SVO matches a band filling of d^1 or—putting it in other words—all V $3d$ electrons contribute to the Fermi surface. At first glance this may be surprising since the lower Hubbard band (LHB) feature that is seemingly split of toward higher binding energies exhibits also V $3d$ character, as demonstrated by the resonant photoemission measurements presented in the previous chapter. Therefore, one may raise the question of how many
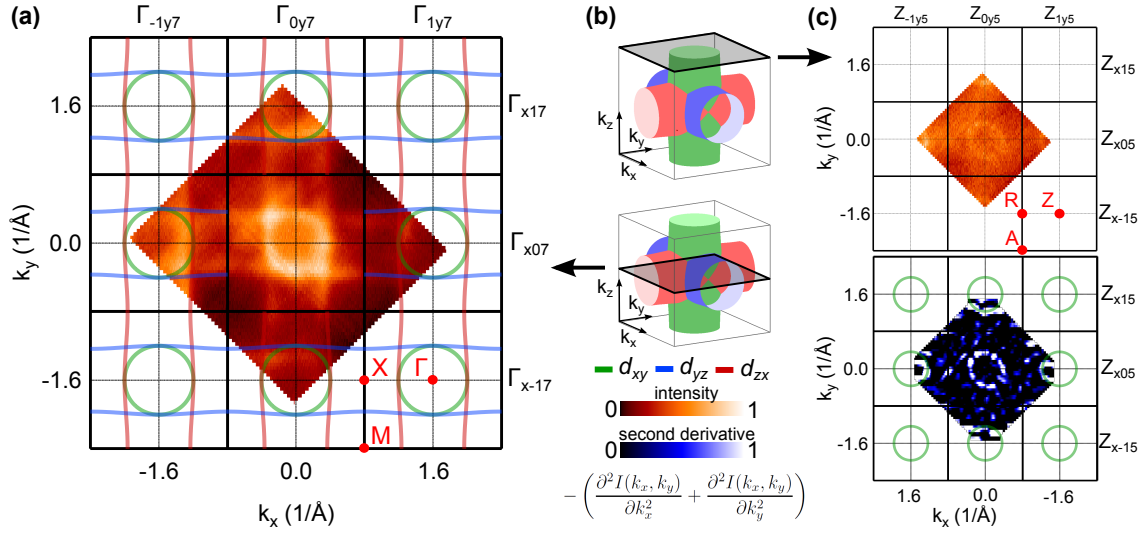
Fig. 7.3: (a) Fermi surface map through the Γ_{007} point measured in VL resonance ($E_{ph} = 519\,\text{eV}$) with LV polarization. The overlayed colored lines are the expected Fermi surface contours from the TB model. Note that the overlay is not plotted in the central zone for better visibility of the data. (b) Location of the measured planes within the 3D Fermi surface. (c) Data taken around Z_{005} in off-resonant conditions ($E_{ph} = 315\,\text{eV}$) and with LV polarized light. Due to the weak signal of the intensity map (upper panel), the second derivative is also plotted (lower panel).

electrons reside in the LHB when the quasiparticle excitation close to the Fermi level already accounts for all of them. The problem is resolved when we remind ourselves that the LHB in a correlated metal is *not* an independent feature arising from localized states, but is part of the same spectral function as the quasiparticle. Therefore, the large Fermi surface measured here is a manifestation of the many body physics of correlated electron materials described by the concept of the spectral function.

Having demonstrated that the charge carrier density of SVO is not altered by the strong electronic correlations with respect to the TB description, we now turn to analyze the renormalization of the bandwidth. To do so, let us inspect a so-called band map, i.e. an intensity map in the binding energy vs. k plane, measured along the XM direction depicted in Fig. 7.4 (a). Note that the data is taken in zone (107) for reasons of intensity optimization.

At the X point only one band is below the Fermi level as is clear from the TB model dispersion relation presented in Fig. 7.1 (c). This band is clearly visible in the false color plot of Fig. 7.4 (a). However, in order to analyze the ARPES data in a more quantitative way, line profiles in energy and momentum direction are extracted from the band map. These energy and momentum distribution curves (EDCs and MDCs) are plotted in Fig. 7.4 (b) and (c), respectively. In the EDCs, the corresponding high symmetry points along k_x are highlighted by the blue spectra. The quasiparticle (QP) close to the Fermi level exhibits a clear dispersion, whereas the LHB around 1.5 eV binding energy shows only a minor k-dependence. The band crosses the Fermi level at k_F (indicated by black
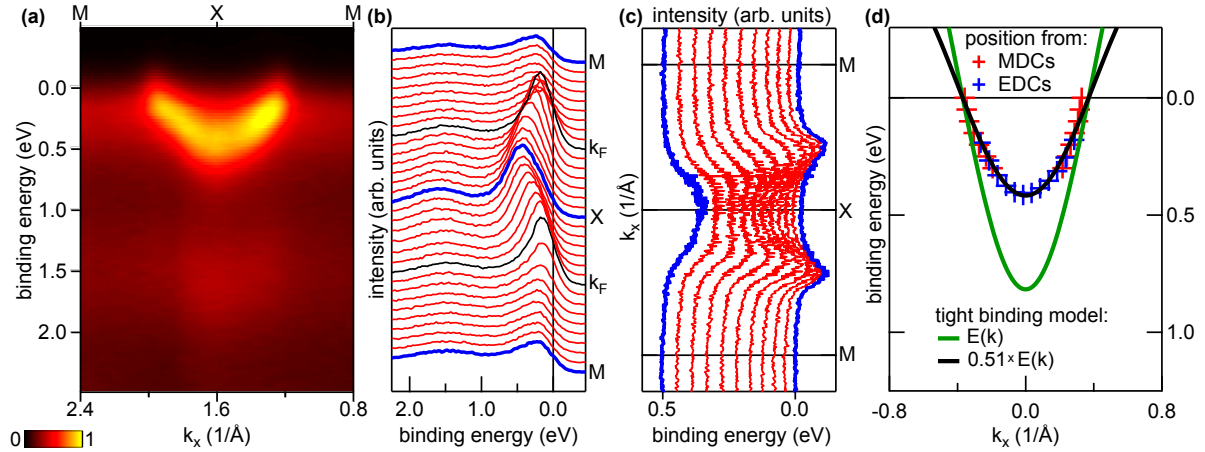
Fig. 7.4: SVO band dispersion. (a) Band map along the MXM path in zone (107) measured on the V L resonance in LH polarization. The corresponding EDCs and MDCs are plotted in (b) and (c), respectively. (d) Band positions extracted from the EDC and MDC maxima are compared to the TB model.

lines) and no QP intensity is expected around the M point. Nonetheless, the EDCs show a clear structure in this k-range. The reason for this is most likely extrinsic: Due to structural imperfections of the lattice—especially at the sample surface—scattering channels for the photoelectrons likely open up that can lift the k conservation in the ARPES spectra and give rise to a seemingly non-dispersive component of the spectral function. Note that in the VUV-ARPES experiments on thin SVO films reported in [85], no QP structure is detected around the M point, corroborating our interpretation in terms of an extrinsic feature. Therefore, the QP intensity at the M point is dismissed and only the dispersive feature around the X point is fitted by a Gaussian profile multiplied with a Fermi cutoff to extract the band positions. Supplementary data is gained by fitting the MDCs by Lorentzians. The resulting positions of the EDC and MDC maxima are presented in Fig. 7.4 (d) together with the TB dispersion relation (green line). It is obvious that the SVO band dispersion is significantly shallower than predicted by the TB model. However, a good agreement is obtained when the energy scale of the model is renormalized by a factor of $Z^{-1} = 0.51$, i.e. $E(k) = 0.51 \times E^{TB}(k)$, in line with the results from Takizawa et al.[83]. Frequently, such a renormalization is also referred to as a mass renormalization, since the narrowing of the band can also be seen as an effective mass enhancement due to the electronic correlations.

In summary, the investigation of the coherent QP dispersion in SVO has provided vital insights into electronic correlation effects and the Mott transition. It has been demonstrated that the carrier density n as inferred from the Luttinger volume determined by ARPES matches the TB description, i.e. the not-correlated case. Or in other words, the correlation effects have no impact on n. The experimentally observed bandwidth, however, is a factor of two smaller than predicted by the TB model. These findings suggest that—coming from the metal phase—the Mott transition driven by increasing
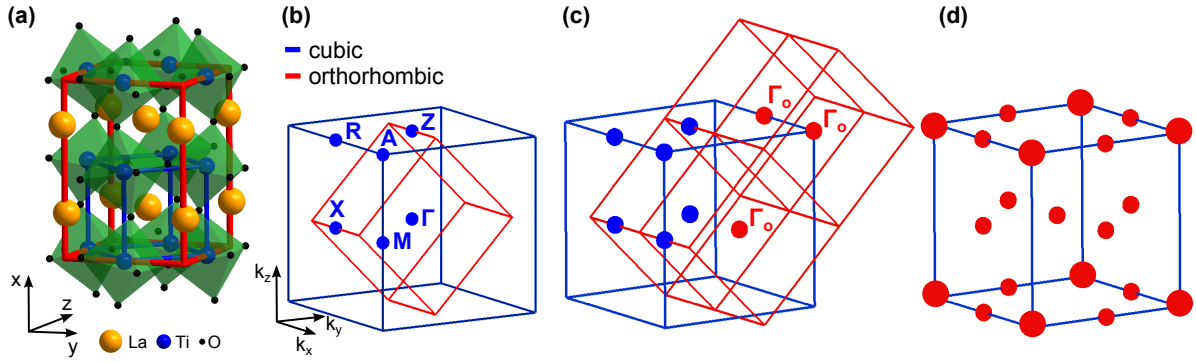
Fig. 7.5: (a) Real space structure of LTO with pseudocubic and orthorhombic unit cells highlighted by blue and red lines, respectively. (b) Corresponding BZs including high symmetry points of the cubic notation. (c) Exemplary positions of higher order gamma points of the orthorhombic cell (Γ_o) with respect to the cubic zone (blue lines). (d) Summary of all Γ_o under consideration of two domains, thicker spheres indicate the overlap of two Γ_o points. See text for details.

correlation strength is characterized by a mass divergence type rather than a vanishing of carriers. Let us now complement these findings by studying another paradigm of correlated electron materials: the doped Mott insulator.

7.3 Band structure of the Doped Mott Insulator LaTiO$_{3+x}$

In chapter 5, it has been demonstrated that the incorporation of excess oxygen ions into LaTiO$_3$ (LTO) thin films is an effective way of p doping, thereby rendering the otherwise Mott insulating material metallic. The filling induced Mott transition into the correlated metal phase causes a strong change of the resistivity (see Fig. 5.14), and the Ti $3d$ angle integrated photoemission spectra comprise a QP and LHB feature reminiscent of the V $3d$ states in SVO. The ARPES experiments presented in the following furthermore allow to gain a deeper insight into the momentum resolved electronic structure of LaTiO$_{3+x}$, and especially to verify that the Luttinger volume corresponds to a $3d^{1-2x}$ filling and not only to the number of dopants, i.e. the amount of excess oxygen ions.

Before discussing the resulting data, we briefly recall the orthorhombic crystal structure of LTO. The TiO$_6$-octahedron tilting system is $(a^+b^-b^-)$, meaning that the octahedra rotations are in-phase along the x axis and out-of-phase along the y and z axis (cf. 7.5 (a)). This is reflected by the extension of the orthorhombic unit cell to $(2 \times \sqrt{2} \times \sqrt{2})$ compared to the cubic case generating one long and two short edges in the real space unit cell as depicted in Fig. 7.5 (a). Therefore, the orthorhombic BZ exhibits one short and two long axes as sketched in Fig. 7.5 (b). For the description of the ARPES data we will, however, not use the orthorhombic notation, but refer to the (pseudo-)cubic zone in order to facilitate the comparison to the SVO case. Due to the reduced symmetry,
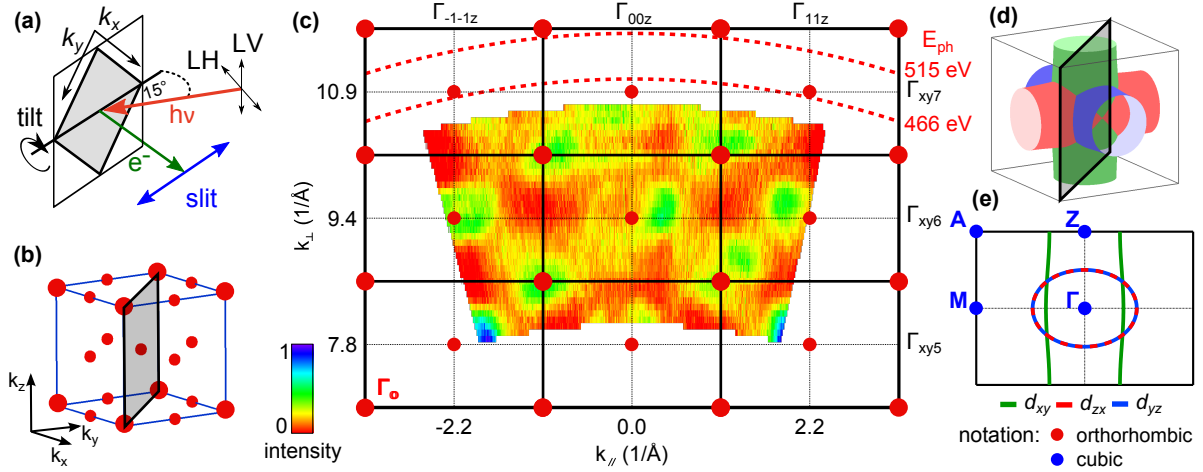
Fig. 7.6: (a) Measurement geometry. (b) Location of Γ_o points with respect to the probed plane, larger red dots indicate the overlap of two Γ_o points. (c) Intensity plot of the measured $LaTiO_{3+x}$ Fermi surface. The coordinate system refers to the pseudocubic structure. Photon energies used for further measurements are represented by the dashed red lines. (d) Fermi surface of the SVO TB model with the measurement plane highlighted. (e) Fermi surface contour expected from the SVO TB model.

higher order Γ points of the orthorhombic cell (Γ_o) overlap with high symmetry points of the cubic zone, which is exemplarily sketched in Fig. 7.5 (c).

Another detail enters the description when we take into account multiple domains for the octahedron tilting scheme, i.e. different orientations of the short axis of the BZ, as has been reported for related materials [185]. In our case the $DyScO_3$ substrate exhibits the same tilting system as LTO, and for the used $(110)_o$-oriented surface the long axis of the real space unit cell is perpendicular to the surface normal. This means that in reciprocal space the short axis of the BZ is in-plane—leaving two possible orientations, either along k_x or along k_y. Most likely both orientations are present in the LTO film forming two domains. Even though the domains have not been detected in experiment, the 2×2 surface reconstruction detected in LEED (see Fig. 5.4) is in line with the assumed in-plane orientation of the short BZ zone axis. Therefore, all resulting Γ_o points of the two-domain scenario are sketched together with the cubic zone in Fig. 7.5 (d). The thicker spheres indicate the overlap of Γ_o points.

Coming to the actual experimental results, let us first inspect a photon energy scan probing the reciprocal space along k_z. The measurement geometry is sketched in Fig. 7.6 (a) and the probed cut through the BZ is highlighted in Fig. 7.6 (b). The detected Fermi surface of this plane is depicted by a false color plot in Fig. 7.6 (c). The measurement is performed with linear horizontally polarized light and the intensity is integrated in the range $E_F \pm 50$ meV. For the conversion from photon energy and angle to units of k, an inner potential of $V_0 = 8$ eV is estimated.

The axes of the Fermi surface map refer to the (pseudo-)*cubic* notation: The thick lines denote the cubic zone boundaries (cf. blue lines of Fig. 7.6 (b)) and the thin lines

cross at the zone centers. The additional Γ_o points of the orthorhombic cell are included by red circles, whereby larger circles indicate the overlap of two Γ_o points from the two domains. The data shows a clear pattern that follows the arrangement of the Γ_o points confirming the above considerations on the orientation of the orthorhombic cell. The quality of the signal is, however, not sufficient to judge whether two domains are present or not, which would manifest itself in higher intensities at k-points where two Γ_o overlap (see larger red dots in Fig. 7.6 (c)). The Fermi surface contours are not as clear and sharp as in the SVO case (cf. Fig. 7.2 (c)). But since the two materials are closely related, we will discuss LTO data on basis of the SVO TB model, which is depicted in Fig. 7.6 (d) for comparison. Following this approach, one can link the regions of high intensity in the data with the ellipse defined by the d_{zx} and d_{yz} contours of the TB Fermi surface as plotted in Fig. 7.6 (e). The data shows not a sharp Fermi contour but rather the range in which the bands are occupied suggesting shallow bands with bandwidths comparable to the integration window (100 meV) and the experimental resolution. Furthermore, no clear trace of the d_{xy} band is identified. Note that the d_{xy} structures are the faintest in the corresponding SVO dataset (see Fig. 7.2 (c)), which may explain their absence here.
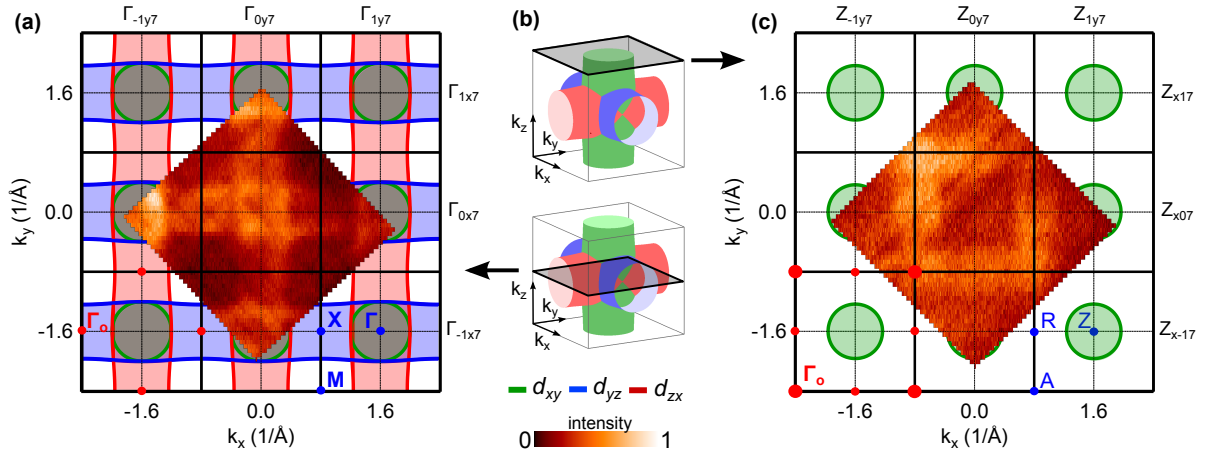

Fig. 7.7: (a) Fermi surface map of LaTiO$_{3+x}$ in the k_x vs. k_y plane measured at $E_{ph} = 466$ eV (Ti L resonance) with LH polarized light and integrated over $E_F \pm 50$ meV. The SVO TB model is included in the background for comparison. High symmetry points of the cubic and orthorhombic notation are marked by blue and red dots, respectively. (b) Probed planes with respect to the SVO Fermi surface. (c) Fermi surface map measured at $E_{ph} = 515$ eV (LH polarization) compiled with an increased integration range of $E_F \pm 200$ meV. Larger red dots indicate the overlap of two Γ_o points.

Further measurements at constant photon energies are carried out at $E_{ph} = 515$ eV and 466 eV in LH polarization to probe the edge and center of the cubic BZ, respectively (see red dashed lines in Fig. 7.6 (c)). The latter photon energy coincides with the Ti L-edge resonance, which is again harnessed to gain a factor of about 30 in intensity. Let us first inspect the cut through the zone center that is depicted in Fig. 7.7 (a). The detected Fermi surface closely resembles the SVO case, which becomes clear from the comparison

to the TB model sketched in the background of the figure. The quantitative agreement of the measured Fermi surface area with the SVO case suggests a *large* Luttinger volume for the doped Mott insulator LTO, i.e. a filling close to d^1. The contours of the intensity map are, however, only weakly pronounced. It seems that signal is picked up not only when a band crosses the Fermi level, but for the whole range in which the band is occupied, i.e. everywhere inside the cylinders of the Fermi surface as sketched in Fig. 7.7 (b). This points again to small bandwidths of the detected structures as discussed above. We note in passing that no additional structures from Γ_o points are detected here.

Clear footprints of the orthorhombic structure are, however, detected in the measurement close to the zone boundary (for orientation see top sketch of Fig. 7.7 (b)). Even though the data integration time has been prolonged by a factor of 4 for this measurement, the detected signal is only weak due to the missing intensity enhancement of the Ti L resonance. To compensate the low intensity, the integration window to compile the Fermi map is enlarged to $E_F \pm 200$ meV. The resulting intensity plot is depicted in Fig. 7.7 (c) together with the expected structures from the SVO TB model in the background. No clear trace of the d_{xy} band around the Z points of the cubic cell is detected. However, intensity is picked up close to the cell edges, which most likely arises from replicas of the d_{yz} and d_{zx} cylinders due to the orthorhombic structure. This becomes clear from the arrangement of the Γ_o points that is exemplarily shown in the lower left edge of Fig. 7.7 (c). Note that both domains are required to explain the signal along the cell edges, when only one domain is present Γ_o points are lined up along k_x or k_y, but not in both directions at the same time (cf. Fig. 7.5 (b) and (c)).

The presented Fermi surface topology of p doped LTO has revealed close similarities to the electronic structure of SVO. The detected additional structures are traced back to the structural orthorhombic distortion. Coming to the dispersion of the involved bands, some indications for a narrow energy scale have already been mentioned above. To gain a more quantitative view on the bandwidth, we now turn to an analysis of the ARPES data in the binding energy vs k plane.

Recalling the measurement geometry (see Fig. 7.6 (a)), it is intuitive to analyze the dispersion along the ΓM direction. To do so, a cut along the tilt direction is extracted from the dataset from which the Fermi surface map presented in Fig. 7.7 (c) has been generated. The bandmap is depicted in Fig. 7.8 (a). A dispersing feature close to the Fermi level and a weak intensity modulation of the LHB located between 1 and 1.5 eV is recognized. Note that within the SVO TB model (cf. Fig. 7.1 (c)), a signal from all three t_{2g} bands is expected along ΓM. Therefore, the dispersing feature detected here most likely comprises more than one band, but the sub-structures cannot be resolved here. Nonetheless, we can investigate the dispersion of this feature more closely in order to quantify its effective band mass and width.

To do so, the EDCs and MDCs are plotted in Fig. 7.8 (b) and (c), respectively. The EDCs have been smoothed for clarity and a dispersing feature around Γ is clearly visible. Similar to the SVO case discussed above, there is also a non-dispersive contribution to the structure, probably due to defects in the sample. Therefore the intensity does not vanish when the dispersing structure crosses the Fermi level and a finite signal close to
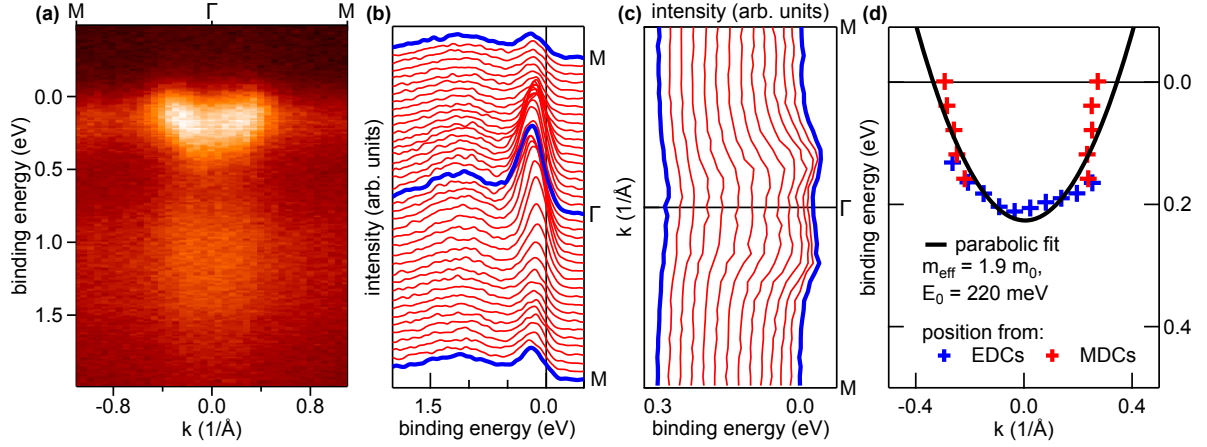
Fig. 7.8: (a) Bandmap of LaTiO$_{3+x}$ along ΓX, k axis is scanned by tilting the sample perpendicular to the slit direction. (b) EDCs extracted from the bandmap. To facilitate the identification of the features, the data has been smoothed. (c) Corresponding MDCs. (d) Band dispersion as inferred from the EDC and MDC maxima together with a parabolic fit to the data.

the M point remains. This non-dispersive contribution has been accounted for during the determination of the band maxima by subtracting the M point spectra from each EDC. The resulting spectra are then fitted by a Gaussian profile multiplied with a Fermi cutoff. Complementary information to trace the dispersion is gained by inspecting the MDCs in Fig. 7.8 (c). Even though the signal is weak, two local maxima are detected close to the Fermi level. The position of these maxima is extracted by fitting the data with two Lorentzians. In this way the dispersion relation is determined from the EDCs and MDCs and the results are compiled in Fig. 7.8 (d). To characterize the dispersion a parabolic fit of the data is performed, which yields an effective band mass of $m_{eff} = 1.9\,m_0$ and a band bottom at $E_0 = 220\,$meV. Even though we cannot identify the exact dispersion for the multiple bands involved here, the simple parabolic fit reveals a is significantly smaller bandwidth here than for SVO (cf. Fig. 7.4). The even shallower dispersion of doped LTO compared to the correlated metal SVO suggests that this doped Mott insulator is closer to the Mott insulating phase.

In summary, the ARPES measurements have revealed that the Luttinger volume of correlated electron systems directly reflects their band filling and that the correlations manifest themselves in a narrowing of the bandwidth. In the case of SVO, the Fermi surface contour is found to quantitatively match the TB model which is in line with a d^1 filling. The electronic correlations induce the emergence of the LHB and a renormalization of the coherent band's energy scale—or in other words a decrease of the effective bandwidth. Coming to the Mott insulator LTO, the ARPES measurements demonstrate that a coherent QP band is induced by excess oxygen doping. The associated Fermi surface compares well to the SVO case, which suggests that the doping induced Mott transition renders *all d* electrons mobile. These results do not only provide vital insights into the Mott transition, but also demonstrate important characteristics that

are of potential use for future electronic devices. As motivated in chapter 5.5, LTO is a promising channel material for Mottronics. These considerations are further underlined by the ARPES results presented here, since they provide experimental evidence that excess oxygen doping of LTO indeed releases *all* previously localized electrons for conductivity, suggesting to harness this phase transition for electronic switches.

8 Summary

Within this thesis, the electronic properties of strongly correlated electron materials are investigated. The focus is set on a variety of photoelectron spectroscopy techniques that are especially useful to characterize the involved many body physics. From the material side, the correlated metal $SrVO_3$ and the Mott insulator $LaTiO_3$ are identified as prototypical samples. Both compounds are synthesized as thin films, which not only allows to study their electronic properties, but also to manipulate their electronic phase.

For $SrVO_3$ thin films, it is demonstrated that the Mott metal-to-insulator transition is driven by reducing the layer thickness, which is referred to as a dimensional crossover. The systematic optimization of the film growth by pulsed laser deposition together with a careful analysis of the vanadium valence by core-level photoemission reveals that excess oxygen ions are adsorbed at the surface, even when samples are handled *in situ*, i.e. without exposure to air. In order to avoid this extrinsic chemical contribution, structures including an epitaxial $SrTiO_3$ capping layer are developed. These samples are not only found to stabilize the correct vanadium valency, but also passivate the surface against exposure to air facilitating sample handling and allowing for complementary transport measurements. The spectral function of these stoichiometric capped thin films is then probed by valence band photoemission in the soft x-ray regime, and the critical thickness for the Mott transition is found to be larger than for the bare—and over-oxidized— films. These results provide instructive experimental data on the Mott transition and demonstrate that seemingly mundane issues as adsorbed oxygen can severely disguise the electronic structure.

The oxygen stoichiometry is an even more delicate problem in the case of $LaTiO_3$ thin films. Usually, these films are grown on $SrTiO_3$ substrates, but by means of *in situ* photoelectron spectroscopy it is shown that such films suffer from a strong over-oxidation impeding an investigation of the Mott insulating phase. The substrate is identified as the source of the excess oxygen and the problem is overcome by switching to the more suitable substrate material $DyScO_3$. Furthermore, and similar to the case of $SrVO_3$ films, the surface is passivated by an $LaAlO_3$ capping layer allowing for the fabrication of fully stoichiometric $LaTiO_3$ thin films. Having gained control of the oxygen stoichiometry, the tendency of $LaTiO_3$ to over-oxidize is harnessed as a way of controlled p doping by simply increasing the oxygen pressure during the growth process. In this way the Mott insulating material is driven into the metallic phase via the band filling controlled Mott transition, which is again verified by photoemission experiments. Furthermore, complementary transport measurements show that this electronic phase transition is characterized by a strong change in resistivity of several orders of magnitude.

These achievements—especially the taming of the oxygen stoichiometry—are significant advancements in material science of the prototypical Mott materials $SrVO_3$ and $LaTiO_3$. The synthesis as thin films and the control of their electronic state as demonstrated in this thesis set the basis for future electronic devices that make use of correlation effects, often referred to as Mottronics.

Besides the prospects for technological developments, the high sample quality also allows for detailed investigations of the electronic structure in clean strongly correlated materials by advanced spectroscopic methods. Resonant photoemission is employed to study the vanadium and titanium $3d$ partial density of states revealing a hybridization of these valence states with oxygen $2p$ electrons. Furthermore, quantitative information on the intensity enhancement of the $3d$ photoemission signal at the L absorption threshold is obtained, which has not been available for related experiments on buried structures such as the $LaAlO_3/SrTiO_3$ heterointerface. The resonant intensity enhancement is also beneficial for the angular-resolved photoelectron spectroscopy (ARPES) measurements, in which hallmarks of the Mott transition, such as the band mass renormalization in the correlated metal $SrVO_3$ or the emergence of a large Fermi surface upon doping the Mott insulator $LaTiO_3$, are verified experimentally.

In conclusion, the thin films of prototypical $3d^1$ transition metal oxides presented in this thesis provide a fascinating playground to investigate and manipulate the electronic phase of Mott materials, once control of their oxygen stoichiometry is gained. It is demonstrated that the Mott transition can be tuned in various ways in thin films of $SrVO_3$ and $LaTiO_3$. As a next step, one can follow Herbert Kroemer's famous statement "the interface is the device" and implement these correlated electron materials in heterostructures to engineer new emergent phases, phenomena or functionalities.

Bibliography

[1] A. Inam, M. S. Hegde, X. D. Wu, T. Venkatesan, P. England, P. F. Miceli, E. W. Chase, C. C. Chang, J. M. Tarascon, and J. B. Wachtman, Applied Physics Letters **53**, 908 (1988).

[2] D. P. Norton, Materials Science and Engineering: R: Reports **43**, 139 (2004).

[3] M. Stafe, A. Marcu, and N. Puscas, *Pulsed laser ablation of solids*, edited by G. Ertl, H. Lüth, and D. Mills (Springer-Verlag, 2014).

[4] D. Norton, *Pulsed laser deposition of thin films*, edited by R. Eason (Wiley, 2007).

[5] R. K. Singh and J. Narayan, Physical Review B **41**, 8843 (1990).

[6] J. Chen, M. Döbeli, D. Stender, K. Conder, A. Wokaun, C. W. Schneider, and T. Lippert, Applied Physics Letters **105**, 114104 (2014).

[7] J. A. Venables, G. D. T. Spiller, and M. Hanbucken, Reports on Progress in Physics **47**, 399 (1984).

[8] P. Scheiderer, F. Pfaff, J. Gabel, M. Kamp, M. Sing, and R. Claessen, Physical Review B **92**, 195422 (2015).

[9] A. Ichimiya and P. Cohen, *Reflection high-energy electron diffraction* (Cambridge University Press, 2004).

[10] T. Terashima, Y. Bando, K. Iijima, K. Yamamoto, K. Hirata, K. Hayashi, K. Kamigaki, and H. Terauchi, Physical Review Letters **65**, 2684 (1990).

[11] M. C. Sullivan, M. J. Ward, A. Gutiérrez-Llorente, E. R. Adler, H. Joress, A. Woll, and J. D. Brock, Applied Physics Letters **106**, 031604 (2015).

[12] G. Leggett, *Surface analysis the principal techniques*, edited by J. Vickerman and I. Gilmore (Wiley, 2009).

[13] O. Kaul, *Forschung mit Synchrotronstrahlung*, edited by J. Falta and T. Möller (Vieweg+Teubner Verlag, 2010).

[14] H. Hertz, Annalen der Physik **267**, 983 (1887).

[15] A. Einstein, Annalen der Physik **17**, 132 (1905).

[16] K. Siegbahn, *Electron spectroscopy for atoms, molecules and condensed matter*, (Nobel lecture, 1981).

[17] A. Damascelli, Physica Scripta **2004**, 61 (2004).

[18] S. Suga and A. Sekiyama, *Photoelectron spectroscopy* (Springer, 2014).

[19] S. Hüfner, *Photoelectron spectroscopy. Principles and Applications* (Springer, 203).

[20] J. B. Pendry, Surface Science **57**, 679 (1976).

[21] C. N. Berglund and W. E. Spicer, Physical Review **136**, A1030 (1964).

[22] S Doniach and M Sunjic, Journal of Physics C: Solid State Physics **3**, 285 (1970).

[23] L. Hedin and J. D. Lee, Journal of Electron Spectroscopy and Related Phenomena, Frontiers in photoemission spectroscopy of solids and surfaces **124**, 289 (2002).

[24] M. Sing, G. Berner, K. Goß, A. Müller, A. Ruff, A. Wetscherek, S. Thiel, J. Mannhart, S. A. Pauli, C. W. Schneider, P. R. Willmott, M. Gorgoi, F. Schäfers, and R. Claessen, Physical Review Letters **102**, 176805 (2009).

[25] P. Scheiderer, M. Schmitt, J. Gabel, M. Zapf, M. Stübinger, P. Schütz, L. Dudy, C. Schlueter, T.-L. Lee, M. Sing, and R. Claessen, Advanced Materials **30**, 1706708 (2018).

[26] P. J. Cumpson and M. P. Seah, Surface and Interface Analysis **25**, 430 (1997).

[27] M. P. Seah and W. A. Dench, Surface and Interface Analysis **1**, 2 (1979).

[28] J. J. Yeh and I. Lindau, Atomic Data and Nuclear Data Tables **32**, 1 (1985).

[29] S. Tanuma, C. J. Powell, and D. R. Penn, Surface and Interface Analysis **21**, 165 (1994).

[30] S. Tanuma, T. Shiratori, T. Kimura, K. Goto, S. Ichimura, and C. J. Powell, Surface and Interface Analysis **37**, 833 (2005).

[31] D. A. Shirley, Physical Review B **5**, 4709 (1972).

[32] U. Fano, Physical Review **124**, 1866 (1961).

[33] J. Ghijsen, L. H. Tjeng, H. Eskes, G. A. Sawatzky, and R. L. Johnson, Physical Review B **42**, 2268 (1990).

[34] A. Tanaka and T. Jo, Journal of the Physical Society of Japan **63**, 2788 (1994).

[35] N. Mårtensson, M. Weinelt, O. Karis, M. Magnuson, N. Wassdahl, A. Nilsson, J. Stöhr, and M. Samant, Applied Physics A **65**, 159 (1997).

[36] P. A. Brühwiler, O. Karis, and N. Mårtensson, Reviews of Modern Physics **74**, 703 (2002).

[37] G. Drera, "Electronic structure of TiO_2 thin films and $LaAlO_3$-$SrTiO_3$ heterostructures: the role of titanium $3d^1$ states in magnetic and transport properties", PhD thesis (University Milano, 2010).

[38] G. Drera, G. Salvinelli, F. Bondino, E. Magnano, M. Huijben, A. Brinkman, and L. Sangaletti, Physical Review B **90**, 035124 (2014).

[39] L. C. Davis, Physical Review B **25**, 2912 (1982).

[40] T. Kashiwakura, S. Suzuki, T. Okane, S. Sato, T. Kinoshita, A. Kakizaki, T. Ishii, Y. Isikawa, H. Yamagami, and A. Hasegawa, Physical Review B **47**, 6885 (1993).

[41] H. Bethe, Annalen der Physik **392**, 55 (1928).

[42] F. Bloch, Zeitschrift für Physik **52**, 555 (1929).

[43] A. Sommerfeld, Zeitschrift für Physik **47**, 1 (1928).

[44] N. F. Mott and R. Peierls, Proceedings of the Physical Society **49**, 72 (1937).

[45] N. F. Mott, *Metal-Insulator Transitions*, the 2nd edition (Taylor & Francis Ltd, London, 1990).

[46] M. Imada, A. Fujimori, and Y. Tokura, Reviews of Modern Physics **70**, 1039 (1998).

[47] N. F. Mott, Proceedings of the Physical Society. Section A **62**, 416 (1949).

[48] N. F. Mott, Philosophical Magazine **6**, 287 (1961).

[49] J. Hubbard, Proc. R. Soc. Lond. A **276**, 238 (1963).

[50] M. C. Gutzwiller, Physical Review Letters **10**, 159 (1963).

[51] J. Kanamori, Progress of Theoretical Physics **30**, 275 (1963).

[52] J. Hubbard, Proc. R. Soc. Lond. A **281**, 401 (1964).

[53] W. F. Brinkman and T. M. Rice, Physical Review B **2**, 4302 (1970).

[54] N. Ashcroft and N. Mermin, *Solid State Physics* (Brooks/Cole, 1976).

[55] A. Georges, G. Kotliar, W. Krauth, and M. J. Rozenberg, Reviews of Modern Physics **68**, 13 (1996).

[56] W. Metzner and D. Vollhardt, Physical Review Letters **62**, 324 (1989).

[57] M. Sing, *Elektronische Korrelationen und kooperative Phänomene in komplexen Festkörpern*, Habilitationsschrift, Julius-Maximilians-Universität Würzburg (2010).

[58] R. Bulla, *private communication with Michael Sing (2001),* see also Phys. Rev. Lett. **83**, 136 (1999).

[59] Z. Zhong, M. Wallerberger, J. M. Tomczak, C. Taranto, N. Parragh, A. Toschi, G. Sangiovanni, and K. Held, Physical Review Letters **114**, 246401 (2015).

[60] J. M. Kurdestany and S. Satpathy, Physical Review B **96**, 085132 (2017).

[61] C.-H. Yee and L. Balents, Physical Review X **5**, 021007 (2015).

[62] J. Zaanen, G. A. Sawatzky, and J. W. Allen, Physical Review Letters **55**, 418 (1985).

[63] V. M. Goldschmidt, Naturwissenschaften **14**, 477 (1926).

[64] R. D. Shannon, Acta Crystallographica Section A: Crystal Physics, Diffraction, Theoretical and General Crystallography **32**, 751 (1976).

[65] A. M. Glazer, Acta Crystallographica Section B Structural Crystallography and Crystal Chemistry **28**, 3384 (1972).

[66] A. M. Glazer, Acta Crystallographica Section A **31**, 756 (1975).

[67] A. Fujimori, I. Hase, H. Namatame, Y. Fujishima, Y. Tokura, H. Eisaki, S. Uchida, K. Takegahara, and F. M. F. de Groot, Physical Review Letters **69**, 1796 (1992).

[68] R. J. O. Mossanek, M. Abbate, T. Yoshida, A. Fujimori, Y. Yoshida, N. Shirakawa, H. Eisaki, S. Kohno, and F. C. Vicentin, Physical Review B **78**, 075103 (2008).

[69] H. Makino, I. H. Inoue, M. J. Rozenberg, I. Hase, Y. Aiura, and S. Onari, Physical Review B **58**, 4384 (1998).

[70] Y. Okimoto, T. Katsufuji, Y. Okada, T. Arima, and Y. Tokura, Physical Review B **51**, 9581 (1995).

[71] E. Pavarini, S. Biermann, A. Poteryaev, A. I. Lichtenstein, A. Georges, and O. K. Andersen, Physical Review Letters **92**, 176403 (2004).

[72] O. Gunnarsson, E. Koch, and R. M. Martin, Physical Review B **56**, 1146 (1997).

[73] S. Florens, A. Georges, G. Kotliar, and O. Parcollet, Physical Review B **66**, 205102 (2002).

[74] N. Manini, G. E. Santoro, A. Dal Corso, and E. Tosatti, Physical Review B **66**, 115107 (2002).

[75] M. W. Haverkort, Z. Hu, A. Tanaka, G. Ghiringhelli, H. Roth, M. Cwik, T. Lorenz, C. Schüßler-Langeheine, S. V. Streltsov, A. S. Mylnikova, V. I. Anisimov, C. de Nadai, N. B. Brookes, H. H. Hsieh, H.-J. Lin, C. T. Chen, T. Mizokawa, Y. Taguchi, Y. Tokura, D. I. Khomskii, and L. H. Tjeng, Physical Review Letters **94**, 056401 (2005).

[76] I. H. Inoue, I. Hase, Y. Aiura, A. Fujimori, Y. Haruyama, T. Maruyama, and Y. Nishihara, Physical Review Letters **74**, 2539 (1995).

[77] M. J. Rozenberg, I. H. Inoue, H. Makino, F. Iga, and Y. Nishihara, Physical Review Letters **76**, 4781 (1996).

[78] A. Sekiyama, H. Fujiwara, S. Imada, S. Suga, H. Eisaki, S. I. Uchida, K. Takegahara, H. Harima, Y. Saitoh, I. A. Nekrasov, G. Keller, D. E. Kondakov, A. V. Kozhevnikov, T. Pruschke, K. Held, D. Vollhardt, and V. I. Anisimov, Physical Review Letters **93**, 156402 (2004).

[79] H. Lee, K. Foyevtsova, J. Ferber, M. Aichhorn, H. O. Jeschke, and R. Valentí, Physical Review B **85**, 165103 (2012).

[80] C. Taranto, M. Kaltak, N. Parragh, G. Sangiovanni, G. Kresse, A. Toschi, and K. Held, Physical Review B **88**, 165119 (2013).

[81] J. M. Tomczak, M. Casula, T. Miyake, and S. Biermann, Physical Review B **90**, 165138 (2014).

[82] A. v. Roekeghem and S. Biermann, EPL **108**, 57003 (2014).

[83] M. Takizawa, M. Minohara, H. Kumigashira, D. Toyota, M. Oshima, H. Wadati, T. Yoshida, A. Fujimori, M. Lippmaa, M. Kawasaki, H. Koinuma, G. Sordi, and M. Rozenberg, Physical Review B **80**, 235104 (2009).

[84] K. Yoshimatsu, T. Okabe, H. Kumigashira, S. Okamoto, S. Aizaki, A. Fujimori, and M. Oshima, Physical Review Letters **104**, 147601 (2010).

[85] K. Yoshimatsu, K. Horiba, H. Kumigashira, T. Yoshida, A. Fujimori, and M. Oshima, Science **333**, 319 (2011).

[86] J. A. Moyer, C. Eaton, and R. Engel-Herbert, Advanced Materials **25**, 3578 (2013).

[87] L. Zhang, Y. Zhou, L. Guo, W. Zhao, A. Barnes, H.-T. Zhang, C. Eaton, Y. Zheng, M. Brahlek, H. F. Haneef, N. J. Podraza, M. H. W. Chan, V. Gopalan, K. M. Rabe, and R. Engel-Herbert, Nature Materials **15**, 204 (2016).

[88] K. Ellmer, Nature Photonics **6**, 809 (2012).

[89] B. Bérini, V. Demange, M. Bouttemy, E. Popova, N. Keller, Y. Dumont, and A. Fouchet, Advanced Materials Interfaces **3**, 16000274 (2016).

[90] S. Backes, T. C. Rödel, F. Fortuna, E. Frantzeskakis, P. Le Fère, F. Bertran, M. Kobayashi, R. Yukawa, T. Mitsuhashi, M. Kitamura, K. Horiba, H. Kumigashira, R. Saint-Martin, A. Fouchet, B. Berini, Y. Dumont, A. J. Kim, F. Lechermann, H. O. Jeschke, M. J. Rozenberg, R. Valentí, and A. F. Santander-Syro, Physical Review B **94**, 241110 (2016).

[91] Y. Okada, S.-Y. Shiau, T.-R. Chang, G. Chang, M. Kobayashi, R. Shimizu, H.-T. Jeng, S. Shiraki, H. Kumigashira, A. Bansil, H. Lin, and T. Hitosugi, Physical Review Letters **119**, 086801 (2017).

[92] G. Koster, B. L. Kropman, G. J. H. M. Rijnders, D. H. A. Blank, and H. Rogalla, Applied Physics Letters **73**, 2920 (1998).

[93] M. Gu, S. A. Wolf, and J. Lu, Advanced Materials Interfaces **1**, 1300126 (2014).

[94] C. Cancellieri, N. Reyren, S. Gariglio, A. D. Caviglia, A. Fête, and J.-M. Triscone, EPL **91**, 17004 (2010).

[95] P. Pal, P. Kumar, A. V., A. Dogra, and A. G. Joshi, Journal of Applied Physics **116**, 053704 (2014).

[96] R. Eguchi, M. Taguchi, M. Matsunami, K. Horiba, K. Yamamoto, A. Chainani, Y. Takata, M. Yabashi, D. Miwa, Y. Nishino, K. Tamasaku, T. Ishikawa, Y. Senba, H. Ohashi, I. H. Inoue, Y. Muraoka, Z. Hiroi, and S. Shin, Journal of Electron Spectroscopy and Related Phenomena **156-158**, 421 (2007).

[97] J. Laverock, J. Kuyyalil, B. Chen, R. P. Singh, B. Karlin, J. C. Woicik, G. Balakrishnan, and K. E. Smith, Physical Review B **91**, 165123 (2015).

[98] K. Horiba, M. Taguchi, A. Chainani, Y. Takata, E. Ikenaga, D. Miwa, Y. Nishino, K. Tamasaku, M. Awaji, A. Takeuchi, M. Yabashi, H. Namatame, M. Taniguchi, H. Kumigashira, M. Oshima, M. Lippmaa, M. Kawasaki, H. Koinuma, K. Kobayashi, T. Ishikawa, and S. Shin, Physical Review Letters **93**, 236401 (2004).

[99] G. Silversmit, D. Depla, H. Poelman, G. B. Marin, and R. De Gryse, Journal of Electron Spectroscopy and Related Phenomena **135**, 167 (2004).

[100] O. Gunnarsson, E. Koch, and R. M. Martin, Physical Review B **54**, R11026 (1996).

[101] L. Dudy, M. Sing, P. Scheiderer, J. D. Denlinger, P. Schütz, J. Gabel, M. Buchwald, C. Schlueter, T.-L. Lee, and R. Claessen, Advanced Materials **28**, 7443 (2016).

[102] E. Dagotto, T. Hotta, and A. Moreo, Physics Reports **344**, 1 (2001).

[103] E. Dagotto, Science **309**, 257 (2005).

[104] V. B. Shenoy, D. D. Sarma, and C. N. R. Rao, ChemPhysChem **7**, 2053 (2006).

[105] K. M. Lang, V. Madhavan, J. E. Hoffman, E. W. Hudson, H. Eisaki, S. Uchida, and J. C. Davis, Nature **415**, 412 (2002).

[106] J. Gabel, M. Zapf, P. Scheiderer, P. Schütz, L. Dudy, M. Stübinger, C. Schlueter, T.-L. Lee, M. Sing, and R. Claessen, Physical Review B **95**, 195109 (2017).

[107] G. Berner, A. Müller, F. Pfaff, J. Walde, C. Richter, J. Mannhart, S. Thiess, A. Gloskovskii, W. Drube, M. Sing, and R. Claessen, Physical Review B **88**, 115111 (2013).

[108] P. Schütz, F. Pfaff, P. Scheiderer, Y. Z. Chen, N. Pryds, M. Gorgoi, M. Sing, and R. Claessen, Physical Review B **91**, 165118 (2015).

[109] S. A. Chambers, T. Droubay, T. C. Kaspar, M. Gutowski, and M. van Schilfgaarde, Surface Science **554**, 81 (2004).

[110] T. Katsufuji, Y. Taguchi, and Y. Tokura, Physical Review B **56**, 10145 (1997).

[111] M. H. Sage, G. R. Blake, and T. T. M. Palstra, Physical Review B **77**, 155121 (2008).

[112] D. Groenendijk, C. Autieri, J. Girovsky, M. C. Martinez-Velarte, N. Manca, G. Mattoni, A. Monteiro, N. Gauquelin, J. Verbeeck, A. Otte, M. Gabay, S. Picozzi, and A. Caviglia, Physical Review Letters **119**, 256403 (2017).

[113] P. Dougier, J. C. C. Fan, and J. B. Goodenough, Journal of Solid State Chemistry **14**, 247 (1975).

[114] D. C. Licciardello and D. J. Thouless, Physical Review Letters **35**, 1475 (1975).

[115] G. Berner, M. Sing, H. Fujiwara, A. Yasui, Y. Saitoh, A. Yamasaki, Y. Nishitani, A. Sekiyama, N. Pavlenko, T. Kopp, C. Richter, J. Mannhart, S. Suga, and R. Claessen, Physical Review Letters **110**, 247601 (2013).

[116] P. Schütz, D. V. Christensen, V. Borisov, F. Pfaff, P. Scheiderer, L. Dudy, M. Zapf, J. Gabel, Y. Z. Chen, N. Pryds, V. A. Rogalev, V. N. Strocov, C. Schlueter, T.-L. Lee, H. O. Jeschke, R. Valentí, M. Sing, and R. Claessen, Physical Review B **96**, 161409 (2017).

[117] R. Eguchi, T. Kiss, S. Tsuda, T. Shimojima, T. Mizokami, T. Yokoya, A. Chainani, S. Shin, I. H. Inoue, T. Togashi, S. Watanabe, C. Q. Zhang, C. T. Chen, M. Arita, K. Shimada, H. Namatame, and M. Taniguchi, Physical Review Letters **96**, 076402 (2006).

[118] H. Ishida, D. Wortmann, and A. Liebsch, Physical Review B **73**, 245421 (2006).

[119] T. Arima, Y. Tokura, and J. B. Torrance, Physical Review B **48**, 17006 (1993).

[120] Y. Tokura, Y. Taguchi, Y. Okada, Y. Fujishima, T. Arima, K. Kumagai, and Y. Iye, Physical Review Letters **70**, 2126 (1993).

[121] B. Vilquin, T. Kanki, T. Yanagida, H. Tanaka, and T. Kawai, Solid State Communications **136**, 328 (2005).

[122] F. B. Wang, J. Li, P. Wang, X. H. Zhu, M. J. Zhang, Z. H. Peng, S. L. Li, L. P. Yong, Y. F. Chen, X. S. Sun, and D. N. Zheng, Journal of Physics: Condensed Matter **18**, 5835 (2006).

[123] S. Gariglio, J. W. Seo, J. Fompeyrine, J.-P. Locquet, and J.-M. Triscone, Physical Review B **63**, 161103 (2001).

[124] J. Li, F. B. Wang, P. Wang, M. J. Zhang, H. Y. Tian, and D. N. Zheng, Physical Review B **75**, 195109 (2007).

[125] F. J. Wong, S.-H. Baek, R. V. Chopdekar, V. V. Mehta, H.-W. Jang, C.-B. Eom, and Y. Suzuki, Physical Review B **81**, 161101 (2010).

[126] F. Lichtenberg, A. Herrnberger, K. Wiedenmann, and J. Mannhart, Progress in Solid State Chemistry **29**, 1 (2001).

[127] F. Lichtenberg, A. Herrnberger, and K. Wiedenmann, Progress in Solid State Chemistry **36**, 253 (2008).

[128] M. A. Petrova, A. S. Novikova, and R. G. Grebenshchikov, Inorganic Materials **39**, 509 (2003).

[129] J. W. Seo, J. Fompeyrine, H. Siegwart, and J.-P. Locquet, Physical Review B **63**, 205401 (2001).

[130] J. A. Baglio and J. N. Dann, Journal of Solid State Chemistry **4**, 87 (1972).

[131] A. Ohtomo, D. A. Muller, J. L. Grazul, and H. Y. Hwang, Applied Physics Letters **80**, 3922 (2002).

[132] M. Takizawa, H. Wadati, K. Tanaka, M. Hashimoto, T. Yoshida, A. Fujimori, A. Chikamatsu, H. Kumigashira, M. Oshima, K. Shibuya, T. Mihara, T. Ohnishi, M. Lippmaa, M. Kawasaki, H. Koinuma, S. Okamoto, and A. J. Millis, Physical Review Letters **97**, 057601 (2006).

[133] J. Biscaras, N. Bergeal, A. Kushwaha, T. Wolf, A. Rastogi, R. C. Budhani, and J. Lesueur, Nature Communications **1**, 89 (2010).

[134] Y. J. Chang, L. Moreschini, A. Bostwick, G. A. Gaines, Y. S. Kim, A. L. Walter, B. Freelon, A. Tebano, K. Horn, and E. Rotenberg, Physical Review Letters **111**, 126401 (2013).

[135] C. Lin, A. Posadas, T. Hadamek, and A. A. Demkov, Physical Review B **92**, 035110 (2015).

[136] M. N. Grisolia, F. Y. Bruno, D. Sando, H. J. Zhao, E. Jacquet, X. M. Chen, L. Bellaiche, A. Barthélémy, and M. Bibes, Applied Physics Letters **105**, 172402 (2014).

[137] P. Xu, Y. Ayino, C. Cheng, V. S. Pribiag, R. B. Comes, P. V. Sushko, S. A. Chambers, and B. Jalan, Physical Review Letters **117**, 106803 (2016).

[138] S. Havelia, K. R. Balasubramaniam, S. Spurgeon, F. Cormack, and P. A. Salvador, Journal of Crystal Growth **310**, 1985 (2008).

[139] J. E. Kleibeuker, Z. Zhong, H. Nishikawa, J. Gabel, A. Müller, F. Pfaff, M. Sing, K. Held, R. Claessen, G. Koster, and G. Rijnders, Physical Review Letters **113**, 237402 (2014).

[140] A. S. Disa, D. P. Kumah, A. Malashevich, H. Chen, D. A. Arena, E. D. Specht, S. Ismail-Beigi, F. J. Walker, and C. H. Ahn, Physical Review Letters **114**, 026801 (2015).

[141] Y. Cao, X. Liu, M. Kareev, D. Choudhury, S. Middey, D. Meyers, J.-W. Kim, P. J. Ryan, J. W. Freeland, and J. Chakhalian, Nature Communications **7**, 10418 (2016).

[142] C. W. Schneider, M. Esposito, I. Marozau, K. Conder, M. Doebeli, Y. Hu, M. Mallepell, A. Wokaun, and T. Lippert, Applied Physics Letters **97**, 192107 (2010).

[143] A. E. Paladino, L. G. Rubin, and J. S. Waugh, Journal of Physics and Chemistry of Solids **26**, 391 (1965).

[144] V. E. Henrich, G. Dresselhaus, and H. J. Zeiger, Physical Review B **17**, 4908 (1978).

[145] A. B. Posadas, K. J. Kormondy, W. Guo, P. Ponath, J. Geler-Kremer, T. Hadamek, and A. A. Demkov, J. Appl. Phys. **121**, 105302 (2017).

[146] J. E. Kleibeuker, B. Kuiper, S. Harkema, D. H. A. Blank, G. Koster, G. Rijnders, P. Tinnemans, E. Vlieg, P. B. Rossen, W. Siemons, G. Portale, J. Ravichandran, J. M. Szepieniec, and R. Ramesh, Physical Review B **85**, 165413 (2012).

[147] M. Schmitt, *Epitaktisches Wachstum und Charakterisierung des d^1-Mott-Isolators Lanthantitanat*, Masterarbeit, Universität Würzburg, Lehrstuhl für Experimentelle Physik 4 (2016).

[148] C. Chang, T. Koethe, Z. Hu, J. Weinen, S. Agrestini, L. Zhao, J. Gegner, H. Ott, G. Panaccione, H. Wu, M. Haverkort, H. Roth, A. Komarek, F. Offi, G. Monaco, Y.-F. Liao, K.-D. Tsuei, H.-J. Lin, C. Chen, A. Tanaka, and L. Tjeng, Physical Review X **8**, 021004 (2018).

[149] A. Ruosi, C. Raisch, A. Verna, R. Werner, B. A. Davidson, J. Fujii, R. Kleiner, and D. Koelle, Physical Review B **90**, 125120 (2014).

[150] M. Taguchi, A. Chainani, N. Kamakura, K. Horiba, Y. Takata, M. Yabashi, K. Tamasaku, Y. Nishino, D. Miwa, T. Ishikawa, S. Shin, E. Ikenaga, T. Yokoya, K. Kobayashi, T. Mochiku, K. Hirata, and K. Motoya, Physical Review B **71**, 155102 (2005).

[151] A. Hariki, T. Uozumi, and J. Kuneš, Physical Review B **96**, 045111 (2017).

[152] S. A. Chambers, M. H. Engelhard, L. Wang, T. C. Droubay, M. E. Bowden, M. J. Wahila, N. F. Quackenbush, L. F. J. Piper, T.-L. Lee, C. J. Nelin, and P. S. Bagus, Physical Review B **96**, 205143 (2017).

[153] Y. Okada, T. Arima, Y. Tokura, C. Murayama, and N. Môri, Physical Review B **48**, 9677 (1993).

[154] Y. Taguchi, T. Okuda, M. Ohashi, C. Murayama, N. Môri, Y. Iye, and Y. Tokura, Physical Review B **59**, 7917 (1999).

[155] T. Yoshida, A. Ino, T. Mizokawa, A. Fujimori, Y. Taguchi, T. Katsufuji, and Y. Tokura, EPL (Europhysics Letters) **59**, 258 (2002).

[156] H. D. Zhou and J. B. Goodenough, Physical Review B **71**, 165119 (2005).

[157] H. Roth, *Single crystal growth and electron spectroscopy of d^1-systems*, PhD Thesis, Universität zu Köln (2008).

[158] C. C. Hays, J.-S. Zhou, J. T. Markert, and J. B. Goodenough, Physical Review B **60**, 10367 (1999).

[159] X. Ke, C. Adamo, D. G. Schlom, M. Bernhagen, R. Uecker, and P. Schiffer, Applied Physics Letters **94**, 152503 (2009).

[160] L. J. van der Pauw, Philipps Technical Review **20**, 220 (1958).

[161] O. Bierwagen, T. Ive, C. G. Van de Walle, and J. S. Speck, Applied Physics Letters **93**, 242108 (2008).

[162] A. Ohtomo and H. Y. Hwang, Nature **427**, 423 (2004).

[163] C. H. Ahn, J.-M. Triscone, and J. Mannhart, Nature **424**, 1015 (2003).

[164] H. Takagi and H. Y. Hwang, Science **327**, 1601 (2010).

[165] D. M. Newns, J. A. Misewich, C. C. Tsuei, A Gupta, B. A. Scott, and A. Schrott, Applied Physics Letters **73**, 780 (1998).

[166] I. H. Inoue, Semicond. Sci. Technol. **20**, 112 (2005).

[167] J. Son, S. Rajan, S. Stemmer, and S. J. Allen, J. Appl. Phys. **110**, 084503 (2011).

[168] F. Chudnovskiy, S. Luryi, and B. Spivak, *Future Trends in Microelectronics: The Nano Millenium*, edited by S. Luryi, J. M. Xu, and A. Zaslavsky (Wiley, Hoboken, New Jersey, 2002), p. 148.

[169] J. Hoffman, X. Hong, and C. H. Ahn, Nanotechnology **22**, 254014 (2011).

[170] H. Yamada, M. Marinova, P. Altuntas, A. Crassous, L. Bégon-Lours, S. Fusil, E. Jacquet, V. Garcia, K. Bouzehouane, A. Gloter, J. E. Villegas, A. Barthélémy, and M. Bibes, Scientific Reports **3**, 2834 (2013).

[171] M. R. Castell, D. A. Muller, and P. M. Voyles, Nature Materials **2**, 129 (2003).

[172] M. Nakano, K. Shibuya, D. Okuyama, T. Hatano, S. Ono, M. Kawasaki, Y. Iwasa, and Y. Tokura, Nature **487**, 459 (2012).

[173] P. Delugas, V. Fiorentini, A. Filippetti, and G. Pourtois, Physical Review B **75**, 115126 (2007).

[174] J. Robertson, The European Physical Journal Applied Physics **28**, 265 (2004).

[175] R. Scherwitzl, P. Zubko, I. G. Lezama, S. Ono, A. F. Morpurgo, G. Catalan, and J.-M. Triscone, Advanced Materials **22**, 5517 (2010).

[176] G. Mazza, A. Amaricci, M. Capone, and M. Fabrizio, Physical Review Letters **117**, 176401 (2016).

[177] J. Kleibeuker, *Reconstructions at complex oxide interfaces*, PhD Thesis, University Twente (2012).

[178] J. Braun, J. Minár, S. Mankovsky, V. N. Strocov, N. B. Brookes, L. Plucinski, C. M. Schneider, C. S. Fadley, and H. Ebert, Physical Review B **88**, 205409 (2013).

[179] P. Schütz, *Growth and characterization of the oxide heterostructure γ-Al_2O_3/$SrTiO_3$*, Masterarbeit, Universität Würzburg, Lehrstuhl für Experimentelle Physik 4 (2014).

[180] M. Wu, J.-C. Zheng, and H.-Q. Wang, Physical Review B **97**, 245138 (2018).

[181] J. Barth, F. Gerken, and C. Kunz, Physical Review B **31**, 2022 (1985).

[182] T. Kaurila, J. Väyrynen, and M. Isokallio, Journal of Physics: Condensed Matter **9**, 6533 (1997).

[183] V. N. Strocov, Journal of Electron Spectroscopy and Related Phenomena **130**, 65 (2003).

[184] E. Pavarini, A. Yamasaki, J. Nuss, and O. K. Andersen, New Journal of Physics **7**, 188 (2005).

[185] P. Schütz, D. Di Sante, L. Dudy, J. Gabel, M. Stübinger, M. Kamp, Y. Huang, M. Capone, M.-A. Husanu, V. N. Strocov, G. Sangiovanni, M. Sing, and R. Claessen, Physical Review Letters **119**, 256404 (2017).

List of Own Publications

- Y. Motoyui, T. Taniuchi, **P. Scheiderer**, L. Jiyeon, J. Gabel, F. Pfaff, M. Sing, M. Lippma, R. Claessen, and S. Shin,
  Imaging the formation of ferromagnetic domains at the $LaAlO_3/SrTiO_3$ interface,
  Journal of the Physical Society of Japan (in print)

- R. Aeschlimann, D. Preziosi, **P. Scheiderer**, M. Sing, S. Valencia, J. Santamaria, C. Luo, H. Ryll, F. Radu, R. Claessen, C. Piamonteze, and M. Bibes,
  A living-dead magnetic layer at the surface of ferrimagnetic $DyTiO_3$ thin films,
  Advanced Materials **30**, 1707489 (2018)

- **P. Scheiderer**, M. Schmitt, J. Gabel, M. Zapf, M. Stübinger, P. Schütz, L. Dudy, C. Schlueter, T.-L. Lee, M. Sing, and R. Claessen,
  Tailoring materials for Mottronics: Excess oxygen doping of a prototypical Mott insulator,
  Advanced Materials **30**, 1706708 (2018)

- P. Schütz, D.V. Christensen, V. Borisov, F. Pfaff, **P. Scheiderer**, L. Dudy, M. Zapf, J. Gabel, Y.Z. Chen, N. Pryds, V. Rogalev, V. Strocov, C. Schlueter, T.-L. Lee, V. Borisov, H.O. Jeschke, R. Valentí, M. Sing, and R. Claessen,
  Microscopic origin of the mobility enhancement at a spinel/perovskite oxide heterointerface revealed by photoemission spectroscop,
  Physical Review B **96**, 161409(R) (2017)

- J. Gabel, M. Zapf, **P. Scheiderer**, P. Schütz, L. Dudy, M. Stübinger, C. Schlueter, T.-L. Lee, M. Sing, and R. Claessen,
  Disentangling specific and generic doping mechanisms for oxide heterostructures,
  Physical Review B **95**, 195109 (2017)

- P. Maier, F. Hartmann, J. Gabel, M. Frank, S. Kuhn, **P. Scheiderer**, B. Leikert, M. Sing, L. Worschech, R. Claessen, and S. Höfling,
  Gate-tunable, normally-on to normally-off memristance transition in patterned $LaAlO_3/SrTiO_3$ interfaces,
  Applied Physics Letters **110**, 093506 (2017)

- L. Dudy, M. Sing, **P. Scheiderer**, J.D. Denlinger, P. Schütz, J. Gabel, M. Buchwald, C. Schlueter, T.-L. Lee, and R. Claessen,
  In situ control of separate electronic phases on $SrTiO_3$-surfaces by oxygen dosing,
  Advanced Materials **28**, 7443 (2016)

- **P. Scheiderer**, F. Pfaff, J. Gabel, M. Kamp, M. Sing, and R. Claessen,
  Surface/interface coupling in an oxide heterostructure: impact of adsorbates on $LaAlO_3/SrTiO_3$,
  Physical Review B **92**, 195422 (2015)

- P. Schütz, F. Pfaff, **P. Scheiderer**, Y.Z. Chen, N. Pryds, M. Gorgoi, M. Sing, and R. Claessen,
  Band bending and alignment at the spinel/perovskite γ-$Al_2O_3/SrTiO_3$ heterointerface,
  Physical Review B **91**, 165118 (2015)

- P. Schütz, F. Pfaff, **P. Scheiderer**, M. Sing, and R. Claessen,
  Monitoring non-pseudomorphic epitaxial growth of spinel/perovskite oxide heterostructures by reflection high-energy electron diffraction,
  Applied Physics Letters **106**, 063108 (2015)

- A. Yamasaki, H. Fujiwara, A. Higashiya, A. Irizawa, O. Kirilmaz, F. Pfaff, **P. Scheiderer**, J. Gabel, M. Sing, T. Muro, M. Yabashi, K. Tamasaku, H. Sato, H. Namatame, M. Taniguchi, A. Hloskovskyy, H. Yoshida, H. Okabe, M. Isobe, J. Akimitsu, W. Drube , R. Claessen, T. Ishikawa, S. Imada, A. Sekiyama, and S. Suga,
  Bulk nature of layered perovskite iridates beyond the Mott scenario: An approach from a bulk-sensitive photoemission study,
  Physical Review B **89**, 121111(R) (2014)

Danksagung

Die letzten Seiten möchte ich nutzen, um mich bei den vielen Menschen zu bedanken, die mich in den vergangenen Jahren unterstützt haben und so diese Arbeit möglich gemacht haben.

Allen voran danke ich Prof. Claessen für die Möglichkeit, meine Promotion an seinem Lehrstuhl anzufertigen. Unter seiner Leitung hat sich eine Arbeitsgruppe entwickelt, die beste Bedingungen für die Forschung bietet. Gut ausgestattete Labors sind dafür natürlich eine Voraussetzung, das freundliche Arbeitsklima, das konstruktive Feedback beispielsweise bei Probevorträgen oder Manuskriptentwürfen, sowie die wissenschaftlichen Diskussionen, bei denen ich sehr viel gelernt habe, sind mindestens genauso wichtig. Ebenso möchte ich mich für die vielen Möglichkeiten bedanken Strahlzeiten an Synchrotrons auf der ganzen Welt durchzuführen. Diese Messzeiten haben für mich einen besonderen Reiz ausgemacht. Darüber hinaus habe ich die Teilnahme an internationalen Konferenzen, Workshops und Sommerschulen als besonders motivierend empfunden, auch dafür vielen Dank!

Als nächstes danke ich Prof. Sing. Michael, vielen Dank für die Bürogespräche, die auch nach meinem Umzug an das andere Ende des Lehrstuhls sehr regelmäßig stattgefunden haben. Dabei habe ich nicht nur von deinem fundierten Fachwissen über Photoemission und korrelierten Elektronensystemen profitiert, sondern auch stets den interessanten Austausch über Tagespolitik genossen. Natürlich möchte ich Dir auch für die zahlreichen Korrekturen von Manuskripten, Strahlzeitanträgen, Postern und vielen weiteren Texten—nicht zuletzt dieser Dissertation—danken. Dieses Feedback war sehr hilfreich und ich habe dadurch viel über das Schreiben und die Darstellung wissentschaftlicher Ergebnisse im Allgemeinen gelernt.

Selbstverständlich geht es in der experimentellen Physik nicht ohne die Hilfe der Kollegen. Deswegen bedanke ich mich bei meinen Mitstreitern Michael Zapf und Judith Gabel dafür, dass wir stets als Team gearbeitet haben, sei es bei Strahlzeiten, den Wartungsarbeiten im Labor oder den regelmäßigen Diskussionen unserer Daten und Experimente. Euch beide nenne ich zuerst, da die Zusammenarbeit sehr weit zurückreicht, bei Zabbi tatsächlich bis zum Vorkurs zu Beginn des Studiums (2007!) und bei Judith bis zu meinem ersten Tag an der EP4, an dem ich das erste Mal die PLD in Aktion gesehen habe (natürlich beim Wachstum von LVO/STO ;-)).

Für die Einarbeitung ins Labor und die Heranführung an das Themengebiet der oxidischen Heterostrukturen möchte ich mich bei Florian Pfaff bedanken. Danke auch an Ozan—the man—Kirilmaz für die Hilfe im Labor, auf Dich kann man immer zählen. Vielen Dank an Lenart, besonders für die tolle Strahlzeit an der ALS. Ein weiteres Danke geht an Florian Adler für das Korrekturlesen dieser Arbeit, die kurzweiligen fachlichen